



UNIVERSITY OF THE BASQUE COUNTRY

DEPARTMENT OF CHEMICAL ENGINEERING

**Development of the dimethyl
ether-to-olefins process: from
fundamentals to the reactor
simulation**

DOCTORAL THESIS

Tomás Cordero-Lanzac

2020



UNIVERSITY OF THE BASQUE COUNTRY
DEPARTMENT OF CHEMICAL ENGINEERING

**Development of the dimethyl
ether-to-olefins process: from
fundamentals to the reactor
simulation**

Author:
Tomás Cordero-Lanzac

Supervisors:
Prof. Javier Bilbao
Prof. Andrés T. Aguayo

*A thesis submitted in fulfillment of the requirements
for the degree of Doctor of Chemical Engineering*

TESI ZUZENDARIAREN BAIMENA TESIA AURKEZTEKO	AUTORIZACIÓN DE LOS DIRECTORES DE TESIS PARA SU PRESENTACIÓN
--------------------------------------------------------	-----------------------------------------------------------------------------

Zuzendariaren izen-abizenak /Nombre y apellidos de los directores:

Javier Bilbao Elorriaga, IFZ /NIF: 14548967H

Andrés T. Aguayo Urquijo, IFZ /NIF: 14703582G

Tesiaren izenburua / Título de la tesis:

Development of the dimethyl ether-to-olefins process: from fundamentals to the reactor simulation

Doktorego programa / Programa de doctorado: **Ingeniería Química**

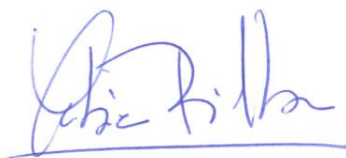
Doktoregaiaren izen-abizenak / Nombre y apellidos del doctorando:

Tomás Cordero Lanzac

Unibertsitateak horretarako jartzen duen tresnak emandako ANTZEKOTASUN TXOSTENA ikusita, baimena ematen dut goian aipatzen den tesia aurkez dadin, horretarako baldintza guztiak betetzen baititu.

Visto el INFORME DE SIMILITUD obtenido de la herramienta que a tal efecto pone a disposición la universidad, autorizo la presentación de la tesis doctoral arriba indicada, dado que reúne las condiciones necesarias para su defensa.

Tokia eta data / Lugar y fecha: Leioa. 24 de Abril de 2020



Fdo: Javier Bilbao Elorriaga



Fdo: Andrés T. Aguayo Urquijo

Tesiaren zuzendaria / Los directores de la tesis

AUTORIZACIÓN DE LA COMISIÓN ACADÉMICA DEL PROGRAMA DE DOCTORADO

La Comisión Académica del Programa de Doctorado en **Ingeniería Química** en reunión celebrada el día 18 de Marzo de 2020, ha acordado dar la conformidad a la presentación de la Tesis Doctoral titulada: **Development of the dimethyl ether-to-olefins process: from fundamentals to the reactor simulation** dirigida por el Dr. **Javier Bilbao Elorriaga** y el Dr. **Andrés T. Aguayo Urquijo** y presentada por Don **Tomás Cordero Lanzac** adscrito al Departamento de **Ingeniería Química**

En Bilbao a 24 de Abril de 2020

EL/LA RESPONSABLE DEL PROGRAMA DE DOCTORADO



Fdo.: José Antonio González Marcos

AUTORIZACIÓN DEL DEPARTAMENTO

El Consejo del Departamento de **Ingeniería Química** en reunión celebrada el día 8 de abril de 2020 ha acordado dar la conformidad a la admisión a trámite de presentación de la Tesis Doctoral titulada: **Development of the dimethyl ether-to-olefins process: from fundamentals to the reactor simulation** dirigida por el Dr. **Javier Bilbao Elorriaga** y el Dr. **Andrés T Aguayo Urquijo** y presentada por Don/ña. **Tomás Cordero Lanzac** ante este Departamento.

En Leioa a 8 de abril de 2020



VºBº DIRECTOR DEL DEPARTAMENTO

SECRETARIO DEL DEPARTAMENTO

Fdo.: Roberto Aguado Zarraga

Fdo.: Rubén López Fonseca

ACTA DE GRADO DE DOCTOR O DOCTORA **ACTA DE DEFENSA DE TESIS DOCTORAL**

DOCTORANDO DON. **Tomás Cordero Lanzac**

TITULO DE LA TESIS: **Development of the dimethy ether-to olefins process: from fundamentals to the reactor simulation**

El Tribunal designado por la Comisión de Postgrado de la UPV/EHU para calificar la Tesis Doctoral arriba indicada y reunido en el día de la fecha, una vez efectuada la defensa por el/la doctorando/a y contestadas las objeciones y/o sugerencias que se le han formulado, ha otorgado por _____ la calificación de:
unanimidad ó mayoría

--

SOBRESALIENTE / NOTABLE / APROBADO / NO APTO

Idioma/s de defensa (en caso de más de un idioma, especificar porcentaje defendido en cada idioma):

Castellano

Euskera

Otros Idiomas (especificar cuál/cuales y porcentaje) _____

En _____ a _____ de _____ de _____

EL/LA PRESIDENTE/A,

EL/LA SECRETARIO/A,

Fdo.:

Fdo.:

Dr/a: _____

Dr/a: _____

VOCAL 1º,

VOCAL 2º,

VOCAL 3º,

Fdo.:

Fdo.:

Fdo.:

Dr/a: _____ Dr/a: _____ Dr/a: _____

EL/LA DOCTORANDO/A,

Fdo.: **Tomás Cordero Lanzac**

Abstract

This thesis is focused on the dimethyl ether(DME)-to-olefins (DTO) process, an alternative to the commercially implemented methanol-to-olefins (MTO). The aim of the work herein is to study this process from mechanistic considerations to the process conception and reactor simulation. Original methodological contributions are proposed within the vast existing knowledge between the selection of the catalyst and the reactor design.

The HZSM-5 catalysts were prepared by the agglomeration of zeolites of different Si/Al ratio in a pseudoboehmite-derived matrix of γ -Al₂O₃. This provides the catalysts with the required mechanical resistance for their industrial application, but also endows them with a hierarchical mesoporous structure that increases the catalyst stability. The characterization of the catalysts by means of N₂ and *tert*-butylamine adsorption-desorption and confocal fluorescence microscopy confirms the efficiency of the preparation method and good dispersion of the zeolite crystals.

The experimental data of DTO reaction were collected in a packed bed reactor for a wide range of conditions (325–400 °C, 1.5 bar, space time up to 6.5 g h mol_C⁻¹ and different DME concentration in the feed, diluted in water and N₂). Especial attention is paid to several factors during the analysis of the results: (i) the relation of the product distribution to the well-known steps of the dual cycle mechanism proposed for the MTO process; (ii) the catalyst deactivation by the deposition of coke and the effect of process variables on its formation, and; (iii) the valorization of the main byproducts in the reaction, the C₅₊ hydrocarbons. Although some synergistic effects are found on the activation of these hydrocarbons in their combined reaction with DME, the valorization of this stream is studied through the catalytic cracking of the less reactive compound in the fraction (*n*-pentane) using the same catalysts. The catalytic cracking experimental runs were carried out at 400–550 °C, 1.5 bar, space time up to 5.0 g h mol_C⁻¹ and different partial pressures of *n*-pentane diluted in N₂.

From the experimental data of both processes, lump-based reaction networks are proposed for kinetic modeling purposes. A mathematical methodology is developed aiming for accurate fittings of the evolution with time of experimental data, for which: (i) the definition of the activity must take the *past history* of the catalyst into account, and; (ii) the reaction and deactivation kinetics are simultaneously computed by a Levenberg-Marquardt-based method with decoupled

Jacobian matrix calculations. After a model discrimination, kinetic models for the DTO process and the catalytic cracking of n -pentane are obtained.

An adaptation of the convection-dispersion-reaction equation based on a balance of available active sites is also proposed for the simulation of different reactor configurations for catalytic processes with deactivation using the computed kinetic models. Modifications of the convection and dispersion terms allow the direct simulation of packed bed (for both processes), moving bed and non-circulating/circulating fluidized bed reactors (for the DTO process). The design of the latter requires the consideration of the residence time distribution of the catalyst that leads to an activity distribution function of the catalytic bed. An original parallel compartment (PC) model is combined with the population balance theory (PB-PC model) for a more rigorous simulation of the circulating fluidized bed reactor (CFBR).

The dual reactor-regenerator system for the DTO process consists of two units operating at the regime of CFBR with a continuous circulation of catalyst between the units. The developed kinetics for the DTO reaction are coupled with a reactivation kinetic model for the regeneration of HZSM-5 zeolite-based catalysts considering that the catalyst at the outlet of each unit is fed into the other. The effect of process variables on the system performance during the unsteady and steady state is analyzed. The most relevant result of these simulations is the approach of the reactor and regenerator performances during the DTO process, provided by kinetic models based on mechanistic considerations. The activity distribution function in each unit, conversion and yields of products are predicted.

Overall, a potential DTO process is described, using HZSM-5 based catalysts and including an integrated process for paraffin byproduct valorization. Moreover, the methodological contributions on kinetic modeling and reactor design proposed in this work can be applied to other processes with catalyst deactivation.

Acknowledgements

Si esta tesis cumple el objetivo propuesto en julio de 2011 es gracias al Prof. Javier Bilbao por aceptar dirigirla. Es imposible agradecer todo lo que he aprendido estos años, no solo de Ingeniería Química y ciencia, sino también muchas otras lecciones en los ámbitos relacionados. Nunca pensé que podría aprender tanto estudiando tan poco, sólo escuchando.

A mi codirector, Prof. Andrés T. Aguayo, por ser parte fundamental del trabajo que refleja esta tesis. Gracias por las múltiples enseñanzas, por ponerme los mayores retos que he afrontado en estos años y por las horas de trabajo codo con codo.

A todas las personas que han colaborado en esta tesis. A la Prof. Ana Gayubo y al Dr. Pedro Castaño por ayudarme a redondear los trabajos. A Héctor Vicente por la colaboración al final de la tesis y a los estudiantes que han aportado su trabajo. Al personal de los servicios generales, Dr. Aitor Larrañaga, Dr. Ricardo Andrade (Sgiker, UPV/EHU) y Dra. María D. Marqués (SCAI, UMA).

A los responsables de las tres estancias realizadas en este periodo de tiempo. Al Prof. Avelino Corma y la Dra. Cristina Martínez del ITQ por la estancia corta, aunque fructífera en Valencia. A la Prof. Unni Olsbye y al Dr. Evgeniy Redekop de la UiO por la gran acogida, confianza y enseñanzas sobre mecanismos de reacción. Al Prof. Jorge Gascón y su grupo por la disponibilidad, libertad ofrecida y trabajo durante tres meses finales en KCC.

A los miembros del grupo CPWV de la UPV/EHU, especialmente a los más afines que tanto me han aportado: Dra. Idoia Hita, Dr. Roberto Palos, Dr. Aitor Arandia, Dra. Beatriz Valle y sobre todo a mi familia de Euskadi: Al Dr. Pablo Rodríguez-Vega por 4 años inolvidables y ser parte de la mayoría de mis historias aquí y a Aitor Atxutegi, porque compartimos una locura similar, y quieras que no, pasar juntos una estancia y una pandemia crea vínculos.

Evidentemente a mi padre, Tomás Cordero, que por razones obvias nadie duda del peso que tiene en este trabajo. No hacerte caso a la hora de elegir la carrera me ha llevado hasta aquí. Y a las mujeres de mi vida, mi hermana Ana y especialmente a mi madre, M^a Ángeles Lanzac, por ser la que peor lleva la distancia, por soportar horas de conversaciones sobre Ingeniería Química, artículos, congresos y experimentos. Gracias a vuestra educación soy lo que soy y nunca podré devolveros todo lo que me habéis enseñado.

Tomás Cordero-Lanzac

La realización de esta tesis ha sido posible gracias a la financiación del Gobierno de España, por la concesión de la beca FPU15/01666, las estancias EST17/00094 y EST18/00101 y los proyectos CTQ2016-77812-R y CTQ2016-79646-P y a la financiación del Gobierno Vasco con el proyecto IT1218-19.

A mi padre

Contents

Abstract	xiii
Acknowledgements	xv
1 Introduction	1
1.1 Dimethyl ether-to-olefins process	2
1.1.1 Dimethyl ether	2
1.1.2 DTO as an alternative to the MTO process	6
1.1.3 Reaction mechanism	10
1.1.4 Formation of coke and deactivation	15
1.2 Catalytic cracking of paraffins	19
1.2.1 Cracking mechanisms	20
1.2.2 Dual conversion of paraffins and oxygenates	23
1.3 Kinetic modeling of complex reaction networks	26
1.3.1 Modeling methodologies	26
1.3.2 Consideration of the deactivation	31
1.4 Design of reactors with catalyst deactivation	35
1.4.1 Operation strategies	36
1.4.2 Consideration of the catalyst circulation	37
1.5 Aim and objectives	41
2 Experimental	43
2.1 Catalyst preparation	44
2.2 Catalyst characterization	46
2.2.1 Crystalline structure	46
2.2.2 Porous structure	46
2.2.3 Acidity	46
2.2.4 Morphology	47
2.3 Reaction equipment and procedures	48
2.3.1 Reaction unit	48
2.3.2 Catalyst pretreatments	50

2.3.3	Reaction conditions	50
2.4	Analysis of reaction products	52
2.5	Analysis of coke by temperature-programmed oxidation	53
2.5.1	Experimental procedure	53
2.5.2	Model for the combustion of coke	53
3	Fundamentals of DTO process	55
3.1	HZSM-5 catalysts	56
3.1.1	Physico-chemical properties	56
3.2	Reaction network and mechanisms	60
3.3	Catalyst deactivation	65
3.3.1	Role of the matrix	65
3.3.2	Role of catalyst acidity	68
3.3.3	Effect of temperature	70
3.3.4	Role of water	72
3.4	Challenges to overcome	76
3.4.1	Catalyst regeneration	76
3.4.2	Byproduct valorization	79
4	Valorization of paraffins	87
4.1	<i>n</i> -Pentane cracking	88
4.1.1	Effect of reaction conditions	88
4.1.2	Catalyst deactivation	89
4.1.3	Role of catalyst acidity	93
4.2	Kinetic modeling considering deactivation	98
4.2.1	Methodology	98
4.2.2	Reaction network for <i>n</i> -pentane catalytic cracking	103
4.2.3	Model discrimination and experimental data fitting	110
4.3	Production of olefins and aromatics	118
5	Kinetic modeling of DTO process	123
5.1	General aspects	124
5.1.1	Reaction network	124
5.1.2	Kinetic equations	126
5.1.3	Deactivation kinetics	128
5.2	Kinetic parameters and model validation	129
5.2.1	CZ140 catalyst	129
5.2.2	Role of catalyst acidity	137
5.3	Relevant magnitudes of the model	140
5.3.1	Water concentration	140

5.3.2	Activity	142
6	Simulation of reactors with catalyst circulation for DTO process	147
6.1	Model of reactors with catalyst circulation	148
6.1.1	Conservation equation for the activity	148
6.1.2	Parallel compartment (PC) model	152
6.1.3	Integration of the population balance (PB) theory	155
6.2	Moving bed reactor	159
6.2.1	Unsteady state	159
6.2.2	Effect of process variables	161
6.2.3	Effect of contact regime	162
6.3	Fluidized bed reactor	165
6.3.1	Unsteady state	165
6.3.2	Effect of process variables	171
6.3.3	Comparison of the catalysts	175
6.4	Fluidized bed regenerator	177
6.4.1	Reactivation kinetics	177
6.4.2	Effect of f_a' at the entrance of the unit	179
6.5	Reactor-regenerator system	183
6.5.1	Unsteady state	184
6.5.2	Effect of process variables	188
6.6	Final remarks on the design of DTO process	193
7	Conclusions	197
	List of Figures	201
	List of Tables	209
	List of Schemes	211
	Nomenclature	213
	References	221

Chapter 1

Introduction

This Chapter gives a first introduction to the state of the art of dimethyl ether (DME) as a reactant aiming for a more sustainable production of hydrocarbons, namely olefins. The advantages of the DME-to-olefins (DTO) process and the proposed variations from the industrially established methanol-to-olefins (MTO) process are discussed. A bibliographic review of the proposed mechanisms for the MTO/DTO process is also provided, as well as the ones that dominate the catalytic cracking of paraffins, one of the undesired byproducts of our main reaction. Catalyst deactivation will be one of the main topics along this thesis, and how this factor has been dealt with for modeling purposes in the literature is also introduced here. From the chemical engineering point of view, the ultimate goal of studying reaction mechanisms and kinetic models should be their application to the reactor design. The methodologies for reactor design reported in the literature are briefly discussed, and the difficulty of considering deactivation in these models is also stated.

1.1 Dimethyl ether-to-olefins process

The environmental crisis related to global warming and the increasing emissions of CO_2 have encouraged alternative routes to crude oil for a more sustainable and efficient production of chemicals and fuels [1]. One of the first priorities must be the development of catalytic processes that allow the increasing demand of light olefins to be satisfied [2]. The goal is to substitute gradually their production from the steam cracking of naphthas, which is a low environmentally friendly process with high energy requirement and CO_2 emissions. Methanol-to-olefins (MTO) process is an interesting alternative. Nonetheless, the analogous production of olefins from dimethyl ether (DME), also called DME-to-olefins (DTO) process, could be even more attractive due to the interest of the one-stage DME synthesis and its potential applications.

1.1.1 Dimethyl ether

Dimethyl ether (DME) is the simplest existing ether, with the chemical formula CH_3OCH_3 . At standard conditions of 1 bar and 25 °C, it is a colorless gas with a boiling point of -24 °C and a relative density of 1.63. Liquid DME has a density of 0.735 g cm^{-3} [3]. Its vapor pressure is similar to that of the liquefied petroleum gas (LPG), making DME storage and transport feasible at the same conditions as the household fuels but in polytetrafluoroethylene (PTFE) cylinders. According to the GESTIS substance database, DME does not present a major toxicity risk to the human health and can be easily detected due to its characteristic ethereal odor [4]. Non-significant environmental impact on the atmosphere has also been reported because of its short mean life of 5 days [5].

DME economy

The estimated demand of DME for 2020 is 80 million tons, mainly directed towards its use as a fuel in Asia (90% of the production). Its first applications were as aerosol [6], and coolant E170 [7]. The increasing demand of DME as a fuel is not only limited for household applications, but also for the automotive industry and electrical energy generation. Apart from these applications, DME is also used at large scale as a green solvent [8], and for enhanced oil recovery processes [9].

As a household fuel, DME has been added to LPG fuels for several decades in rural areas of China and other Asian countries [10]. Moreover, it is a suitable additive for diesel engines because of its high cetane index (ca. 58) and the short delay time in the injection, which are consequences of the weakness of the C–O bonds. Similar to other oxygenated additives (methanol or ethanol), DME does not provide the fuel with S and significantly reduces the emissions of fumes, NO_x and particles [11]. Nevertheless, studies on CO emissions are not conclusive, as

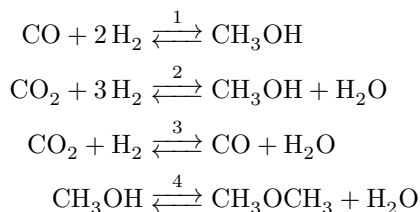
well as those of hydrocarbons and formaldehyde [12]. So, their injection in engines should be regulated. DME vapor has a calorific value of 28620 kJ kg⁻¹, which makes it a promising alternative to methane (49900 kJ kg⁻¹) for the electrical energy generation in gas turbines. For this particular application, pure DME is not required and a mixture of DME (89 wt%), methanol (8 wt%) and water (3 wt%) is considered acceptable in order to facilitate the combustion in the turbine.

The possibilities of DME as a sustainable source of chemicals have increased the value of the DME economy. Among the targeted products, attention has been mostly paid to the production of H₂, aromatics, gasoline [13] and the process in-depth dealt with in this thesis: the conversion of DME into olefins. The lack of C–C bond in its structure and its higher hydrogen content than that of methanol (13 wt%) make DME an encouraging source of H₂ through the steam reforming at low temperature (< 300 °C) [14]. This process is a cleaner alternative for satisfying part of the vast demand of H₂ as energy vector and raw material, due to the sustainable production of DME detailed below.

Production

The industrial production of DME is performed in a two-stage process. The first one is the synthesis of methanol over a metallic catalyst, generally based on CuO-ZnO-Al₂O₃ [15]. In this reaction, the formation of methanol (steps 1 and 2 of Scheme 1.1) is carried out in parallel with the reverse water-gas shift reaction (step 3). In the second stage, methanol is selectively dehydrated to DME over catalysts of moderate acidity, such as γ-Al₂O₃ or passivated HZSM-5 zeolite [16] (step 4).

The one-stage production of DME (STD process) is getting more attention because it offers the possibility of valorizing CO₂, co-fed with *syngas*, at large scale [17]. This *syngas* can also be obtained from alternative sources to crude oil as coal or natural gas, or even from more sustainable ones, such as used plastics, tires and biomass [18]. The integration of the overall process in one reactor using bi-functional catalysts decreases the thermodynamic constraints associated with the



Scheme 1.1. Reaction network for the direct synthesis of DME.

synthesis of methanol. The *in-situ* conversion of methanol into DME displaces the equilibrium of methanol formation, thus favoring the conversion of CO and CO₂. Moreover, feedstocks with lower H₂/CO ratio can be processed in the STD process [19]. Considering these factors, the net CO₂ emissions are notably decreased in the one-stage production of DME [20].

Researches on the direct production of DME are mainly focused on the design and formulation of novelty catalysts [21], and the development of kinetic models for different reactor configurations [22]. The bifunctional catalyst design for the STD process should consider the intermediate temperature and pressure required for the one-stage reaction, between that of methanol synthesis and its dehydration to DME. The thermal stability of the Cu sites have been enhanced by adding different promoters of metallic oxides (Fe, Mg, Mn, Sn, Zr) to the CuO-ZnO main function [23–26]. Aiming for maximum CO₂ valorization and selectivity to methanol, the best results were reported by the substitution of the Al₂O₃ for MnO and ZrO₂ promoters [27].

The most used acid function is γ -Al₂O₃, which is highly selective to DME. However, it is hydrophilic and presents a significant deactivation due to the blockage of the pores in the presence of water. HZSM-5 zeolites with low acidity and silicoaluminophosphates as SAPO-11 and -18 have been used as alternatives with lower hydrophilic character. The catalyst passivation for reducing the acidity and the decrease in the crystal size are among the used strategies in order to attenuate the deactivation by coking [28]. The two introduced strategies for producing DME with these metallic and acid catalysts are displayed in Figures 1.1 (a, two-stage and b, one-stage STD process).

Catalyst design investigations are now targeting the synthesis of structured materials for optimizing the process. The preparation of bifunctional catalysts by physical mixture (b in Figure 1.1) can be enhanced by the separation of both functions in a core-shell structure (metallic core and acid shell, c in Figure 1.1) [29]. An increase in the activity and stability was reported due to the hindered migration of the catalyst component and coupling of the coke formation mechanisms in each function [30].

At industrial scale, the production of DME in two stages is carried out using multitubular packed bed reactors for the first stage of methanol synthesis [22] and a packed bed reactor for its dehydration [31]. The most interesting option for the STD process as an alternative of the methanol production reactor is a packed bed membrane reactor using a highly hydrophilic membrane. The *in-situ* removal of water from the reaction medium displaces the equilibrium of methanol synthesis, the dehydration to DME and the reverse water-gas shift (steps 2, 3 and 4 in Scheme

1.1). This favors the conversion of CO_2 into CO , which is more reactive, thus increasing the total conversion of CO_x (Figure 1.2).

The advantages of the packed bed membrane reactor were simulated for different catalysts and conditions [32, 33]. Rodríguez-Vega [34] validated experimentally

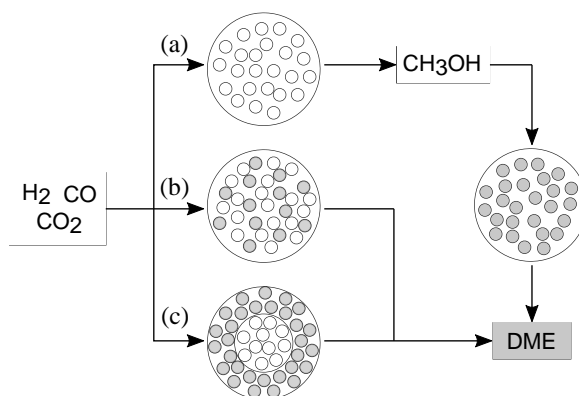


Fig. 1.1. Production of DME in (a) two stages with metallic (white) and acid catalysts (gray) and in one stage with (b) a bifunctional catalyst and (c) a structured core-shell catalyst.

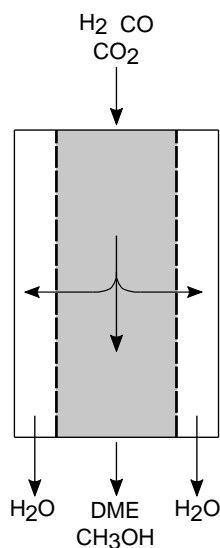


Fig. 1.2. Schematic packed bed membrane reactor for the direct synthesis of DME over a bifunctional catalyst.

the enhancement of DME production, achieving an improvement of 66% of the yield of DME at the worst tested experimental conditions (300 °C, 30 bar and CO/CO₂ ratio of 1).

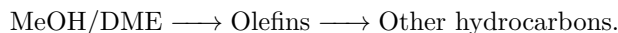
1.1.2 DTO as an alternative to the MTO process

The original interest on the role of DME in the conversion of methanol to hydrocarbons was due to its presence in the reaction medium [35], described by the equilibrium methanol/DME



During the past three decades, great amounts of works have been published on the MTO reaction and certainly, there is not clear consensus in the literature about the existence of different pathways for methanol and DME or which one presents advantages in terms of reactivity, productivity and stability. Moreover, a marked influence of the catalyst and reaction conditions can be deduced from different researches. Which seems clear is the interest of the DTO process regarding their favored and more sustainable synthesis explained above. The commercialized Lurgi process feeds a mixture of methanol/DME/water in the second reactor in series, which is the only example of DME utilization as source of chemicals at industrial scale [36]. The studies on the DME reactivity and DTO reaction are limited to academia and laboratory scale, and are mainly focused on the comparison of catalyst performance and mechanistic pathways that lead the reaction.

Some differences have been observed in the transformation of DME with respect to that of methanol to olefins. Faster reaction and deactivation rates were reported for the transformation of DME using HZSM-5 zeolites [37, 38]. DME was reported to be more reactive than methanol due to its higher proton affinity [39, 40] and its ability to react easily with the intermediate species yielding propylene [41]. Experiments with the same content of water in the reaction medium also proved the higher reactivity of DME using this zeolite [42], which indicates a higher extent of the simplified methanol-to-hydrocarbons (MTH) reaction network



A consequence of the higher reactivity of DME is the absence of an induction period characteristic in the conversion of methanol.

Nevertheless, the shape selectivity of the catalyst and reaction conditions have a strong influence on the reactivity of both oxygenates. Li et al. [43] observed a higher reactivity of methanol (yielding products and coke) using SAPO-34 and very

low partial pressure of the reactant. At similar reaction conditions and catalyst acidity, the higher reactivity of DME over HZSM-5 zeolites than that of SAPO-34 is attributed to the easier evolution of the dual cycle mechanism toward hydrocarbons due to the lower steric constraints [44]. The evolution of the oxygenate conversion using a HZSM-5 catalyst was studied at similar conditions and higher conversions of DME were reported (Figure 1.3a) [45]. The differences are remarkable at 350 and 400 °C, where increases of the conversion of ca. 65 and 80% are observed. Likewise, experiments co-feeding methanol or DME with ethylene (50%) confirm the higher conversion of DME (Figure 1.3b) [45]. In this case, the product distribution is also function of the fed reactant and DME leads to higher yields of aromatics and C₄₊ hydrocarbons.

All in all, the differences between the conversions of DME and methanol suggest that distinct catalysts and conditions are required for maximizing the production of olefins and the stability of the catalyst.

Catalysts

The conversion of methanol or DME into hydrocarbons takes place over acid catalysts. The shape selectivity of the catalyst has driven most of the researches until now, trying to reach optimal operation conditions considering the targeted product and catalyst stability. Among the studied acid catalysts, SAPO-34 zeotype and HZSM-5 zeolite have been the ones grabbing more attention.

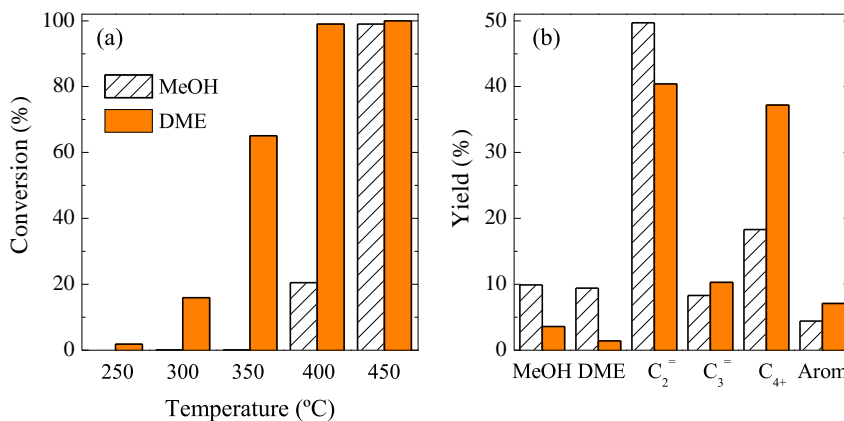


Fig. 1.3. (a) Effect of temperature on the methanol and DME conversions and (b) product distribution in the presence of ethylene (50%) at 350 °C (adapted from [45]).

SAPO-34 is a small-pore silicoaluminophosphate (CHA framework) consisting of channels with 8-membered rings and a size of $3.8 \times 3.8 \text{ \AA}$ with cavities of $12.7 \times 9.4 \text{ \AA}$ in their interceptions [46]. The cages of the three-dimensional channels are much larger than the channels and admit aromatic and branched hydrocarbons. However, the small size of the cages windows only admits the diffusion of linear and short-chained olefins and paraffins. For this reason, SAPO-34 possesses a severe shape selectivity that directs the product distribution towards light olefins, with more than 90% selectivity at full conversion conditions [47, 48]. Aromatic and polyaromatic structures have been identified within the cages of SAPO-34 during the MTO reaction, whose diffusion towards the reaction medium is avoided. This leads to a fast deactivation of the catalyst because of the blockage of the channels by coke structures [46, 49].

HZSM-5 zeolite is classified as a medium-pore zeolite (MFI framework) formed for a three-dimensional porous network with ellipsoidal ($5.3 \times 5.6 \text{ \AA}$) and sinusoidal ($5.1 \times 5.5 \text{ \AA}$) interconnected channels and without cages in their intersections [50]. In contrast to the performance of SAPO-34, the pores of the HZSM-5 zeolite allows bigger molecules to diffuse towards the reaction medium. Significant selectivities to C_{5+} hydrocarbons and branched aromatics were detected in the product stream [51]. For the same reason, the stability of HZSM-5 zeolite is much higher. The sweeping of the precursors of coke outside the crystal channels delays the formation of coke and extends the lifetime of the catalyst [52]. Olsbye et al. reported clear evidences on the effect of zeolite/zeotype shape selectivity on the product distribution [53, 54], attaining significant concentrations of aromatics with a HZSM-5 zeolite, but negligible ones with SAPO-34. Figure 1.4a shows a comparison of the product distribution obtained with both catalysts at certain similar conditions, where the strong influence of the shape selectivity is highlighted. Most of these studies were reported for MTO reaction, but the same effect can be expected for DTO reaction according to the results for a DME feed (Figure 1.4b) [44, 55].

Other properties that can modify the activity, selectivity and stability of the catalyst are the acidity and the crystal size [56, 57]. In zeolites, Brønsted acidity originates from the presence of Al in the Si–O framework (Scheme 1.2a) [58]. So, the presence of Al determines the total acidity and acid strength of a catalyst, which plays a key role in the activity and deactivation [59]. Dealumination, dehydroxylation and the addition of promoters are followed strategies in order to regulate the acidity of the catalyst. Almutairi et al. [60] reported a procedure of tuning the acidity via steaming, whereas Lee et al. [61] incorporated Fe_3^+ into the MFI framework in order to control acid strength. In both cases, they optimized the methanol conversion into hydrocarbons. Some promoters, such as Ca or Mg, proved to not only reduce the Brønsted acidity, but also enhance the Lewis acidity

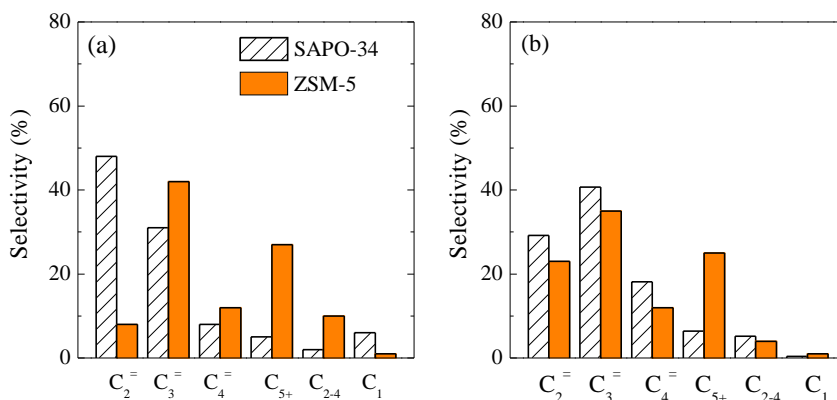
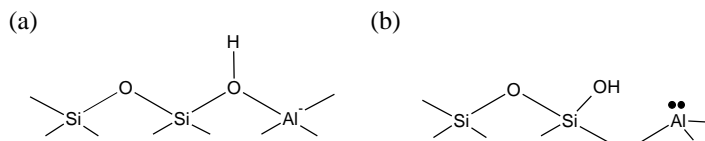


Fig. 1.4. Comparison of the product distribution for the conversion of (a) methanol (adapted from [45]) and (b) DME (adapted from [44] and [55]). 350 °C.

(Scheme 1.2b) that can play a crucial secondary role in maximizing the production of propylene [57, 62]. An optimal Brønsted/Lewis acid site ratio enhanced the activity of the methylation [63], which determines the extent of the dual cycle mechanism, as will be explained in details in the following Sections. There is also a great research interest in the crystal size, which was reported to influence the product distribution and catalyst activity. In this case, the driving force of these studies is to decrease the residence time of olefins within the crystals, minimizing the side reactions by avoiding the diffusion limitations. Different synthesis methods or the use of different templates were reported for decreasing the crystal size of HZSM-5 zeolite [64] and SAPO-34 zeotype [65], thus enhancing their performance.

The impact of scaling-up the catalyst from a research to a technical point of view has also been evidenced in catalytic process. Experimental results highlighted that the configuration of catalyst particles can enhance the mass and heat transfer properties or provide the catalyst with improved chemical, mechanical or thermal stability [66]. Most of the studies on MTO/DTO reaction at laboratory scale are performed with pelletized bare zeolites or zeotypes in packed bed reactors. Nevertheless, this process is carried out at industrial scale in fluidized bed reactors due to the required circulation of the catalyst for being regenerated [67]. Consequently, the catalyst should possess high mechanical resistance. Michels et al. [68] tested different binders for agglomerating a HZSM-5 zeolite and they evaluated their performance. They found that some agglomerated catalysts in a matrix



Scheme 1.2. Origin of (a) Brønsted and (b) Lewis acid sites in zeolites.

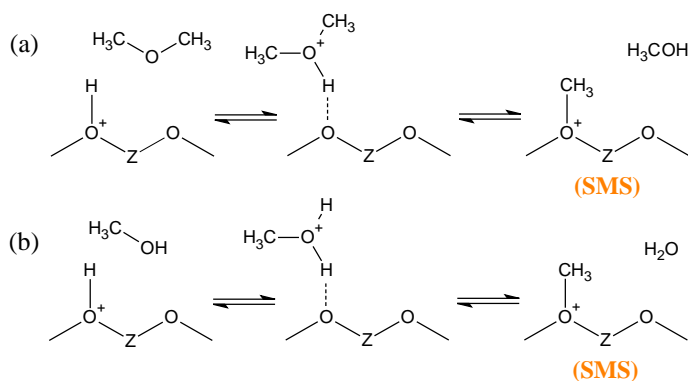
not only match the performance of bare zeolites (increasing their mechanical resistance), but also improve the catalytic behavior, maintaining a great selectivity and stability. The hierarchical mesoporous structure provided by a matrix of $\gamma\text{-Al}_2\text{O}_3$ was reported to play a role in increasing the catalyst stability and lifetime of the HZSM-5 zeolite [59, 69]. Moreover, Shoinkhorova et al. [70] synthesized formulated catalysts adding different fillers to a HZSM-5 zeolite. They reported a significant modification in the product distribution as a function of the inert filler properties.

1.1.3 Reaction mechanism

Despite the differences found between methanol and DME, both are widely accepted to follow the same overall mechanism over acid catalysts. First, the reactant is adsorbed on the Brønsted acid sites of the catalyst and forms a surface methoxy species (SMS). The interaction of this species with methanol or DME yields the first C–C bond. This step is the subject of many researches on the field and the nature of this first C–C bond is still debated today [71–73]. Once olefins are present in the reaction medium, an autocatalytic reaction with the oxygenated reactant takes place. Then, two main autocatalytic cycles are defined and well-accepted in the literature and are responsible for the formation of hydrocarbons during the MTO/DTO reaction [74].

Formation of the surface methoxy species (SMS)

The surface methoxy species (SMS) are the primary observed intermediates on the surface of the catalyst. They are formed by the adsorption of DME or methanol on a Brønsted acid site as highlighted in the Scheme 1.3. The works of Forester and Howe pointed out the presence of this SMS on the surface of acid catalysts by spectroscopic results [39]. The interaction of the unpaired electrons of the O in DME with H generates a SMS through the formation of a methanol molecule. This methanol can be adsorbed in the same way on the acid site by generating a water molecule. As easily deduced, a DME molecule yields two SMS whereas methanol can only generates one. The equilibrium between the species in the Scheme 1.3 is also worth mentioning, as water can displace the equilibrium, thus



Scheme 1.3. Proposed route for the formation of the methoxy species from (a) DME and (b) methanol (adapted from [75]).

yielding methanol [75]. The double ability of DME to form SMS and the reversible reaction of water limiting the methanol conversion have been proposed as the easiest explanations for the higher reactivity of DME than that of methanol in the literature [37]. Note that methanol can also yield DME reacting with a SMS. However, the reactivity of methanol for the propagation of the below explained mechanism is more probable than the desorption of the SMS.

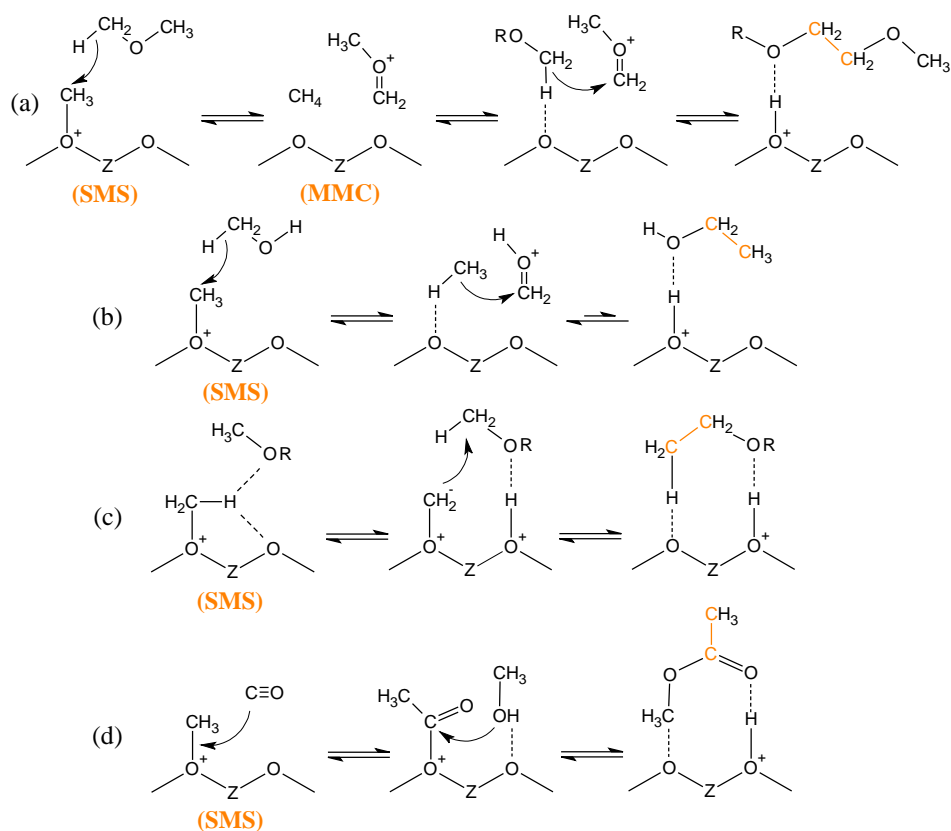
Formation of the initial C–C bond

The formation of the initial C–C bond, the formation of primary olefins, the initiation step or the formation of intermediates during the induction period have been recurrent names used in order to describe this step of the MTO/DTO mechanism. There is no doubt in the literature about the difficulty of monitoring it and faithfully describing the pathway that takes place between the SMS and the first olefin formation. Researches are making great efforts and many works have been published in the recent years trying to elucidate the formation of the first C–C bond. The pioneer work of Jiang et al. [75] demonstrated the high reactivity of SMS on the surface of acid catalysts. Moreover, the formation of olefins in the initial steps of the reaction was observed by Aguayo et al. [76], and more recently confirmed for a DME feed and deuterated SMS [41]. Pulsing DME in a temporal analysis product (TAP) reactor using a HZSM-5 zeolite not only indicated the direct formation of propylene from the reactant, but also the high reactivity of DME towards hydrocarbons [77].

Originally, some pathways were proposed based on a free radical propagation or impurities in the feed, but have been demonstrated unlikely [45]. Recent spectroscopic and theoretical calculations have suggested the low probability of these

initiation pathways, opting in favor of more plausible ones [57]. Methoxymethyl cation (MMC) is recently emerged as the critical intermediate that could explain the formation of the first C–C bond (Scheme 1.4a). Li et al. found experimental and *ab initio* simulation correlations on the presence of this cation from SMS and DME [78]. They also reported its fast reaction with other methanol/DME molecule, thus forming the first olefins. These observations were corroborated in a different reaction set-up (TAP reactor) by Omojola et al. [80], who also provided a microkinetic model validating the experimental data.

The works of Wei et al. [79, 81] also pointed at the same direction. These



Scheme 1.4. Proposed routes for the formation of the first C–C bond from methoxy species through (a) methoxymethyl cation mechanism, (b) methane-formaldehyde mechanism (both adapted from [79]), (c) carbene insertion mechanism and (d) carbonylation mechanism (both adapted from [73]).

authors highlighted the difficulty of detecting MMC species because of its high reactivity. Nevertheless, they monitored the concentration of CH_4 in the initial steps of the reaction, which is presumably formed with the cation (Scheme 1.4a). They also proposed the counterpart pathway evolving from the reaction of methanol (instead of DME) with the SMS, which leads to the formation of formaldehyde (Scheme 1.4b).

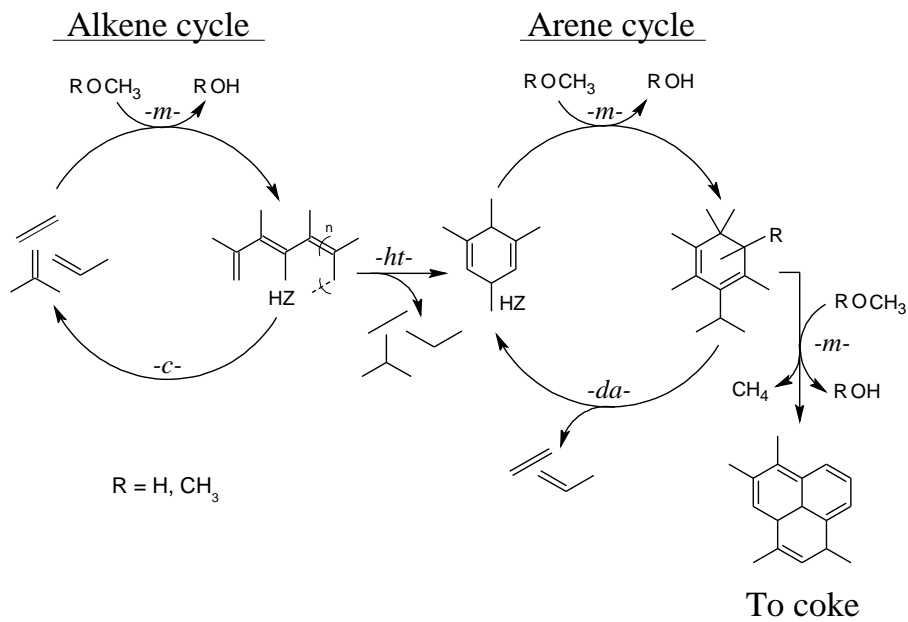
Chowdhury et al. [73] proposed alternative pathways based on *in-situ* spectroscopic results. They suggested a cooperative mechanism involving two acid sites. Then, a C–H bond of the SMS is polarized due to its interaction with the neighboring O, and the first C–C bond formation takes place through the typical insertion reaction of carbene/ylide from SMS into the sp^3 C–H bond of methanol/DME (Scheme 1.4c). Their observations also identified the intermediates related to a carbonylation pathway with CO (methanol/acetaldehyde, Scheme 1.4d). This formation of CO and its subsequent coupling with the SMS was also proposed by Plessow and Studt as the most probable mechanism due to its lower energy barrier [82].

Hydrocarbon pool and dual cycle mechanism

After the formation of the first olefins, the MTO/DTO reaction occurs through the widely known autocatalytic dual cycle mechanism. The reaction between methanol and/or DME with hydrocarbons (better known as *hydrocarbon pool*) takes place at steady state [83]. By definition, this reaction is faster than the above discussed formation of the first C–C bond, but it is affected by the catalyst deactivation. Some research groups reported experimental data and theoretical calculations on the presence of linear and cyclic carbenium ion intermediates in the early stages of the reaction that could explain the coupling of the SMS and the first olefins into the dual cycle mechanism [84, 85]. Nevertheless, most of the studies pointed out a direct methylation of the formed olefins by methanol/DME as the initiation of the autocatalytic mechanism [86, 87].

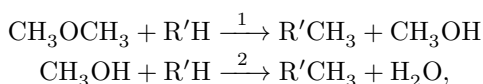
In the original version, the proposed mechanism consisted of two carbon pool cycles: an aromatic/ethylene cycle and an olefin cycle, which are respectively controlled by methylation/dealkylation and oligomerization/cracking pathways [88]. The two main cycles that describe the mechanism are commonly known as alkene cycle and arene cycle. Both operate simultaneously at the steady-state conditions and are interconnected as illustrated in the Scheme 1.5. However, the great evolution of the state of the art in recent years has allowed a significant refinement of the mechanism. Different pathways drive each of the cycles and their relative contribution can direct the reaction towards selective products [86, 89].

The incorporation of the first formed olefins into the alkene cycle takes place



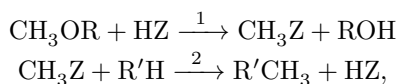
Scheme 1.5. Proposed scheme for the dual cycle mechanism (adapted from [87]).

through a methylation pathway (-*m*- in Scheme 1.5) with the methanol/DME reactant. Likewise, aromatic intermediates of the arene cycle are methylated following the same pathway, which explains the autocatalytic character of the mechanism [90]. Schematically,



where $R' = \text{alkene/arene}$.

Two different methylation mechanisms were described in the literature [91]. In the stepwise mechanism, methanol/DME first forms a SMS (step 1), which subsequently reacts with the alkene or arene intermediate (step 2), yielding a methylated olefin or aromatic, respectively



where $R = H/CH_3$.

The direct or concerted methylation mechanism considers a one-step reaction between a physisorbed methanol/DME and an also physisorbed alkene or arene intermediate



The other two main pathways involved in the alkene cycle are the oligomerization and cracking pathways. Through the oligomerization pathway, two short-chained olefins react forming an olefin of longer carbon chain [92]. The cracking pathway (*-c-* in Scheme 1.5) consists of the opposite reaction, where an olefin is adsorbed on an acid site and yields a lighter olefin through β -scission. These two pathways, with cyclization and aromatization pathways of hydrocarbon, will be later detailed in Section 1.2. One of the byproducts derived from the alkene cycle are long C_{5+} hydrocarbons [93], which are promoted on medium-pore zeolites as HZSM-5 because the diffusion of the alkene intermediates within the straight channels of the zeolite is allowed [94].

The two autocatalytic cycles are coupled by the hydrogen transfer pathway (*-ht-* in Scheme 1.5) [86, 88]. The hydrogen transfer reaction, in parallel with a cyclization-aromatization pathway, extracts the required H of the alkene chain yielding a methylbenzene, intermediate of the arene cycle. This goes hand in hand with the formation of saturated compounds (alkanes). Polymethylbenzenes are considered for most authors as the main intermediate species residing in the zeolite or zeotype pores during the MTO/DTO reaction. Two categories of intermediates can be differentiated: the reactive and the unreactive polymethylbenzenes [95]. Highly methylated benzenes are very reactive intermediates and are the responsible for the production of light olefins through the dealkylation mechanism (*-da-* in Scheme 1.5) [88, 89, 93]. The presence of 1,2,4-trimethylbenzene and 1,2,4,5-tetramethylbenzene were identified in the reaction medium, and their concentration was directly related to the ethylene production [96]. Nonetheless, hexamethylbenzene is considered virtually unreactive over a HZSM-5 zeolite [88]. These larger species are no longer active for producing olefins *via* dealkylation, and tend to polymerize to more condensed structures that finally lead to the formation of coke [97].

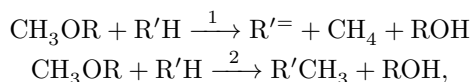
1.1.4 Formation of coke and deactivation

During acid-catalyzed reactions involving organic molecules, the formation of coke is an inevitable reaction that leads to the degradation of the catalyst properties and finally to the catalyst deactivation [98]. The growth of small molecules within the catalyst channels produces secondary heavy products, which block the pores

of the catalyst [99]. In the particular case of the MTO/DTO reaction, the initial olefins evolve towards aromatic structures according to the dual cycle mechanism of Scheme 1.5 and the growth of this arene intermediates is considered the main responsible for the formation of coke [100]. According to the thermodynamic considerations reported by Olsbye et al. [94], the formation of arene species is more favored than the one of alkene species at MTH conditions with HZSM-5 zeolite. Their results also point out that the condensation of highly methylated benzenes towards structures with two aromatic rings is favored with respect to their competitive dealkylation producing olefins (*-da-* in Scheme 1.5).

Borodina et al. [101] corroborated this condensation capacity, identifying highly methylated benzene carbocations by UV-vis at low reaction temperatures, which led to slow rates of coke formation. Increasing temperature, they also observed the presence of methylated naphthalene carbocations, which were the only observed species at temperatures higher than 400 °C. The formation of these unreactive species explains the fast deactivation of SAPO-34 during the MTO reaction at this temperature due to the formation and deposition of coke.

The growth of coke species was reported to follow a similar methylation pathway than that previously explained. Schultz [102] proposed a condensation mechanism during the MTH reaction over HZSM-5 zeolite based on two different pathways and highlighted in Scheme 1.5. First, the polyaromatic structure is dehydrogenated with the formation of CH₄ and water (step 1). And second, it is methylated with DME or methanol reactant through the analogous methylation pathway that takes place in the cases of alkene and arene cycles (step 2),



where R = H/CH₃ and R' = polyaromatic.

These reactions were observed even when the catalyst is totally deactivated, thus confirming the thermodynamic favored condensation of the unreactive alkyl-benzenes at MTH conditions. According to these results, methanol and DME reactants are the component in the gas phase responsible for the formation of coke. Then, their concentration in the reaction medium is a key parameter for monitoring the catalyst deactivation.

Following this reactant-driven deactivation, a clear deactivation profile can be observed during the reaction. In a packed bed reactor with initial full conversion, three different zones are described along the reactor (Figure 1.5) [94].

- (i) Spent catalyst zone at the top of the reactor, where the reactants are fed. Methanol is converted into DME and the catalyst is not active for the dual

cycle mechanism.

- (ii) Autocatalytic reaction zone. The oxygenates react with the intermediates and the product formation is dominated by the autocatalytic reaction. Catalyst deactivation is maximized by the formation of coke species.
- (iii) Product zone. The concentration of oxygenates is low and the interconversion of products dominates the reaction. Catalyst deactivation is minimum due to the absence of reactants.

This schematic profile is not always observed and the catalyst shape selectivity, acidity and reaction conditions have a strong influence on the oxygenate conversion and the delimitation and width of each zone [103, 104].

The *in-situ* spectroscopic results of Goetze and Weckhuysen [105] on methanol conversion over HZSM-5 zeolites also confirmed this reactant-driven hypothesis. Nonetheless, they observed two different coke fractions based on their nature. The primary coke is directly formed from methanol/DME reactants, and causes the most severe deactivation. The secondary coke derives from the aromatization of reaction products, such as propylene and ethylene, and its formation can be mitigated by reducing the acidity of the catalyst. Wan et al. [106] also differentiated two coke fractions through thermogravimetric and microscopic analyses of used HZSM-5 zeolites, and correlated them with their location on the catalyst surface.

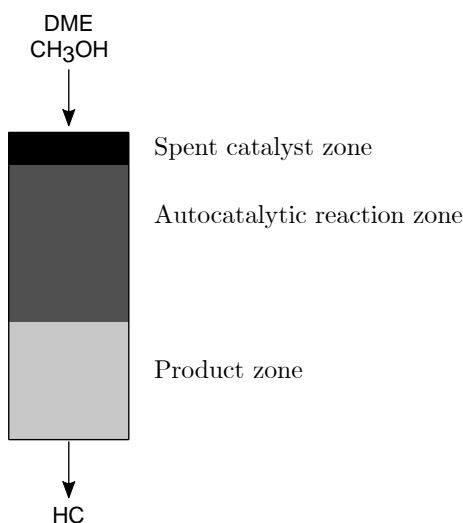


Fig. 1.5. Schematic three-zone packed bed reactor profile for the MTO/DTO reaction (adapted from [94]).

The so-called internal coke causes the fast deactivation, whereas the external one is not detrimental to the catalyst performance. The XRD analyses reported by Wragg et al. [107] and the confocal fluorescence microscopy results of Mores et al. [108] corroborated the existence of different coke fractions deposited on the surface of deactivated catalysts.

The identification of different coke fractions, the deactivation mechanisms and the observed reactor profiles of coke depend on the topology of the catalyst. Varied lifetimes, product distributions and trapped species were detected for different SAPO catalysts based on the size of the framework cavity [109]. Likewise, the coke profiles of the reactor changed from a narrow reaction zone to an almost full reaction zone in the catalytic bed using MOR, MFI and BEA zeolite framework, leading to lifetimes from 5 to 25 h on stream [104]. Paying attention to the most commonly used catalysts, SAPO-34 and HZSM-5 catalysts present a markedly different behavior. The diffusion of methylbenzenes within the SAPO-34 channels is inhibited [110], which led to an exponential deactivation after the formation of the arene intermediates [111]. On the other hand, the better diffusivity within the HZSM-5 channels results in a two-stage deactivation [52, 111]: (i) a fast initial deactivation stage due to the initial formation of some carbonaceous species and; (ii) a steady slow deactivation stage, allowed by the diffusion of these intermediates. In HZSM-5 catalysts, deactivation was ascribed to the poor mobility of tetra- and pentamethylbenzenes, which condense towards coke structures causing an overloading effect of the zeolite channels [112].

The formation and deposition of coke also change when structured catalysts of zeolites or zeotypes are used. As previously discussed, the preparation of catalysts by agglomeration of the crystals in a matrix is required for their industrial use and affects its topology. Different content and distributions of coke fractions were observed when HZSM-5 zeolite crystals were agglomerated with pseudoboehmite, which forms a mesoporous γ -Al₂O₃ matrix [52, 59]. In fact, the presence of wider pores favored the coke precursors sweeping outside the zeolite channels, thus improving the catalyst stability and lifetime. A similar result was reported by Lee et al. [55] with DME as a feed and an agglomerated SAPO-34 catalyst with ZrO₂ as a binder.

1.2 Catalytic cracking of paraffins

One of the challenges of the processes involving acid catalysis is to obtain fuels or chemicals (light olefins or BTX aromatics) from less interesting, heavy or waste feeds. In processes as the fluid catalytic cracking (FCC) unit or the previously introduced MTO/DTO process, low value-added paraffins with 5–11 carbons (C_{5+}) are also obtained as byproducts, normally through hydrogen transfer reactions catalyzed by the acid sites. C_{5+} paraffins have a relatively low octane number [113] and low commercial interest, so they need to be separated, upgraded or recirculated to the conversion units [114]. In this scenario, the valorization of this paraffin fraction is an encouraging challenge in order to enhance the efficiency of these processes and intensify the reactant conversion [115, 116]. Additional attention should be paid to this side valorization in the case of MTO/DTO process under the conditions presented in this thesis. According to the previously displayed preliminary results, the use of DME instead of methanol as a feed (Figure 1.3) and especially the use of HZSM-5 zeolite instead of SAPO-34 catalysts (Figure 1.4) significantly increase the yield of this C_{5+} fraction.

There is a strong drive in the market to valorize paraffins, but the problem is the relatively unreactive C–H bond. The main current process for paraffin valorization is the steam cracking, where olefins (mainly ethylene) are produced with high amounts of energy required and considerable CO_2 emissions [115, 117]. These two drawbacks are remarkably lessened in the catalytic cracking of paraffins, whereby the ability to selectively produce propylene is increased [116, 117]. On the other hand, the catalytic aromatization of paraffins is one of the most encouraging ways to satisfy the current demand for BTX aromatics [118], which are starting materials for manufacturing plastics, fibers or rubbers [119].

Both catalytic cracking and aromatization processes are usually carried out over HZSM-5 zeolite catalysts [120]. The presence of Al in the framework endows the zeolite with Brønsted acidity (Scheme 1.2), which was found crucial for the selective conversion of paraffins into olefins [121, 122]. Olefins can subsequently form aromatic compounds on the zeolite acid sites [123, 124]. He et al. [125] studied the important role of the framework and extra-framework Al sites in these aromatization reactions, whereas Li et al. [126] reported the remarkable enhancement of the yield of BTX aromatics by adding Zn and Ga to the HZSM-5 zeolite.

Inevitably, olefins and aromatics finally condense to coke structures on the acid sites of the catalyst, thus leading to catalyst deactivation [98, 127]. The coke formation during the catalytic cracking of *n*-hexane on a HZSM-5 zeolite was studied by Urata et al. [128], mainly focusing the work on the location of each coke fraction and the effect of the crystal size. As happened during the MTO/DTO reaction,

the properties of the catalyst and the reaction conditions strongly affect the deactivation rate of the catalyst [129], and the amount and location of coke in the catalytic cracking of paraffins [130].

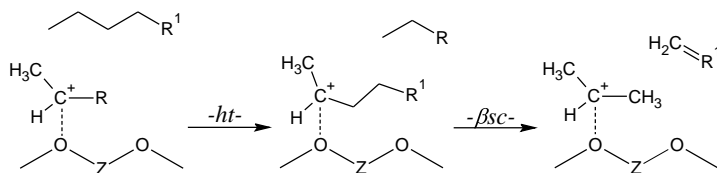
1.2.1 Cracking mechanisms

The cracking of paraffins require catalysts with relatively high density of Brønsted acid sites [131–133] and high temperatures [127, 134]. Three main routes are widely accepted for the mechanisms of catalytic cracking [135]: (i) the bimolecular or classical cracking mechanism; (ii) the monomolecular or protolytic cracking mechanism, and; (iii) the oligomerization-cracking mechanism.

Bimolecular catalytic cracking mechanism

Despite the discussions on the cracking mechanism, it is generally accepted that it involves the formation of carbenium ions [58]. Carbenium ions are species of C with a positive charge and bonded to three atoms. The carbenium ion abstracts a hydride from a paraffin and forms a new carbenium ion by hydride transfer (*-ht-* in Scheme 1.6). Subsequently, an olefin and a smaller carbenium ion are yielded through β -scission (*- β sc-* in Scheme 1.6). This carbenium ion can continue the propagation reaction *via* β -scission, or be desorbed forming a second olefin. There is variety of ways the initial carbenium ion can be created:

- (i) Brønsted acid sites donate a proton to an olefin that must be formed beforehand. This carbenium ion is formed *via* alkoxide on the acid site [136]. Dupain et al. [137] described that the initial stages involve mostly thermal (radical) cracking on the outer surface that yield this initial olefin.
- (ii) Lewis acid sites directly abstract a hydride from the paraffin. Super acid Brønsted sites could also abstract this hydride by forming H_2 . Corma et al. [138] concluded that (i) and (ii) occur in parallel during the first stages of cracking.

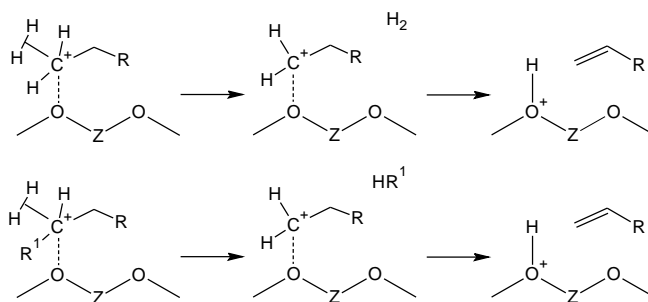


Scheme 1.6. Proposed route for the bimolecular cracking mechanism of paraffins (adapted from [135]).

- (iii) Strong Brønsted acid sites donate a proton to the paraffin and form a penta-coordinated carbonium ion. This is better known as monomolecular, protolytic or Haag-Dessau cracking mechanism.

Monomolecular or protolytic cracking mechanism

Kotrel et al. [135] proposed the Haag-Dessau mechanism of monomolecular or protolytic cracking of paraffins (Scheme 1.7). Paraffins are directly protonated, forming a penta-coordinated carbonium ion [139]. If the formed carbonium is a primary carbocation, then it will decompose into H_2 forming the carbenium ion. Otherwise, it will form a lighter paraffin (HR^1 in Scheme 1.7). The carbenium ion can follow the bimolecular cracking mechanism or an olefin can be yielded through the desorption of this carbocation (Scheme 1.7). Highly acid HZSM-5 zeolites are appropriate catalysts in order to activate the initial monomolecular pathway of paraffin cracking and selectively produce olefins. According to Rahimi et al. [117], the high density of Brønsted acid sites increase the adsorption and protonation capability of the zeolite. Moreover, the shape selectivity and the absence of cavities in the HZSM-5 zeolite structure (with pores of 5.5 Å that favor the diffusion of linear paraffins) could hinder certain bimolecular pathways, which involve the hydride transfer reaction between two molecules [140, 141].

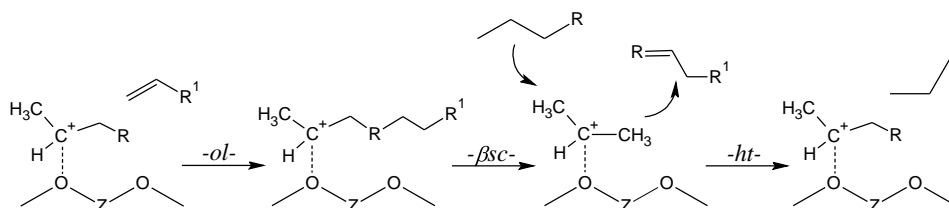


Scheme 1.7. Proposed route for the monomolecular cracking mechanism of paraffins (adapted from [135]).

Oligomerization-cracking mechanism

During the catalytic cracking of paraffins not only smaller molecules than the reactants are observed, but also longer hydrocarbons including olefins, paraffins, cyclic and aromatic compounds. The oligomerization-cracking mechanism explains the formation of longer linear and branched hydrocarbons by the carbenium chain

growth (Scheme 1.8) [135]. The carbenium ion can react with one of the beforehand produced olefins. Then, a long-chained carbenium is formed (*-ol-* in Scheme 1.9), that leads to a longer olefins through the β -scission pathway. The propagation of this mechanism occurs in the same way as the bimolecular cracking, through the hydride transfer reaction and the formation of other carbenium ion or desorption of the formed carbenium ion. The oligomerization of light olefins towards longer molecules starts a sequenced set of reactions, leading to the formation of aromatics. Hence, the inhibition of this reaction pathway is sometimes sought for attenuating the subsequent aromatic condensation into polyaromatic structures of coke that cause the catalyst deactivation [142].

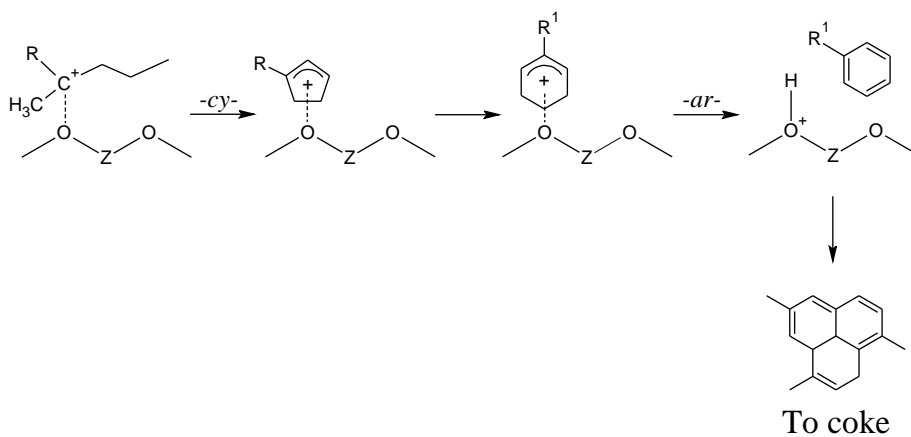


Scheme 1.8. Proposed route for oligomerization-cracking mechanism of paraffins (adapted from [135]).

Cyclization-aromatization mechanism

The production of aromatics compounds from paraffins requires the above discussed formation of long-chained carbenium ions. In case of light paraffin reactants, the oligomerization of the intermediate carbenium ion is also necessary. Aromatics are formed through a cyclization-aromatization pathway (Scheme 1.9) [143]. Alkylcyclopentane were already observed in the 80-90s as the main intermediate that initiates the production of cyclic compounds (*-cy-* in Scheme 1.9) [144, 145]. This is a consequence of the higher stability of the tertiary carbocation derived from a branched olefin (first structure in Scheme 1.9). The dehydrogenation of the cyclic compounds that results in aromatics is based on three hydride transfer reactions, indicated in the Scheme 1.9 as aromatization pathway (*-ar-*). Consequently, three saturated molecules are formed in parallel during the aromatization pathway, corresponding to each unsaturation of the aromatic ring [143]. Several studies demonstrated that this cyclization-aromatization of longer carbenium ions is promoted by doping HZSM-5 zeolites with metals as Ga, Zn or Mo [126].

The aromatization of olefins is more thermodynamically favored than the dehydrogenation of paraffins [143]. In this regards, the presence of high concentration of olefins in the reaction medium with highly acid catalysts can direct the reaction



Scheme 1.9. Proposed route for cyclization-aromatization mechanism of paraffins (adapted from [143]).

to the formation of aromatics. And the condensation of this aromatics towards polyaromatic structures of coke on acid sites is well-established (Scheme 1.9) [98]. In most cases, the catalyst deactivation by coke deposition is fast and usually restricts the feasibility of the paraffin cracking process [128, 146].

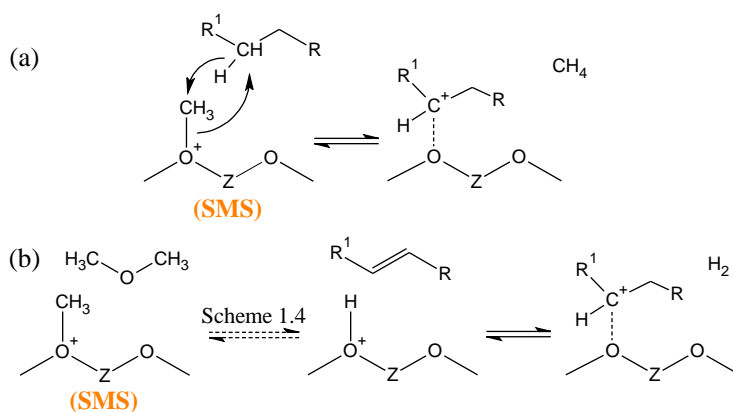
1.2.2 Dual conversion of paraffins and oxygenates

Within the possible process modifications for activating light paraffins and promoting a selective cracking towards light olefins, Martin et al. [147, 148] proposed the so-called coupled methanol and hydrocarbon cracking (CMHC). The first goal was to take advantage of the exothermic character of MTO process in order to overcome the energy requirements of the catalytic cracking. The synergies between both reactions were observed for a feed mixture of *n*-butane/methanol in the temperature range of 500–550 °C and low values of space time [149]. The clearest evidences of C–C paraffinic bond activation using methanol were reported by Yu et al. [150] in experiments with propane and labeled carbon reactants. The combined reaction of paraffins and methanol were also studied aiming for the intensification of propylene in the MTO process. A significant enhancement of its yield was reported by Roohollahi et al. [151] in reactions co-feeding *i*-butane at 470–500 °C and full conversion of methanol. Likewise, a positive synergy was observed by recirculating C₄₊ byproducts into the MTH reactor [152].

Coupling the reactions of paraffins and methanol means the coexistence of the

two above introduced mechanisms on the same acid sites of the zeolite: the dual cycle mechanism and the carbocationic mechanism of paraffin cracking. The kinetic studies of Chang et al. [153] related both mechanisms during the dual conversion and revealed a faster rate for the catalytic cracking of *n*-hexane due to the formation of intermediates from methanol. Their results suggest that the formation of the carbenium ion from the paraffin is quite slower than that of methoxy species from oxygenates. Regarding the above discussed Schemes 1.3 and 1.4, two main possibilities could explain this enhancement.

- (i) The direct hydride transfer between the surface methoxy species (SMS) and the paraffin (Scheme 1.10a). This route assumes a faster hydride abstraction by the methoxy than that by the acid sites. In addition, it considers that the formation of the first C–C bond in the MTO/DTO reaction is slower than the interaction between SMS and the paraffin reactant. This mechanism was proposed by Yu et al. [150] in the activation of propane at conditions of great excess of the paraffin.
- (ii) The formation of a carbenium ion from the first olefin of the dual cycle mechanism (Scheme 1.10b). According to this route, the formation of the first C–C bond in the MTO/DTO reaction dominates the mechanism. Then, the competitive reactions are the methylation of these olefins (dual cycle mechanism, Scheme 1.5) and the formation of the carbenium ions *via* alkoxide intermediates on the Brønsted acid sites [136].



Scheme 1.10. Plausible routes for the enhanced catalytic cracking of paraffins by the intermediates of methanol conversion (a) *via* hydride transfer by a SMS or (b) *via* carbenium ion from the first olefin.

Unraveling the mechanism that dominates the dual or combined conversion of oxygenates and paraffins is a complicated goal due to the difficult definition of a clear reaction network. As explained in previous Sections, each individual reaction possesses a complex reaction network *per se*. This aim is even harder targeting the mechanisms of coke formation and catalyst deactivation. Presumably, the methylation/dehydrogenation mechanisms derived from the dual cycle would be promoted by the presence of aromatic species from the cyclization-aromatization pathway of the paraffin reactant and olefins (product of both processes).

1.3 Kinetic modeling of complex reaction networks

Kinetic modeling is an indispensable tool for the prediction of product distribution and reactor design, including heat management, simulation and optimization [154]. The computation of kinetic models for catalytic processes with a complex kinetic network requires a big set of experimental data collected in kinetic regime at isothermal conditions and using differential and integral packed bed reactors. In order to consider the catalyst deactivation, experiments at different time on stream values are also necessary. The extrapolation of the data for the design of reactors at larger scales implies the implementation of non-ideal gas flow models [155]. By definition, the intrinsic kinetics of a reaction requires of experiments without any diffusion limitation. However, these limitations can also be included in the models [156, 157], as well as other related factors, such as the crystal size of the particles [158]. In essence, the choice of the modeling strategy depends on the complexity, accuracy and reliability of the studied process.

1.3.1 Modeling methodologies

The most commonly used kinetic models can be classified depending on their complexity. There are several possibilities between the simplest power law model and the microkinetic model with the highest level of detail. Briefly, the simplest models give a great overview of the general process and describe the reaction rates at the experimental conditions by empirical equations. On the other hand, the consideration of more thermodynamic factors, adsorption events, and the incorporation of more individual steps in a reaction network provide insights into the intermediates and mechanisms of the reaction [154].

According to the used methodologies in the literature, kinetic models can be divided in three different big groups in terms of the simulation goal (Figure 1.6). (i) Models based on density functional theory (DFT) usually target the specific study of one independent step of a reaction, as the formation of the first C-C bond during the MTO/DTO reaction. (ii) Models that describe a reaction network and predicts the performance of an integral reactor. These models can take the adsorption of the reaction medium components into account using Langmuir-Hinshelwood equations. Depending on the level of accuracy they can be divided in microkinetics and lumped models. (iii) Models that consider the hydrodynamics of the process by means of computational fluid dynamics (CFD). From an industrial or implementation point of view, the prediction accuracy of the process performance also depends on the used model (gray area in Figure 1.6). The more specific the study case, the lower description of the industrial process.

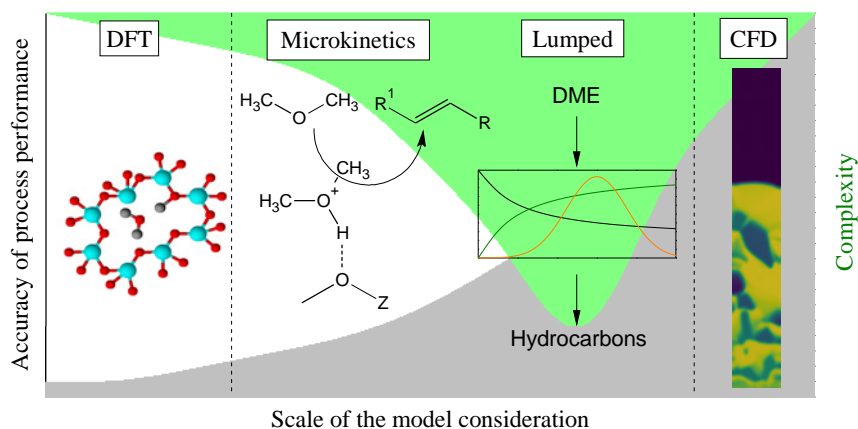


Fig. 1.6. Relation between the scale of modeling strategy and the prediction of the process performance.

Apart from this classification, there are also studies that extract kinetic parameters for complex reaction networks based on a simple Arrhenius plot or stochastic methods. They are not included in this discussion because the calculations are made without any underlying kinetic network or based on statistical fitting with a lack a physico-chemical basis [154].

DFT models

Classical density functional theory (DFT) is based on statistical calculations on the most probable interaction between molecules in a given environment. It is based on molecular dynamic techniques and are able to account for dynamical effects such as zeolite framework flexibility and the influence of solvent molecules on the chemical reaction [159]. The simulation scale for this method is the lowest (atomic scale) and the accuracy of the results are the highest from a mechanistic point of view. The main application of these models in catalysis is to unravel new reaction mechanisms and intermediates [159]. Energy diagrams can be calculated by giving the initial and final state of the mechanism and some plausible intermediates. Then, the most energy favorable pathway can be computed.

Van Speybroeck et al. [159, 160] reported detailed mechanistic information on the dual cycle mechanism based on DFT calculations. They simulated the effect of acid sites and zeolite topology on most of the steps of the mechanism, including the formation of large aromatics that lead to deactivation [160]. Other groups focused their research on individual steps of the mechanism performed in a single acid

site. Li et al. [78] and Wei et al. [81] suggested the formation of methoxymethyl cations (MMC) as intermediates during the formation of the first C–C bond in the MTO/DTO reaction over HZSM-5 zeolite (Scheme 1.4a and 1.4b). Similar to those works, Plessow and Studt [82] developed the hypothesis of the CO formation and carbonylation of surface methoxy species (SMS) as the most probable route for the formation of this C–C (Scheme 1.4d).

Microkinetic models

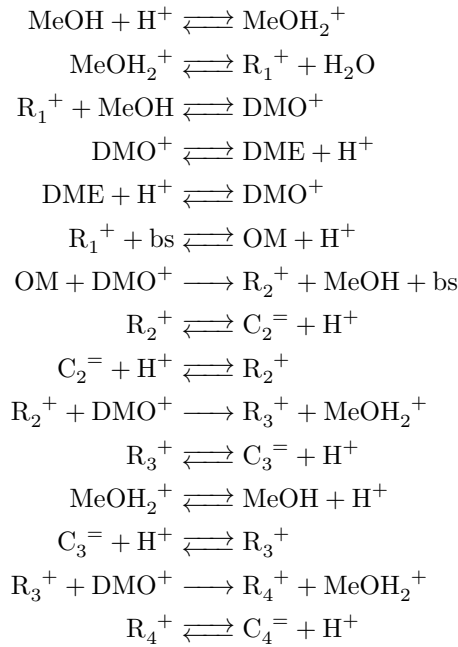
Microkinetic models describe the behavior of an integral reactor but without giving up thermodynamic fundamentals. The consideration of most of the individual steps or single events involved in a chemical process leads to gigantic reaction networks but consisted of a limited number of types of steps and homologous species [161]. The rate of each elementary step is computed according to all the possible single events between the reactant, activated complex and product, considering molecular symmetry, entropy contribution and enthalpy estimations [162].

Park and Froment [163] developed a microkinetic model for a very simple reaction network of MTO process consisting of 33 parameters. They were allowed to simulate the performance of a packed bed reactor by using a model that even considers the participation of oxonium intermediate. However, the simulation of a more complex reaction network considering the formation of longer hydrocarbons required a kinetic network formed by 225 species and 726 elementary steps [161]. One of the advantages of this modeling strategy is the possible evaluation of individual steps of a complex mechanism in a simpler way than that provided by molecular dynamics. Omojola et al. [80] evaluated the formation of the first C–C bond in the direct conversion of DME to propylene. The computational cost in this case is far lower than the one require for DFT simulations.

By way of example, Scheme 1.11 displays the required steps for a simple reaction network in which methanol is converted into ethylene ($C_2^=$), propylene ($C_3^=$) and butene ($C_4^=$). The microkinetic network was proposed by Sedighi et al. [164] and comprises fifteen individual steps.

Lump-based models

Lump-based models are probably the most used in the literature for catalytic process with multiple reaction steps because of the possibilities of developing easy reaction networks that lead to computationally cheap calculations [165]. The lack of thermodynamic considerations provide the model with an intrinsic empiricism. Hence, these models are not recommended for comparing the reactivity of products or unraveling mechanisms. However, as thermodynamic and physical restriction are included in the apparent constants, the level of accuracy in terms of reactor performance is high. As observed in Figure 1.6, lump-based models present the minimum complexity of all the introduced strategies but they are well-located in

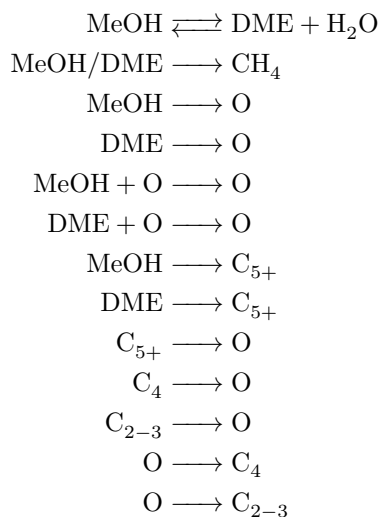


Scheme 1.11. Proposed MTO reaction network for a microkinetic model (adapted from [164]). MeOH_2^+ , DMO^+ = adsorbed species; R^+ = alkoxy species; H^+ , bs = acid and basic sites; OM = oxonium methyllide.

terms of reactor performance predictions. There is a point in the graph where the green and gray areas are overlapped, thus pointing that these models are the suitable selection in the relation complexity/reactor performance. Of course, they have an important gap in the mechanistic considerations from a chemistry point of view, but it is translated to a preferred situation in terms of reactor design.

These models also present an interesting flexibility and the complexity of the reaction network can be easily increased. Thermodynamic considerations as adsorption or chemical equilibrium can also be included, then approaching their accuracy to that obtained with microkinetic models. An example is given by Aguayo et al. [166], who proposed a lump-based kinetic model for the MTH reaction using a HZSM-5 zeolite (Scheme 1.12). The reaction network consists of 13 steps and considers methanol and DME as independent lumps, indicating the higher kinetic constant for the conversion of DME.

Ying et al. [167] directed their research to the development of a kinetic model



Scheme 1.12. Proposed lump-based reaction network for the MTH reaction (adapted from [166]). $\text{O} = \text{C}_2^= + \text{C}_3^= + \text{C}_4^=$.

for the MTO process able to be scaled-up at industrial scale. They proposed an easier reaction network with 7 lumps and steps (all products formed from methanol), used the industrial SAPO-34 catalyst and validated the results with the experimental data collected in a fluidized bed reactor. DTO reaction were also studied by means of a lump-based kinetic modeling [168]. The consideration of a single reactant lump with methanol and DME is one advantage of these models, as most of the works discussed in Section 1.1 do not really distinguish between the behavior of both. Nonetheless, rigorous analyses of the product stream and design of the experiments can provide enough information for differentiating between both reactant [37].

CFD models

The simulation of the real operation requires not only taking the kinetics into account but also the hydrodynamics of the reactor. Especially, this is important in reactions performed in circulating fluidized bed reactors as MTO/DTO process [67], because the continuous movement of the gas and catalyst must be considered. Computational fluid dynamics (CFD) models can predict the performance of the solid and gas phases in the reactor during the process. However, the consideration

of particle movement in the reactor increases the complexity of the model as observed in Figure 1.6.

A good implementation of attrition and drag models is a big goal as individual study case [169], but the design of the reactor requires to couple it with one of the previously discussed kinetic models. This normally leads to simplifications in the CFD or kinetic models because of computational limitations. In most cases, CFD models are coupled with easy lump-based reaction network and the obtained results are quite good. Lu et al. [170] reported a coupled CFD-lumped model for MTO process and studied the configuration and size of the fluidized bed reactor. They used a simplified CFD methodology based on the two-phase model and an energy-minimization multi-scale drag model. In addition, they incorporated a reaction network formed by 9 lumps and reactions and, more important, a catalyst deactivation model.

1.3.2 Consideration of the deactivation

As above discussed in Section 1.1, the catalyst deactivation plays an important role in acid-catalyzed processes. The short lifetime of the catalyst is specially remarkable in MTO/DTO process with SAPO-34, due to the topology of the catalyst that favors the pore blockage by the deposition of coke. Although it is improved using a HZSM-5 zeolite, deactivation by coking should be considered for modeling purposes.

The different modeling methodologies can be used for studying some steps of the catalyst deactivation. There are some studies on models that relate the deposition of coke with physical phenomena within the pores of the catalyst particle. Among them, Brogard et al. [171] used DFT simulations for modeling the adsorption of aromatics compounds of different sizes within the cavities of different zeotypes. They discussed the most plausible coke precursors regarding the affinity precursor/cavity. Other authors studied deactivation as a process with increasing diffusion limitations as the coke is deposited. A diffusion model for the formation, adsorption and deposition of coke was proposed by Gao et al. [157], whereas Izadbakhsh and Khatami [172] used the percolation theory and included heat transfer considerations, looking for higher accuracy on the diffusion limitation.

At larger scale than the catalyst particle, the incorporation of deactivation equations into a microkinetic model for MTO process was described by Froment [173]. He defined an accurate methodology for describing the deactivation process in an easy reaction network by combining the models at three different levels: the active site, the particle and the reactor. The deactivation of the catalyst was defined as a function of the formed coke, which affects the occupancy of active sites

and the reactant diffusion within the catalyst pores. Most of the works are simplifications applied at integral reactor level and using lump-based kinetic models. The difficulty of a rigorous consideration of deactivation in reactions with complex reaction networks makes this type of models the most suitable selection for reactor modeling.

An easy reaction network using four lumps (reactant, intermediate, product and coke) was proposed for the MTO reaction [174]. The attenuation of the rate of each j step of the reaction network (r_j) with respect to that at zero time on stream ($r_{j,0}$) was considered with a deactivation function (ϕ) that affects all the steps of the reaction network,

$$r_j = \phi r_{j,0}, \quad (1.1)$$

with

$$\phi = 1 - hC_C, \quad (1.2)$$

where C_C is the content of coke in the catalyst, h is a constant that depends on the reaction conditions, and with the coking rate being defined as

$$\frac{dC_C}{dt} = k_C(T)C^{*d}\phi, \quad (1.3)$$

where k_C is the rate of coke formation, C^* is the concentration of the precursor of coke and d is the deactivation order [175]. Later on, hyperbolic and exponential functions were proposed by Rostami et al. [176]

$$\phi = \frac{1}{1 - hC_C}, \quad (1.4)$$

$$\phi = \exp(-hC_C). \quad (1.5)$$

Yuan et al. [177] proposed a more complex reaction network based on the dual cycle mechanism and included a deactivation function considering a maximum amount of coke measured from experimental observations (C_C^{max}).

$$\frac{d\phi}{dC_C} = -k_C\phi \left(\frac{C_C^{max} - C_C}{C_C^{max} - h} \right)^d. \quad (1.6)$$

The assumption of a direct relation between deactivation rate and content of coke is conceptually the most accurate way of giving the model a mechanistic sense. Nevertheless, a coke-dependent deactivation equation has some disadvantages. First, it assumes that all carbonaceous species deposited on the catalyst surface contribute to deactivation equally without considering demonstrated factors as the aging of coke [102], or its nature and location [59, 106, 178]. Gao et al.

[179] reported the important effect of the location of coke on the reactant diffusion towards Brønsted acid sites and Muller et al. [180] studied the evolution with time of the nature of coke from oxygenated and higher-deactivating species to lower-deactivating polyaromatic structures. Moreover, several authors provided further insights into the contribution of coke structures to the reaction mechanisms [176, 181, 182]. Secondly, reproducibility issues always exist when analyzing the content of coke of deactivated catalysts, mainly depending on the experimental protocol. Especially, the previous sweeping or pretreatment of the samples (temperature and/or vacuum) was reported as a crucial factor in the subsequent analysis [183]. The dependency on the longitudinal position in packed bed reactors [102] and the homogeneous distribution in fluidized bed ones [167, 184] also hinder the use of a unique coke content-based deactivation equation for all configurations.

Other similar perspective of the deactivation rate by coking was proposed by Levenspiel [185]. An activity parameter (a) is defined as the relation between the rate of each j step of the reaction network and the one at zero reaction time

$$a = \frac{r_j}{r_{j,0}}. \quad (1.7)$$

And hence, he defined the deactivation rate (r_d) as

$$r_d = -\frac{da}{dt} = k_d(T)f(C)a^d, \quad (1.8)$$

where k_d is the deactivation rate and $f(C)$ is a determined function of the composition of the reaction medium. This function can be an empirical potential expression dependent on the coke precursors or a Langmuir-Hinshewood-type equation deduced from the mechanisms of coke formation and evolution. This definition allows the loss of the catalyst activity to be described as a function of the reaction medium in a given time without requiring the content of deposited coke. The works of Levenspiel [185], Fogler [186] and Kunii and Levenspiel [187] demonstrated the efficiency of this methodology for computing deactivation kinetics targeting the design of reactors.

Aguayo et al. [188] used this definition of activity in order to study the deactivation of a HZSM-5 catalyst during the MTH process in packed and fluidized bed reactors. They proposed an easy lump-based reaction network of four lumps with four steps and a simplified form of equation (1.8), considering a deactivation order of 1 and a single deactivation constant for each i lump

$$-\frac{da}{dt} = \sum_i (k_{di}y_i)a, \quad (1.9)$$

where y_i is the molar fraction of each i lump.

A rigorous data analysis was the key point for the quantification of the evolution with time of the activity parameter from experiments collected in an integral packed bed reactor. The rates at zero and t time on stream in equation (1.7) should correspond to the same composition of the reaction medium in order to take the *past history* of the catalyst into account. This methodology leads to higher flexibility for considering some experimental observations regarding the catalyst deactivation. For example, the existence of an initial period where the conversion increases while the activity decreases can be modeled.

One of the most interesting factors to be investigated during the MTO/DTO reaction is the role of water in the catalyst deactivation. Gayubo et al. [189] described the attenuation role of water in the conversion and deactivation during the MTO reaction using a SAPO-34 catalyst. The experimental observations published by Luo et al. [190] and the *in-situ* DRIFT experiments reported by Batova et al. [191] confirmed this theory. Furthermore, the *in-situ* microspectroscopy and DFT calculations of De Wispelaere et al. [192] attributed this attenuation role to the competitive adsorption of water and the lower reactivity of methanol in the presence of water. But independently on the amount of water in the reaction medium, the direct correlation between methanol/DME concentration and catalyst deactivation is well-accepted in the literature [38, 193].

All these experimental premises can be easily included in the deactivation equation. Gayubo et al. [194] fulfilled these requirements in the MTO reaction with a Langmuir-Hinshelwood-type deactivation equation, which was also validated in the DTO reaction afterwards [38]

$$-\frac{da}{dt} = \frac{k_d(y_{\text{MeOH}} + y_{\text{DME}})}{1 + K_w y_{\text{H}_2\text{O}}} a^d. \quad (1.10)$$

The consideration of different influences of deactivation on each step of the reaction is also a useful tool for a better description of deactivation. This requires a selective deactivation model with individual activities. In the same work, Gayubo et al. [194] also proposed a selective deactivation model with a lower influence of deactivation on the methanol dehydration step.

1.4 Design of reactors with catalyst deactivation

The important role of stability in the productivity of a catalytic process is so relevant as to be considered one of the three *virtues* of catalytic performance, along with activity and selectivity [195]. A key point to study in catalytic processes should be the attenuation of deactivation, which is usually investigated by designing catalysts with enhanced stability or controlling the composition of the reaction medium [196]. Nonetheless, catalyst deactivation has a strong influence on the optimization of the whole process, conditioning the selection of the catalyst, reactor, reaction-regeneration strategy and operating conditions (Figure 1.7). Even a more important role could be given to the catalyst regenerability in this scheme, almost considering it as the four *virtue* of catalytic performance.

The design of reactors including catalyst deactivation has received less attention than the improvement of catalyst performance and kinetic modeling of deactivation. Indeed, the main conceptual contributions in this topic are the pioneering and groundbreaking works reported by Levenspiel [185], Fogler [186], and Kunii and Levenspiel [187]. The lack of scientific publications may be due to their low impact into the industrial implementation and scaling-up of processes, and to the added complexity of the design models when deactivation is considered. The computation complexity is significantly increased with reactor-regenerator systems that couple reaction and deactivation kinetic models. Therefore, deactivation can be minimized by prevention actions but it must be understood as an inevitable

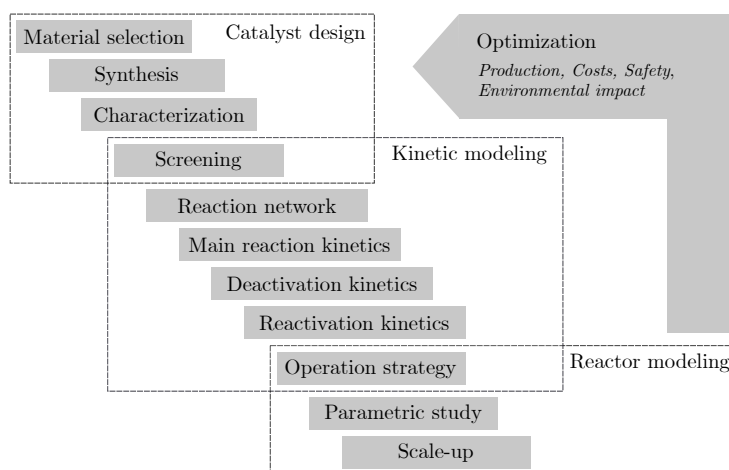


Fig. 1.7. Stages of the design and optimization of catalytic processes (adapted from [197]).

problem for reactor design and should be considered in the optimization of a catalytic process [198].

1.4.1 Operation strategies

The selection of the reactor and operation strategy depends on deactivation rate (Figure 1.8) [199]. When deactivation is too slow (months or even years), packed bed reactors are commonly used because of their simplicity. The reactor is submitted to a temperature ramp trying to overcome deactivation by attaining a constant conversion and selectivity. In these situations, the kinetic model is computed at conditions of accelerated deactivation and consequently, with some deviations from the real operation. After the catalyst is totally spent, a fresh catalytic bed replaces the deactivated one, which is regenerated or treated for recovering its valuable components. A set of parallel packed bed reactors is preferred for moderate deactivation rates, in such a way as one of them can be regenerated meanwhile the remainders operate. Catalytic processes with fast deactivation (days, hours or even minutes) likely operate with *ex-situ* regeneration and catalyst circulation. Moving bed and especially bubbling fluidized bed reactors are the most used configuration in these cases. The *ex-situ* regeneration is carried out in a combustor that preferentially operates in bubbling fluidized bed configuration because of the easier temperature control. And the extreme case of deactivation in seconds requires entrained-flow reactors, where the residence time of the catalyst inside the reactor is as low as needed.

Time scale of deactivation	Reactor configuration	Operation strategy
Years	Packed bed	Constant or ramp temperature Independent regeneration
Months	Packed bed	Reaction-regeneration cycles Regeneration <i>in-situ</i>
Weeks	Packed bed	Reaction-regeneration cycles Regeneration <i>in-situ</i> in swing mode
	Moving bed	Regeneration <i>ex-situ</i> in moving or fluidized bed
Minutes-Days	Bubbling fluidized bed	Dual reactor-regenerator system
Seconds	Entrained-flow (riser)	Dual reactor-regenerator system

Fig. 1.8. Relationship between the time scale of deactivation, reactor configuration and operation strategy (adapted from [199]).

Levenspiel and Sadana [200] and Krisnaswamy and Kittrell [201] first studied the operation using a ramp temperature, easy reaction networks and kinetic equations. Other authors deepened on this methodology by applying more complex Langmuir-Hinshelwood-type deactivation equations that depend on the composition of the reaction medium [202]. Gayubo et al. [203] reported a procedure for the computation of kinetics during the operation with a ramp temperature and complex reaction networks and deactivation equations.

The operation with reaction-regeneration cycles in packed bed reactors was first reported aiming for the calculation of the optimal operation time in the situation where the reaction and regeneration times are independent [204, 205]. Le Goff [206] added to these studies other non-scientific variables as the production cost, but assuming concentration-independent deactivation kinetics. The reaction-regeneration dependency in this sequenced strategy was also studied by other authors [207, 208]. This strategy implies the consideration of deactivation and reactivation kinetic equations, which became more complicated when the composition of the reaction medium was taken into account. Yurchak [209] explained how this relationship is considered in the MTG plant at New Zealand (nonoperational nowadays) consisting of five parallel packed bed reactors. Gayubo et al. [210] studied the combined strategy of the operation in reaction-regeneration cycles with a ramp of temperature in each reaction cycle.

1.4.2 Consideration of the catalyst circulation

A significantly fast deactivation requires the catalyst circulation for the *ex-situ* regeneration of the catalyst. One of the alternatives is a moving bed reactor with descending catalyst flow (downer) [211]. Among the reactions studied with this configuration, the reforming of naphthas [212, 213], dehydrogenation of paraffins [214, 215] and steam reforming of methane [216] can be worth mentioning due to their high commercial interest. MTO/DTO process was also studied in moving bed reactors at laboratory scale [217], with moving bed combustors for the catalyst regeneration [218]. Nonetheless, its poor heat transfer limits these applications.

Fluidized bed reactors offer advantages that have made them the suitable selection for gas-solid catalytic processes at industrial scale. First, the higher ability for heat exchange makes isothermal conditions to be obtained easier than in packed or moving bed reactors. This is an important factor for highly exothermic or endothermic reactions. Moreover, the continuous movement of particles enables a better control of the catalyst deactivation by adjusting the circulation of particles between the reactor and regenerator. As the main goal of this thesis, the MTO/DTO process is industrially carried out in this dual reactor-regenerator system, where the SAPO-34 catalyst circulates between the fluidized bed reactor and

regenerator [67]. Nevertheless, there are other catalytic processes that are also carried out using this configuration, such as the catalytic pyrolysis of bio-oil [219], the dehydrogenation of paraffins [220] or the polymerization of olefins in gas phase [221].

There is a situation where the use of fluidized bed reactors is no longer a possibility due to the extremely fast deactivation of the catalyst (Figure 1.8). A paradigmatic example of this case is the fluid catalytic cracking (FCC) unit. The catalyst is deactivated by coking in few seconds, which requires a faster movement of the catalyst than that provided by a bubbling fluidized bed reactor. The reaction is industrially performed in entrained-flow (riser) reactors. This is no other than a specific case of the moving bed reactor, with ascending and fast catalyst circulation. The deactivated catalyst circulates to a significantly bigger fluidized bed combustor for its regeneration [222].

Simulation of circulating fluidized bed reactor and regenerator

Basic reactor design and fluidization literature [185–187] proposed the methodology for designing circulating fluidized bed reactors (CFBR) and simplifications of reactor-regenerator systems. The random movement of particles in a fluidized regime and the continuous circulation of catalyst particles lead to a residence time distribution (RTD) [223]. According to Kunii and Levenspiel [187], the RTD of solids in a fluidized bed reactor with complete mixing can be defined with the E curve as a function of the mean residence time of the solids (τ_m)

$$E = \frac{1}{\tau_m} \exp\left(-\frac{t}{\tau_m}\right). \quad (1.11)$$

Hofer et al. [224] studied different RTD curves for fluidized bed reactors using tracers and correlated them with different shapes of the E curve, estimating values of dispersion coefficients associated with the particle movement. Bachmann et al. [225] worked with horizontal fluidized bed reactors, and validated the correlations between the dispersion and convection coefficients using the dimensionless Bodenstein number. Experimental observations on the RTD were also simulated by Geng et al. [226]. Their model predicts modifications of the E curve caused by changes in the fluidization conditions. And Zhang et al. [227] reported evidences of how the E curve varies depending on the reactor scale, which significantly hinders the extrapolation of the models for a possible scale-up.

In reactions with catalyst circulation, such as MTO/DTO, the presence of a RTD in the catalyst particles would finally leads to an unwanted activity distribution due to different deactivation degrees by coking. As explained in details in Section 1.3, some authors focused their work on relating the catalyst deactivation with the content of coke deposited during the reaction. Then, the presence of a

RTD in fluidized bed reactors leads to a coke distribution function. Yuan et al. [228] and Zhang et al. [229] reported a methodology to extrapolate the experimental measurements of coke content to a coke distribution and its effect on the yield of each product during MTO/DTO process. One of the most relevant publications on the design of reactor-regenerator systems was reported by Li et al. [230]. They coupled the reactor design equation with the population balance theory in order to calculate the coke distribution at the outlet of each unit using the above introduced equation (1.6). Nevertheless, they also pointed out the difficulty of considering the RTD of the catalyst when the fed particles are partially deactivated using experimental relations content of coke-time.

In Section 1.3, the advantages of defining an activity parameter (a) that strictly depends on the reaction medium composition were described. In addition, the possibility of modeling reactor-regeneration systems with an activity distribution function at the entrance of the reactor should be included. Weng and Chen [231] described the methodology for computing the activity distribution function (f_a) in the reactor, regenerator and reactor-regenerator system, using simple kinetic equations. They considered a complete mixed reactor model and used the E curve and population balance theory in order to calculate these activity distribution functions

$$-\frac{d}{da} \left(f_a \frac{da}{dt} \right) = \frac{q_{cat}}{V} [(f_a(z=0) - f_a)], \quad (1.12)$$

where q_{cat} is the catalyst flow rate, V is the reactor volume and the rate of activity change is defined for the reactor and regenerator as

$$\frac{da}{dt} = \begin{cases} -k_1 a^d & \text{reactor} \\ k_2 (1-a)^m & \text{regenerator} \end{cases}, \quad (1.13)$$

with k_1 , k_2 , d and m constant.

The use of simplifications in the reactor design equation (complete mixing model for the catalyst and steady state conditions) and kinetic equations (concentration independent-deactivation) allowed them for deducing mathematical integrated expressions of the activity distribution function. An interesting advance in the reactor-regenerator system design was proposed by Gayubo et al. [232], who applied a simplified calculation method for the activity distribution function in complex reaction networks. They took the methanol-to-gasoline (MTG) process as a model and were able to estimate the yields of products. Nonetheless, there is still a gap in the literature regarding the simulation of reactor-regenerator systems with a rigorous consideration of: (i) the activity distribution function in the reactor and regenerator; (ii) the dependency of this distribution in each unit as a consequence

of the catalyst circulation, and; (iii) the relation of the yields of products to the activity distribution function in the reactor.

1.5 Aim and objectives

This work aims to widen the understanding of the dimethyl ether-to-olefins (DTO) process from the microscopic perspective of the catalyst to the macroscopic scale of the process conception and simulation. Regarding the state of the art of this process, some aspects are in-depth targeted herein, such as the performance of catalysts with the required industrial properties and the development of computational methodologies. Here, one can include the calculation of kinetic models for processes with significant deactivation, the simulation of reactors for these processes and the design of a dual reactor-regeneration system. In this sense, DTO process is a paradigmatic example of a complex reaction network consisted of several steps, which undergo a fast deactivation by coking. The mechanism of the process presents interesting unknown aspects by its own, as the higher reactivity of DME than that of methanol and the key role played by water. Deactivation is also defined by complex equations due to its dependency on the composition of the reaction medium, mainly affected by the conversion level and the amount of water.

The objective of this work is to deal with an overall process of DME conversion, considering the catalyst deactivation and the byproduct valorization as key points. The effect of deactivation is taken into account on: (i) the catalyst selection, using HZSM-5 zeolite; (ii) the catalyst agglomeration, providing a mesoporous matrix that stabilizes the catalyst; (iii) the reaction mechanism, mainly proposed in the literature for its counterpart MTO process using SAPO-34; (iv) the catalyst regeneration; (v) the catalytic cracking of paraffins, as the main byproduct of the reaction; (vi) the kinetic model and the development of an enhanced modeling methodology; (vii) the reactor and regenerator design, with the incorporation of an activity distribution function in circulating fluidized bed reactors, and; (viii) the simulation of the operation strategy, with a dual reactor-regenerator system being the most suitable selection. The following specific objectives were set in order to achieve this main goal:

- To collect the required experimental data for the conversion of DME into hydrocarbons in a wide range of reaction conditions in order to be able to discuss the role played by HZSM-5 zeolite acidity and reaction medium composition in terms of activity, selectivity and stability.
- To select the catalyst and the optimal conditions for maximizing the yields of the targeted products and attenuating the catalyst deactivation from the DTO and catalytic cracking experimental results obtained in an integral packed bed reactor.

- To establish a relationship between the proposed rational lump-based networks and the mechanistic pathways of the MTO/DTO process or the catalytic cracking of paraffins.
- To propose an enhanced methodology for the computation of kinetic models for catalytic processes with complex reaction networks and deactivation equations dependent on the composition of the reaction medium.
- To develop conceptual designs and simulations of different reactor configurations for these specific catalytic processes, being able to solve a dual reactor-regenerator system applied to the DTO process where the HZSM-5 zeolite-based catalyst circulates between two bubbling fluidized bed units.

These individual objectives are addressed in an orderly manner in each of the Chapters of the thesis.

Chapter 2

Experimental

This Chapter provides detailed information about the materials and experimental methods used for the preparation and characterization of the catalysts. A complete description of the experimental setup, where the reaction runs were carried out, and the product analysis systems are also described. The method for the analysis of coke are detailed as catalyst deactivation plays an important role in this work.

2.1 Catalyst preparation

The catalysts were prepared from HZSM-5 zeolites provided by Zeolyst with two different Si/Al ratios, 15 and 140. These two HZSM-5 zeolites were selected after a preliminary study about the influence of Si/Al ratio on the herein studied reactions. An agglomeration method was used for the sake of dispersing the zeolite crystals into an inert matrix with improved mechanical resistance. α -Al₂O₃ was used as inert filler and pseudoboehmite was used as a binder. The preparation method is detailed step by step in the Figure 2.1. A colloidal dispersion of 20 wt% α -Al₂O₃ (provided by Alfa Aesar) was first mixed with the pseudoboehmite (70 wt% Al₂O₃, provided by Sasol). When a homogeneous mixture was obtained, the HZSM-5 zeolite was slowly added into the solution, ensuring a suitable mixture and dispersion in the slurry. Then, the mixture was extruded in cylinders of ca. 2 mm and dried for 12 h at room temperature. The relatively fragile extrudates were sieved to a particle size between 0.15 and 0.30 mm and the resulting particles were calcined in air at 575 °C for 2 h using a heating rate of 5 °C min⁻¹ up to this temperature. The calcination of the HZSM-5 catalyst at this temperature removes the strongest Brønsted acid sites by dehydroxylation. These sites play an

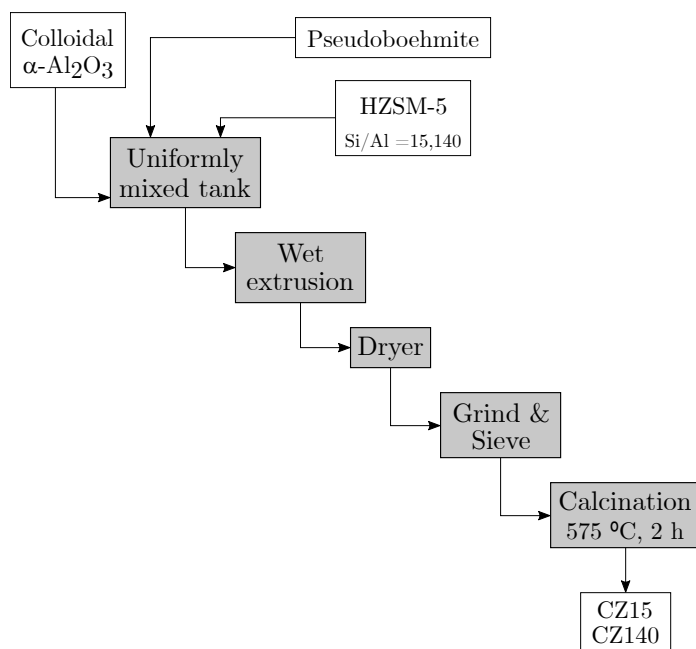


Fig. 2.1. Stages of the preparation procedure for the zeolite-based catalysts.

important role in the formation of coke. They are deactivated very fast and are not recovered in a regeneration by combustion at 550 °C. Consequently, the catalyst calcined at 575 °C is stable in reaction-regeneration cycles.

During the calcination, pseudoboehmite was converted into $\gamma\text{-Al}_2\text{O}_3$, which is its stable phase at this temperature. The amounts of precursors were calculated in order to achieve a zeolite/ $\gamma\text{-Al}_2\text{O}_3$ / $\alpha\text{-Al}_2\text{O}_3$ ratio of 50/30/20 (wt%) in the final catalyst. Tough particles were obtained after the calcination. The formed $\gamma\text{-Al}_2\text{O}_3$ is a mesoporous material that acts as a matrix for the prepared catalyst. Hence, this agglomeration of the zeolites not only endows the final catalyst with an improved mechanical resistance, but also with a hierarchical mesoporous structure, which favors the stability of the catalyst due to the promoted diffusion of coke precursors outside the zeolite [59]. The procedure was repeated for both zeolites with different Si/Al ratios. Pure zeolites were named Z15 (Si/Al = 15) and Z140 (Si/Al = 140). The nomenclature used for the final catalysts was also based on the Si/Al ratio of the zeolites: CZ15 and CZ140 catalysts.

2.2 Catalyst characterization

2.2.1 Crystalline structure

The crystalline structure of the zeolites and catalysts was analyzed by means of X-ray diffraction (XRD), measured in a Bruker D8 Advance diffractometer provided with a $\text{CuK}\alpha 1$ radiation. The device is equipped with a Germanium primary monochromator, Bragg-Brentano geometry and a $\text{CuK}\alpha 1$ wavelength of 1.5406 Å, corresponding to a X-ray tube with Cu anticathode. A sol-X dispersive energy detector was employed, with a wavelength window optimized for limiting fluorescence. The data collection was carried continuously from 10° to 80°, with steps of 0.04° in 2θ .

2.2.2 Porous structure

The porous structure of the fresh and used catalysts was characterized by N_2 adsorption-desorption at $-196\text{ }^\circ\text{C}$ in a Micromeritics ASAP 2010. Samples were degassed at $150\text{ }^\circ\text{C}$ for 8 h in order to remove impurities and water adsorbed within the pores. From N_2 isotherms, the specific surface area (S_{BET}) was determined using the Brunauer-Emmett-Teller equation, whereas micropore volume (V_{micr}) and external surface area (S_{ext}) were determined with the t -plot method, based on the Harkins-Jura equation. The mesopore volume (V_{mes}) was computed as the difference between the total pore volume (from the adsorbed amount at 0.995 relative pressure) and the micropore volume.

2.2.3 Acidity

The catalyst acidity was determined by adsorption of *tert*-butylamine (*tBA*), performed in a Setaram DSC-111 calorimeter coupled to a mass spectrometer Balzers Thermostar. Prior to the analysis, samples were submitted to a He stripping at $550\text{ }^\circ\text{C}$ and then, the probe molecule was adsorbed at $100\text{ }^\circ\text{C}$. After saturation, physisorbed *tBA* was removed by He stripping at the same temperature. Afterwards, a temperature-programmed desorption (TPD) was performed by raising the temperature at a heating rate of a $5\text{ }^\circ\text{C min}^{-1}$ up to $500\text{ }^\circ\text{C}$ in a He flow of $50\text{ cm}^3\text{ min}^{-1}$. The cracking of *tBA* molecules chemisorbed on the acid sites can be monitored by recording the signal of butene (the main *tBA* cracking product, $m/z = 56$) during the TPD experiment. This experiment evaluates the capability of the acid sites for cracking hydrocarbon chains, which is commonly attribute to the Brønsted acid sites. In this case, strong acid sites are identified at low desorption temperature, since the presence of butene indicates an easier cracking of the *tBA* chain.

2.2.4 Morphology

The morphology of the fresh and used catalysts was studied by confocal fluorescence microscopy (CFM) with a ZEISS LSM 800 microscope, provided with a turbo pumped chamber, a motorized stage and multi-alkali, GaAsP and Airyscan detectors. The microscope is also provided with three excitation channels with diode lasers at 405, 488 and 561 nm, making the samples emit fluorescence in the wavelength of blue, green and red ranges, respectively. The used accelerating voltage was 20 kV. Brightness and contrast were equally set for all samples in order to compare the intensity of emitted fluorescence with the surface concentration. Images were formed by stacking 10–20 samples of different z axes corresponding to 0–50 μm deep on the particle surface. Reflection images of the samples were also obtained, for which particles were submitted only to the 405 nm laser and the reflected beam was collected by the detector. This is an analogous technique to scanning electron microscopy (SEM) but using a laser beam instead of irradiating the sample with electrons.

2.3 Reaction equipment and procedures

2.3.1 Reaction unit

The reaction runs were carried out in an automated reaction equipment (Microactivity Reference, PID Eng&Tech), schematized in Figure 2.2. Three different sections are identified: a reactant feeding section, a reaction section and a product collection section.

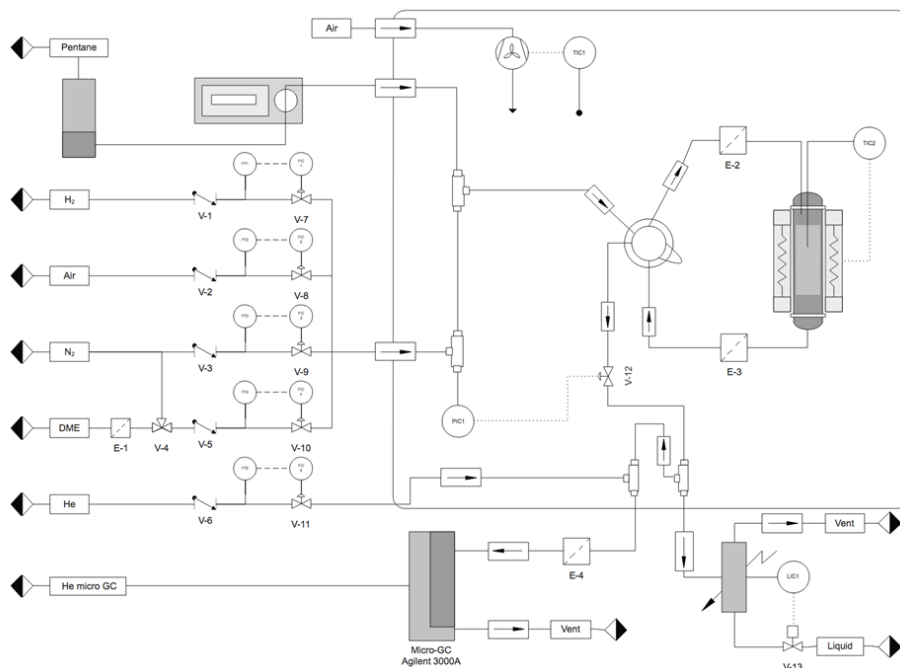


Fig. 2.2. Diagram of the reaction system.

Feeding section

The system is provided with five inputs for gases and one for liquids. Gases are directly fed into the reaction section through individual lines, each one with mass flow controllers (Bronkhorst High-Tech) that allows feeding maxima of $100\text{--}200\text{ cm}^3\text{ min}^{-1}$. The available gases are:

- (i) H_2 : Auxiliary reactive gas.
- (ii) Air: Oxidant gas for the catalyst pretreatment and regeneration.

- (iii) N₂: Inert gas for conditioning and cooling down the system and controlling the reactant partial pressure.
- (iv) Dimethyl ether (DME): Reactive gas. The N₂ line is also connected to that of DME in order to clean pipe tubes and the mass flow controller after each reaction run.
- (v) He: Carrier gas for the chromatographic analyses. It is fed in a different line, directly to the outlet stream, in order to dilute samples before the injection in the microGC.

Liquid input allows different reactants to be fed, for which specific pumps are required:

- (i) H₂O: Co-fed with DME. It is fed using a HPLC 307 pump (Gilson), provided with a pressure restrictor of 20 bar (overpressure), allowing liquid flow rates from 0.01 to 5 mL min⁻¹.
- (ii) Methanol: Alternative reactant to DME. It is also fed with the HPLC pump.
- (iii) *n*-Pentane (nC₅): Co-fed with DME or methanol and also used as the main reactant for the studies of valorization of paraffins. The addition of the nC₅ was done by a high pressure syringe pump (Harvard Apparatus PHD 400) and a 100 mL high pressure stainless steel syringe (5 bar), allowing stable flow rates from 0.01 to 30 mL min⁻¹.

Reaction section

Reactants, gases and liquids, are mixed inside a hotbox. The system is provided with a 6 port valve (Valco VICI) that allows bypassing the reactor. The stainless steel packed bed reactor has an internal diameter of 9 mm and is heated with a cylindrical ceramic oven, able to operate up to 600 °C. The temperatures in the hotbox and reactor are measured by K-type thermocouples and controlled by TOHO TTM-005 controllers.

Product collection section

Before exiting the hotbox, the reaction products are mixed with He and small samples of the mixture are extracted for analyses. The majority of the exiting stream is cooled down in a Peltier cell at 0 °C, where the liquid products are condensed. Gaseous samples are systematically sampled and analyzed every 8 min, whereas the liquid products are collected at the end of each run.

2.3.2 Catalyst pretreatments

For reactor loading, the catalyst was mixed with inert SiC in order to obtain a constant bed height in all the experiments and ensure isothermal conditions. Because of catalyst particles were sieved between 0.15–0.30 mm, SiC of 0.5 mm was used for ensuring a satisfactory separation of the used catalyst after reactions. The catalytic bed was formed by the mix of a certain amount of catalyst and SiC. This catalytic bed is located in the reactor between quartz wool plug and cap at the bottom and top of the reactor, respectively. The effective catalytic bed height was set to ca. 10 cm.

Before the reactions, the catalyst was submitted to a pretreatment at 550 °C for 2 h under a continuous flow of air ($30 \text{ cm}^3 \text{ min}^{-1}$) for sweeping water and impurities trapped within the pores of the catalyst. Several authors reported the necessity of not only removing water but also of activating the zeolite acid sites. Different pretreatment procedures were reported, being the most used those with pure O_2 [87], inert gases as He or N_2 , and air [233]. In most of the cases, 550 °C is used as the pretreatment temperature.

2.3.3 Reaction conditions

The same reaction setup was used for all reaction runs, but the conditions were set as a function of the studied process: DME-to-olefins, catalytic cracking of paraffins, using *n*-pentane as a model compound, and the combined reaction of oxygenates (OX, DME or methanol) and *n*-pentane.

Dimethyl ether-to-olefins

The DME-to-olefins reaction was studied using the prepared HZSM-5 zeolite-based catalysts with different acidity, CZ15 and CZ140. The following operation conditions were used: 325–400 °C, total pressure of 1.5 bar, space time (τ) of 0–6.5 g h mol_C^{-1} (in contained C units) and time on stream up to 15 h. Different mixtures of DME with N_2 and water (W) were fed to the reactor, using DME: N_2 molar ratios of 1:0–1:2 and DME:W molar ratios of 1:0–1:8.

Catalytic cracking of *n*-pentane

The catalytic cracking of *n*-pentane was carried out using the same CZ15 and CZ140 catalysts and these reaction conditions: 350–550 °C, total pressure of 1.5 bar, space time of 0–5 g h mol_C^{-1} and time on stream up to 15 h. The partial pressure of $n\text{C}_5$ in the experiments was ranged from 0.2 to 1 bar (diluted in N_2).

Combined reaction of oxygenates and *n*-pentane

The combined conversion of oxygenated compounds and *n*-pentane was performed with the CZ15 and CZ140 catalysts at 400–500 °C, total pressure of 1.5 bar, space

time of $0-1 \text{ g h mol}_C^{-1}$ and time on stream up to 15 h. The space time is defined in terms of C contained units and a constant ratio of fed C to catalyst was used in all cases. The partial pressure of the C-containing reactants was 1.0 bar diluted in N_2 , and different mixtures of oxygenate and $n\text{C}_5$ were used. The oxygenate-to- $n\text{C}_5$ molar ratios ($\text{OX}:n\text{C}_5$) were varied from 9:1 to 1:9. The flow rates of each reactant were set and the N_2 flow rate and catalyst weight were modified in each reaction in order to perform the runs with the same space time (in contained C units) and partial pressure of C-containing reactants.

2.4 Analysis of reaction products

The reaction products were analyzed in a micro gas chromatograph (Agilent 3000A microGC), provided with 4 columns and TCD detectors that allow the identification of the following products:

- (i) Molecular sieve (MS-5), which separates the permanent gases: H_2 , O_2 , N_2 , CH_4 and CO .
- (ii) Parapak Q (PPQ), which separates CO_2 , H_2O and DME.
- (iii) Alumina, which separates short-chained paraffins and olefins (C_{2-5}).
- (iv) Stabilwax, which separates C_{6-8} hydrocarbons, methanol and BTX aromatics.

Before starting a set of experimental runs, the microGC was calibrated using a gas standard provided by Air Liquide: CH_4 (1.37 vol%), C_2H_6 (0.94 vol%), C_2H_4 (1.98 vol%), C_3H_8 (1.41 vol%), C_3H_6 (2.85 vol%), C_4H_{10} (1.39 vol%), C_4H_8 (0.94 vol%), CO (2.05 vol%), CO_2 (2.86 vol%). Calibration factors were obtained from the analysis of the gas standards, by referring them to CO_2 concentration. The analysis conditions of the microGC are detailed in the Table 2.1.

Liquid product was also collected after reactions, but the amount of carbon products was negligible in both DTO process and catalytic cracking of nC_5 . In fact, the total yield of liquid product was only significant during the DTO runs when water was co-fed into the reactor or in reactions with high DME conversions during more than 10 h on stream. As displayed in Figure 2.2, sampling of reaction products was always performed before the condenser and the microGC is able to analyze hydrocarbons with up to 8 carbon atoms. In all cases, the carbon balance closure was higher than 90 %, including the small amount of C_{8+} liquid product and the experimental errors in the chromatograms integration.

Table 2.1. Analysis conditions for the chromatographic columns.

	MS-5	PPQ	Alumina	Stabilwash
Injector temperature ($^{\circ}\text{C}$)	100	100	100	80
Column temperature ($^{\circ}\text{C}$)	85	60	120	65
Backflush (s)	9	30	8	0
Inject time (ms)	0	5	20	30
Analysis time (s)	480	480	480	480
Column pressure (psi)	27	25	30	25

2.5 Analysis of coke by temperature-programmed oxidation

After each reaction run, the catalytic bed was cooled down to 150 °C and submitted to a sweeping with 20 cm³ min⁻¹ of N₂ for 20 min in order to remove the adsorbed volatile products. The purpose is to obtain reproducible results of the used catalyst characterization for all the experiments. Subsequently, the catalytic bed was cooled down to room temperature and the catalyst was separated from the inert SiC for its characterization. The porous structure and acidity of the used catalyst were analyzed following the procedures detailed in Section 2.2.

2.5.1 Experimental procedure

The content and location of coke were studied by means of thermogravimetric and temperature-programmed oxidation (TG-TPO) in a thermobalance TGA Q5000 IR (TA Instruments). Before the combustion, samples of used catalyst were submitted to a temperature-programmed desorption (TG-TPD) in order to sweep water and potential coke precursors adsorbed on the surface of the catalyst. During the TG-TPD, the temperature was stabilized at 50 °C and then, raised up to the reaction temperature of each used catalyst at a heating rate of 10 °C min⁻¹ in a continuous N₂ flow of 50 cm³ min⁻¹. After 15 min at this temperature, samples were cooled again at 50 °C. N₂ flow was changed for air and the temperature was maintained isothermal until the air flow of 50 cm³ min⁻¹ was stable. TG-TPO analyses were carried out by increasing the temperature from 50 to 550 °C at a heating rate of 10 °C min⁻¹. This final temperature was maintained isothermal for 2 h, after which it was decreased to room temperature.

2.5.2 Model for the combustion of coke

A simple combustion kinetic model can be used in order to simulate the weight loss during the TG-TPO experiments. Different kind of models have been proposed, but the simplest power-law kinetic models are generally used [234–236]. Querini et al. [237] first explained the possibility of obtaining accurate fitting of experimental TPO profiles by their deconvolution with a linear combination of power-law expressions. According to our previous results [38], three different coke fractions can be defined for describing the carbonaceous species deposited during these reactions. Their combustion was modeled assuming a complete combustion of each fraction, no diffusion limitations and a uniform combustion model of coke particles. In this sense, a power-law kinetic equation of first order with respect to the content of each k coke fraction (C_{C_k}) and the partial pressure of oxygen (P_{O_2}) is defined. A

reparameterized form of the Arrhenius equation is considered

$$-\frac{dC_{C_k}}{dt} = k_k^* \exp \left[-\frac{E_k}{R} \left(\frac{1}{T} - \frac{1}{T^*} \right) \right] C_{C_k} P_{O_2}, \quad (2.1)$$

where k_k^* and E_k are the apparent kinetic constant at the reference temperature T^* (500 °C) and activation energy for the combustion of each k coke fraction, respectively, and R is the universal gas constant. The initial condition for solving equation (2.1) is given by

$$C_{C_k}(0) = x_k C_C, \quad (2.2)$$

with C_C being calculated as the difference between the total mass of the used (after the TG-TPD) and the regenerated catalyst (after the TG-TPO) and x_k defined as the mass fraction of each k coke fraction. The optimal parameters of k_k^* and E_k were computed using a MATLAB routine, which allows for minimizing the sum of squares errors between experimental and calculated values as

$$SSE_C = \sum_{n=1}^{n_e} \left[\left(\frac{dC_{C_k}}{dt} \right)_{\text{exp}} - \left(\frac{dC_{C_k}}{dt} \right)_{\text{calc}} \right]_n^2, \quad (2.3)$$

where n is the number of experimental data and n_e the total number of experiments during the complete combustion of coke.

Chapter 3

Fundamentals of DTO process

This Chapter gives a first overview of the dimethyl ether-to-olefins (DTO) process. The characterization of the HZSM-5 catalyst is detailed, as well as the mechanistic basis that will lead to the lump-based kinetic model in the following Chapters. A main goal of this thesis is to predict the catalyst deactivation with our models. Therefore, an in-depth study about the influence of DTO process variables on the catalyst deactivation is presented in this Chapter. The effect of catalyst properties and reaction conditions on the evolution of DTO process and the formation of coke is explained. Finally, two big concerns for chemical processes are dealt with, the regeneration of the catalyst and the possibilities for valorizing the byproducts. Part of the results in this Chapter have been published in *Ind. Eng. Chem. Res.* **2018**, *57*, 13689-13702.

3.1 HZSM-5 catalysts

As explained with more details in Chapter 1, the methanol-to-olefins (MTO) process is currently carried out using SAPO-34 catalysts. SAPO-34 has a severe shape selectivity, which allows very high selectivity to ethylene and propylene to be obtained [47, 238]. HZSM-5 zeolite presents a three-dimensional microporous structure with wider and open channels. This of course leads to a lower selectivity to light olefins but yields higher propylene/ethylene ratios. The HZSM-5 structure also favors the contact of reactants with acid sites in these wide channels and more important, delays the catalyst deactivation [69]. Overall, HZSM-5 catalysts are more stable and present longer lifetimes than those of SAPO-34. This is a great advantage as DME is more reactive than methanol, thus deactivating the catalyst faster.

3.1.1 Physico-chemical properties

The use of catalysts at industrial scale requires particles with high mechanical resistance. In general, zeolites present low particle size and are fragile, so they are usually embedded in a tougher matrix [68]. This changes the physico-chemical properties of the catalyst particle. In our case, the zeolite was agglomerated using pseudoboehmite as a binder. Once calcined, the γ -Al₂O₃ matrix is an amorphous phase that does not modify the crystalline structure of the HZSM-5 zeolite. Figure 3.1 shows the XRD patterns of the Z15 zeolite and the CZ15 catalyst. A neater pattern can be observed for the fresh zeolite. However, the main peaks are equal in both cases, highlighting the more intense peaks in the 2θ range of 22-25°. The effect of the matrix is mainly the addition of noise to the XRD signal due to the dilution of the zeolite and some background at 2θ values $> 30^\circ$.

Pseudoboehmite-derived mesoporous matrix provides the catalyst with a hierarchical porous structure, which favors the diffusion of the reactants and is able to attenuate the blockage of the zeolite micropores [239]. Figure 3.2a displays the N₂ adsorption-desorption isotherms of the Z140 zeolite, the matrix and the final CZ140 catalyst. The matrix was prepared following the same procedure detailed in Section 2.1 but without adding zeolite to the initial slurry. HZSM-5 zeolite exhibits an isotherm typical of microporous materials, adsorbing the majority of N₂ at very low relative pressures. In contrast, the γ -Al₂O₃ matrix has a type IV isotherm, taking the main amount of N₂ at relative pressures higher than 0.4 (in the mesoporous range). The presence of the matrix decreases the N₂ adsorption at low relative pressure compared to that of the bare zeolite. However, the catalyst adsorbs N₂ in a wide range of relative pressure, which suggests that the matrix provides the final catalyst with a mesoporous structure additional to that of the

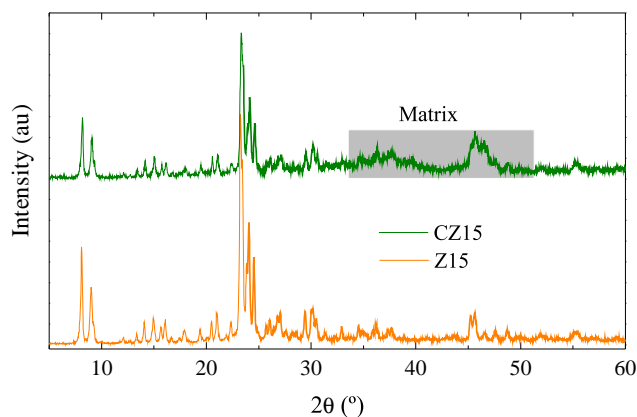


Fig. 3.1. Comparison of the XRD patterns of the Z15 zeolite and the CZ15 catalyst.

zeolite crystals.

Table 3.1 shows the main structural parameters calculated from the N_2 adsorption-desorption isotherms of the bare zeolites with Si/Al molar ratio of 15 (Z15) and 140 (Z140), the matrix after the calcination and the final catalysts (CZ15 and CZ140). The highest S_{BET} values are observed for the bare zeolites, with similar 421 and 436 $m^2 g^{-1}$ and negligible contributions of the external surface (S_{ext} of 45 and 41 $m^2 g^{-1}$), for Z15 and Z140, respectively. This result is typical of solids with a developed microporous structure (V_{micr} of 0.16 and 0.18 $cm^3 g^{-1}$, respectively). In contrast, the matrix exhibits a higher value of S_{ext} than that of S_{BET} (198 and 189 $m^2 g^{-1}$, respectively), which is associated with mesoporous solids without thinner pores than 2 nm. The CZ15 and CZ140 catalysts respectively exhibit S_{BET} of 288 and 271 $m^2 g^{-1}$, and S_{ext} of 136 $m^2 g^{-1}$ and 131 $m^2 g^{-1}$. This indicates that the microporous crystals of the zeolite are dispersed in the mesoporous matrix, without decreasing the accessibility of N_2 toward its channels (V_{micr} of 0.06 and 0.07 $cm^3 g^{-1}$, for CZ15 and CZ140 catalysts, respectively). Further results on the dispersion of the zeolite crystals within the matrix will be discussed in Chapter 4, with the catalysts being tested in the catalytic cracking of *n*-pentane.

Figure 3.2b shows the TPD profile of *t*BA for the Z140 zeolite and the agglomerated catalyst. As previously stated in Section 2.2, the lower the temperature of the peak, the stronger the acid site, since the temperature needed for *t*BA cracking is lower. The TPD profile for Z140 zeolite shows two defined peaks related to strong and weak acid sites (208 and 260 °C, respectively). Otherwise, the $\gamma-Al_2O_3$

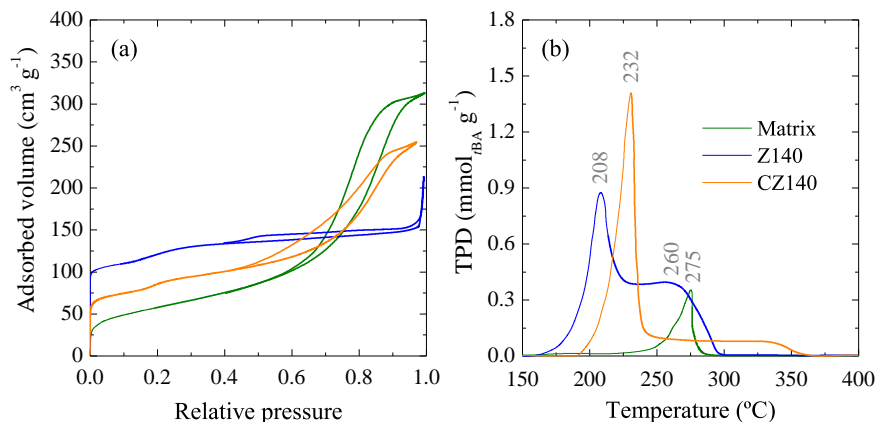


Fig. 3.2. (a) N₂ adsorption-desorption isotherms and (b) *t*BA TPD of the Z140 zeolite, the matrix and the CZ140 catalyst.

Table 3.1. Porous and acid properties of the zeolites, the matrix and the catalysts from N₂ and *t*BA adsorption-desorption.

	S_{BET} (m ² g ⁻¹)	V_{micr} (cm ³ g ⁻¹)	V_{mes} (cm ³ g ⁻¹)	S_{ext} (m ² g ⁻¹)	Acidity (mmol _{<i>t</i>BA} g ⁻¹)
Z15	421	0.16	0.11	41	0.80
Z140	436	0.18	0.16	45	0.41
Matrix	189	0.00	0.48	198	0.12
CZ15	288	0.06	0.34	136	0.42
CZ140	271	0.07	0.29	131	0.33

matrix only shows one peak attributed to acid sites even weaker than those of the zeolite (275 °C). The final catalyst shows a well-defined peak at 232 °C (not as strong as the first one of the zeolite) and a second broad hump in the 250–350 °C temperature range. The shift of the peak attributed to strong acid sites can be associated with the partial covering of the zeolite crystals by the matrix, thus hindering the adsorption of *t*BA on the strongest sites located on the external surface of the crystals. The broad hump corresponds to the weak acid sites and can be related to the γ -Al₂O₃ matrix [69]. In terms of total acidity, Z15 zeolite has a double value than Z140 zeolite (0.80 and 0.41 mmol_{*t*BA} g⁻¹, respectively, Table 3.1). In both cases, the agglomeration leads to a decrease in the total acidity, more pronounced for CZ15 catalyst (0.42 mmol_{*t*BA} g⁻¹).

The matrix presents a very low total acidity ($0.12 \text{ mmol}_{t\text{BA}} \text{ g}^{-1}$), which is insufficiently active for DTO conversion. Presumably, this is also related to the weak strength of those sites (see Figure 3.2b). This was proven in a reaction using only the matrix without zeolite. The results at $400 \text{ }^\circ\text{C}$, the highest tested temperature for this process, can be observed in Figure 3.3. Low DME conversion was observed (7%), only yielding CH_4 and CO_x (mainly CO) as the products of the thermal cracking of DME. Nevertheless, the faster activity of catalytic pathways than the thermal one leads to lower yields of CH_4 and CO_x using the zeolites than those depicted here, as can be observed in the following Sections.

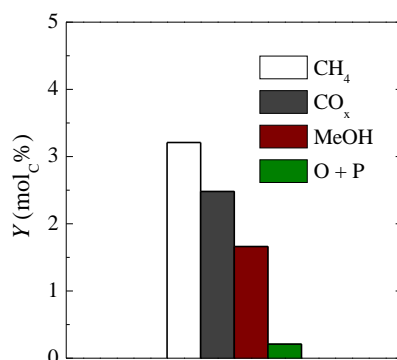


Fig. 3.3. Product distribution for DTO process using the matrix. $400 \text{ }^\circ\text{C}$, $\tau = 2 \text{ g h mol}_C^{-1}$, $t = 0 \text{ h}$.

3.2 Reaction network and mechanisms

The agglomerated HZSM-5 zeolite-based catalysts with two different Si/Al ratio were tested in the dimethyl ether-to-olefins (DTO) reaction. DTO runs were carried out in the 325–400 °C temperature range under the conditions previously detailed in Chapter 2. From the chromatographic analyses, a wide spectrum of reaction products can be analyzed. An oxygenate (OX) conversion is defined, by taking into account the transformed DME and methanol into products. Then, the conversion in terms of C units (X) is calculated as

$$X = \frac{F - F_{\text{DME}} - F_{\text{MeOH}}}{F} \quad (3.1)$$

where F is the total molar flow rate and F_{DME} and F_{MeOH} are respectively the molar flow rates of DME and methanol in terms of C units at the outlet of the reactor. The yield (Y_i) and the selectivity (S_i) of each i lump are defined as

$$Y_i = \frac{F_i}{F}, \quad (3.2)$$

$$S_i = \frac{Y_i}{X} = \frac{F_i}{F - F_{\text{DME}} - F_{\text{MeOH}}}, \quad (3.3)$$

where F_i is the molar flow rate of each i lump at the outlet of the reactor in terms of C units.

A detailed chromatographic study allows the reaction network of the process to be analyzed. A set of experiments for each catalyst was selected in order to consider the complete range of conversion. Figure 3.4 shows the evolution with conversion of the selectivity to each product with the less acid CZ140 catalyst. Products are grouped as a function of their expected behavior in the reaction network according to its analogous performance in the MTO reaction [88].

Figure 3.4a depicts the trends for the primary olefins formed from the methoxy intermediates adsorbed on the Brønsted sites of the zeolite [87]. Ethylene and propylene are the main products observed and both present a maximum in the selectivity trend, suggesting that they act as intermediates of the reaction. Some controversy still exists in the literature on the formation of the initial C–C bond and on the role of these two olefins as primary products. According to the data revealed by Chowdhury et al. [73], the formation of ethylene during the early stages of the reaction is required in order to initiate the dual cycle mechanism. Our results are in accordance with this conclusion as the maximum of ethylene is located at lower conversion than that of propylene. The three linear butenes (1-butene, *trans*-butene and *cis*-butene) are also observed as reaction products. In this case, clear

maxima are not observed but the selectivities reach a plateau at high conversions, denoting a similar kinetic behavior to those of ethylene and propylene. The overall sum of this olefins (O, solid line) also presents a clear maximum at a conversion value of ca. 90%.

Linear paraffins show much lower concentrations and a different tendency of their selectivity with the conversion (Figure 3.4b). The selectivity to ethane is negligible and those of propane and *n*-butane are lower than 2% at any conversion value. However, they tend to increase with conversion as final products of the

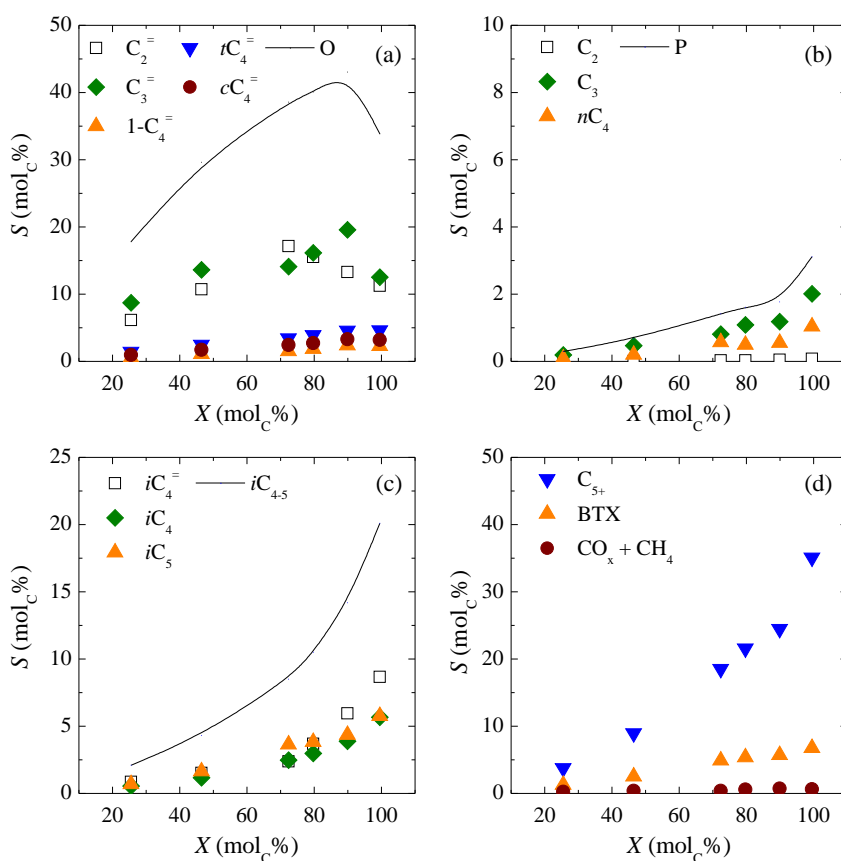


Fig. 3.4. Evolution with oxygenate conversion of the selectivity to (a) the primary olefins, (b) C_{2-4} paraffins, (c) *i*-butene and *i*- C_{4-5} paraffins and (d) C_{5+} hydrocarbons, BTX and $CO_x + CH_4$ using CZ140 catalyst.

mechanisms. Likewise, *i*-butene and *i*-paraffins show increases in their selectivities with the conversion (Figure 3.4c). The selectivity values in this case are significantly higher, thus attaining a maximum of 20% at conditions of full conversion.

This is consistent with the reported data on the dual cycle mechanism. Along with propylene, *i*-butene can be considered as one of the main product from the dealkylation of the arene cycle intermediates [94]. Both olefins are two of the main products of the reaction medium, suggesting the promotion of this cycle. From *i*-butene, the saturated *i*-paraffins can be formed by the hydrogen transfer/methylation pathway proposed by Martínez-Espín et al. [87]. As observed in Figure 3.4c, the trends in their selectivity are equal.

HZSM-5 was originally reported for the methanol-to-gasoline (MTG) process due to its selectivity to C_{5–11} hydrocarbons [35]. This can be observed in Figure 3.4d, where the increase of long-chained hydrocarbon with the conversion is remarkable. C₅₊ hydrocarbon lump is mainly formed by unsaturated and saturated hydrocarbons with 5 to 8 carbons atom. Aromatics are also commonly reported to be promoted with the MFI framework shape selectivity. In our system, a maximum yield of BTX (benzene, toluene and xilenes) of ca. 8% can be achieved with this CZ140 catalyst, and as a final products, the selectivity to BTX aromatics increases with conversion. In all the conversion range, the production of C₁ compounds (CO_x and CH₄) is negligible.

The same analysis is made with the more acid CZ15 catalyst. The analogous results are depicted in Figure 3.5. Although the trends are not as clear as those observed with CZ140 catalyst, a similar behavior can be deduced. Minor but significant differences can be noted. The selectivity to ethylene does not exhibit a maximum but increases linearly with the conversion (Figure 3.5a). The groundbreaking work from Bjørgen et al. [88] explained that this is caused by a promotion of the arene cycle, which is favored by the catalyst acidity. The displacement of the mechanism towards the arene cycle should go in parallel with higher productions of aromatics. Nevertheless, this is not observed in our case (Figure 3.5d) but can be easily explained by the competitive and promoted condensation of aromatics to coke in-depth studied in the next Section.

Two more important observations can be made regarding the results with this catalyst compared to those obtained with the CZ140 catalyst. The selectivity to propane (Figure 3.5b) and *i*-paraffins (Figure 3.5c) are favored, in such a way as the one to *i*-butene presents a maximum instead of an exponential growth as observed before (Figure 3.4c). All these are evidences of the promoted hydrogen transfer pathway, which again points out a favored arene cycle and aromatic formation. The significant decrease in the selectivity to C₅₊ is also worth mentioning (Figure 3.5d), with values almost half of those obtained with CZ140 catalyst. The

higher acidity and density of acid sites of CZ15 catalyst undoubtedly increase the contribution of the cracking pathway. Then, hydrocarbons with long carbon chain are easily converted into short-chained olefins or paraffins, as well suggested by the results of Figure 3.5.

From these results and considering the HCP and dual cycle mechanisms explained in Chapter 1, a lump-based adaptation of the mechanism is proposed. Scheme 3.1 will allow us to discuss the results in the following Chapters and propose a lump-based kinetic model for DTO process in Chapter 5.

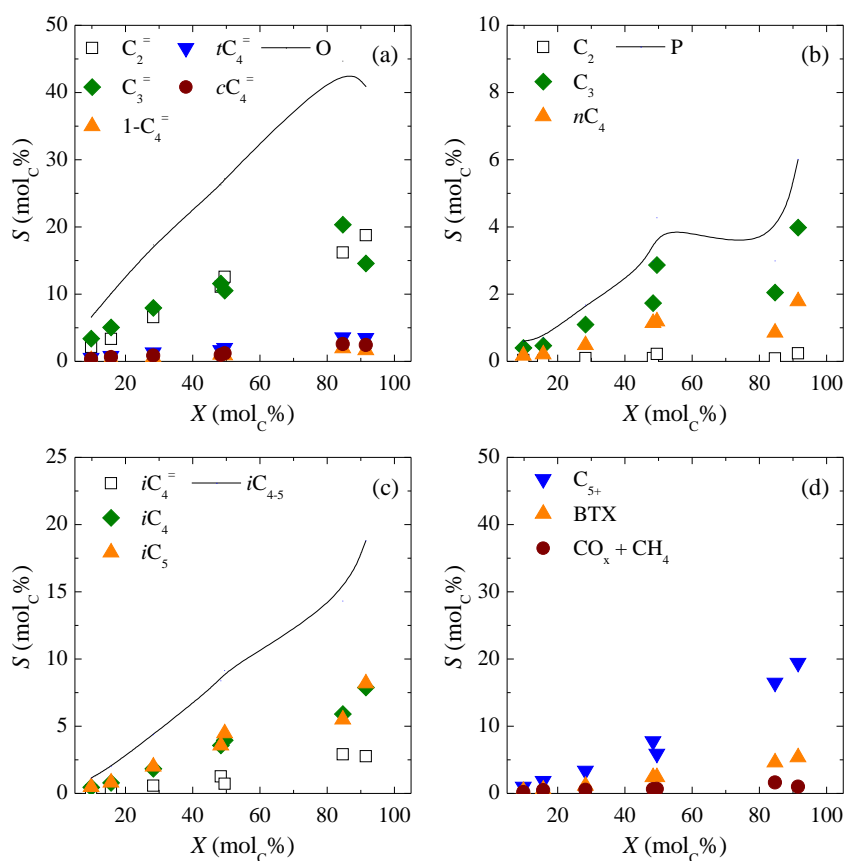
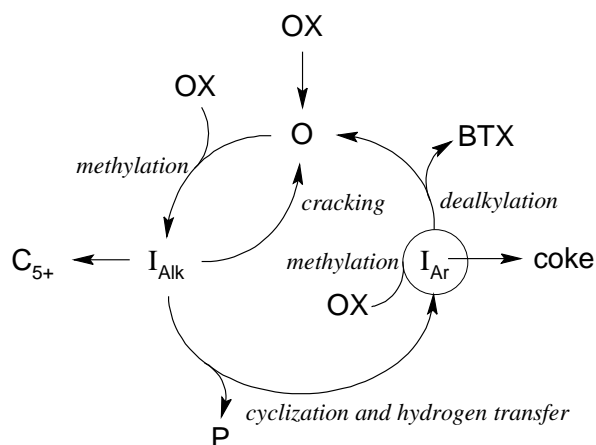


Fig. 3.5. Evolution with oxygenate conversion of the selectivity to (a) the primary olefins, (b) C_{2-4} paraffins, (c) i -butene and i - C_{4-5} paraffins and (d) C_{5+} hydrocarbons, BTX and $CO_x + CH_4$ using CZ15 catalyst.



Scheme 3.1. Lump-based adaptation of the dual cycle mechanism for DTO process.

According to the network, the initial C–C bond formation and propagation yields the primary olefins (O), then initiating the dual cycle mechanism. Two reaction intermediates are associated with each of the cycles. The alkene cycle intermediates (I_{Alk}) should consist of long-chained unsaturated hydrocarbons. These species are formed from the methylation of the primary olefins, and can directly derive into C_{5+} hydrocarbons or produce light olefins by cracking. Both cycles are connected through the cyclization/hydrogen transfer pathway, and the arene cycle intermediates (I_{Ar}) are produced with the parallel formation of light paraffins (P). Similar to the methylation of olefins, the arene cycle intermediates can be directly alkylated from methoxy species. The dealkylation of these intermediates yields olefins and aromatics with lower alkylation degree (BTX). Depending on the acidity and morphology of the catalyst, the condensation of the arene cycle intermediates towards coke can play an important role in the evolution of the reaction.

3.3 Catalyst deactivation

Catalyst deactivation by coking is a crucial issue for the viability of DTO process and it is influenced by the properties of the catalyst and reaction conditions. The effect of agglomerating the zeolite in a mesoporous matrix and of zeolite acidity are analyzed, as well as the influence of reaction temperature and diluting the DME in N_2 and water.

3.3.1 Role of the matrix

Figure 3.6a displays the evolution with time of the DTO conversion for the zeolite (Z15) and the catalyst (CZ15). The composition of the catalyst is 50 wt% of zeolite, which is in accordance with the almost double acidity value of Z15 compared to that of CZ15 catalyst (Table 3.1). For a direct comparison, the results of Figure 3.6 are given for space time values in terms of contained zeolite ($\tau = 1.0 \text{ g}_Z \text{ h mol}_C^{-1}$), i.e. using the double weight of CZ15 catalyst in the catalytic bed. The initial conversions of Z15 zeolite and CZ15 catalyst are similar (44 and 50%, respectively in Figure 3.6a). However, the decrease in the conversion with time is significantly faster for Z15 zeolite. Both Z15 zeolite and CZ15 catalyst reach conversions lower than 5% after 15 h.

The deposition of coke is the cause of this activity loss, so TPO analyses of the

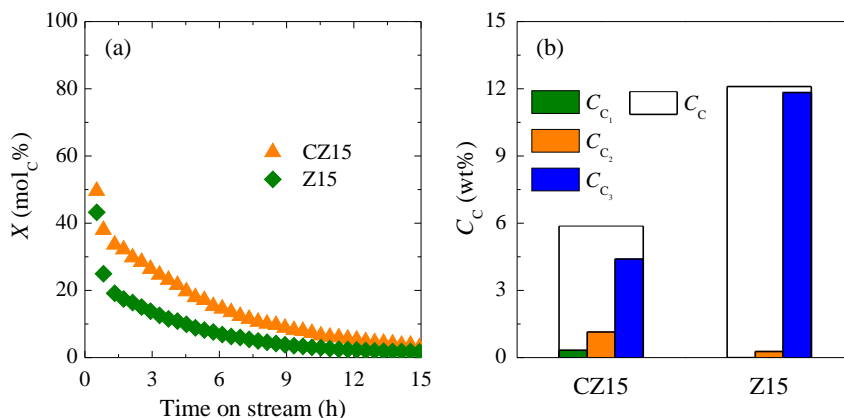


Fig. 3.6. Effect of the matrix on (a) the evolution with time of the conversion and (b) the content of each coke fraction deposited on the used CZ15 catalyst and Z15 zeolite. 350 °C, $\tau = 1.0 \text{ g}_Z \text{ h mol}_C^{-1}$.

used catalysts were carried out. The total content of coke (C_C) can be calculated from thermogravimetric measurements. These values are illustrated by the white and broader columns in Figure 3.6b. A double content of coke (in wt% of solid) is observed on the surface of the Z15 zeolite. Hence, the content of coke per zeolite weight is similar in both cases (ca. 12 wt%), but the coke properties significantly change.

For the characterization of the coke, the obtained TPO profiles were deconvoluted according to the combustion kinetic model previously described in Section 2.5. Figures 3.7a and 3.7b respectively show the TPO profiles obtained for the used Z15 zeolite and CZ15 catalysts for given reaction conditions. From the deconvolution of the TPO profiles of used catalysts at different conditions, three peaks can be identified, located at 390, 465 and 550 °C. Each peak is attributed to the combustion of the defined coke fractions C_1 , C_2 and C_3 . The content of each coke fraction (C_{C_1} , C_{C_2} and C_{C_3}) is illustrated in Figure 3.6b with the colored and thinner columns. The kinetic constant at the reference temperature (500 °C) and apparent activation energy of the combustion of each coke fraction were computed. The computation was performed considering the TPO profiles of used catalysts at different conditions, and the obtained values are listed in Table 3.2.

The computed kinetic constants for the CZ15 catalyst are 190.0, 61.1 and ca. 7.6 h⁻¹ bar⁻¹ and the apparent activation energy values are ca. 70, ca. 89 and 144 kJ mol⁻¹ for C_1 , C_2 and C_3 , respectively. The same trend is followed by the kinetic parameters computed for the CZ140 catalyst, indicating that coke fractions burn off in the order $C_1 > C_2 > C_3$. The existence of three coke fractions with different combustion rates deposited on the surface of an agglomerated HZSM-5-based catalyst is related to their different composition and location in the particle [52]. Coke fractions C_1 and C_2 are located outside the microporous structure of the zeolite because they are not observed in the TPO of the bare zeolite (Figure 3.7a). Coke fraction C_1 , which exhibits low combustion temperature, is located on the mesoporous structure of the matrix and its formation is a consequence of the sweeping

Table 3.2. Kinetic parameters of the combustion of each coke fraction deposited on the surface of CZ15 and CZ140 catalysts.

	CZ15	CZ140
k_1^* (h ⁻¹ bar ⁻¹)	(1.90 ± 0.25) 10 ²	(1.68 ± 0.20) 10 ²
k_2^* (h ⁻¹ bar ⁻¹)	(6.11 ± 0.90) 10 ¹	(4.89 ± 0.19) 10 ¹
k_3^* (h ⁻¹ bar ⁻¹)	(7.56 ± 1.23) 10 ⁰	(1.01 ± 0.09) 10 ¹
E_1 (kJ mol ⁻¹)	(6.96 ± 1.25) 10 ¹	(8.10 ± 0.31) 10 ¹
E_2 (kJ mol ⁻¹)	(8.89 ± 2.50) 10 ¹	(1.07 ± 0.07) 10 ²
E_3 (kJ mol ⁻¹)	(1.44 ± 0.21) 10 ⁰	(1.16 ± 0.04) 10 ²

of coke precursors from the acid sites of the zeolite. Without the presence of the strong acid sites of the zeolite, the precursors of coke are deposited on the matrix surface but do not develop such a condensed structure. Consequently, it burns at this low temperature (390 °C). Coke fraction C_2 is associated with carbonaceous species located on the external surface of the zeolite crystals. This nature can explain its intermediate values of combustion kinetic parameters (Table 3.2) and its minimum presence in the Z15 zeolite (Figure 3.7a), because the external surface of the HZSM-5 zeolite is very low (41–45 m² g⁻¹, Table 3.1).

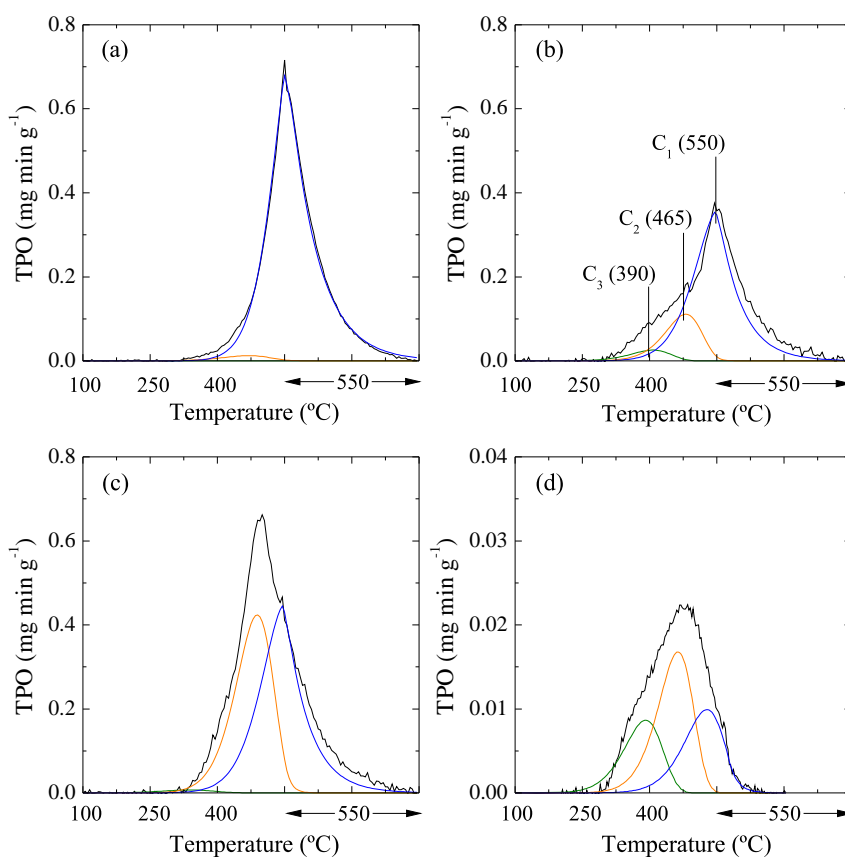


Fig. 3.7. TPO profiles of (a) the used Z15 zeolite at 350 °C, the used CZ15 catalyst at (b) 350 °C and (c) 400 °C and (d) the used CZ140 catalyst at 400 °C. $\tau = 1.0 \text{ g z h mol}^{-1}$.

The combustion of coke fractions C_2 and C_3 (orange and blue lines in Figure 3.7) are overlapped in the Z15 zeolite because their crystals are not dispersed in a matrix but form clusters within which coke fraction C_2 is also deposited. For this reason, coke fraction C_3 is the only noticeable one in the used Z15 zeolite. Its high combustion temperature (550 °C) suggests that this coke fraction presents a developed and condensed structure. This is presumably a consequence of its formation over the acid sites of the zeolite, thus partially blocking the micropores. Several authors have associated the formation of coke from methanol [102, 105, 108, 240] and DME [52] with the condensation of polyalkyl aromatics (trapped in the channels of the zeolite) toward developed carbonaceous structures. Therefore, the location of this coke fraction C_3 within the micropores of the zeolite (blocking the acid sites) hinders its combustion, which could explain the position of the peak in the TPO profile and the values of the kinetic parameters. Leistener et al. [241] also reported a linear correlation between the activation energy of each carbonaceous species and its C/H ratio. They found values of activation energy for coke combustion in the same range that the ones listed in Table 3.2. According to their results, the coke fraction C_1 should be more aliphatic than the coke fractions C_2 and C_3 . In this regard, the latter presents the most developed structure due to the activity of acid sites for condensing the components of coke.

3.3.2 Role of catalyst acidity

Figure 3.8a shows the evolution with time of the conversion for the CZ15 and CZ140 catalysts at 350 and 400 °C. As shown in Table 3.1, the acidity of these catalysts are respectively 0.42 and 0.33 mmol_{tBA} g⁻¹. The strong influence of Si/Al molar ratio on the amount of acid sites in a HZSM-5 zeolite was previously observed in our research group [69], and was also demonstrated by other authors [242]. The initial conversions are similar for both catalysts at the same temperature, yielding values of 28.4 and 25.6% at 350 °C and of 99.5 and 89.5% at 400 °C (for CZ15 and CZ140 catalysts, respectively). Nevertheless, the conversion decays much faster for the CZ15 catalyst, being remarkable the total loss of the activity after 4.5 h at 400 °C. The remaining conversion of 2% is the results of the thermal cracking of DME forming CO_x and CH₄. On the other hand, CZ140 catalyst presents a linear and slower decay of the conversion, and only losses ca. 10% of the initial conversion after 15 h on stream at both temperatures.

The different deactivation rate of the catalysts could be related to the different nature of the coke fractions observed in the TPO profiles of Figure 3.7. The TPO profile of the used CZ140 catalyst at 400 °C (Figure 3.7d) shows a wider peak with a maximum located at lower temperatures than the one of the used CZ15 catalyst at the same condition (Figure 3.7c). A coke with a more heterogeneous

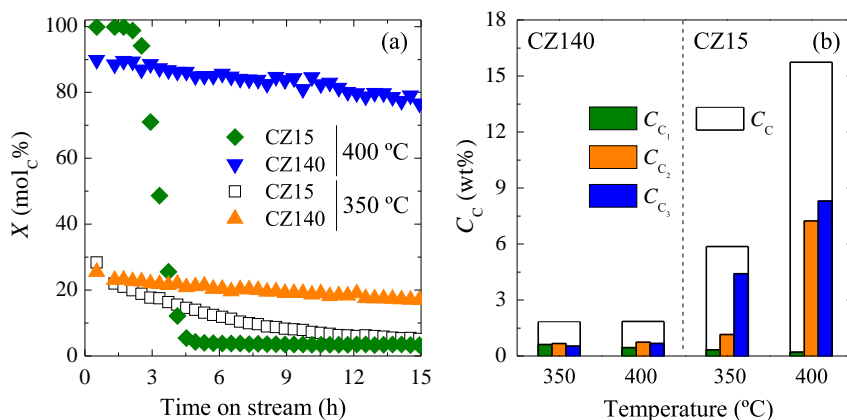


Fig. 3.8. Effect of catalyst acidity on (a) the evolution with time of the conversion and (b) the content of each coke fraction deposited on these used catalysts at 350 and 400 °C. $\tau = 1.0 \text{ g h mol}^{-1}$.

nature is deposited on the surface of CZ140 catalyst. This also leads to the small deviations between the kinetic parameters of the combustion of each coke fraction deposited on the surface of both catalysts (Table 3.2). The kinetic constants of the combustion of the coke fractions C_1 and C_2 are lower and their apparent activation energy values are higher for the CZ140 catalyst. However, the combustion of the coke fraction C_3 shows higher apparent kinetic constant ($10.1 \text{ h}^{-1} \text{ bar}^{-1}$) and lower activation energy (116 kJ mol^{-1}), which means that it is easily burnt off. This is in accordance with the lower capability of condensing species of coke exhibited by the weaker acid sites of the Z140 zeolite.

The total content of coke and the ones of each fraction can be observed in Figure 3.8b. The increase in the reaction temperature with CZ140 catalyst does not significantly change the amount of deposited coke (ca. 1.9 wt%). However, a slightly higher amount of coke fraction C_3 is observed at 400 °C, as a consequence of the promoted condensation of the hydrocarbon pool species at higher temperatures. On the other hand, used CZ15 catalysts exhibit higher content of coke and especially of coke fraction C_3 deposited within the micropores of the zeolite. This is presumably explained by the faster condensation of the species involved in the dual cycle mechanism. The increase in the coke fraction C_2 is also significant at 400 °C, which points out the higher deposition of coke outside the zeolite crystals upon increasing temperature.

The structural parameters of selected used catalysts are displayed in Table 3.3

and corroborate the previous assignation of each coke fraction location. The S_{ext} values calculated for the CZ15 catalyst at both temperatures are similar or even higher than those of S_{BET} . This means that the used catalysts present a totally blocked microporous structure but show certain external surface. In contrast, used CZ140 catalysts present higher specific surface area with a considerable contribution of micro- and mesopores ($S_{\text{BET}} > S_{\text{ext}}$). The lower blockage of the zeolite micropores is in accordance with the lower deactivation, the lower content of coke and the more heterogeneous nature of coke exhibited by the CZ140 catalyst. The total acidity values of the used catalysts are also consistent with the discussed structural parameters (Table 3.3), showing the used CZ140 catalysts higher values at both temperatures.

3.3.3 Effect of temperature

The evolution with time of the conversion at different temperatures is shown in Figures 3.9a and 3.9b for the CZ15 and CZ140 catalysts, respectively. The corresponding evolution of the total content of coke and the one of each coke fraction are depicted in Figures 3.9c and 3.9d. CZ15 catalyst exhibits an increase in the conversion and deactivation rate when temperature is increased from 325 to 400 °C. The total content of coke also increases in this catalyst when temperature is raised, with an inverse tendency for the coke fraction C_1 due to the promoted condensation at higher temperatures. As explained before, coke is predominantly

Table 3.3. Porous and acid properties of the used CZ15 and CZ140 catalysts at different reaction conditions from N_2 and *t*BAA adsorption-desorption.

	S_{BET} ($\text{m}^2 \text{g}^{-1}$)	S_{ext} ($\text{m}^2 \text{g}^{-1}$)	Acidity ($\text{mmol}_{t\text{BA}} \text{g}^{-1}$)
CZ15			
350 °C; 0.5 g h mol_C^{-1} ; ^a	94	108	0.10
350 °C; 1.0 g h mol_C^{-1} ; ^a	91	90	0.11
350 °C; 1.0 g h mol_C^{-1} ; ^b	89	105	0.09
350 °C; 1.0 g h mol_C^{-1} ; ^c	127	119	0.15
400 °C; 1.0 g h mol_C^{-1} ; ^a	74	85	0.06
CZ140			
350 °C; 1.0 g h mol_C^{-1} ; ^a	180	117	0.20
400 °C; 1.0 g h mol_C^{-1} ; ^a	192	105	0.24

^a Pure DME

^b DME and N_2 (1:2)

^c DME and H_2O (1:2)

formed within the channels of the zeolite (coke fraction C_3), which could diffuse outside them when the amount of deposits is relatively high (coke fraction C_2). Up to 375 °C, the conversion undergoes a fast deactivation due to the formation of this coke fraction C_3 , whose increase goes hand in hand with that of coke fraction C_2 . A different behavior is observed with this catalyst at 400 °C, with full conversion during 3 h on stream and a sudden and very fast deactivation. The massive formation of coke fraction C_3 leads to the coke growing outside the zeolite crystals according to the reported overloading of the zeolite pores [112]. This can explain

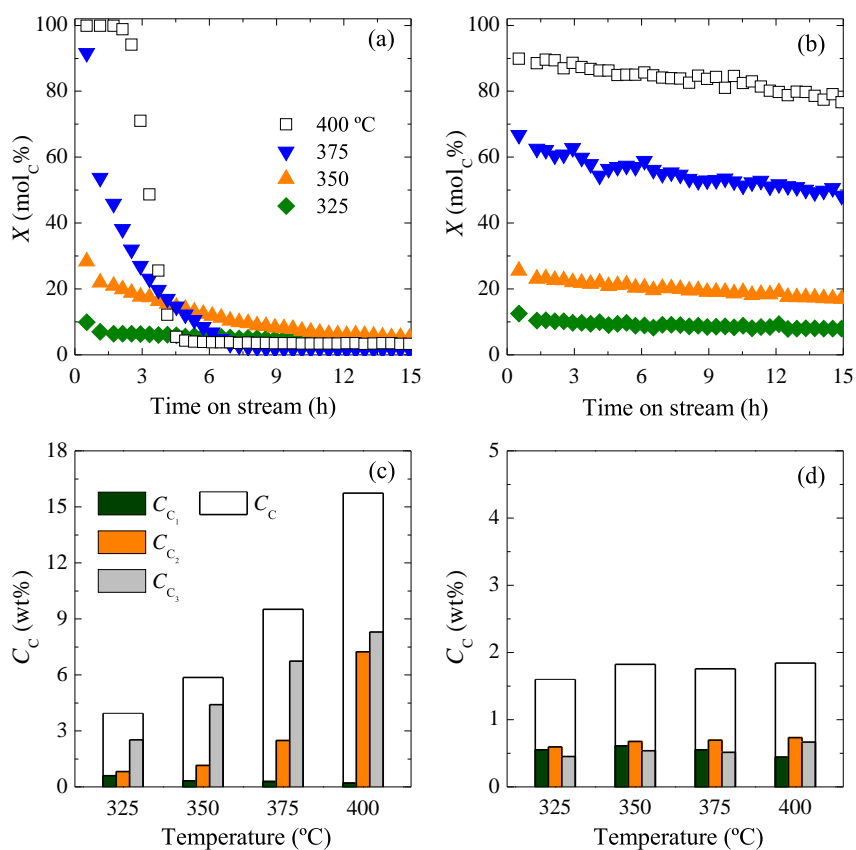


Fig. 3.9. Effect of temperature on the evolution with time of the conversion for (a) the CZ15 and (b) the CZ140 catalysts and on the content of each coke fraction deposited on the used (c) CZ15 and (d) CZ140 catalysts. $\tau = 1.0 \text{ g h mol}_C^{-1}$.

the similar content of the coke fraction C_3 at 375 and 400 °C, and the significant increase in the coke fraction C_2 .

The lower acidity of the CZ140 catalyst has a strong influence on the decay of the conversion with time (Figure 3.9b) and the deposition of coke (Figure 3.9d). With this catalyst, deactivation is not only slower than that observed with CZ15 catalyst (Figure 3.9a), but also the dependency on temperature decreases. Almost parallel trends are observed for the evolution with time of the conversion, which is also translated to similar coke contents (ca. 1.9 wt%) and coke fraction distributions. Only a slightly decrease in the content of coke fraction C_1 and an increase in that of coke fraction C_3 can be noticeable. The lower initial activity of the CZ140 catalyst and the also lower density and strength of the acid sites hinder the direct formation of coke through the oligomerization of olefins [98, 99].

According to these results, mild conditions, such as moderate acidity or low temperature (350 °C), allow the extent of the mechanism and the formation of coke to be controlled. In these cases, the main cause of deactivation should be the mask of acid sites by coke. The absence of cages and relatively wide channels of the MFI framework ease the sweeping of the precursors of coke, thus delaying the formation of polyaromatic structures that block the zeolite micropores. Otherwise, the total blockage of micropores was reported as the main cause of deactivation of SAPO-34 catalysts during the conversion of methanol [49, 243]. This is also observed in our reaction when harsher conditions were used (high acidity and 400 °C), and is attributed to the zeolite pores overloading with coke. A negligible value of acidity is registered at these conditions ($0.06 \text{ mmol}_{\text{tBA}} \text{ g}^{-1}$ in Table 3.3). Hence, low temperatures and acidity should be used when DME is fed as a reactant, with the aim of controlling the extent of the condensation reactions that yield coke.

3.3.4 Role of water

The encouraging interest of co-feeding water (W) for mitigating the catalyst deactivation in the conversion of methanol is well-established in the literature [194, 244]. In fact, this strategy is used at industrial scale in MTO process [67]. This attenuation of deactivation was also observed in the conversion of DME and was attributed to several factors [38, 42]: (i) the reduction of the partial pressure of reactants, which delays the advance of the reaction; (ii) the limitation of the formation of methoxy species; (iii) the competitive adsorption of water and coke precursors on the acid sites, and; (iv) the sweeping of the precursors of coke from the zeolite to the mesoporous matrix. The influence of co-feeding water with DME on catalyst deactivation is stronger than that observed in the conversion of methanol [194], because pure methanol tends to easily dehydrate to DME, forming water at the entrance of the reactor. Consequently, the concentration of water in the reaction

medium is lower in the DME conversion. In order to determine the influence of water on the deposition of coke and catalyst deactivation, additional DTO runs were carried out by diluting DME in water but maintaining the same space time with respect to the fed C units ($1.0 \text{ g h mol}_C^{-1}$). Experiments were carried out with CZ15 catalyst trying to prevent the massive formation of the coke fraction C_3 observed in the previous Sections.

Figures 3.10a and 3.10b show the evolution with time of the conversion at 350 and 400 °C, respectively, for different DME dilutions in N_2 and water. The corresponding evolution of the total content of coke and the one of each coke fraction are depicted in Figures 3.10c and 3.10d. At 350 °C, a drop of the initial conversion is observed when DME is co-fed with N_2 , due to the slower initial rate as a consequence of the reduction of DME partial pressure [37]. However, only a slightly decrease in the deactivation rate is achieved by following this dilution strategy with ca. 1 wt% drop of the total content of coke.

The effect of co-feeding water at 350 °C has higher impact on the deposition of coke and the attenuation of catalyst deactivation. A pronounced drop of the coke fraction C_3 , and consequently of the total content of coke, is observed using a DME:W molar ratio of 1:2 (Figure 3.10c). The sweeping of the precursors of coke to the mesopores of the matrix and the competitive adsorption of DME and water on the acid sites could explain this interesting result. The relative concentrations of coke fractions C_1 and C_2 also increase when water is co-fed. This sweeping of reaction intermediates leads to the aforementioned decay of the initial conversion but allows a steady conversion state to be achieved using a DME:W ratio of 1:4. Structural and acid parameters are in concordance with this hypothesis (Table 3.3). The values obtained for the catalyst used with a DME: N_2 molar ratio of 1:2 are similar to those registered for the catalyst used with pure DME. Co-feeding water with the same ratio leads to a used catalyst with higher S_{BET} and some remaining accessible micropores ($S_{\text{BET}} > S_{\text{ext}}$), which could explain the higher values of conversion after 15 h on stream.

A similar initial conversion trend is observed increasing the temperature up to 400 °C. A decrease in the initial conversion and a slower deactivation are achieved increasing the amount of co-fed water, but the desired situation of catalytic stability is not reached at this higher temperature. Although a reduction of the total content of coke from 15.7 to 2.2 wt% is achieved with a DME:W molar ratio of 1:8, the deposited coke is mainly formed by the coke fraction C_3 (Figure 3.10d). Steam seems to favor the sweeping of coke precursors outside the particle and coke fractions C_1 and C_2 are not observed for high DME:W molar ratios. However, the oligomerization and condensation mechanisms that lead to catalyst deactivation are not avoided at this temperature.

Reaction temperature plays a key role in the influence of water on the deposition of coke on the CZ15 catalyst. At 400 °C, the high activity of this catalyst, which rapidly forms the reaction intermediates and coke precursors, makes more difficult to attenuate the coke deposition inside the zeolite crystals. Undoubtedly, the high acidity of the CZ15 catalyst contributes to this outstanding activity of condensing coke at 400 °C. The combination of temperature and water in the reaction medium should be also taken into account for the irreversible deactivation

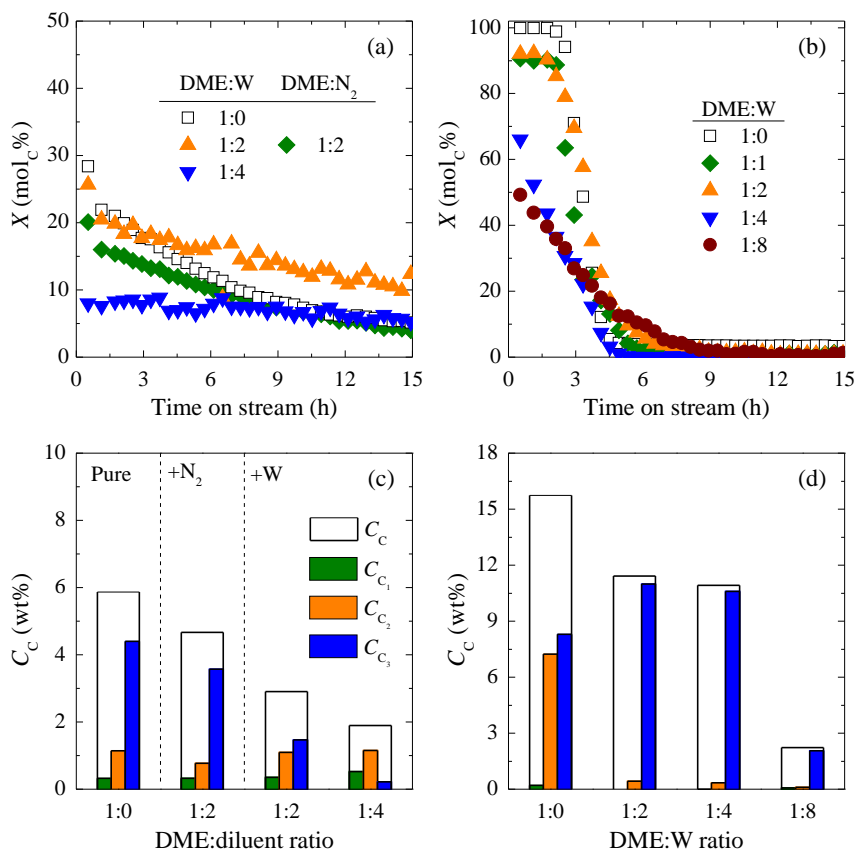


Fig. 3.10. Effect of the dilution in N₂ and water (W) on the evolution with time of the conversion at (a) 350 °C and (b) 400 °C and on the content of each coke fraction deposited on the used CZ15 catalysts at (c) 350 °C and (d) 400 °C. $\tau = 1.0 \text{ g h mol}_C^{-1}$.

of the catalyst due to dealumination. According to Gayubo et al. [245], this temperature is the limit for a HZSM-5 zeolite with such a low Si/Al ratio. In any case, these harsh conditions of temperature and acidity are not recommended according to the results in this Section.

3.4 Challenges to overcome

According to the previous results, there are some hurdles that should be considered in the DTO process. The most important is the catalyst deactivation. As in many industrial processes, the regeneration of the catalyst is required for a continuous production of the targeted compounds. On the other hand, high selectivity to long-chained hydrocarbons is obtained using the HZSM-5 catalyst (Figures 3.4 and 3.5). An easy strategy for its valorization should be recycling them with DME as the catalytic cracking of paraffins to olefins is a well-established process [120]. In this section, the viability of catalyst regeneration and co-feeding paraffins are analyzed trying to elucidate possible actions for DTO process improvement.

3.4.1 Catalyst regeneration

Regenerability is one of the most important properties of the catalyst from an operating point of view. Especially, it is crucial in acid-catalyzed reactions, such as the catalytic cracking (FCC) or MTO process, in which deactivation by coking is fast. Although a complete combustion of deposited coke is observed at 550 °C (Figure 3.7), it does not necessary mean a total recovery of the catalytic activity. Different reaction-regeneration cycles were carried out with both catalysts varying the reaction and regeneration conditions.

Figure 3.11 shows the evolution with time of the conversion and yields of olefins (O) and the rest of hydrocarbons (HC) during two reaction cycles after a regeneration treatment. The results correspond to the CZ15 catalyst used at 350 °C and regenerated through two different treatments as indicated in the graphs: (i) sweeping with N₂ at 550 °C for 2 h (Figure 3.11a) and; (ii) combustion of coke with air at 550 °C for 2 h (Figure 3.11b). The aging of coke under an inert or reductive atmosphere at high temperature is well-known [246]. However, these possible modifications of the coke structure do not allow any catalytic activity to be recovered. As observed in Figure 3.11a, the conversion and yields at the beginning of the second reaction cycle are practically overlapped with the last ones of the first cycle. Otherwise, the catalyst totally recovers the activity of the fresh one after a regeneration treatment based on the combustion of coke under an air continuous flow (Figure 3.11b). The same result is obtained just regenerating the catalyst during the temperature ramp between 350 and 550 °C, but 2 h at 550 °C in air is used for being consistent with the catalyst pretreatment before the first cycle. In the second reaction cycle, the regenerated catalyst exhibits a perfectly reproducible evolution with time of the conversion and product distribution.

Although the deactivation of the CZ15 catalyst is much more severe at 400 °C, this regeneration treatment is likewise effective for recovering the catalytic activity

(Figure 3.12a). In this case, the applied temperature ramp for regeneration was between 400 and 550 °C, and this final temperature was maintained for 2 h. At this higher temperature, the conversion decays faster, the total content of coke is higher and it is mainly formed by coke fraction C₃ deposited within the zeolite channels (Figure 3.8b). Catalyst acidity does not significantly affect the recovery of the activity, and CZ140 catalyst also presents similar conversion and yields in the second reaction cycle at 400 °C (Figure 3.12b).

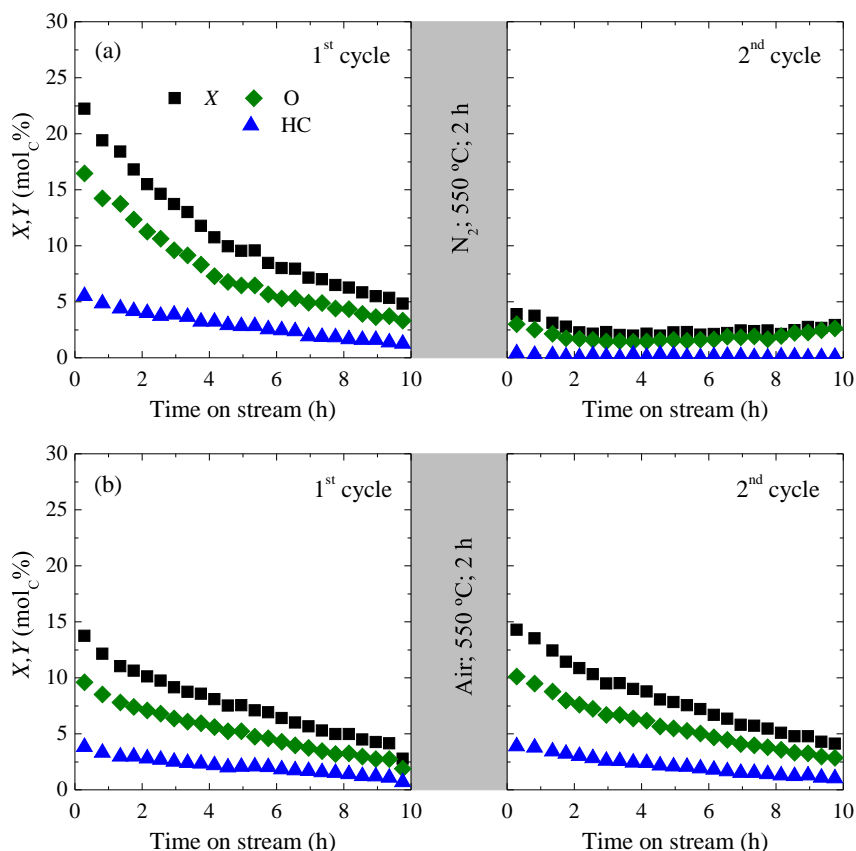


Fig. 3.11. Evolution with time of the conversion and yields of olefins and the rest of hydrocarbons in reaction-regeneration cycles using the CZ15 catalyst. (a) 350 °C, $\tau = 1.0 \text{ g h mol}_C^{-1}$; (b) 350 °C, $\tau = 0.5 \text{ g h mol}_C^{-1}$. Regeneration conditions indicated in the figure after a temperature ramp from 350 to 550 °C.

The results of this Section highlight the easy regeneration of the HZSM-5 zeolite-based catalyst deactivated during the DTO process, which is certainly interesting for its implementation. Independently on the content, location or nature of coke, a combustion treatment with air at 550 °C totally recovers the initial activity of the catalyst. This is presumably attributed to the low condensation degree of the structures of coke, which is limited by the shape selectivity of the HZSM-5 zeolite. Irreversible deactivation is not observed due to the thermal stability of the catalyst.

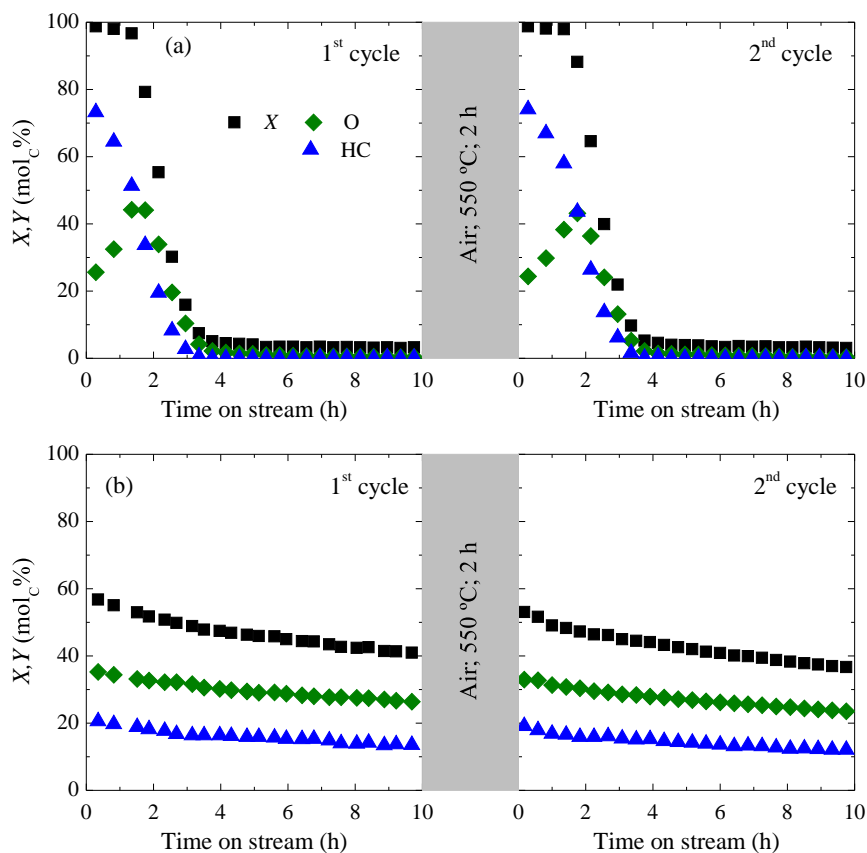
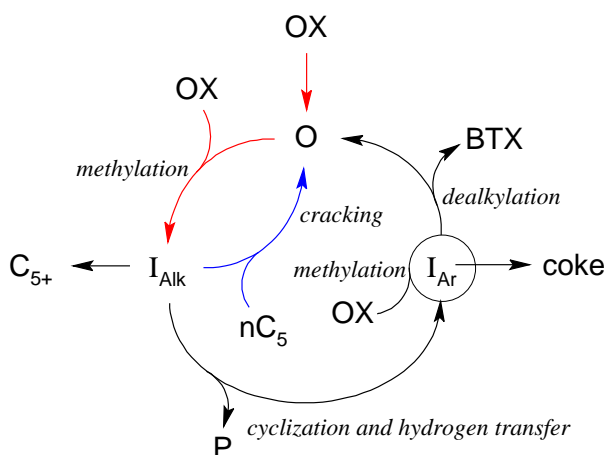


Fig. 3.12. Evolution with time of the conversion and yields of olefins and the rest of hydrocarbons in reaction-regeneration cycles at 400 °C and $\tau = 0.5 \text{ g h mol}_C^{-1}$ using the (a) CZ15 and (b) CZ140 catalysts. Regeneration conditions indicated in the figure after a temperature ramp from 400 to 550 °C in air.

3.4.2 Byproduct valorization

The combined reaction of DME and *n*-pentane (nC_5) is studied to analyze the feasibility of recycling the C_{5+} byproducts from DTO process, thus intensifying the production of olefins. nC_5 is selected as model compound because it is the less reactive component of the C_{5+} hydrocarbon lump. The recycling strategy is addressed because of the previously reported results by Martin et al. [147], who explored the coupled methanol and hydrocarbon cracking (CMHC) due to energy considerations. Thereby, the exothermic character of the methanol-to-olefins (MTO) process can be leveraged in order to overcome the energy requirements of the catalytic cracking of paraffins in an autothermal overall process. The combined cracking of oxygenates and hydrocarbons (especially paraffins) was also studied in the literature seeking synergistic effects in the mechanisms. Considering mechanistic aspects, the strategy of co-feeding paraffins is illustrated in Scheme 3.2. This modification of the Scheme 3.1 presents the incorporation of the nC_5 feed into the cracking pathway of the alkene cycle. Theoretically, the exothermic first stages of the dual cycle mechanism (red lines) could promote the endothermic initiation of the nC_5 cracking (blue line).

The other possible valorization route for the C_{5+} hydrocarbon byproducts in



Scheme 3.2. Lump-based adaptation of the dual cycle mechanism for co-fed DME and nC_5 conversion.

the MTO/DTO process is its separation and processing in a different unit. In this Section, the conversion of nC_5 co-fed with DME is compared to that obtained in its individual cracking. Recycling strategy will require the use of the MTO/DTO conditions, so temperatures higher than 400 °C are not recommended according to the results in Section 3.3. At this temperature, the cracking of nC_5 cannot be performed using the CZ140 catalyst due to its low acidity [129]. Then, co-feeding experiments were carried out at 400 °C with the CZ15 catalyst. The obtained results are depicted in Figure 3.13.

These results show the comparison of the nC_5 conversion in the individual reaction and the ones obtained in the combined reactions with DME: nC_5 molar ratios of 1:1, 4:1 and 9:1. Note that the latter refers to a situation in which a stream of pure DME would be mixed with a stream of C_{5+} hydrocarbons that represents a 10% of the reactor feed. The comparison of the results is made in terms of conversions (X), for which different indexes are defined. For individual reactions, DME conversion is calculated from the expression in equation (3.1) and the one of nC_5 is defined as

$$X_{nC_5} = \frac{F - F_{nC_5}}{F}, \quad (3.4)$$

where F is the total molar flow rate and F_{nC_5} is the molar flow rate of nC_5 at the outlet of the reactor in terms of C units. In the combined reactions, three different conversions are defined, accounting for the total C conversion, and the individual nC_5 and DME conversions. The total C conversion is calculated from the total molar flows of reactants at the outlet of the reactor

$$X = \frac{F - F_{nC_5} - F_{DME} - F_{MeOH}}{F}. \quad (3.5)$$

The definition of the individual conversions is based on the previously introduced equations (3.1) and (3.4). In this case, the total molar flow rate (F) takes the value of the individual molar flow rates of nC_5 and DME at the entrance of the reactor in terms of C units ($F_{nC_5}^0$ and F_{DME}^0 , respectively)

$$X_{nC_5} = \frac{F_{nC_5}^0 - F_{nC_5}}{F_{nC_5}^0} \quad (3.6)$$

$$X_{DME} = \frac{F_{DME}^0 - F_{DME} - F_{MeOH}}{F_{DME}^0}. \quad (3.7)$$

As observed in Figure 3.13a, the initial nC_5 conversion significantly drops as the amount of DME is increased. In fact, the most realistic situation of a feed stream with a DME: nC_5 ratio of 9:1 presents a negative value of nC_5 conversion.

This means that nC_5 concentration is higher in the product stream than that co-fed with DME. The results in Figure 3.5 suggest that the secondary pathways of oligomerization and hydrogen transfer (Scheme 3.2) are promoted at these conditions. Therefore, the reaction of surface methoxy intermediates with the gas phase DME is favored through the MTO/DTO pathway and the conversion of nC_5 is inhibited with this highly active catalyst and high DME concentration in the feed.

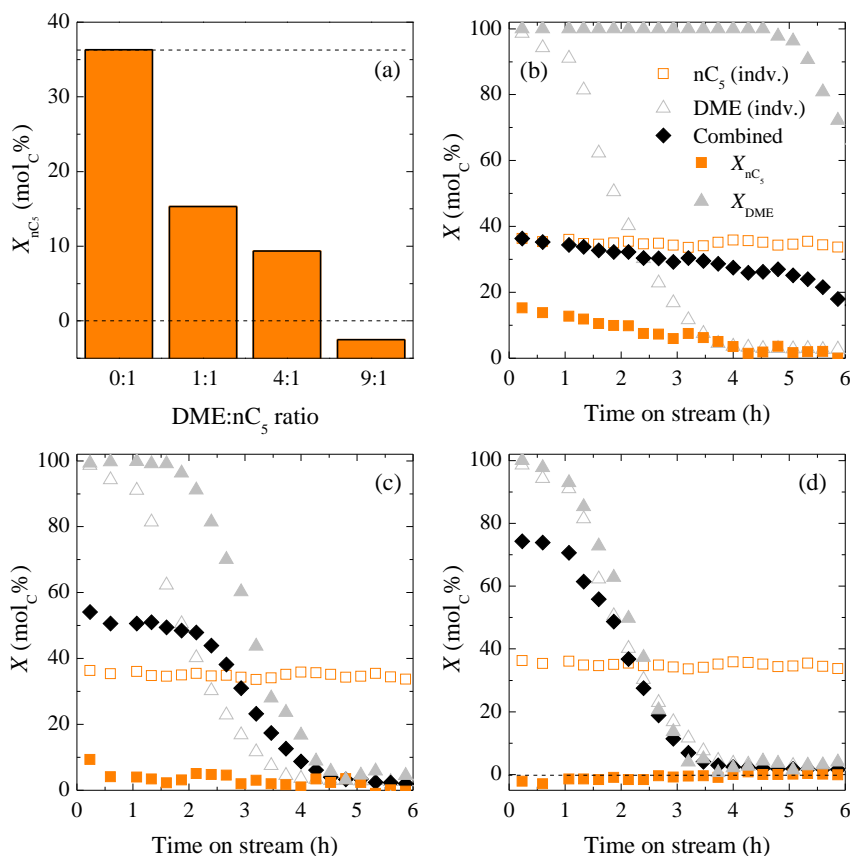


Fig. 3.13. Effect of co-feeding different DME/ nC_5 ratios on (a) the initial nC_5 conversion and evolution with time of nC_5 and DME conversions in individual (hollow symbols) and combined reactions (filled symbols) with DME: nC_5 ratios in the feed of (b) 1:1, (c) 4:1 and (d) 9:1, using the CZ15 catalyst. 400 °C, $\tau = 0.5$ g h mol $^{-1}$.

The influence of co-feeding both reactants on the catalyst deactivation is also evaluated. Thus, the evolution with time of nC_5 and DME conversions in their individual reactions (hollow symbols) and the combined reactions (filled symbols) and the total C conversion in the combined reaction (black diamonds) using DME: nC_5 ratios of 1:1, 4:1 and 9:1 are displayed in Figures 3.13b, 3.13c and 3.13d, respectively. A relatively stable nC_5 conversion is observed in its individual reaction, whereas DME conversion undergoes a fast drop during the first 4 h on stream. After 4 h, only CO_x and CH_4 are observed as a consequence of the thermal degradation of DME. The combined reactions are clearly dominated by the MTO/DTO reaction and catalyst deactivation is influenced by the presence of DME. Hence, the lowest amount of DME in the reaction medium (Figure 3.13b) leads to the highest increase in the catalyst lifetime. This could be attributed to different factors as: (i) the lower partial pressure of DME, which seems to be the driving force of deactivation; (ii) the competitive adsorption of nC_5 on the active sites, and; (iii) the active contribution of nC_5 in the mechanism.

Regarding the obtained results at 400 °C with the CZ15 catalyst, the focus of the research was changed to those conditions at which a positive synergy that enhances the cracking of nC_5 can be observed. Then, the CZ140 catalyst was used because of its lower activity and higher stability in order to avoid a mechanism dominated by DME conversion. Moreover, a temperature of 500 °C was set for promoting the cracking of nC_5 . In this case, a comparison between the reactivity of DME and methanol was also studied.

Figure 3.14 shows the initial nC_5 conversion when DME or MeOH were co-fed with different molar OX: nC_5 ratios using the CZ140 catalyst at 500 °C. nC_5 conversion is ca. 7% in its individual reaction and it notably increases (up to ca. 12%) when DME: nC_5 molar ratios of 1:9 and 1:4 are co-fed. The increase in the amount of co-fed DME drops nC_5 conversion, ultimately leading to the situation previously observed in Figure 3.13a with the CZ15 catalyst and 400 °C. A small improvement of nC_5 conversion is even observed feeding a mixture with a DME: nC_5 ratio of 1:1. The reactivity of methanol and DME in these combined reactions are also compared. An increase in the nC_5 conversion is observed when methanol is co-fed with the lowest MeOH: nC_5 ratio of 1:9 (ca. 9.5%). Nevertheless, this improvement is quite lower than that observed by co-feeding DME, which is in accordance with the higher reactivity of DME in the MTO/DTO reaction. The drop of nC_5 conversion upon increasing the amount of oxygenate in the feed is more noticeable in the case of methanol. And the use of a MeOH: nC_5 ratio of 1:1 leads to a decrease in the nC_5 conversion to values of ca. 4%, which is lower than that obtained in the individual reaction of nC_5 .

The reaction mechanism of paraffin cracking catalyzed by acid zeolites has been

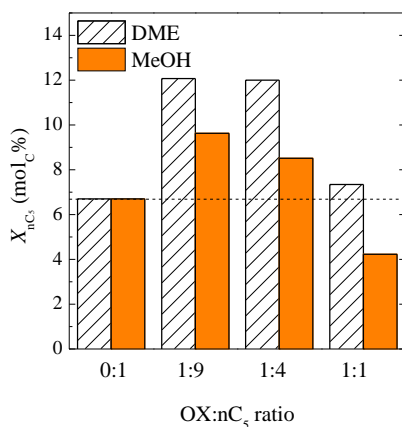


Fig. 3.14. Effect of OX:nC₅ ratio in the feed on the initial nC₅ conversion using the CZ140 catalyst. 500 °C, $\tau = 1.0 \text{ g h mol}_C^{-1}$.

thoroughly studied and, it is generally accepted that the involved acid sites are the Brønsted ones and the intermediates are carbenium and carbonium ions (see section 1.2). The activation of the paraffin on a Brønsted acid site is a highly demanding step, and the addition of olefins or oxygenates can increase the reaction rate. Under our reaction conditions, nC₅ conversion is increased at low concentrations of oxygenate, in good agreement with the observations of paraffin activation made by Chang et al. [153]. Nonetheless, the increase in the molar ratio of oxygenates in the feed causes a drop of the nC₅ conversion, which could be associated with the competitive reaction of the gas phase oxygenated reactant with the already formed methoxy species on the acid sites. This promotes the MTO/DTO pathway instead of the catalytic cracking of nC₅, which is clearly observed with the more acid CZ15 catalyst in the Figure 3.13.

Figures 3.15a, 3.15b and 3.15c show the evolution with time of the nC₅ and DME conversions in their individual reactions (hollow symbols) and the combined reactions (filled symbols) and the total C conversion in the combined reaction (black diamonds) using DME:nC₅ ratios of 1:9, 1:4 and 1:1, respectively. As observed at 400 °C with the CZ15 catalyst (Figures 3.13b, 3.13c and 3.13d), a drastic deactivation is also shown after 2 h of full conversion in the individual reaction of DME. In contrast, full DME conversion is achieved for 6 h when it is co-fed with nC₅, with no apparent catalyst deactivation in any case. Moreover, nC₅ conversion is maintained constant during 6 h for DME:nC₅ ratios of 1:9 and 1:4, as occur in its individual conversion. The increase in the fed DME concentration (DME:nC₅

ratios of 1:1) leads to a faster drop of nC_5 conversion. Then, the observed improvement of the conversion (Figure 3.14) is only available in the first stages of reaction ($t < 1$ h).

Nevertheless, the presence of the paraffin in the reaction medium plays a key role in the deactivation rate of DME conversion, which was also observed with the CZ15 catalyst and a DME: nC_5 ratio of 1:1 (Figure 3.13b). The same partial

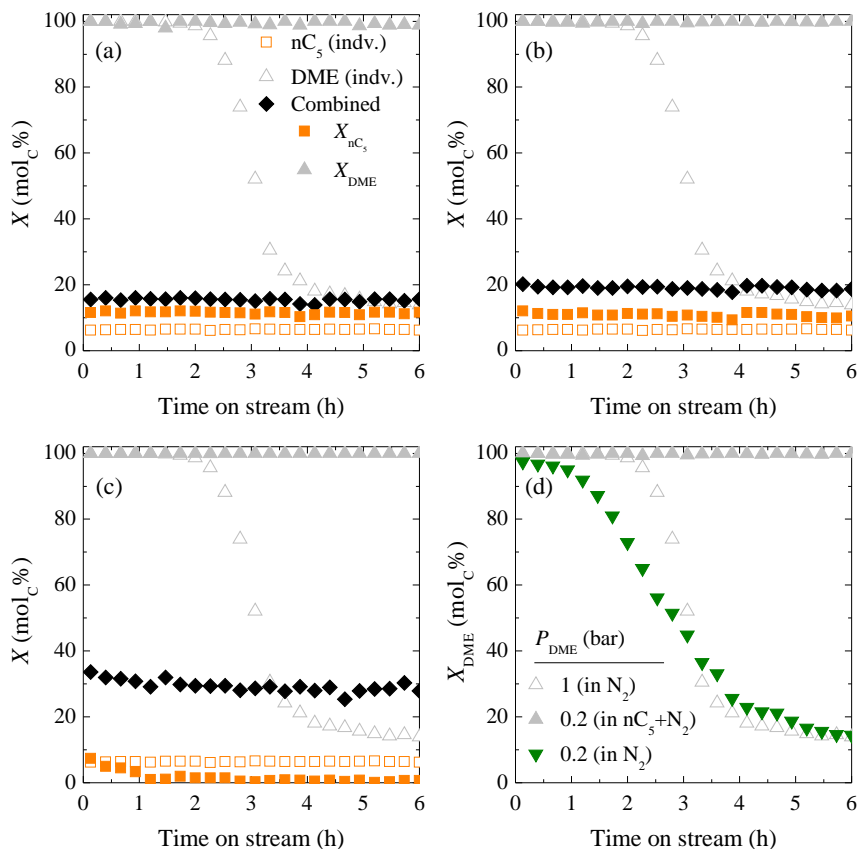


Fig. 3.15. Effect of OX: nC_5 ratio in the feed on the evolution with time of nC_5 and DME conversions in individual (hollow symbols) and combined reactions (filled symbols) with co-fed DME: nC_5 ratios of (a) 1:9, (b) 1:4 and (c) 1:1 using the CZ140 catalyst and (d) effect of co-feeding N_2 and nC_5 on the evolution with time of DME conversion. 500 °C, $\tau = 1.0$ g h mol $^{-1}$.

pressure of carbon-containing reactants was used for all experiments described up to now. However, the partial pressure of each reactant in the feed is varied when changing the proportion of nC_5 and oxygenate. Reducing DME partial pressure was shown to decrease the catalyst deactivation rate during its individual conversion into hydrocarbons [38]. Thus, the effect of diluting DME in an inert (N_2) was studied in order to discard the role of nC_5 as diluting agent. Figure 3.14d depicts the evolution with time of DME conversions for three different experiments: individual DME reaction (partial pressure of 1 bar), combined reaction of nC_5 and DME (0.8 and 0.2 bar, respectively) and individual reaction of DME (0.2 bar). In this latter, the initial DME conversion and deactivation rate decrease (note the decrease in the conversion decay slope) as a consequence of its lower concentration in the reaction medium. The final DME conversion after 6 h on stream is similar for both experiments of individual DME reaction despite these differences in the catalyst deactivation profile. These results are far from the surprising stability of DME conversion registered when it was co-fed with nC_5 . Therefore, the improvement observed co-feeding nC_5 cannot be only attributed to a dilution effect. The attenuation of catalyst deactivation could be explained by the competitive adsorption of both reactants on the acid sites and by the participation of the paraffin (nC_5) in the dual-cycle mechanism, presumably promoting the alkene cycle and delaying the formation of coke (Scheme 3.2).

From the results in this Section, two synergistic effects can be deduced on the combined reactions of nC_5 with DME. On the one hand, nC_5 conversion increases as compared to its individual reaction and this higher conversion is stable during 6 h on stream using DME: nC_5 ratios of 1:9 and 1:4. This situation occurs at 500 °C, low oxygenate concentrations and using the CZ140 catalyst, conditions at which DME conversion does not dominate the mechanism. On the other hand, the stability of DME conversion is ostensibly improved, shifting from a pronounced activity loss in the absence of nC_5 to an inappreciable deactivation within 6 h on stream when nC_5 is co-fed.

In any case, the main goal of this study was to evaluate the feasibility of recycling C_{5+} hydrocarbons for the industrial implementation of the DTO process. However, the advantages of co-feeding DME and nC_5 are only observed in the unrealistic situation of a feed consisting of 50% of C_{5+} at MTO/DTO conditions or using operating conditions far from the ones required in the MTO/DTO process. Therefore, the recycling strategy is not recommended and an individual valorization of the C_{5+} stream is suggested as the best option, considering the possibility of optimizing each process separately. Nonetheless, the observed synergies could be interesting for understanding the reaction mechanisms. This information could be valuable for designing catalysts that promote the cracking of paraffins in the

presence of oxygenates and the attenuation of deactivation during the MTO/DTO process when hydrocarbons are recirculated.

Chapter 4

Valorization of paraffins

In this Chapter, the valorization of the C₅₊ paraffin byproducts of the DTO process is studied. *n*-Pentane is selected as a representative compound of this group of products, and its catalytic cracking is used as a model reaction for introducing the kinetic modeling methodology. The performance of the catalyst including deactivation and the role of catalyst acidity is evaluated. A vector form of the convection-dispersion-reaction equation allows the simultaneous computation of the kinetic parameters of the reaction network and deactivation kinetics. The extracted parameters are used for displaying operation maps of the production of olefins and aromatics from *n*-pentane using HZSM-5 zeolite catalysts. The results in this Chapter have been published in *Chem. Eng. J.* **2018**, *331*, 818-830 and *React. Chem. Eng.* **2019**, *4*, 1922-1934.

4.1 *n*-Pentane cracking

Different experimental runs for the catalytic cracking of *n*-pentane using HZSM-5 zeolite catalysts were carried out in a packed bed reactor at laboratory scale. Detailed information about the catalyst preparation method can be found in Chapter 2, as well as the reaction conditions studied in this Chapter.

For monitoring the evolution of the catalytic cracking of *n*-pentane, the conversion (X) was previously defined in equation (3.4), whereas the yield (Y_i) and the selectivity (S_i) of each i lump are defined as

$$Y_i = \frac{F_i}{F} \quad (4.1)$$

$$S_i = \frac{Y_i}{X} = \frac{F_i}{F - F_{nC_5}}, \quad (4.2)$$

where F is the total molar flow rate and F_{nC_5} and F_i are the molar flow rate of nC_5 and of each i lump at the outlet of the reactor in terms of C units, respectively.

From the analyses of the reaction products, five lumps of products were defined based on their similar kinetic behavior: CH_4 , O (light olefins), P (light paraffins), BTX (benzene, toluene and xylenes) and C_{5+} (long chain paraffins). Each of these lumps is respectively composed of: (i) CH_4 ; (ii) ethylene, propylene and butenes (*i*-butene, 1-butene, *trans*-2-butene and *cis*-2-butene); (iii) ethane, propane and butanes (*i*-butane and *n*-butane); (iv) benzene, toluene and xylenes (*o*-, *m*- and *p*-xylene) and; (v) *i*-pentane, hexanes and heptanes. The carbon mass balance closure was higher than 90 wt% comparing with the nC_5 feed.

4.1.1 Effect of reaction conditions

Figure 4.1a depicts the effect of temperature on the evolution with space time of the conversion at $t = 0$ using the CZ15 catalyst. An increase in the conversion is observed upon increasing both reaction temperature and space time. High conversions are shown at 550 °C, reaching a value of 66% at relatively low space time ($\tau = 0.15 \text{ g h mol}^{-1}$). As observed, the used experimental conditions allow a large spectrum of conversion to be obtained (from 4 to 99%). This is the suitable scenario in order to deal with the kinetic modeling of data obtained in an integral packed bed reactor.

Figure 4.1b shows the evolution with time of the conversion at different temperatures. A constant catalytic activity is observed at 350 and 400 °C, whereas a linear decrease in the conversion is shown at 450, 500 and 550 °C (during 15 h on stream). Similar results were obtained by using different space time values,

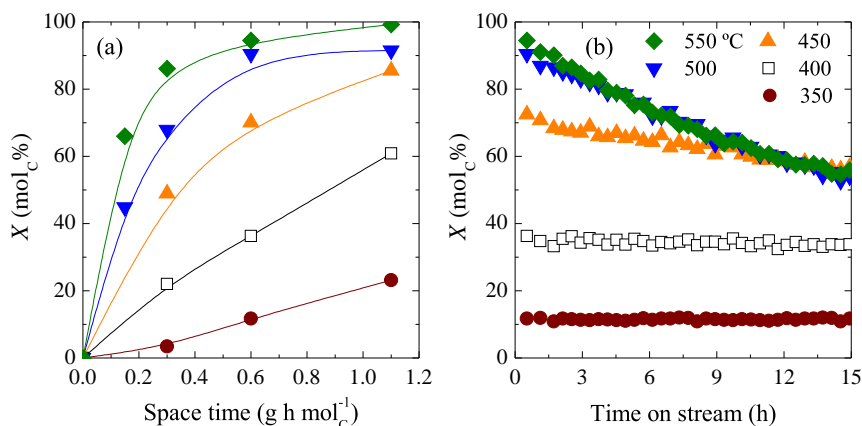


Fig. 4.1. Effect of temperature on the evolution with (a) space time ($t = 0$) and (b) time ($\tau = 0.6$ g h mol $_C^{-1}$) of the nC_5 conversion with the CZ15 catalyst.

observing faster deactivation (and almost linear in all cases) when temperature is increased and space time is decreased.

Figure 4.2a and 4.2b display the evolution with time of the yields of products at different reaction conditions by way of example. Figure 4.2a corresponds to the results obtained at the highest temperature (550 °C) and a low space time ($\tau = 0.3$ g h mol $_C^{-1}$). At these conditions, relatively high initial yields of light paraffins (P), light olefins (O) and BTX (maxima at 48, 23 and 12%, respectively) are observed. Upon time, catalyst deactivation modifies the product lump distribution. The yield of olefins becomes higher than that of paraffins after 7 h on stream and the one of BTX is lower than 5% after 10 h on stream. On the other hand, the results obtained at 400 °C and $\tau = 1.1$ g h mol $_C^{-1}$ exhibit very different behavior (Figure 4.2b). In this case, only the yield of paraffins is significant and it does not exhibit a remarkable decrease with time (from 48% to 45% after 15 h on stream). Furthermore, the yield of C_{5+} hydrocarbons is higher than those of olefins and BTX and the formation of CH_4 is negligible. This result suggests that the formation of saturated compounds is favored at these conditions, but catalyst deactivation is attenuated.

4.1.2 Catalyst deactivation

The main cause of catalyst deactivation is the active site blockage by coke deposition. The location of coke and the effect of reaction conditions on its formation and

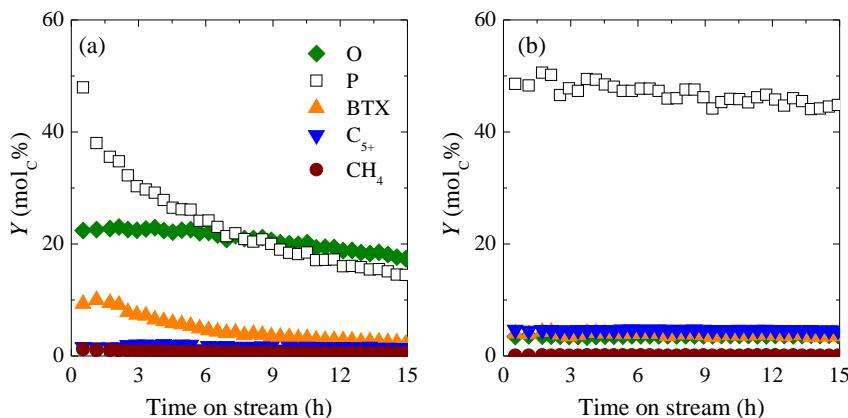


Fig. 4.2. Evolution with time of the yields of products at (a) 550 °C with $\tau = 0.3$ g h mol_C⁻¹ and (b) 400 °C with $\tau = 1.1$ g h mol_C⁻¹ using the CZ15 catalyst.

deposition are studied. The influence on the deterioration of the catalyst properties is also shown in this Section.

Location of coke

The morphology of the used catalysts was characterized by means of confocal fluorescence microscopy (CFM) and compared to that of the fresh catalyst. The results are illustrated in Figure 4.3. The fluorescence of the fresh catalyst is limited. However, we are able to locate small domains of the zeolite, which were well dispersed in the matrix by reflection (Figure 4.3a). The reflection images provide relatively low information of the dispersion of the zeolite due to the insufficient penetration of the technique within the catalytic particles.

After reactions, some coke structures were deposited on the surface of the catalysts. The conjugated dienes and aromatics of coke are fluorescent under the type of radiation used in the microscope [247]. This methodology is then able to faithfully analyze the zeolite or coke domains within the catalyst bodies [248]. Figure 4.3b shows a representative particle of the used CZ15 catalyst at certain reaction conditions. Small and well-dispersed domains of high fluorescence intensity are observed, corresponding to the zeolite crystals, in which the reaction takes place. Valuable information can be extracted from this CFM result, as the good performance of the agglomeration method to prepare the catalyst. Similar results were previously reported for agglomerated catalysts, where these zeolite domains were also differentiated [248, 249]. The intensity of the brightness suggests the

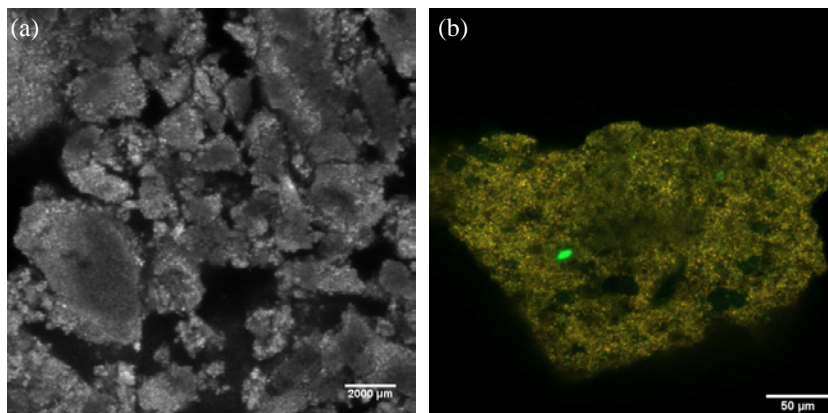


Fig. 4.3. CFM images of (a) the fresh (reflection) and (b) a used CZ15 catalyst (excitation wavelength, 488 and 561 nm).

presence of coke outside zeolite domains, which is in agreement with our previous hypothesis on the diffusion of some coke structures outside the zeolite crystals as a path for attenuating deactivation (see Section 3.3).

Effect of reaction conditions

The effect of temperature and space time (τ) on the TPO profiles is displayed in Figure 4.4. Two main peaks are observed at 490 and 550 °C (peaks I and II, respectively) in the TPO profiles of used CZ15 catalysts at 500 °C with $\tau = 0.6$ g h mol_C⁻¹ and $\tau = 1.0$ g h mol_C⁻¹ (Figure 4.4a and 4.4b, respectively). These peaks could be related to the combustion of two different coke fractions as better explained for DTO process in Section 3.3. Here, these peaks can be more or less related to the C₂ and C₃ fractions defined from the combustion model of TPO. The former (peak I) can be associated with carbon species that are easier to burn off, presumably aliphatic structures located outside the zeolite crystals or on the mesoporous structure of the γ -Al₂O₃ matrix. The latter (peak II) requires higher combustion temperature, and can be correlated with the coke fraction deposited within the micropores of the zeolite (see Figure 3.7) [128, 250]. The presence of these two coke fractions is consistent with the more intense fluorescence observed in the zeolite domains in Figure 4.3b.

The TPO profiles for the used catalyst tested at the conditions of Figure 4.1b, are depicted in Figure 4.4a. Together with the increase in the coke content (area below TPO profile), the nature of deposited coke also undergoes modifications increasing temperature. The presence of heterogeneous coke deposited on the surface of the used catalyst at low temperature is suggested (similar result is obtained at

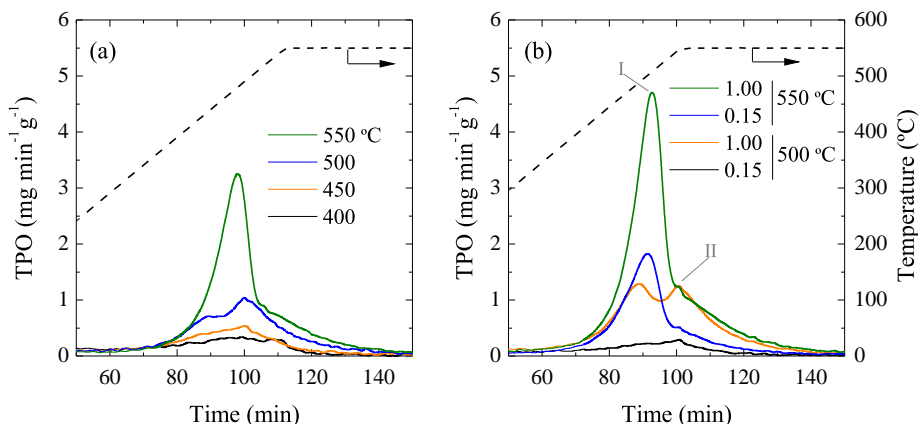


Fig. 4.4. TPO profiles of the used CZ15 catalyst at (a) different temperatures ($\tau = 0.6 \text{ g h mol}^{-1}$) and (b) space time values (in g h mol^{-1}). $t = 15 \text{ h}$.

350 and 400 °C). No defined peaks are observed, hence this coke is presumably distributed on the external surface of the $\gamma\text{-Al}_2\text{O}_3$ matrix and does not contribute to the catalyst deactivation (See Figure 4.1b). The presence of peak I and II can be observed increasing the temperature and a well-defined peak is registered for the catalyst used at 550 °C. This could be related to the combustion of polyaromatic coke species [98, 110, 251] mainly deposited on the matrix surface, but blocking the micropore mouths of HZSM-5 zeolite, which leads to the faster observed deactivation.

This trend is confirmed after analyzing the evolution with space time of coke species at high temperature (Figure 4.4b). The two coke fractions are noticeable at 500 °C when the space time value was increased up to $\tau = 1.0 \text{ g h mol}^{-1}$. However, only one peak is observed for used CZ15 catalysts at 550 °C, with the amount of deposited coke being increased with space time.

Figure 4.5a shows the content of coke calculated by means of TPO analyses of used catalysts at all tested reaction condition and 15 h on stream. The coke content presents an almost linear tendency with space time at low temperatures. The maximum amount of coke registered is 7.4 wt% at 550 °C and $\tau = 1.0 \text{ g h mol}^{-1}$. In Figure 4.2a, an important presence of olefins and BTX is observed in the reaction medium at this high temperature. This is consistent with the reported role of these lumps in catalyst deactivation during *n*-pentane cracking [123].

Figure 4.5b displays the effect of coke deposition on the physico-chemical properties of the catalyst, namely surface area and total acidity at $\tau = 1.0 \text{ g h mol}^{-1}$.

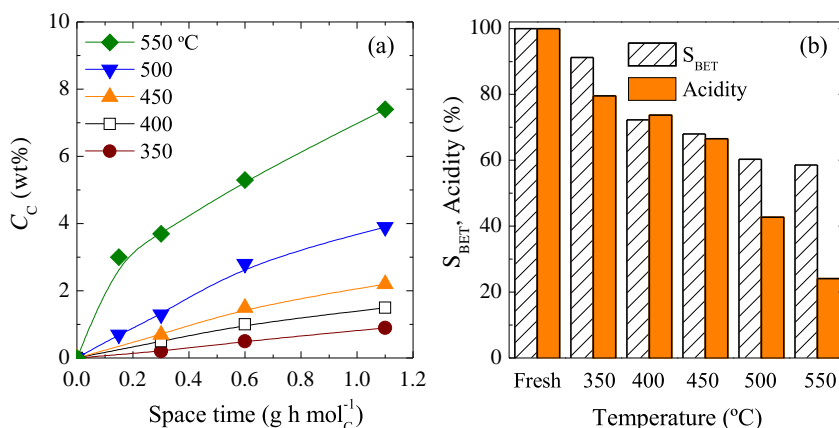


Fig. 4.5. (a) Evolution with space time of the content of coke at different temperatures and (b) its effect on the BET specific surface area and acidity of the CZ15 catalyst with $\tau = 1.0 \text{ g h mol}_C^{-1}$. $t = 15 \text{ h}$.

The fresh catalyst has a surface area S_{BET} of $285 \text{ m}^2 \text{ g}^{-1}$ and an acidity of $0.43 \text{ mmol}_{\text{tBA}} \text{ g}^{-1}$, which correspond with the 100% in the Y axis of Figure 4.5b. As content of coke does, a softer decrease in the S_{BET} and acidity is observed at lower temperature ($> 72\%$ at $400 \text{ }^\circ\text{C}$). An increase in the temperature up to $550 \text{ }^\circ\text{C}$ leads to a pronounced decrease in the catalyst surface. The used CZ15 catalyst at $550 \text{ }^\circ\text{C}$ exhibits a S_{BET} of $167 \text{ m}^2 \text{ g}^{-1}$ and an acidity of $0.10 \text{ mmol}_{\text{tBA}} \text{ g}^{-1}$, which correspond to the 60 and 24% of the initial values, respectively. This significant blockage of the pores is explained by the high content of coke (7.4 wt%) registered at these conditions.

4.1.3 Role of catalyst acidity

The role of catalyst acidity was studied using the catalyst with higher Si/Al ratio (CZ140 catalyst). Its performance is compared to that of CZ15 catalyst. Both catalysts were tested in the catalytic cracking of $n\text{C}_5$ at similar conditions. The initial values of selectivity to the main products (olefins, paraffins, BTX and C_{5+} hydrocarbons) and the evolution with time of the conversion at the same conditions are depicted in Figure 4.6. The amount of CH_4 is negligible, so its concentration is not included in these results. At $500 \text{ }^\circ\text{C}$, the more acid CZ15 catalyst mainly produces paraffins, with conversions higher than 45% using $\tau = 0.15 \text{ g h mol}_C^{-1}$ (Figure 4.6a). When conversion is increased up to 90% ($\tau = 1.0 \text{ g h mol}_C^{-1}$), values

of selectivity to BTX higher than 20% are observed. In contrast, olefins are the main products obtained with the CZ140 catalyst at the same τ value. An increase in the temperature up to 550 °C (Figure 4.6b) promotes the selective production of olefins and reduces the selectivity to paraffins in all cases. The olefins/paraffins (O/P) ratio is then boosted using both catalysts and the CZ140 catalyst achieves a maximum selectivity to olefins of 65% ($\tau = 0.3 \text{ g h mol}_C^{-1}$). The maximum selectivity to BTX is reached with the CZ15 catalyst (24% with $\tau = 1.0 \text{ g h mol}_C^{-1}$).

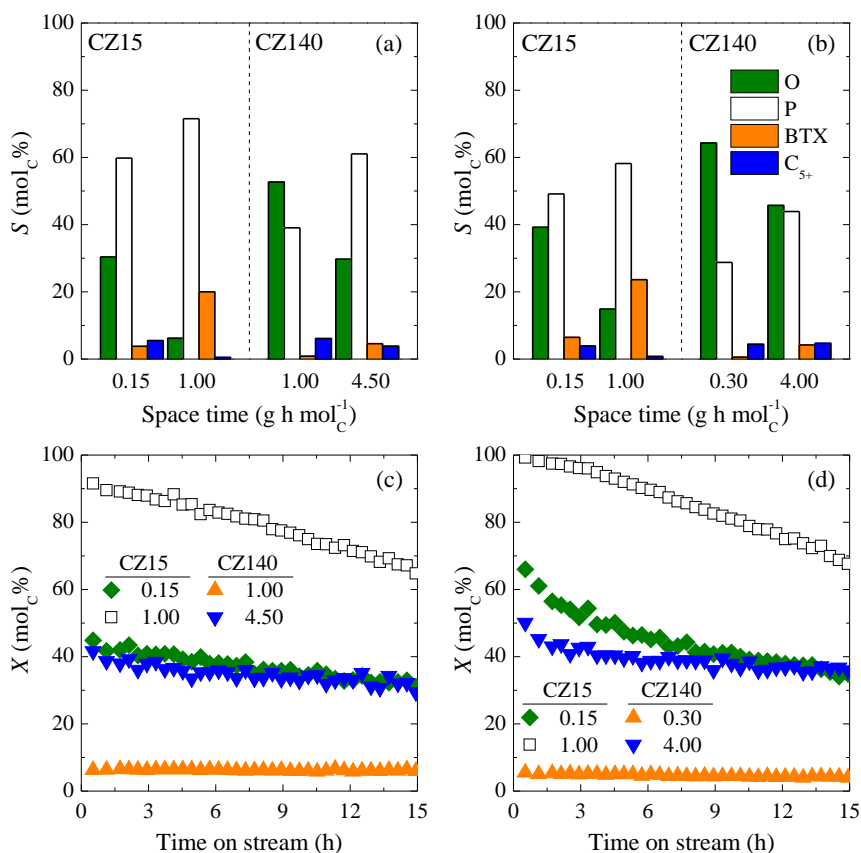


Fig. 4.6. Selectivity to products with CZ15 and CZ140 catalysts at (a) 500 °C and (b) 550 °C and evolution with time of each conversion at (c) 500 °C and (d) 550 °C using different space time values (in g h mol_C⁻¹).

As explained in previous sections, both catalysts show a progressive deactivation during the reaction due to the deposition of coke that causes the blockage of the active sites. This loss of activity is quantified following the evolution with time of the reaction. In all cases of Figure 4.6, the rapidity of conversion drop is directly related to the catalyst activity, and therefore, faster deactivation is observed at conditions with higher conversion. At 500 °C, almost linear trends are shown by the two catalysts at any condition (Figures 4.6c), reaching the maximum slope with the CZ15 catalyst and $\tau = 1.0 \text{ g h mol}^{-1}$ (initial conversion of 92%). Although similar values of conversion are achieved by both catalysts under certain conditions, CZ140 catalyst seems to be deactivated slightly slower. Indeed, at very low values of conversion, this catalyst shows a stable performance, maintaining a constant conversion during 15 h on stream. These behaviors are emphasized at 550 °C (Figure 4.6d), where linear decays of the conversion are no longer observed. With the highest τ value (1.0 g h mol^{-1}), CZ15 catalyst shows an initial period of slow deactivation, which is followed by a fast drop of the conversion (from 100 to 68% after 15 h). Conversely, the initial fast deactivation tends to level off with time when τ or catalyst acidity decrease (CZ140 catalyst).

The activity drop due to coking is directly related to the catalyst acidity, apart from temperature and space time. All these variables finally affect the composition of the reaction medium [59, 252]. The evolution with time of the yields of products at 550 °C, corresponding to the experiments in Figure 4.6d, is displayed in Figure 4.7. As previously mentioned, the higher initial conversions attained with the CZ15 catalyst produce olefins and paraffins (35 and 25%, respectively, Figure 4.7a) and remarkable yields of BTX at $\tau = 1.0 \text{ g h mol}^{-1}$ (24%, Figure 4.7b). However, the fast deactivation mainly affects the latter two, thus observing faster decreases in the yields of paraffins and BTX upon time. The yield of olefins slightly decreases at low τ and even increases with time at $\tau = 1.0 \text{ g h mol}^{-1}$.

A negligible decay of the reaction products is otherwise observed under conditions of low conversions with the CZ140 catalyst when $n\text{C}_5$ is the main component of the reaction medium (Figure 4.7c). Here, low but constant yields of all products are observed during 15 h on stream, with olefins being the main products (4%). Regarding those conditions of similar conversions with both catalysts, an initial yield of olefins of ca. 24% is observed in Figure 4.7a and 4.7d. However, a faster decay of the yields of olefins and particularly paraffins is observed with the more acid CZ15 catalyst.

The role of catalyst acidity on the coke deposition and catalyst deterioration is analyzed in Table 4.1. A more pronounced drop of S_{BET} is observed for the more acid CZ15 catalyst as temperature increases. The maximum decay up to $238 \text{ m}^2 \text{ g}^{-1}$ (12%) registered for the CZ140 is further below the 41% loss observed for

CZ15 catalyst at 550 °C. This is the result of the higher ability to form coke of CZ15 than that of CZ140 catalyst (3.9 and 7.4 wt% vs. 0.2 and 0.8 wt% of coke at 500 and 550 °C, respectively, Table 4.1). The same tendency is observed for the catalyst acidity, with values of 0.24 and 0.21 $\text{mmol}_{\text{tBA}} \text{g}^{-1}$ for CZ15 catalysts used at 500 and 550 °C, respectively, and negligible drops for the used CZ140 catalysts.

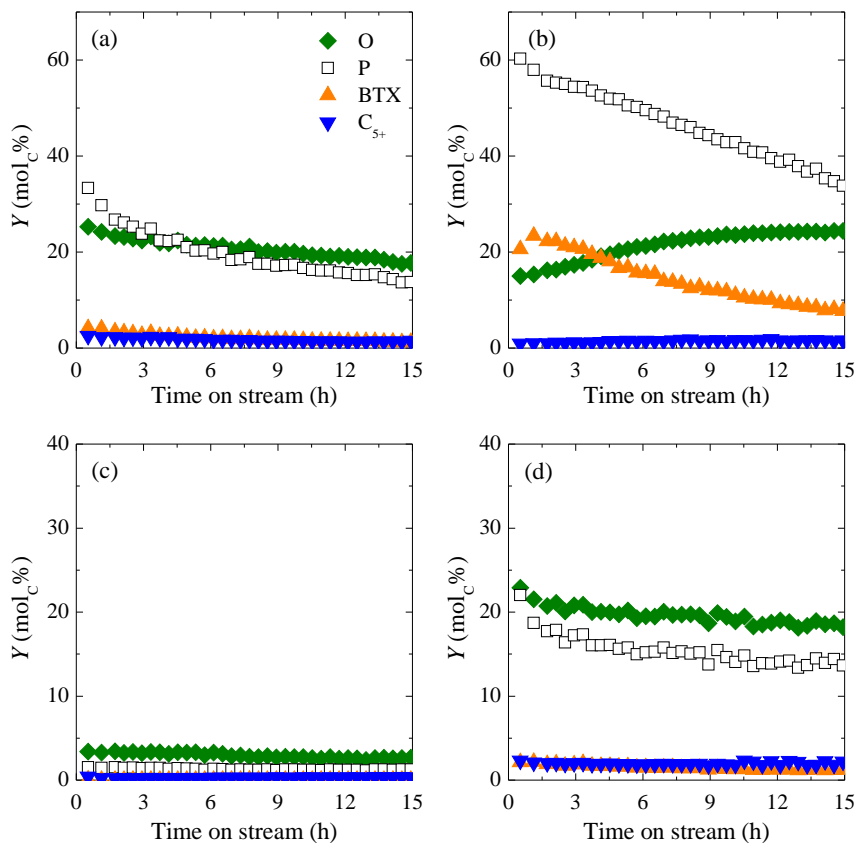


Fig. 4.7. Evolution with time of the yields of products using the CZ15 catalyst with (a) $\tau = 0.15 \text{ g h mol}_C^{-1}$ and (b) $\tau = 1.00 \text{ g h mol}_C^{-1}$ and the CZ140 catalyst with (c) $\tau = 0.30 \text{ g h mol}_C^{-1}$ and (d) $\tau = 4.00 \text{ g h mol}_C^{-1}$. 550 °C.

Table 4.1. Total content of coke, specific surface area and acidity of the fresh and used catalysts at 500 and 550 °C. $\tau = 1.0 \text{ g h mol}_C^{-1}$.

	C_C (wt%)	S_{BET} $\text{m}^2 \text{g}^{-1}$	Acidity $\text{mmol}_{t\text{BA}} \text{g}^{-1}$
CZ15	–	285	0.43
500 °C	3.9	205	0.24
550 °C	7.4	167	0.21
CZ140	–	271	0.16
500 °C	0.2	250	0.15
550 °C	0.8	238	0.15

4.2 Kinetic modeling considering deactivation

The experimental data collected for both CZ15 and CZ140 catalysts are used for developing a kinetic model that considers the catalyst deactivation. Herein, the methodology for the computation of kinetic models is explained. Moreover, its application to the experimental results of *n*-pentane catalytic cracking using different reaction networks is discussed.

4.2.1 Methodology

The kinetic modeling methodology is based on solving the convection-dispersion-reaction equation for each lump in the reaction medium. Pressure drop is not observed at the studied conditions in the integral reactor and less than 1 °C of difference in all bed positions was determined by using two thermocouples at different position of the bed. Hence, isothermal and isobaric conditions are assumed. As deactivation plays an important role in these catalytic reactions, the time-dependent form of the conservation equations is used. Considering a vector of molar fractions of each *i* lump $\mathbf{y}_i(z, t)$,

$$\varepsilon \frac{\partial \mathbf{y}_i}{\partial t} = -\frac{\partial}{\partial z} \left[v \mathbf{y}_i - D \frac{\partial \mathbf{y}_i}{\partial z} \right] + \frac{RT}{PN_C} \rho \mathbf{r}_i, \quad i = 1, \dots, n_l \quad (4.3)$$

defined for a time value $t > 0$ and a longitudinal position $0 < z < L$, where ε is the effective bed-particle porosity, v is the linear velocity, D is effective dispersion coefficient of the gas, R is the universal gas constant, T is the reactor temperature, P is the total pressure, N_C is the (carbon molar flow rate)/(total molar flow rate) ratio, ρ is the catalytic bed density, n_l is the number of lumps and L is the catalytic bed length. The vector \mathbf{r}_i contains the formation rate of each *i* lump, which is defined as

$$\mathbf{r}_i = \frac{d\mathbf{p}_i}{d\tau}, \quad (4.4)$$

where τ is the space time expressed in terms of the carbon molar flow rate.

The calculation of \mathbf{r}_i requires the introduction of different rate vectors: \mathbf{r}_j is the column vector of reaction rates of each *j* step of the reaction network and; \mathbf{r}_d is the column vector of deactivation rates of each activity defined in the deactivation kinetic model. Two auxiliary mixed vectors of rates are also defined, being

$$\mathbf{r} = \begin{pmatrix} \mathbf{r}_j \\ \mathbf{r}_d \end{pmatrix} \quad (4.5)$$

and

$$\mathbf{r}_1 = \begin{pmatrix} \mathbf{r}_i \\ \mathbf{r}_d \end{pmatrix}, \quad (4.6)$$

related by the matrix \mathbf{A} of C balance coefficients

$$\mathbf{r}_1 = \mathbf{A}\mathbf{r}. \quad (4.7)$$

Suppose a given kinetic network consisted of i lumps and j reaction steps. Also suppose a selective deactivation model, in which each j reaction step is affected by a different activity a_j . Then, \mathbf{r}_d is a column vector of j elements and the matrix

$$\mathbf{A} \in \mathbb{R}^{(i+j) \times (2j)}. \quad (4.8)$$

Defining \mathbf{a}_j as the vector of the previously defined j activity parameters and assuming elementary reactions for all j steps of the reaction network, the reaction rates are defined as

$$\mathbf{r}_j = \mathbf{r}_{j,0} \circ \mathbf{a}_j = \left(\mathbf{k}_j \prod_R P_R \right) \circ \mathbf{a}_j, \quad (4.9)$$

where $\mathbf{r}_{j,0}$ and \mathbf{k}_j are the vectors of the initial reaction rates and of the kinetic constants of each j step of the reaction network, and P_R is the partial pressure of the reactant R . Note that the symbol \circ in equation (4.9) denotes the Hadamard or componentwise product of each element of the vectors (“element-by-element” multiplication) [253]. The reaction rate of each j step is then calculated as the product of its initial reaction rate $\mathbf{r}_{j,0}$ and its activity \mathbf{a}_j .

Deactivation rate can be defined as a function of the reaction temperature and the partial pressure of the coke precursors P_{cp} as

$$-\frac{d\mathbf{a}_j}{dt} = \mathbf{r}_d = \left(\mathbf{k}_d \sum_{cp} P_{cp} \right) \circ \mathbf{a}_j^d, \quad (4.10)$$

with \mathbf{k}_d being defined as the vector of deactivation kinetic constants and d as the deactivation order of each a_j activity.

Equation (4.10) can be considered as a particular case of the conservation equation for \mathbf{a}_j when the convection-dispersion term is negligible. Therefore, equations (4.3) and (4.10) can be solved simultaneously using a simple mixed vector of variables \mathbf{u} defined as

$$\mathbf{u} = \begin{pmatrix} \mathbf{y}_i \\ \mathbf{a}_j \end{pmatrix}. \quad (4.11)$$

The problem is then reduced to solve the vector conservation equation for \mathbf{u} , which is a modification of the equation (4.3) with the above introduced new variables,

$$\Phi_0 \frac{\partial \mathbf{u}}{\partial t} = -\Phi_I \frac{\partial}{\partial z} \left[v \mathbf{u} - D \frac{\partial \mathbf{u}}{\partial z} \right] + \Phi_{II} \mathbf{r}_I, \quad (4.12)$$

with

$$\Phi_0 = \varepsilon, \quad \Phi_I = 1, \quad \Phi_{II} = \frac{RT}{P N_C} \rho \iff \mathbf{u} = \mathbf{y}_i \quad (4.13)$$

and

$$\Phi_0 = -1, \quad \Phi_I = 0, \quad \Phi_{II} = 1 \iff \mathbf{u} = \mathbf{a}_j. \quad (4.14)$$

According to the plug flow model, a pure convective transport is assumed for the gas flow. However, the presence of the dispersion term in equation (4.12) turns out to be required for the stability of the calculation methodology. The Peclet (Pe) number relates the convection and dispersion terms as

$$Pe = \frac{vL}{D} \quad (4.15)$$

and is assumed to take values of $Pe > 10^3$ in all cases for ensuring an insignificant contribution of the dispersion in the gas model.

The resulting system of parabolic partial differential equations (PDEs) was solved by a transformation of each PDE into a system of ordinary differential equations (ODEs) by means of the finite differential method developed by Skeel and Berzins [254]. The generated set of ODEs for all the dependent variables was integrated by using an implicit Runge-Kutta method based on the numerical differentiation formulas of orders 1–5, suitable for solving the herein studied stiff problem.

The required initial conditions for $\mathbf{y}_i(z, t)$ and $\mathbf{a}(t)$ are given by

$$\mathbf{y}_i(z, 0) = \mathbf{y}_0 \quad (4.16)$$

$$\mathbf{a}_j(0) = 1, \quad (4.17)$$

with \mathbf{y}_0 containing the initial concentrations in the gas phase (at $t = 0$).

Due to the presence of the dispersion term in equation (4.12), mixed or Robin conditions are used at the entrance of the reactor instead of Dirichlet. Neumann boundary conditions are used at the outlet of the reactor

$$-v [\mathbf{y}_i(0, t) - \mathbf{y}_0] + D \frac{\partial}{\partial z} \mathbf{y}_i(0, t) = 0 \quad (4.18)$$

$$\frac{\partial}{\partial z} \mathbf{y}_i(L, t) = 0 \quad (4.19)$$

The same procedure previously carried for defining the mixed vectors \mathbf{r} and \mathbf{u} is also applied for the kinetic constants. All \mathbf{k}_j and \mathbf{k}_d are considered to follow the Arrhenius equation and in order to reduce the correlation between the pre-exponential factor and the activation energy, a reparameterized form of the equation is used

$$\mathbf{k} = \begin{pmatrix} \mathbf{k}_j \\ \mathbf{k}_d \end{pmatrix} = \mathbf{k}^* \circ \exp \left[-\frac{\mathbf{E}}{R} \left(\frac{1}{T} - \frac{1}{T^*} \right) \right], \quad (4.20)$$

where \mathbf{k}^* is the vector of kinetic constants at the reference temperature T^* and \mathbf{E} is the mixed vector of apparent activation energies, including \mathbf{E}_j and \mathbf{E}_d .

These kinetic parameters \mathbf{k}^* and \mathbf{E} are the ones to be optimized for fitting the experimental data. A modification of the Levenberg-Marquardt (LM) algorithm [255, 256] was implemented for the computation. The algorithm can be defined as a multiobjective and multivariable nonlinear least square minimization and avoids the error associated with the kinetic parameters calculation in two stages. A calculation of the kinetic parameters at zero time on stream ($t = 0$) is usually made by minimizing one objective function. Subsequently, these kinetic parameters are used for the deactivation kinetic modeling through the minimization of a second objective function. With this method in series, the possible errors in the first calculation stage are intrinsically committed in the computation of deactivation kinetics. Because of that, the proposed parallel method allows for bypassing this kind of errors associated with the dependency of both, zero time on stream and deactivation kinetics.

An objective function vector (**OF**) with two components is then required. The first term is related to the kinetics for each j step of the reaction scheme at $t = 0$ and the second one to the deactivation kinetics. Both terms are defined as the differences between the experimental results ($y_{i,0}^e$ and y_i^e , molar fractions at $t = 0$ and at t time on stream, respectively) and the corresponding values calculated by the kinetic model ($y_{i,0}$ and y_i)

$$\mathbf{OF} = \begin{pmatrix} \sum_{i=1}^{n_l} \omega_i \sum_{n=1}^{n_{e,0}} \frac{\xi}{n_{e,0}} (y_{i,0}^e - y_{i,0})^2 \\ \sum_{i=1}^{n_l} \omega_i \sum_{n=1}^{n_{e,d}} \frac{\xi}{n_{e,d}} (y_i^e - y_i)^2 \end{pmatrix}, \quad (4.21)$$

where ω_i is the weight factor for each i lump, ξ is the number of runs repeated at the same conditions, and $n_{e,0}$ and $n_{e,d}$ are the total number of experimental data

used for the calculation of the first and second terms of \mathbf{OF} , respectively.

LM algorithm is based on a blend of gradient descent and Gauss-Newton iteration, in which the calculation of the Jacobian matrix (\mathbf{J} , first derivatives of the objective function) is the key for approaching the minimum value of the \mathbf{OF} [255]. In our case, a decoupling of \mathbf{J} calculation is made, thus obtaining two different matrices \mathbf{J}_j and \mathbf{J}_d , associated with each component of the \mathbf{OF} vector in equation (4.21). The new values of \mathbf{k}_j and \mathbf{E}_j in each iteration are therefore estimated independently to those of \mathbf{k}_d and \mathbf{E}_d . A consistent and faster fitting of the experimental data at $t = 0$ and the deactivation models is obtained, due to the independent optimization of each one but the minimization of a \mathbf{OF} that includes both. Figure 4.8 shows the block diagram used for the computation of the kinetic parameters, schematizing the decoupling of the Jacobian calculation, which allows the simultaneous computation of kinetics explained in this Section.

Significance of the kinetic models

Once obtained the kinetic parameters, a statistic study based on the Fisher exact test was carried out for studying the experimental data fitting of the different models. These models are formed by different reaction networks and deactivation equations. Each fitting result was compared by determining if the improvement of

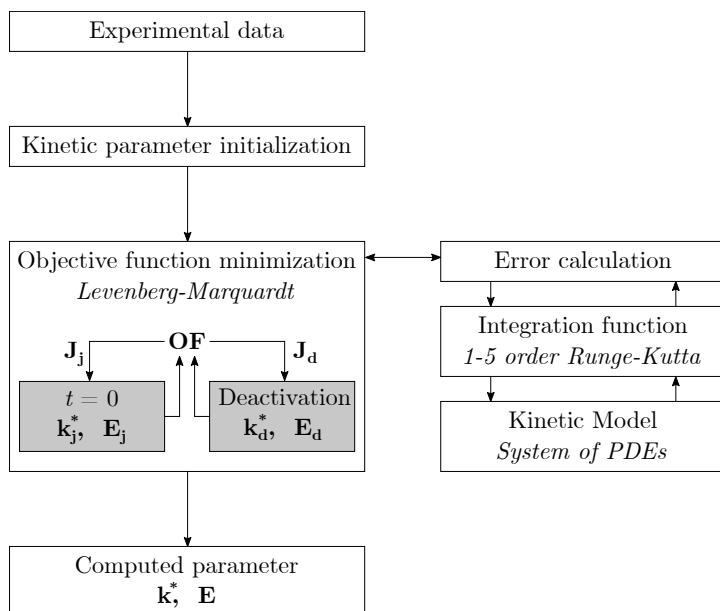


Fig. 4.8. Block diagram for the computation of the kinetic parameters.

the model with respect to the simplest one is significant. For the statistic study, the sum of square errors (SSE) is defined as

$$SSE = \sum_{i=1}^{n_l} \left[\sum_{n=1}^{n_{e,0}} (y_{i,0}^e - y_{i,0})_n^2 + \sum_{n=1}^{n_{e,d}} (y_i^e - y_i)_n^2 \right]. \quad (4.22)$$

Then, let A and B be different models with different degrees of freedom ($\nu_A > \nu_B$), being B the one that presents lower sum of square errors ($SSE_A > SSE_B$). The improvement obtained with B is significant if the following expression is fulfilled [37]

$$F_{A-B} = \frac{\frac{SSE_A - SSE_B}{\nu_A - \nu_B}}{\frac{SSE_B}{\nu_B}} > F_{1-\alpha}(\nu_A - \nu_B, \nu_B), \quad (4.23)$$

where $F_{1-\alpha}(\nu_A - \nu_B, \nu_B)$ is the critical value of the Fisher distribution function (using $\alpha = 0.05$). If the inequality of equation (4.23) is fulfilled, the result obtained with the model B is significantly better than that obtained with the simpler model A . This criterion cannot be applied for comparing those models with the same degrees of freedom ($\nu_A = \nu_B$). In such cases, the improvement of model B in comparison to model A is evaluated through an analysis of variances (σ_A^2 and σ_B^2 , being $\sigma_A^2 > \sigma_B^2$) [38, 151]

$$F_{A-B} = \frac{\frac{SSE_A}{\nu_A}}{\frac{SSE_B}{\nu_B}} = \frac{\sigma_A^2}{\sigma_B^2} > F_{1-\alpha}(\nu_A, \nu_B). \quad (4.24)$$

4.2.2 Reaction network for n -pentane catalytic cracking

From the general fundamentals of paraffin catalytic cracking mechanisms proposed by Kotrel et al. [135] and detailed in Section 1.2, and the advances in the knowledge of n -pentane cracking pathways [123], the reaction scheme must consider the following sequenced steps: (i) the formation of a carbonium species from the reactant; (ii) the formation of light alkanes (P lump) and carbenium species through protolytic cracking; (iii) the formation of light alkanes (P) through hydride transfer; (iv) the formation of light olefins (O lump) through β -scission and carbenium deprotonation; (v) the formation of long chain olefins through the oligomerization of light olefins; (vi) the formation of long chain alkanes (C_{5+} lump) through hydride transfer, and; (vii) the formation of aromatics (BTX lump) through the cyclization-aromatization of light olefins.

These general seven steps are widely accepted for the catalytic cracking of paraffins. However, their relative advance depends on the alkane chain length due to different energy considerations [257–259]. The effect of the alkane chain length on the paraffins cracking was studied and Figure 4.9 displays the product lump distribution and the conversion obtained at $t = 0$ for n -butane (nC_4), n -pentane (nC_5) and n -hexane (nC_6) with CZ15 catalyst. The behavior of representative molecules of the light paraffins (nC_4) and C_{5+} lumps (nC_6) are compared to that of the feed (nC_5).

An almost linear and pronounced decrease in the cracking conversion is observed when the hydrocarbon chain length is decreased. In this sense, nC_4 exhibits a conversion of 30% whereas nC_6 presents a remarkable higher value (85%). This confirms the higher reactivity of alkanes with longer carbon chain in our particular system. The selectivity to each lump also presents different trends depending on the feed. Paraffins are the main product lump, whose selectivity is similar in all three cases. However, the selectivity to olefins decreases and the ones to BTX and C_{5+} increase upon increasing the length of the carbon chain. This corroborates the kinetic model and operando results respectively reported by Narbeshuber et al. [139] and Li et al. [258]. The more plausible explanation is the promotion of some pathways as β -scission for light paraffins and of others as cyclization and aromatization for longer alkanes (C_{5+} hydrocarbons) [250].

Three different reaction networks are herein proposed for the evaluation of the experimental data fitting. In ascending order of complexity, they are displayed in Schemes 4.1, 4.2 and 4.3 and are respectively named RN_1 , RN_2 and RN_3 . In all

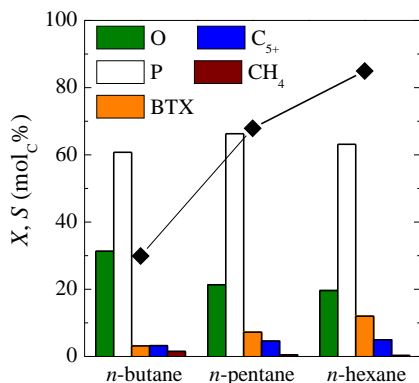
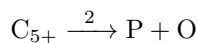
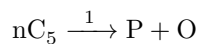
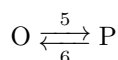
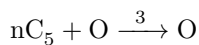


Fig. 4.9. Effect of hydrocarbon chain length on the conversion of paraffins and the selectivity to products to CZ15 catalyst. 500 °C, $\tau = 0.3 \text{ g h mol}_C^{-1}$, $t = 0 \text{ h}$.

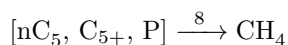
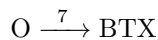
Formation of olefins



Conversion of olefins



Formation of final products

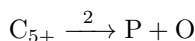
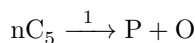
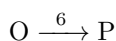
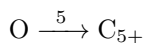
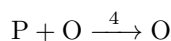
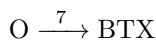


Scheme 4.1. Proposed reaction network RN_1 for the catalytic cracking of nC_5 .

cases, the lump-based steps of the reaction network are defined considering the aforementioned seven reaction pathways for paraffin catalytic cracking.

A previous work of our research group proposed a kinetic model for n -butane cracking using similar lumps than those we use [250]. In that case, olefins were considered the only primary product of the catalytic cracking and the intermediates of the rest of products. Other authors likewise reported that only olefins are adsorbed on the acid sites and form the final products [260]. In these reaction networks, initial steps for the formation of paraffins and olefins from the cracking of alkanes are considered. They include the protolytic or monomolecular cracking of a long-chained alkane forming a lighter one (from the previously formed carbonium species) and the subsequent β -scission of the carbenium species. According to the results in Figure 4.9, paraffin lump is significantly less reactive than longer alkanes. For this reason, the protolytic cracking is assumed negligible in the simplified RN_1 and RN_2 .

The formation of light olefins activates the mechanism previously indicated, as they are easily adsorbed on the acid sites and react faster [122]. Adsorbed olefins react with alkanes, accelerating the reaction rates of alkane catalytic cracking (but also the side reaction of coke condensation). The formation of olefins is then assumed partially autocatalytic. The concentration of each alkane in the reaction medium is taken into account for the simplifications of the reaction networks. RN_1 only considers nC_5 reactant for the autocatalytic formation of olefins (Scheme 4.3),

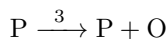
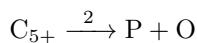
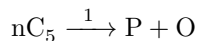
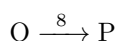
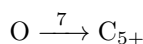
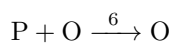
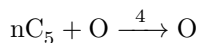
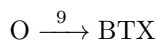
Formation of olefins*Conversion of olefins**Formation of final products*

Scheme 4.2. Proposed reaction network RN_2 for the catalytic cracking of nC_5 .

whereas paraffins are also considered in RN_2 as the main product of the reaction (Scheme 4.2). All the alkanes, nC_5 , C_{5+} hydrocarbons and light paraffins, are considered in the most complex reaction network RN_3 (Scheme 4.3).

Based on the oligomerization-cracking mechanism [135], long-chained carbenium species are formed from light olefins, which can subsequently yield long-chained paraffins through hydride transfer. This pathway is illustrated in the three proposed reaction networks with the direct formation of C_{5+} hydrocarbons from olefins (step 4 in RN_1 , 5 in RN_2 and 7 in RN_3). The hydride transfer pathway also explains the formation of paraffins from olefins, assumed reversible only in RN_1 . BTX aromatics are the heaviest compounds observed, and therefore, the formation of these compounds by the condensation of olefins is proposed as a final step in all reaction networks. From a mechanistic point of view, this step is a consequence of the cyclization of long-chained carbenium species and its subsequent aromatization on the acid sites [261]. The aromatization of olefins also starts the undesirable condensation mechanism of coke formation [259]. Finally, the formation of methane from alkanes is considered in all cases as a final step.

As the reaction rate of each j step of the reaction network (\mathbf{r}_j) is defined in contained C units but is a function of the partial pressure of each reactant, average carbon atom numbers must be given to each lump defined in the reaction networks. According to the previously detailed composition of each lump, an average carbon

Formation of olefins*Conversion of olefins**Formation of final products*

Scheme 4.3. Proposed reaction network RN₃ for the catalytic cracking of nC₅.

value of 3 is assigned to the olefins and paraffins lumps, 6 to the C₅₊ lump and 7 to the BTX lump.

Consideration of the catalyst deactivation

The rate of each j step of the reaction network is calculated from the previously defined equation (4.9). A quasi non-selective deactivation kinetic model is used for describing the catalyst deactivation. This means that only one activity parameter is used for quantifying deactivation in all the reaction steps (non-selective), but considering no deactivation in the methane formation steps. Methane is assumed to be only formed from the thermal cracking of alkanes and therefore, they do not have to be adsorbed for undergoing a chain cleavage. According to the monomolecular protolytic cracking mechanism of alkanes, the formation of a carbonium species in the second carbon of the paraffin (C–C⁺–C–C) yields a methane molecule and a long-chained carbenium species [258]. However, the amount of methane observed at low temperature is negligible (Figure 4.2b) and so, only the thermal cracking mechanism is considered for methane formation.

Blank experiments were carried out in order to validate this assumption. Figure 4.10 shows the yields of the different products obtained without catalyst due to

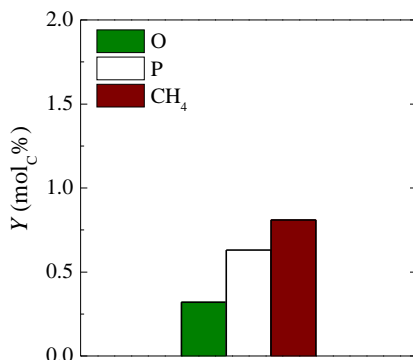


Fig. 4.10. Yields of products in the thermal cracking of nC₅. 550 °C; $\tau = 0$ g h mol_C⁻¹; $t = 0$ h.

the thermal cracking of nC₅ at the highest tested temperature (550 °C). At these extreme conditions, the low yield of methane attained (1 wt%) is similar to those observed with the most acid CZ15 catalyst at the same conditions (Figure 4.2b). Therefore, the catalytic formation of methane is considered negligible.

In our non-selective deactivation kinetic model, the activity parameter is defined with only one deactivation equation, and so, the vector of activities \mathbf{a}_j , defined in equation (4.9), can be simplified to a scalar variable (a). Then, equation (4.7) is described by $\mathbf{r}_1 \in \mathbb{R}^{(i+1) \times (1)}$, $\mathbf{A} \in \mathbb{R}^{(i+1) \times (j+1)}$ and $\mathbf{r} \in \mathbb{R}^{(j+1) \times (1)}$, with

$$\mathbf{r}_1 = \begin{pmatrix} r_{nC_5} \\ r_O \\ r_P \\ r_{BTX} \\ r_{C_{5+}} \\ r_{CH_4} \\ r_d \end{pmatrix}, \quad \mathbf{r} = \begin{pmatrix} r_1 \\ r_2 \\ r_3 \\ r_4 \\ r_5 \\ r_6 \\ r_7 \\ r_8 \\ r_9 \\ r_{10a} \\ r_{10b} \\ r_{10c} \\ r_d \end{pmatrix} \quad (4.25)$$

and

$$\mathbf{A} = \begin{pmatrix} -2 & 0 & 0 & -1 & 0 & 0 & 0 & 0 & 0 & -1 & 0 & 0 & 0 \\ 1 & 1 & 1 & 1 & 1 & 1 & -1 & -1 & -1 & 0 & 0 & 0 & 0 \\ 1 & 1 & -1 & 0 & 0 & -1 & 0 & 1 & 0 & 0 & 0 & -1 & 0 \\ 0 & 0 & 0 & 0 & 0 & 0 & 0 & 0 & 1 & 0 & 0 & 0 & 0 \\ 0 & -2 & 0 & 0 & -1 & 0 & 1 & 0 & 0 & 0 & -1 & 0 & 0 \\ 0 & 0 & 0 & 0 & 0 & 0 & 0 & 0 & 0 & 1 & 1 & 1 & 0 \\ 0 & 0 & 0 & 0 & 0 & 0 & 0 & 0 & 0 & 0 & 0 & 0 & 1 \end{pmatrix} \quad (4.26)$$

for the most complex RN_3 . Note that the last row and column of the matrix \mathbf{A} are associated with the deactivation kinetics, and therefore, consist of zeros with a 1 in the diagonal position of the matrix. In the case of a selective deactivation model of j activities, it will consist of an identity matrix and two auxiliary matrix of zeros. Then generalizing

$$\mathbf{A} = \begin{pmatrix} \mathbf{A}_{i,j} & \mathbf{0}_{i,j} \\ \mathbf{0}_{j,j} & \mathbf{I}_j \end{pmatrix}. \quad (4.27)$$

As previously proceed with the reaction networks, different deactivation equations were tested for fitting the evolution of the catalyst activity with time. All the equations are based on the before introduced equation (4.10) and are listed in Table 4.2. The deactivation equation DE_1 , as the simplest one, assumes that all the lumps in the reaction medium (reactants and products) exhibit the same capacity of coke formation, and the catalyst deactivation is independent on the

Table 4.2. Proposed deactivation equations for the catalytic cracking of nC_5 .

DE_1	$-\frac{da}{dt} = k_d(P_{\text{nC}_5} + P_{\text{O}} + P_{\text{P}} + P_{\text{C}_{5+}} + P_{\text{BTX}})a^d$	(4.28)
DE_2	$-\frac{da}{dt} = k_d(P_{\text{nC}_5} + P_{\text{O}} + P_{\text{C}_{5+}} + P_{\text{BTX}})a^d$	(4.29)
DE_3	$-\frac{da}{dt} = k_d(P_{\text{O}} + P_{\text{P}} + P_{\text{C}_{5+}} + P_{\text{BTX}})a^d$	(4.30)
DE_4	$-\frac{da}{dt} = k_d(P_{\text{O}} + P_{\text{C}_{5+}} + P_{\text{BTX}})a^d$	(4.31)
DE_5	$-\frac{da}{dt} = k_d(P_{\text{O}} + P_{\text{BTX}})a^d$	(4.32)

reaction extent. In any case, CH_4 is not considered as a potential coke precursor molecule. In equation DE_2 , light paraffins are dismissed as coke precursor and thus, unsaturated hydrocarbons (O and BTX) and paraffins with 5 or more carbon (nC_5 reactant and C_{5+}) are considered as coke precursors. Equations DE_3 , DE_4 and DE_5 consider that the coke precursors are the reaction products. Therefore, the formation of coke occurs in steps in series to those of the main reaction scheme. DE_3 assumes that coke is formed from all products, DE_4 does not take light paraffins into account as coke precursors, and DE_5 only considers unsaturated compounds as responsible for coke formation.

4.2.3 Model discrimination and experimental data fitting

Experimental data collected with the CZ15 catalyst allows a large conversion range to be obtained within the studied temperatures (Figure 4.1). For this reason, this catalyst was selected for a more accurate and reliable discrimination of the proposed models based on the Fisher distribution. Different combinations of the reaction networks and deactivation kinetics were used for fitting the experimental data. First, the reaction networks were studied. Three kinetic models were formed by the combination of the reaction networks RN_1 , RN_2 and RN_3 with the deactivation equation DE_3 (equation (4.30)). The models are respectively named *A*, *B* and *C*. These results are representative of all the alternatives tested (a total of 15) because the deactivation equation DE_3 offers the lowest value of *SSE* with all the reaction networks. The main statistic parameters of the experimental data fitting using the models *A*, *B* and *C* are shown in Table 4.3.

The evaluation of the sum of square errors (*SSE*) points out that the model *C* exhibits the best fitting. The number of experimental data ($n_{e,0}$ and $n_{e,d}$) and lumps (n_l) used for the experimental data fitting are the same in all three cases. The number of parameters (n_p) is also the same for models *A* and *B* but is increased

Table 4.3. Statistic comparison of the kinetic models formed by the reaction networks RN_1 , RN_2 or RN_3 and the deactivation equation DE_3 .

	<i>A</i> ($\text{RN}_1\text{-DE}_3$)	<i>B</i> ($\text{RN}_2\text{-DE}_3$)	<i>C</i> ($\text{RN}_3\text{-DE}_3$)
$n_{e,0} + n_{e,d}$	144	144	144
n_l	6	6	6
n_p	22	22	26
$\nu = (n_{e,0} + n_{e,d})n_l - n_p$	842	842	838
<i>SSE</i>	$6.47 \cdot 10^{-3}$	$7.70 \cdot 10^{-3}$	$5.97 \cdot 10^{-3}$
<i>F</i>	$17.74_{(A-C)}$	$61.04_{(B-C)}$	
$F_{1-\alpha}$	2.38	2.38	

for the model C . This leads to a reduction of the degrees of freedom (ν), so that the following expressions are fulfilled

$$\nu_A = \nu_B > \nu_C, \quad (4.33)$$

$$SSE_B > SSE_A > SSE_C. \quad (4.34)$$

Consequently, the significance of the fitting improvement with the model C , with respect to the models A and B , was individually evaluated by using the equation (4.23). The results obtained based on the Fisher distribution function,

$$F_{A-C} > F_{1-\alpha}, \quad (4.35)$$

$$F_{B-C} > F_{1-\alpha}, \quad (4.36)$$

confirm that the fitting obtained with the model C is significantly better than those obtained with the other ones.

The same statistic analysis was carried out for analyzing the significance of the improvements attained with each deactivation equation. The reaction network RN_3 was selected as the most suitable for the experimental data fitting, so it was used for testing the deactivation equations listed in Table 4.2. Five models are formed by their combination, resulting in the models $C1$ to $C5$. Table 4.4 shows the main statistic parameters of the experimental data fitting using these models. The highest values of SSE are exhibited by $C1$ and $C2$, suggesting that nC_5 does not act as coke precursor and then, a parallel deactivation mechanism (nC_5 feed as coke precursor) should be discarded. Indeed, the lowest value of SSE is achieved with model $C3$ in which deactivation in series is considered.

The value of ν is the same for all models, 838 as illustrated in Table 4.3 for model C . Then, the statistic study of the significance of the improvement with the different models was evaluated using the variance analysis in equation (4.24). The values of variance obtained for each model are also shown in Table 4.4, as well as the relation between the variances of the different models (compared models

Table 4.4. Statistic comparison of the kinetic models formed by the reaction network RN_3 and the deactivation equations DE_1 - DE_5 .

	$C1$	$C2$	$C3$	$C4$	$C5$
SSE	$9.57 \cdot 10^{-3}$	$16.61 \cdot 10^{-3}$	$5.97 \cdot 10^{-3}$	$6.90 \cdot 10^{-3}$	$6.90 \cdot 10^{-3}$
σ^2	$1.14 \cdot 10^{-5}$	$1.98 \cdot 10^{-5}$	$7.12 \cdot 10^{-6}$	$8.23 \cdot 10^{-6}$	$7.87 \cdot 10^{-6}$
F	$1.60_{(C1-C3)}$	$1.74_{(C1-C3)}$		$1.16_{(C1-C3)}$	$1.10_{(C1-C3)}$
$F_{1-\alpha}$	1.12	1.12		1.12	1.12

in brackets) and the critical values of the Fisher distribution function (1.12 in all cases). As expected regarding the *SSE* values, a significantly better fitting is obtained with model *C1* than that with model *C2*. However, the fitting is significantly improved when only the products are considered as coke precursors (*C3*, $1.60 > 1.12$). According to these results, nC_5 feed cannot be directly related to the formation of coke. Comparing the fitting results of model *C3* with those of models *C4* and *C5*, model *C3* fits the experimental data significantly better than model *C4* ($1.16 > 1.12$) as suggested by the *SSE* values. Interestingly, this does not happen in the case of the simplest model *C5*. The improvement obtained with the model *C3*, which reduces the *SSE* value, is not significant compared with the model *C5* ($1.10 < 1.12$). Therefore, a significant good fitting of experimental data can be achieved with the model *C5*, which only assumes olefins and BTX aromatics as coke precursors.

CZ15 catalyst

The computed values of the kinetic constants at the reference temperature of 500 °C and the apparent activation energy values corresponding to this model are listed in Table 4.5. The accuracy of the fitting is also shown, with the confidence intervals being calculated from the discrepancies of predicted and experimental data (confidence intervals at 95%). Comparing the kinetic constants for the direct olefin formation from paraffins ($k_2^* \approx k_1^* > k_3^*$) and for the autocatalytic olefin formation ($k_5^* \approx k_4^* > k_6^*$), the model predicts a faster cracking of longer paraffins, which is consistent with the results in Figure 4.9 and with the experimental and theoretical ones in literature [139, 258]. The high value of k_8^* (olefin conversion into paraffin) explains the registered yields of light paraffins and suggests that hydride transfer reaction is favored at the reaction conditions. This reaction also shows the lowest *E* value, pointing out the lower dependency on temperature of hydride transfer reaction than other steps.

By way of example, a comparison of the experimental data (symbols) to the results predicted by the model (lines) of the molar fractions at the outlet of the reactor at some selected conditions is observed in Figure 4.11. The space time is related to the longitudinal position (*z*) in the model as

$$\tau = \frac{\rho S}{F} z, \quad (4.37)$$

where *S* is the reactor section.

The values of molar fractions of the products are equal to the corresponding yields. The molar fraction of nC_5 decreases with space time at $t = 0$, whereas the ones of paraffins and BTX increase. Indeed, paraffins are the main products obtained in the reaction, with remarkable yields at low temperatures (Figure 4.11a).

Table 4.5. Kinetic constants at 500 °C and apparent activation energy values for the catalytic cracking of nC₅ over CZ15 catalyst.

	k^*	E (kJ mol ⁻¹)
<i>Steps of the reaction network</i>		
k_1 (mol _C g ⁻¹ h ⁻¹ bar ⁻¹)	$(8.54 \pm 0.07) 10^{-1}$	$(6.15 \pm 0.15) 10^1$
k_2 (mol _C g ⁻¹ h ⁻¹ bar ⁻¹)	$(8.57 \pm 0.27) 10^{-1}$	$(3.84 \pm 1.13) 10^1$
k_3 (mol _C g ⁻¹ h ⁻¹ bar ⁻¹)	$(2.45 \pm 0.89) 10^{-1}$	$(7.07 \pm 1.65) 10^1$
k_4 (mol _C g ⁻¹ h ⁻¹ bar ⁻²)	$(4.13 \pm 1.15) 10^0$	$(3.77 \pm 1.11) 10^1$
k_5 (mol _C g ⁻¹ h ⁻¹ bar ⁻²)	$(4.14 \pm 1.29) 10^0$	$(3.74 \pm 1.15) 10^1$
k_6 (mol _C g ⁻¹ h ⁻¹ bar ⁻²)	$(1.34 \pm 0.47) 10^0$	$(2.62 \pm 0.48) 10^2$
k_7 (mol _C g ⁻¹ h ⁻¹ bar ⁻¹)	$(6.56 \pm 0.62) 10^{-1}$	$(2.66 \pm 0.12) 10^1$
k_8 (mol _C g ⁻¹ h ⁻¹ bar ⁻¹)	$(3.40 \pm 0.08) 10^0$	$(1.01 \pm 0.10) 10^1$
k_9 (mol _C g ⁻¹ h ⁻¹ bar ⁻¹)	$(5.72 \pm 0.13) 10^{-1}$	$(1.54 \pm 0.26) 10^1$
k_{10} (mol _C g ⁻¹ h ⁻¹ bar ⁻¹)	$(1.05 \pm 0.41) 10^{-3}$	$(2.36 \pm 0.31) 10^1$
<i>Deactivation</i>		
k_d (h ⁻¹ bar ⁻¹)	$(3.14 \pm 0.06) 10^{-1}$	$(3.00 \pm 0.15) 10^1$
d	$(1.01 \pm 0.12) 10^0$	

This result suggests the promotion of hydride transfer pathway on the acid sites of the zeolite. Other authors reported the attenuation of this undesired pathway and the promotion of the yield of olefins by modifying the zeolite surface acidity [262] or using catalysts with different porous structure [259], which increases the severity of the shape selectivity.

A maximum of olefins is observed at the studied temperatures. The molar fraction maximum increases and is located at lower τ values with higher temperatures (26% at 550 °C and $\tau = 0.15$ g h mol_C⁻¹, Figure 4.11b). This behavior is a consequence of the role of olefins as reaction intermediates. A different tendency is shown by BTX, whose molar fraction increases with temperature and τ , with the typical curve shape of final products in the reaction network. Aromatization reactions on the acid sites were reported to be favored at high temperatures [261]. The deactivation equation of the model C5 predicts that the main coke precursors are olefins and BTX, which is in agreement with these results. Hence, catalyst deactivation is not observed at low temperatures (350 and 400 °C), with the reaction medium being mainly formed by nC₅ and paraffins (more than 90%, Figure 4.11a). An increase in temperature leads to an increase in the concentrations of olefins and BTX, and also to a faster deactivation (Figure 4.1b), which indicates a correlation between the unsaturated compounds and the formation of coke. The shape of olefins and BTX curves suggests a mechanism in series in which aromatics are formed through olefin cyclization-aromatization reactions and they subsequently

form the polyaromatic structures of coke [98].

The proposed kinetic model also provides an accurate experimental data fitting of the evolution with time of the molar fractions. A comparison of experimental and predicted values for selected conditions is displayed in Figures 4.11c and 4.11d. As observed, the data fitting is relatively good using the equation (4.32) for deactivation kinetics and therefore, more complex kinetic equations were not considered. Critical deactivation examples are depicted as flat curves are mainly observed at

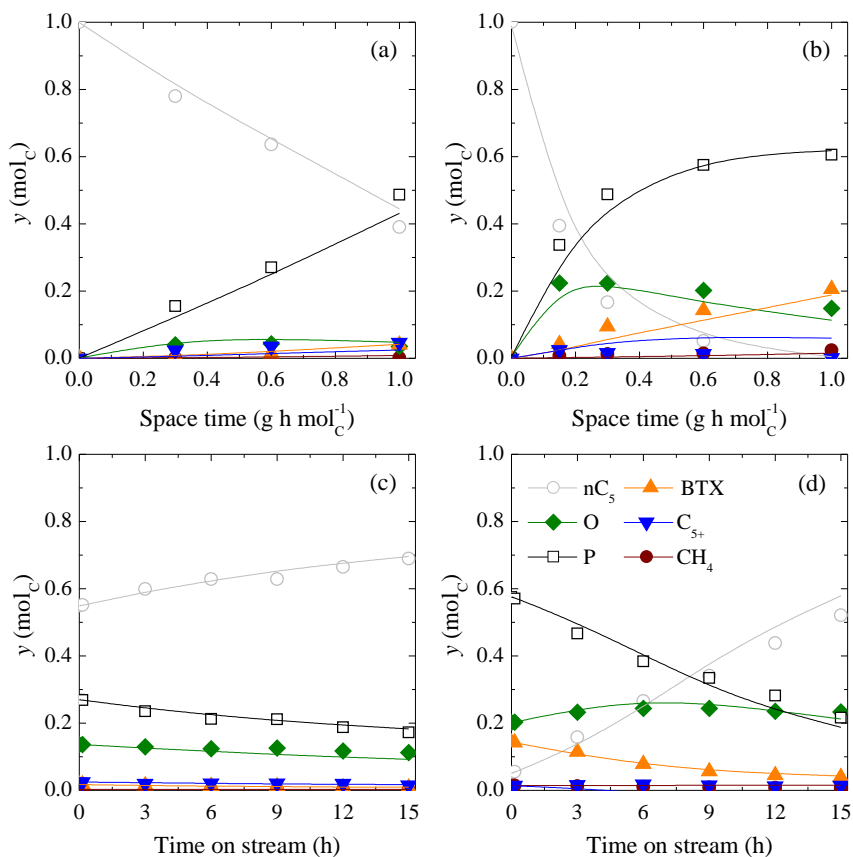


Fig. 4.11. Comparison of the experimental data (symbols) to those predicted by the model (lines) for the evolution with (a, b) space time and (c, d) time of the molar fractions using the CZ15 catalyst. (a) 400 °C, $t = 0$ h; (b) 550 °C, $t = 0$ h; (c) 500 °C, $\tau = 0.15$ g h mol_C⁻¹; (d) 550 °C, $\tau = 0.6$ g h mol_C⁻¹.

lower temperatures. At these conditions, a relatively pronounced increase in nC_5 molar fraction is observed, particularly at 550 °C (Figure 4.11d). The faster drop of the molar fraction of paraffins in comparison to that of olefins supports the previously observed faster deactivation of the hydride transfer reaction.

Role of catalyst acidity

The comparison of the kinetic parameters computed for the process using both catalysts allows an evaluation of the role of acidity in the reaction rate of each step of the reaction network. The same kinetic model is used for fitting the experimental data obtained with the less acid CZ140 catalyst. As previously presented in Section 4.1, high temperature and τ values are required in order to attain significant conversions of nC_5 . Table 4.6 lists the corresponding kinetic parameters for this catalyst and Figure 4.12 depicts the fitting results. All kinetic parameters are lower for this catalyst, fulfilling the same trend of the values previously observed for CZ15 catalyst. This is translated to higher concentrations of nC_5 reactant in the reaction medium, but also to higher selectivity to olefins due to the limitation of secondary reactions, as hydride transfer (Figures 4.12a and 4.12b). Deactivation is predicted slower mostly due to this change in the composition of the reaction medium (Figures 4.12c and 4.12d).

The kinetic constants can be divided into three different groups related with the steps of the reaction network RN_3 in the Scheme 4.3, including the initiation

Table 4.6. Kinetic constants at 500 °C and apparent activation energy values for the catalytic cracking of nC_5 over CZ140 catalyst.

	k^*	E (kJ mol ⁻¹)
<i>Steps of the reaction network</i>		
k_1 (mol _C g ⁻¹ h ⁻¹ bar ⁻¹)	$(2.50 \pm 1.66) 10^{-2}$	$(6.74 \pm 1.89) 10^1$
k_2 (mol _C g ⁻¹ h ⁻¹ bar ⁻¹)	$(6.46 \pm 4.15) 10^{-2}$	$(3.91 \pm 1.66) 10^1$
k_3 (mol _C g ⁻¹ h ⁻¹ bar ⁻¹)	$(1.42 \pm 0.81) 10^{-2}$	$(7.24 \pm 0.45) 10^1$
k_4 (mol _C g ⁻¹ h ⁻¹ bar ⁻²)	$(2.45 \pm 0.12) 10^{-1}$	$(3.76 \pm 0.69) 10^1$
k_5 (mol _C g ⁻¹ h ⁻¹ bar ⁻²)	$(4.19 \pm 1.52) 10^{-1}$	$(3.81 \pm 1.51) 10^1$
k_6 (mol _C g ⁻¹ h ⁻¹ bar ⁻²)	$(1.27 \pm 0.13) 10^{-1}$	$(2.72 \pm 0.54) 10^2$
k_7 (mol _C g ⁻¹ h ⁻¹ bar ⁻¹)	$(2.63 \pm 0.16) 10^{-2}$	$(2.78 \pm 0.92) 10^1$
k_8 (mol _C g ⁻¹ h ⁻¹ bar ⁻¹)	$(1.64 \pm 0.86) 10^{-1}$	$(1.04 \pm 0.15) 10^1$
k_9 (mol _C g ⁻¹ h ⁻¹ bar ⁻¹)	$(1.77 \pm 0.22) 10^{-2}$	$(1.59 \pm 0.75) 10^1$
k_{10} (mol _C g ⁻¹ h ⁻¹ bar ⁻¹)	$(1.07 \pm 0.95) 10^{-3}$	$(2.29 \pm 1.07) 10^1$
<i>Deactivation</i>		
k_d (h ⁻¹ bar ⁻¹)	$(1.05 \pm 0.29) 10^{-1}$	$(3.21 \pm 0.78) 10^1$
d	$(1.13 \pm 0.20) 10^0$	

reactions (k_{1-3}), the autocatalytic formation of olefins (k_{4-6}) and the secondary reactions (k_{7-9}). The average values of k^* and E for each of these groups are displayed in Table 4.7. For comparison of the results, the ratios between the kinetic parameters of both catalysts ($R_{15/140}$) are also calculated and listed in Table 4.7. Values higher than unity are observed for these three groups of reactions (18.8, 12.2 and 22.3 for k_{1-3}^* , k_{4-6}^* and k_{7-9}^* , respectively), thus pointing out their promotion with the CZ15 catalyst. Consequently, the initiation of the catalytic mechanism

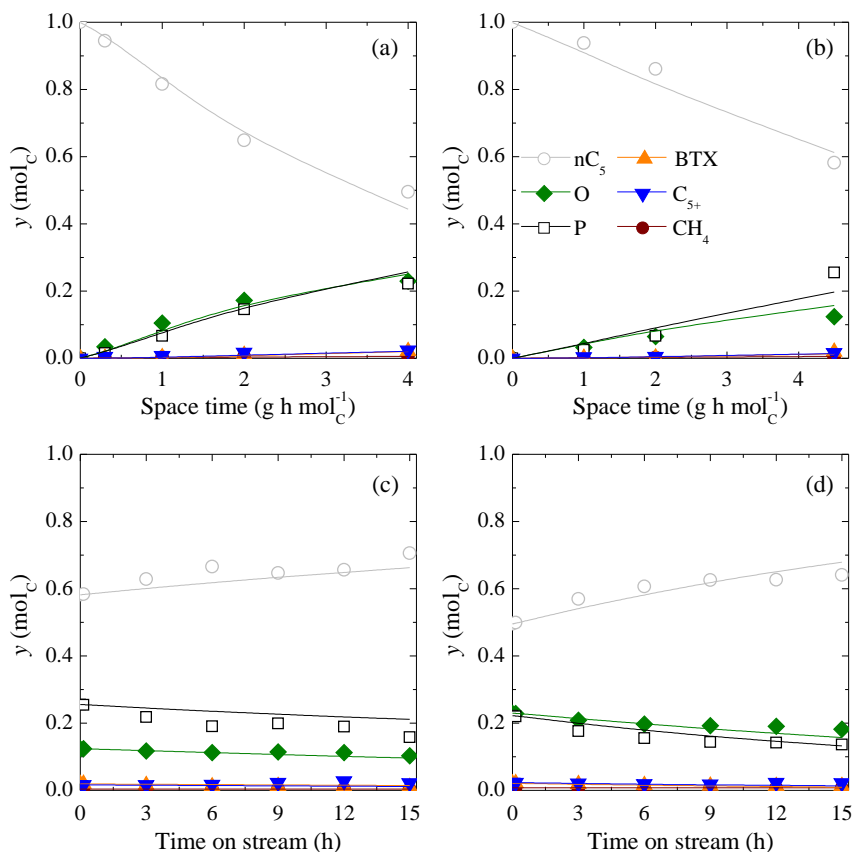


Fig. 4.12. Comparison of the experimental data (symbols) to those predicted by the model (lines) for the evolution with (a, b) space time and (c, d) time of the molar fractions using the CZ140 catalyst. (a) 500 °C, $t = 0$ h; (b) 550 °C, $t = 0$ h; (c) 500 °C, $\tau = 4.5$ g h mol_C⁻¹; (d) 550 °C, $\tau = 4.0$ g h mol_C⁻¹.

Table 4.7. Average kinetic constants at 500 °C, apparent activation energy values and kinetic parameter ratios for CZ15 and CZ140 catalysts.

	CZ15	CZ140	$R_{15/140}$
<i>Reaction network</i>			
k_{1-3}^*	$(6.52 \pm 0.41) 10^{-1}$	$(3.46 \pm 2.21) 10^{-2}$	18.8
k_{4-6}^*	$(3.20 \pm 0.97) 10^0$	$(2.64 \pm 0.59) 10^{-1}$	12.2
k_{7-9}^*	$(1.54 \pm 0.05) 10^0$	$(6.94 \pm 2.99) 10^{-2}$	22.3
E_{1-3}	$(5.69 \pm 0.98) 10^1$	$(5.96 \pm 1.33) 10^1$	0.95
E_{4-6}	$(3.38 \pm 0.91) 10^1$	$(3.43 \pm 0.91) 10^1$	0.98
E_{7-9}	$(1.74 \pm 0.16) 10^1$	$(1.80 \pm 0.61) 10^1$	0.96
<i>Deactivation</i>			
k_d	$(3.14 \pm 0.06) 10^{-1}$	$(1.05 \pm 0.29) 10^{-1}$	3.00
E_d	$(3.00 \pm 0.15) 10^1$	$(3.21 \pm 0.78) 10^1$	0.93

through a paraffinic C–C bond cleavage is predicted almost 20 times faster using the more acid CZ15 catalyst (k_{1-3}^*). At the same time, the higher increase in the $R_{15/140}$ ratio for secondary reactions (k_{7-9}^*) than that for olefin formation reactions (k_{4-6}^*) is consistent with the higher selectivity to olefins with the CZ140 catalyst and those to paraffins and BTX with the CZ15 catalyst. The values of apparent activation energy are very similar for all the steps of the reaction network using both catalysts. In all cases, the average E values are in the range of 17.4–59.6 kJ mol⁻¹, with minimum $R_{15/140}$ ratios of 0.95 (E_{1-3}). The similar E values for both catalysts indicates the coherence on defining the steps of Scheme 4.3 according to the reaction mechanism. The general trend is a decrease in E with the more active CZ15 catalyst, which is the expected result in catalytic processes.

A similar tendency is observed comparing the deactivation kinetic parameters obtained for each catalyst. A threefold value of k_d^* is observed for the CZ15 catalyst, whereas the value of E is slightly lower (practically with the same deactivation order, ca. 1). This behavior is in accordance with the well-established role of the HZSM-5 zeolite acidity in activating the condensation reactions of olefins and aromatics towards polyaromatic structures of coke [98, 252].

This kinetic model for nC₅ catalytic cracking could presumably be useful for predicting the performance of other paraffins, because the reaction scheme is proposed according to the fundamental aspects of paraffin catalytic cracking mechanisms (Scheme 4.3). Likewise, the deactivation kinetic equation could presumably be considered in order to predict the catalyst deactivation during the catalytic cracking of different paraffins, since olefins and aromatics have been reported as the main coke precursors in the literature [128, 142, 146].

4.3 Production of olefins and aromatics

The ultimate goal of a kinetic model should be the simulation of the reactor in order to provide operation maps in which the reaction conditions are set for maximizing the production of the desired compounds. The kinetic parameters summarized in Tables 4.5 and 4.6 were used in the simulation of an isothermal packed bed reactor in order to establish the optimal operation conditions (temperature and space time) and maximize the yields of olefins and BTX with the CZ15 and CZ140 catalysts. The reactor was simulated considering the conditions of experimental runs, within the 450–550 °C range and τ values up to $5.0 \text{ g h mol}_C^{-1}$. The results obtained for catalyst activity values of 1 ($t = 0$) are shown in Figure 4.13. Figure 4.13a displays the evolution of the maximum yield of olefins obtained at certain τ values, and that of BTX is depicted in Figure 4.13b. From a commercial point of view, these two products are the most interesting alternatives for valorizing paraffins. As observed, the CZ15 catalyst allows higher yields of olefins to be obtained at 450 °C than those attained with CZ140 catalyst (Figure 4.13a). However, the CZ140 catalyst is clearly the best catalyst for producing olefins at higher temperatures. Otherwise, this catalyst does not practically show significant yields of BTX under any conditions, whereas yields higher than 50% can be achieved with the CZ15 catalyst (Figure 4.13b). In any case, the increase in the temperature up to 550 °C enhances the production of olefins and BTX with both catalysts.

This temperature was then selected for studying the conversion of nC_5 and the

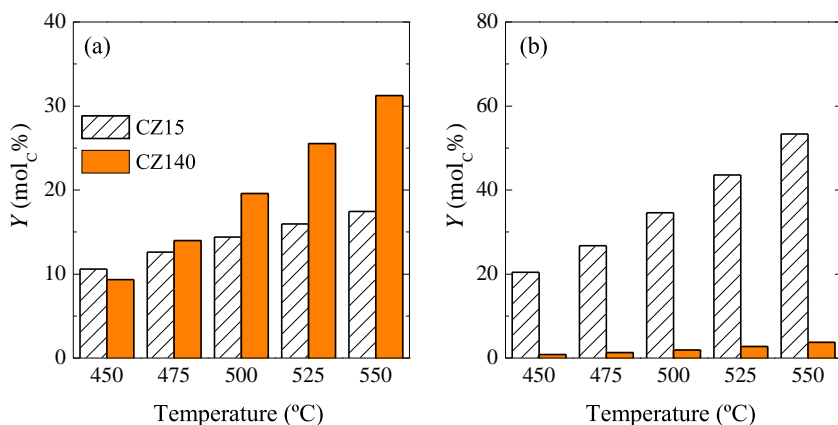


Fig. 4.13. Simulated maximum yields of (a) olefins and (b) BTX obtained at different temperatures with the CZ15 and CZ140 catalysts, respectively.

simulated contour maps of activity with τ and time for CZ15 and CZ140 catalysts are displayed in Figures 4.14a and 4.14b, respectively. A more abrupt decay of the activity with τ is observed for the CZ15 catalyst, which leads to a minimum value in the range of 0.5–1 g h mol_C⁻¹. This means that CZ15 catalyst undergoes a more severe deactivation near the entrance of the reactor regarding the activity profiles in the packed bed reactor. This profile is obviously reproduced at lower values of activity upon increasing time. A softer activity profile is observed for CZ140 catalyst, finding the minimum activity value at the outlet of the reactor in all cases. Apart from the different activity profiles of each catalyst, a faster deactivation is also predicted for the CZ15 catalyst, and activity values lower than 0.2 are estimated in all reactor positions after 15 h on stream. The drop of the activity for the CZ140 catalyst is much more dependent on the reactor position. Activity values from 0.7 to 0.35 are respectively predicted for values of τ from 1.0 to 5.0 g h mol_C⁻¹. This is in agreement with the above discussed experimental results and goes hand in hand with the product distribution in each case. Then, a higher activity for the transformation of nC₅ also leads to more abrupt activity longitudinal profiles and faster deactivation rates.

Considering the evolution of the activity for each catalyst and the results of Figure 4.13, the contour maps with τ and time of yields and selectivities of olefins and BTX are displayed in Figure 4.15. The production of BTX is promoted with CZ15 catalyst (Figures 4.15a and 4.15c), whereas the one of olefins is maximized

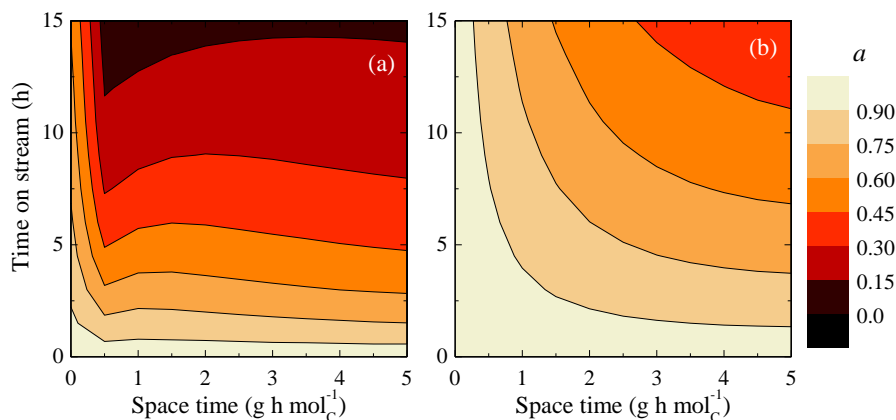


Fig. 4.14. Simulated contour maps with space time and time of the activity for the (a) CZ15 and (b) CZ140 catalysts at 550 °C.

with CZ140 catalyst (Figures 4.15b and 4.15d). One of the main consequences of CZ15 catalyst deactivation is the progressive decrease in the yield of BTX with time (Figures 4.15a). Then, the maximum yield of BTX is predicted to be close to 55% at $t \rightarrow 0$ and $\tau = 5.0 \text{ g h mol}_C^{-1}$. With this catalyst, olefins are predicted to be intermediates, with a maximum yield at low τ values. A different behavior is exhibited by the CZ140 catalyst. The lower acidity of this catalyst and the restricted extent of secondary reactions explain the negligible yields of BTX (Figure 4.13b) and the maximum yield of olefins (31%) obtained at the highest τ value (Figure

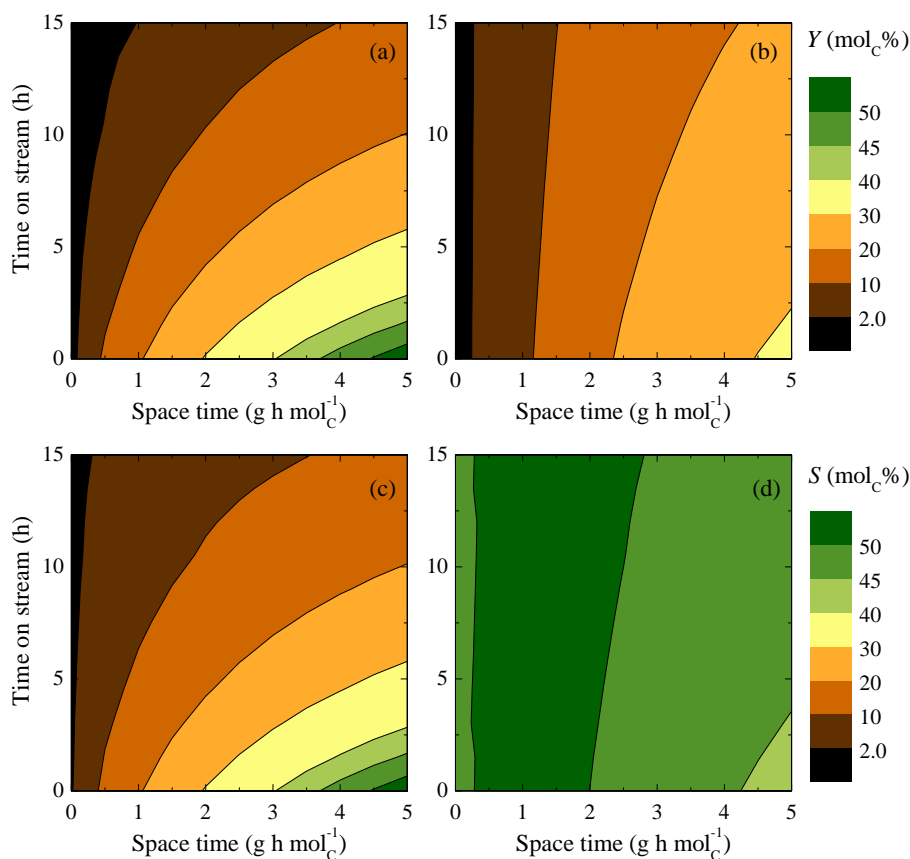


Fig. 4.15. Simulated contour maps with space time and time of the yield of (a) BTX and (b) olefins and the selectivity to (c) BTX and (d) olefins for the (a, c) CZ15 and (b, d) CZ140 catalysts at 550 °C.

4.15b). A remarkably slower deactivation with time is also predicted, which results in a relatively wide range of yields of olefins between 25 and 31% from 0 to 10 h on stream.

In terms of production, the selectivity to targeted products is also an important index, aiming to achieve the best isolation of the desired products. The maximum selectivity to BTX is located at the highest τ value (Figure 4.15c for CZ15 catalyst), with a full conversion situation in which the maxima of yield and selectivity coincide. Nevertheless, the most encouraging result in terms of selectivity is achieved with the CZ140 catalyst. In all the studied range, values of selectivity to olefins of 44–51% are predicted (Figure 4.15d). This result is slightly lower than those reported by Hou et al. [123] in the catalytic cracking of nC_5 with modified HZSM-5 zeolites, which suggests the satisfactory performance of these zeolites for the valorization of this paraffin.

According to the simulation results, some of the most interesting operation conditions are located at the extreme studied points of temperature or space time. Higher values than those depicted could allow higher maxima of olefin and BTX yields/selectivities to be reached. However, temperature is restricted by the catalyst stability (550 °C) in order to avoid the dealumination of the HZSM-5 zeolite [263]. In our study, the space time was also limited by the experimental reactor size, which could hypothetically be solved with a scale-up of the process, which will require further studies and validation of the kinetic model at these conditions.

Chapter 5

Kinetic modeling of DTO process

The kinetic modeling methodology explained in Chapter 4 is now applied to the DTO process. The higher complexity of the reaction network and the presence of water in the reaction medium make some of the kinetic equations change. The equations and parameters that best fit the experimental data for both CZ140 and CZ150 catalysts are detailed in this Chapter. The selected model results from the same statistical test previously explained. The model is used for analyzing the effect of operation conditions on the product distribution. Namely, the influence of space time, temperature, time on stream and acidity is evaluated. Special importance is given to the activity parameter, which will be a key factor for the reactor design models developed in Chapter 6. Part of the results in this Chapter have been published in *Chem. Eng. J.* **2017**, 311, 367-377.

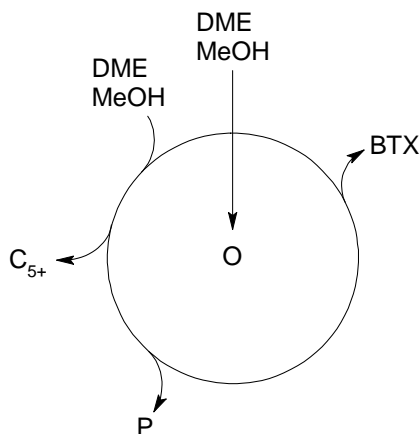
5.1 General aspects

According to the general requirements explained in Chapter 4, the kinetic model for a catalytic process needs the definition of: (i) a reaction network that considers the fundamental steps in the mechanisms; (ii) kinetic equations, with expressions dependent on the composition of the reaction medium, that faithfully describe the role of each one in the reaction steps and; (iii) deactivation kinetics that truly describe this phenomenon, with a dependency on the composition of the reaction medium and especially, on the precursors of deactivation.

5.1.1 Reaction network

In Section 3.2, an adaptation of the dual cycle mechanism was proposed for the DME conversion (Scheme 3.1) based on the experimental data collected with the CZ140 and CZ15 catalysts. Two intermediates were defined corresponding to the alkene and arene cycle. But according to the discussion in Section 4.2, lump-based models strictly consider macroscopic and experimental observations. Therefore, a simplification of the lump adaptation must be assumed, avoiding the steps in which intermediates are involved. Scheme 5.1 shows the proposed simplification.

Light olefins (O) are again the primary product and the intermediates for the production of the rest of hydrocarbons. The methylation pathway is considered



Scheme 5.1. Lump-based simplification of the dual cycle mechanism for DTO process.

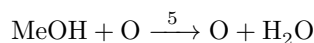
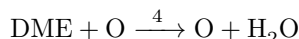
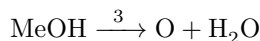
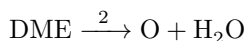
by the reaction of this light olefins with the oxygenates in the so-called autocatalytic production of olefins [37, 193]. Similar to the steps proposed for the catalytic cracking of *n*-pentane, the C₅₊ hydrocarbon, light paraffin (P) and aromatic (BTX) lumps are produced from the primary olefins through the oligomerization, hydrogen transfer and cyclization/dealkylation pathways, respectively.

All these steps of the reaction network are included in the Scheme 5.2, where the kinetic constants are defined. As happened before, the lump-based reaction network is defined in terms of contained C units, so stoichiometric coefficients are not given. The first step is the DME/methanol equilibrium. However, an equilibrium restriction is not considered from a methodological point of view, due to the uncertainty of reaching it at all conditions. Martínez-Espín et al. [87] reported the dependency on the HZSM-5 catalyst properties and the reaction conditions in order to operate at equilibrium conditions. Moreover, acidity can play an important role in the equilibrium so different constants should be used for CZ140 and CZ15 catalysts, thus hindering the direct comparison of the results. Standl and Hinrichsen [154] also recommended to avoid the use of equilibrium in lump-based models because lumps might deviate from an equilibrium distribution and thermodynamic consistency has to be retained.

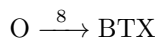
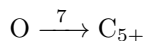
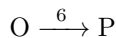
DME/MeOH equilibrium



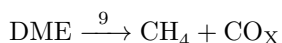
Formation of olefins



Formation of final products



Formation of C₁



Scheme 5.2. Proposed reaction network for DTO process.

Both oxygenates are independently considered in Scheme 5.2 due to the ability of quantifying them by the chromatographic analyses. The steps 2–5 correspond to the formation of olefins, directly from each oxygenated reactant (steps 2 and 3) or through the autocatalytic reaction (steps 4 and 5). In all these first 5 steps, water plays a key role, as one mol of water is formed with each produced carbon of olefins and the presence of water directly affects the methanol production (step 1).

The formation of secondary products from olefins is directly considered in steps 6–8, where a carbon from olefins yields a carbon of paraffin (P), long-chained hydrocarbon (C_{5+}) or BTX lumps. Step 9 is related to the thermal degradation of the reactant yielding C_1 products (CO_x and CH_4). This reaction is considered although their yields are too low even to be reliably computed (Figures 3.4 and 3.5).

Due to their similar behavior to other compounds, i - C_{4-5} products are re-distributed in different lumps. With CZ15 catalyst, i -butene showed the typical performance of an intermediate (Figure 3.5), so it is included in the olefin lump. i -Butane and i -pentane are respectively included in the light paraffin and C_{5+} lumps due to their final product behavior and their different number of carbon atoms. Then, the same average carbon number can be used for the DTO process and the catalytic cracking of n -pentane, with 3 average carbons for the olefin and paraffin lumps, 6 for the C_{5+} lump and 7 for the BTX lump.

5.1.2 Kinetic equations

Potential expressions of kinetic equations were considered for the catalytic cracking of n -pentane (Section 4.2), which allowed a good fitting of experimental data to be achieved. In the DTO process, a clear effect of the competitive adsorption of methanol and water was observed in previous works of our research group [37]. A Langmuir-Hinshelwood-type term is then considered for the quantification of the adsorption resistance. For a vector of reaction rates

$$\mathbf{r}_j = (r_j)_{j \times 1}, \quad (5.1)$$

a quasi non-selective deactivation model is defined, with

$$r_j = k_j \prod_R P_R \theta, \quad j = 1, 9, \quad (5.2)$$

and

$$r_j = k_j \prod_R P_R \theta a, \quad j = 2, \dots, 8. \quad (5.3)$$

The term θ quantifies the attenuation of the reaction rate of each j step by the adsorption of methanol and water on the acid sites following a Langmuir-Hinshelwood expression

$$\theta = \frac{1}{1 + K(P_{\text{MeOH}} + P_{\text{W}})}, \quad (5.4)$$

where K is associated with the adsorption constant for methanol and water, and P_{MeOH} and P_{W} are the partial pressure of methanol and water, respectively.

As deduced from equation (5.2), the catalyst deactivation does not affect the extent of the steps 1 and 9 of the reaction network. These are related to the DME/methanol equilibrium and the formation of C_1 products, respectively. According to the literature [38, 264], very low acidity is required for yielding DME from methanol or vice versa. Then, even a partially deactivated HZSM-5 catalyst can catalyze this reaction. On the other hand, the results from Figures 3.4 and 3.5 denoted a negligible but constant production of CO_x and CH_4 with time. A thermal nature is assumed for this reaction of oxygenate cracking, being unnecessary the presence of the catalyst.

The attenuation of the catalyst deactivation by the presence of water is widely reported in the literature for the MTO/DTO reactions [87, 192, 194]. A similar procedure to that applied for \mathbf{r}_j is then considered for the deactivation rate. An attenuation term due to the adsorption of water on the acid sites (θ_d) is included in the definition of r_d . The equation (4.10) is then rewritten as

$$-\frac{da}{dt} = r_d = k_d \sum_{cp} P_{cp} \theta_d a^d, \quad (5.5)$$

with θ_d being defined as

$$\theta_d = \frac{1}{1 + K_d P_{\text{W}}}, \quad (5.6)$$

where K_d is associated with the adsorption constant for water related to the attenuation of catalyst deactivation.

A dependency of the adsorption constants (K and K_d) on temperature is considered by using the van't Hoff equation

$$K = K^* \exp \left[\frac{\Delta H}{R} \left(\frac{1}{T^*} - \frac{1}{T} \right) \right], \quad (5.7)$$

where K^* is the value of the adsorption constant at the reference temperature (T^*) and ΔH is the heat associated with the adsorption.

5.1.3 Deactivation kinetics

As explained in details in Section 4.2, deactivation kinetics were computed simultaneously with reaction kinetics. More complex equations are used for the DTO process, considering the hyperbolic shape of a Langmuir-Hinshelwood expression that quantifies the attenuation of deactivation by water adsorption. In Section 3.3, we studied experimentally these effects of water on deactivation and on the structure of the formed coke. Different possible deactivation equations are proposed considering different coke precursors (Table 5.1): (i) a parallel-in series deactivation with DME, methanol, olefins and BTX as coke precursors (DE_A); (ii) a parallel deactivation with DME and methanol as coke precursors (DE_B), and; (iii) a mixed parallel-in series deactivation with DME, methanol, olefins and BTX as coke precursors but using two kinetic constants k_{d1} and k_{d2} (DE_C).

Table 5.1. Proposed deactivation equations (DE) for the DTO process.

DE _A	$-\frac{da}{dt} = k_d(P_{\text{DME}} + P_{\text{MeOH}} + P_{\text{O}} + P_{\text{BTX}})\theta_d a^d$	(5.8)
DE _B	$-\frac{da}{dt} = k_d(P_{\text{DME}} + P_{\text{MeOH}})\theta_d a^d$	(5.9)
DE _C	$-\frac{da}{dt} = [k_{d1}(P_{\text{DME}} + P_{\text{MeOH}}) + k_{d2}(P_{\text{O}} + P_{\text{BTX}})]\theta_d a^d$	(5.10)

5.2 Kinetic parameters and model validation

Experimental data were fitted using the methodology explained in Chapter 4 with the kinetic equations above introduced in Section 5.1. Following the order used in Chapter 3, the results for the CZ140 catalyst are firstly fitted and used for studying the process variables. This catalyst presents the best performance for olefins production, the lowest formation of coke and the longest stability and lifetime. The experimental results obtained with the CZ15 catalyst are later fitted to the model in order to study the role of catalyst acidity

5.2.1 CZ140 catalyst

The experimental data collected in this work using the CZ140 catalyst were complemented with those previously reported for the same catalyst [38], in order to gather the highest possible amount of experimental data points. Some of the reactions were repeated, which allowed a better statistical discrimination to be performed (see the model discrimination in Section 4.2 and calculations in Table 4.3).

The values of the kinetic parameters that offer this best fitting of experimental data are listed in Table 5.2. The kinetic parameters are quite similar to those previously reported for DTO process [37, 38]. The confidence intervals at 95% were calculated from the discrepancies of predicted and experimental data and are also displayed in Table 5.2. Values of the kinetic constants of different order of magnitude are observed, with the autocatalytic formation of olefins (k_4 and k_5 in Scheme 5.2) being the fastest steps. The apparent activation energy values are in all cases above 79 kJ mol^{-1} , highlighting that the process is controlled by the reaction regime. Although the deactivation constant is in the range of those previously observed for the catalytic cracking of *n*-pentane, the adsorption model with the presence of K_d term and the significantly higher deactivation order (4.72 *vs* ca. 1) point out the different behavior of the same catalyst in the two processes. Note that the kinetic parameters listed in Table 5.2 correspond to the reaction network of Scheme 5.2 and the deactivation equation DE_B (equation (5.9) in Table 5.1). This combination provides the best fitting of experimental data as better explained below.

The parity plots of experimental and calculated data (without repetitions) at 325, 350, 375 and 400 °C are shown in Figures 5.1a, 5.1b, 5.1c and 5.1d, respectively. A good overall fitting is achieved. Most of the points are located within the $\pm 10\%$ error range, indicated with dashed lines. A better fitting is obtained at 325 and 350 °C (Figures 5.1a and 5.1b), where a bimodal distribution of points is observed due to the low conversion of oxygenates (points at high *y* values) into hydrocarbons (points at low *y* values). Some more deviations, even higher than

Table 5.2. Kinetic and adsorption constants at 350 °C, apparent activation energy and adsorption heat values for the DTO process over CZ140 catalyst.

	k^*, K^*	$E, \Delta H$ (kJ mol ⁻¹)
<i>Steps of the reaction network</i>		
k_1 (mol _C g ⁻¹ h ⁻¹ bar ⁻²)	$(1.54 \pm 0.61) 10^{-1}$	$(1.45 \pm 0.35) 10^2$
k_2 (mol _C g ⁻¹ h ⁻¹ bar ⁻¹)	$(1.77 \pm 0.51) 10^{-2}$	$(8.79 \pm 0.73) 10^1$
k_3 (mol _C g ⁻¹ h ⁻¹ bar ⁻¹)	$(3.31 \pm 0.25) 10^{-2}$	$(2.70 \pm 0.25) 10^2$
k_4 (mol _C g ⁻¹ h ⁻¹ bar ⁻²)	$(1.13 \pm 0.57) 10^0$	$(1.06 \pm 0.09) 10^2$
k_5 (mol _C g ⁻¹ h ⁻¹ bar ⁻²)	$(1.02 \pm 0.99) 10^0$	$(1.62 \pm 0.12) 10^2$
k_6 (mol _C g ⁻¹ h ⁻¹ bar ⁻¹)	$(1.41 \pm 0.92) 10^{-1}$	$(1.02 \pm 0.43) 10^2$
k_7 (mol _C g ⁻¹ h ⁻¹ bar ⁻¹)	$(4.75 \pm 0.54) 10^{-1}$	$(8.67 \pm 0.37) 10^1$
k_8 (mol _C g ⁻¹ h ⁻¹ bar ⁻¹)	$(2.39 \pm 0.92) 10^{-1}$	$(7.92 \pm 0.29) 10^1$
k_9 (mol _C g ⁻¹ h ⁻¹ bar ⁻¹)	$(1.76 \pm 0.81) 10^{-3}$	$(1.11 \pm 0.47) 10^2$
K (bar ⁻¹)	$(3.16 \pm 0.84) 10^{-1}$	$(-1.52 \pm 0.16) 10^0$
<i>Deactivation</i>		
k_d (h ⁻¹ bar ⁻¹)	$(3.19 \pm 0.93) 10^{-1}$	$(6.88 \pm 0.13) 10^0$
K_d (bar ⁻¹)	$(1.14 \pm 0.49) 10^0$	$(-1.66 \pm 0.70) 10^0$
d	$(4.72 \pm 0.20) 10^0$	

the indicated $\pm 10\%$, are found at 375 and 400 °C. The complex reaction network and the consideration of Langmuir-Hinshelwood adsorption expressions for reaction and deactivation rates make the experimental data fitting more difficult. But precisely for this reason, the fitting is good enough for kinetic modeling purposes.

Similar to how we proceed with the kinetic parameters computed in Chapter 4, groups of steps can be set for the reaction network. In this case, the steps are merged following the nature of the product formation according to the dual cycle mechanism simplification in Scheme 5.1. There are five types of steps, distinguishing between steps independent and dependent on a : (i) the formation of C₁ products (step 9, a -independent); (ii) the formation of methanol (step 1, a -independent); (iii) the formation of the first olefins (steps 2 and 3, a -dependent); (iv) the autocatalytic formation olefins/Dual cycle mechanism propagation (steps 4 and 5, a -dependent) and; (v) the formation of final products (steps 6 to 8, a -dependent).

Figure 5.2a shows the tendency followed by the average kinetic constant of each group of reactions defined by (i) to (v) and Figure 5.2b illustrates an energy diagram based on the average values of the apparent activation energy computed (Table 5.2). Average kinetic constant values of different order of magnitude are observed. The slowest step is predicted to be the formation of the first olefins, which is marked with the dashed line in Figure 5.2a. This step could be related

to the formation of the initial C–C bond, reported as the limiting stage in the dual cycle mechanism [73]. As expected, the formation of methanol is faster than the one of this C–C bond. Interestingly, the autocatalytic formation of olefins is faster than their conversion into final products, which explains the high selectivity to olefins observed in Chapter 3 and detailed below.

Consistent conclusions can be deduced from the energy diagram of Figure 5.2b. The highest apparent activation energy barrier is set by the formation of the first olefins. The production of methanol shows a lower value and once overcome the

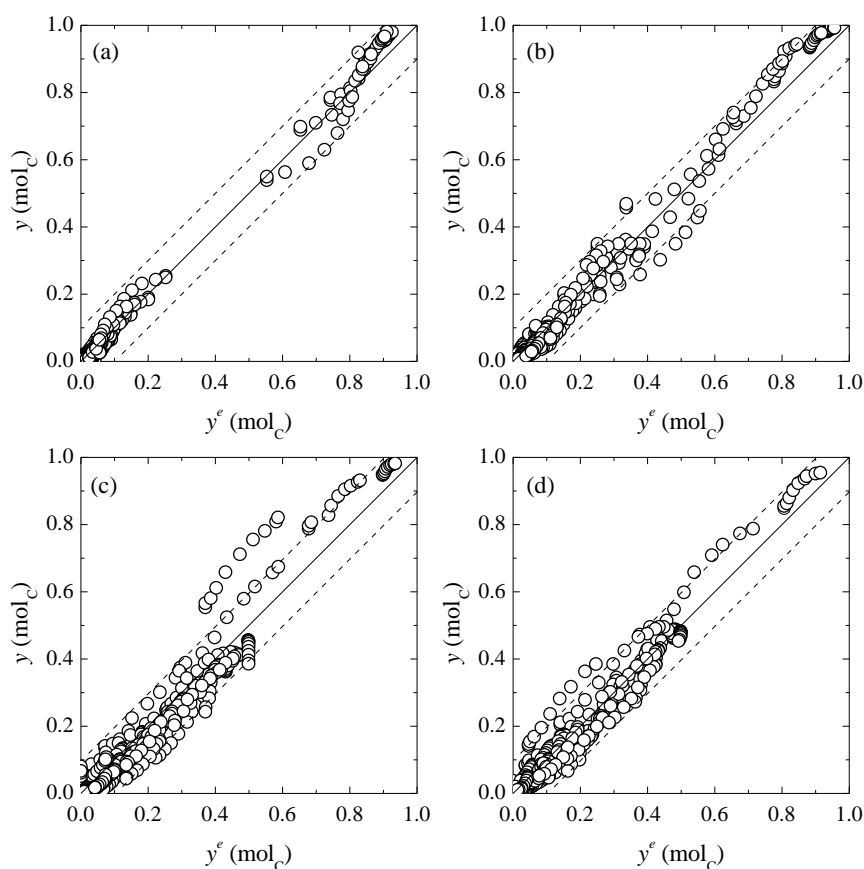


Fig. 5.1. Parity plot for the calculated and experimental data of molar fractions in the DTO process using the CZ140 catalyst at (a) 325 °C, (b) 350 °C, (c) 375 °C, (d) 400 °C.

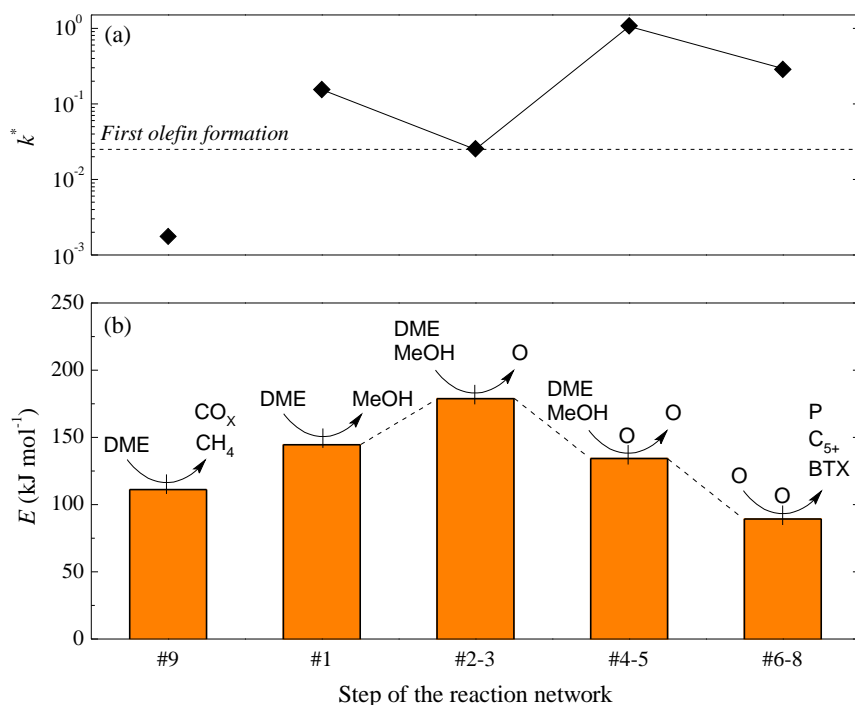


Fig. 5.2. Comparison of the average (a) kinetic constants and (b) apparent activation energy values for the groups of steps of the reaction network of DTO process using the CZ140 catalyst.

formation of olefins, the olefins-involved steps have lower apparent activation energy values. These values are also in accordance with those reported by Kumar et al. [265] from microkinetic computation. They reported values of ca. 121 kJ mol⁻¹ for the methane formation, ca. 164 kJ mol⁻¹ for the methoxy formation and 54–138 kJ mol⁻¹ for the different methylation reactions that finally yields the rest of hydrocarbons. These values are in agreement with our calculated 111, 179 and 89 kJ mol⁻¹ for the analogous lump-based steps of the macrokinetic model.

A very low kinetic constant value and a relatively low apparent activation energy are exhibited by the formation of C₁ products. This step was attributed to a thermal nature, and its contribution to the reaction network is negligible. For this reason, the results of CO_x and CH₄ are not shown from now on, because they hinder the interpretation of the rest of the data.

Discrimination of deactivation equations

The errors achieved with each deactivation equation, and the results of the significance test based on equation (4.23) are displayed in Figure 5.3. The lowest error is obtained with the deactivation equation DE_C (equation (5.10)) that includes a second deactivation constant. Nevertheless, the significance of the improvement is not enough, having to include one more parameter and

$$F_{B-C} < F_{1-\alpha}. \quad (5.11)$$

So, the most significant fitting is achieved with a parallel deactivation that considers the reactants as coke precursors (equation (5.9)). Aguayo et al. [188] observed this parallel deactivation under the same conditions after collecting experimental data in both packed and fluidized bed reactors. This situation is opposed to that observed in Chapter 4 for the catalytic cracking of *n*-pentane (deactivation in series). Indeed, these two reactions present different deactivation mechanisms and the lifetime, rate and shape of deactivation curves are completely different. The reactants-driven deactivation is in accordance not only with the previously reported kinetic models for the DTO process [38], but also with the experimental observations for the MTO reaction with HZSM-5 zeolite of Schulz [102], the spectroscopy results of Bleken et al. [103] and the burning cigar deactivation mechanism proposed by Olsbye et al. [94], based on the pictorial representation of Haw and

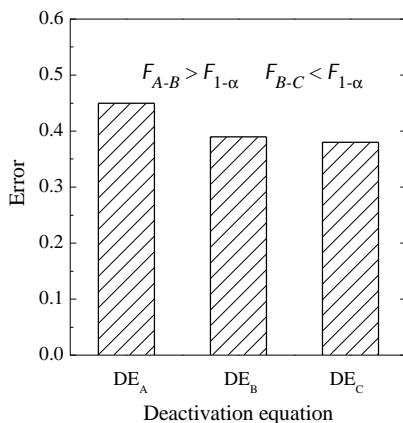


Fig. 5.3. Comparison of the errors and significance test result for the deactivation equation tested for DTO process using the CZ140 catalyst.

Marcus [266]. Janssens et al. [193] also attained well-fitted experimental data using a deactivation constant that depends on the concentration of methanol during the MTO reaction.

Experimental data fitting

Figure 5.4 shows the comparison of the experimental and calculated data from the model for the evolution with space time of the product distribution. The results correspond to $t = 0$ and different temperatures: 325 °C (Figure 5.4a), 350 °C (Figure 5.4b), 375 °C (Figure 5.4c) and 400 °C (Figure 5.4d). The effect of space time

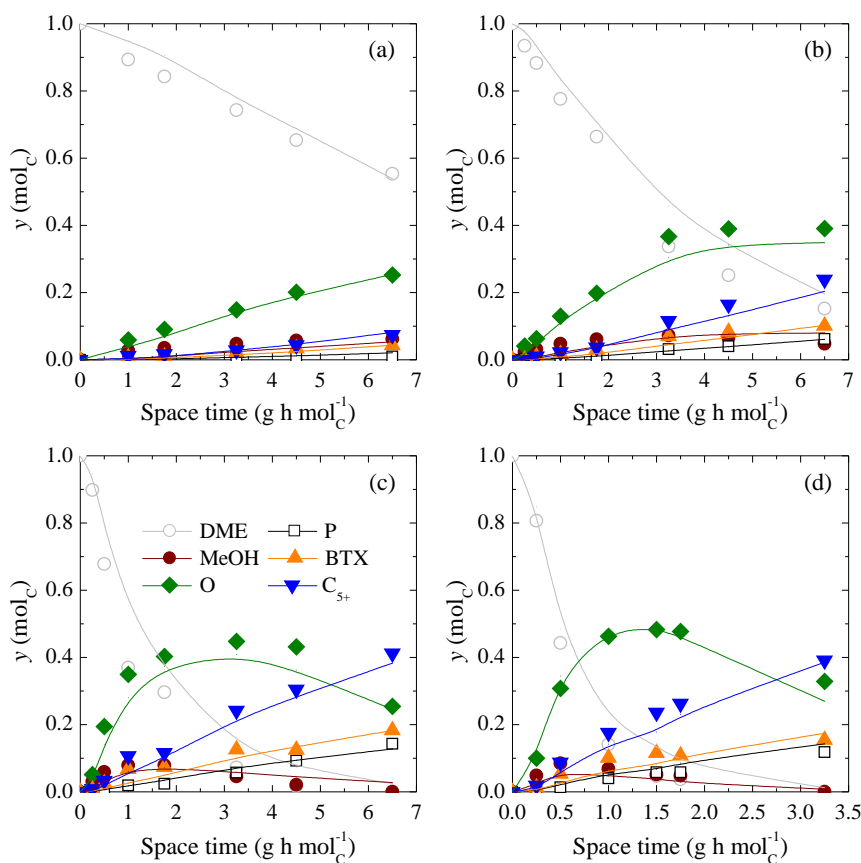


Fig. 5.4. Comparison of the experimental data (symbols) to those predicted by the model (lines) for the evolution with space time of the molar fractions using the CZ140 catalyst at (a) 325 °C, (b) 350 °C, (c) 375 °C and (d) 400 °C. $t = 0$.

(τ) and temperature can be analyzed simultaneously from these results. Moreover, the behavior of each lump can be compared with the ones deduced from the experimental observations presented in Section 3.2.

In all cases, the concentration of DME decreases with τ , being more pronounced the concentration decay as temperature is increased. The typical behavior of a reaction intermediate is observed for the concentration of olefins. Initially, its value increases with τ . At the lowest temperature, the maximum concentration of olefins is observed at the highest τ due to the low DME conversion. However, DME and olefins are more reactive when temperature is increased and the reaction front advance in the reactor longitudinal position or τ (see equation (4.37)). Then, maximum concentrations of olefins are found, being located at lower τ values as the temperature is increased ($\tau = 6 \text{ g h mol}^{-1}$ at 350 °C in Figure 5.4b and $\tau = 1.25 \text{ g h mol}^{-1}$ at 400 °C in Figure 5.4d). The concentrations of the rest of hydrocarbons (paraffins, BTX and C_{5+}) increase when the one of olefins decreases. At any condition, C_{5+} lump is the main byproduct in the reaction medium, reaching molar fraction values of 0.4 at 375 and 400 °C with the highest studied τ value (Figures 5.4c and 5.4d). The predicted trends for paraffins and BTX lumps are almost overlapped, which is in agreement with the parallel formation of saturated and aromatic compounds through the cyclization and hydrogen transfer pathways (Scheme 3.1). Small concentrations of methanol are only observed when DME conversion is low. Otherwise, methanol is completely converted at high values of τ or temperature. This is in accordance with the reactivity of oxygenates at these conditions and with the displaced equilibrium indicated in the Scheme 5.2.

The comparison of the experimental data to those predicted by the model, considering a parallel deactivation, is illustrated in Figure 5.5. The evolution with time of the product distribution is shown for some selected conditions at 325 °C (Figure 5.5a), 350 °C (Figure 5.5b), 375 °C (Figure 5.5c) and 400 °C (Figure 5.5d). Four clearly differentiated conversions degrees are depicted, observing DME molar fraction from 0.8 to 0. The two deactivation zones reported for DTO process [52] can be easily identified at low temperature in Figures 5.5a and 5.5b: a fast deactivation zone followed by a very slow deactivation zone, where the molar fractions tend to a constant final value. This is mathematically solved with the deactivation order d . A high value of ca. 4.7 is calculated, which is close to that reported by Pérez-Uriarte et al. [38]. The assumption of values of $d > 2$ allows this kind of deactivation kinetics to be fitted without include any term of activity in the steady state. The calculation of the activity in the steady state (residual activity) could improve the fitting [267], but require long DTO runs and adds some more empiricism to the kinetics. Therefore, the use of high d values is preferred in this case.

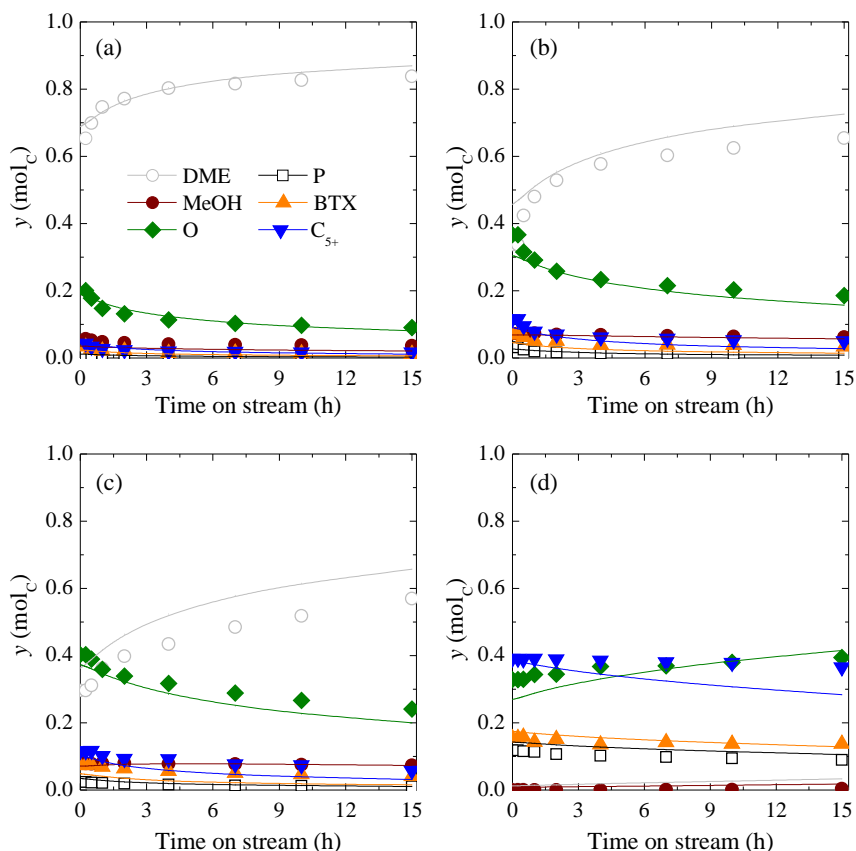


Fig. 5.5. Comparison of the experimental data (symbols) to those predicted by the model (lines) for the evolution with time of the molar fractions using the CZ140 catalyst. (a) 325 °C, $\tau = 4.5 \text{ g h mol}_C^{-1}$; (b) 350 °C, $\tau = 3.25 \text{ g h mol}_C^{-1}$; (c) 375 °C, $\tau = 1.7 \text{ g h mol}_C^{-1}$; (d) 400 °C, $\tau = 3.25 \text{ g h mol}_C^{-1}$.

At 400 °C and full conversion conditions, C_{5+} lump is the main product observed. The concentrations of paraffins and BTX are also noteworthy and similar in both cases (see the cyclization and hydrogen transfer mechanism explained in Chapter 3). The model predicts a decrease in the concentration of C_{5+} hydrocarbons as the catalyst is deactivated. This leads to an increase in the concentration of olefins, which are the main products at most of the reaction conditions studied.

5.2.2 Role of catalyst acidity

From the experimental results in Section 3.3 on the effect of Si/Al ratio, the role of the acidity is also analyzed by means of kinetic modeling. The same procedure was used and the computed kinetic constant values for the DTO process using the CZ15 catalyst are listed in Table 5.3. Regarding the kinetic constant values, the most important difference is the higher value of the constants of secondary reactions. The formation of light paraffins and C₅₊ hydrocarbons is faster than using the CZ140 catalyst, with one order of magnitude higher k_6^* and k_7^* . BTX formation is also boosted with almost four times higher k_8^* .

The evolution with τ of the product distribution at 350 and 375 °C is respectively shown in Figures 5.6a and 5.6b. Please note that τ values in the X axis are 3 times lower than those required with the CZ140 catalyst for obtaining the same performance. The higher activity of CZ15 catalyst makes possible to obtain higher yields of other hydrocarbons as paraffins or C₅₊ with this lower catalyst loading. Overall, this catalyst does not allow high yields of olefins to be achieved, as the strength of the acid sites tends to convert the intermediate olefins into final products according to the extent of the proposed reaction network (Scheme 5.2).

Deactivation kinetics are also quite different for CZ15 catalyst. The value of k_d^* is almost triplicated, K_d^* is half of the value for CZ140 catalyst and d is near

Table 5.3. Kinetic and adsorption constants at 350 °C, apparent activation energy and adsorption heat values for the DTO process over CZ15 catalyst.

	k^*, K^*	$E, \Delta H$ (kJ mol ⁻¹)
<i>Steps of the reaction network</i>		
k_1 (mol _C g ⁻¹ h ⁻¹ bar ⁻²)	$(9.56 \pm 0.57) 10^{-1}$	$(1.84 \pm 0.42) 10^2$
k_2 (mol _C g ⁻¹ h ⁻¹ bar ⁻¹)	$(8.21 \pm 0.43) 10^{-2}$	$(1.29 \pm 0.48) 10^2$
k_3 (mol _C g ⁻¹ h ⁻¹ bar ⁻¹)	$(8.44 \pm 0.22) 10^{-2}$	$(2.67 \pm 0.33) 10^2$
k_4 (mol _C g ⁻¹ h ⁻¹ bar ⁻²)	$(4.29 \pm 0.46) 10^0$	$(1.79 \pm 0.71) 10^2$
k_5 (mol _C g ⁻¹ h ⁻¹ bar ⁻²)	$(5.67 \pm 0.15) 10^0$	$(1.87 \pm 0.38) 10^2$
k_6 (mol _C g ⁻¹ h ⁻¹ bar ⁻¹)	$(1.81 \pm 0.13) 10^0$	$(1.13 \pm 0.56) 10^2$
k_7 (mol _C g ⁻¹ h ⁻¹ bar ⁻¹)	$(3.54 \pm 0.25) 10^0$	$(8.53 \pm 0.49) 10^1$
k_8 (mol _C g ⁻¹ h ⁻¹ bar ⁻¹)	$(7.54 \pm 0.62) 10^{-1}$	$(7.20 \pm 0.78) 10^1$
k_9 (mol _C g ⁻¹ h ⁻¹ bar ⁻¹)	$(1.94 \pm 0.85) 10^{-3}$	$(1.40 \pm 0.75) 10^2$
K (bar ⁻¹)	$(9.04 \pm 0.85) 10^0$	$(-1.31 \pm 0.62) 10^0$
<i>Deactivation</i>		
k_d (h ⁻¹ bar ⁻¹)	$(8.97 \pm 0.34) 10^{-1}$	$(6.87 \pm 0.26) 10^0$
K_d (bar ⁻¹)	$(5.42 \pm 0.23) 10^{-1}$	$(-8.81 \pm 0.56) 10^0$
d	$(1.62 \pm 0.14) 10^0$	

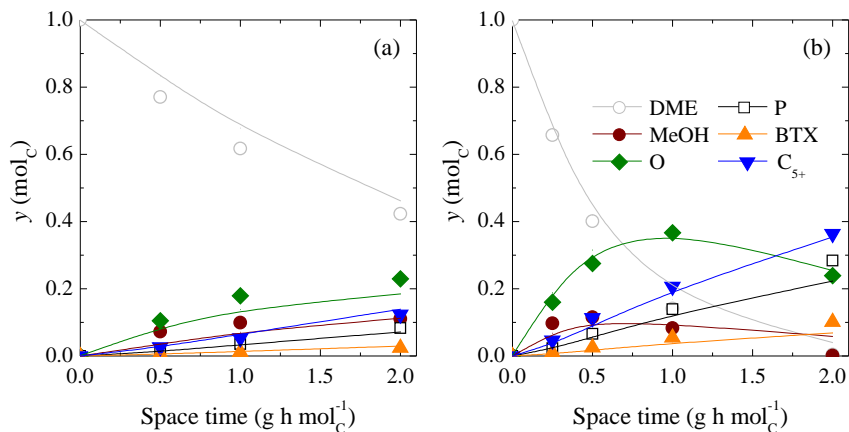


Fig. 5.6. Comparison of the experimental data (symbols) to those predicted by the model (lines) for the evolution with space time of the molar fractions using the CZ15 catalyst at (a) 350 °C and (b) 375 °C. $t = 0$.

1. As experimentally observed (Section 3.3), CZ15 catalyst is deactivated much faster than CZ140 catalyst. This is in accordance with the increase in the deactivation constant. According to the decrease in K_d^* , water affects in a lower extent to the deactivation using the CZ15 catalyst. This was also observed when different ratios of co-fed water were studied in Section 3.3 aiming for the stabilization of the conversion with this catalyst. The d value of 1.62 suggests that the decrease in the conversion is faster and a final value of activity in the steady state is not reached. The comparison of the experimental data to those predicted by the model at selected conditions using this catalyst is shown in Figure 5.7.

Again, the two-zone deactivation behavior can be observed. At 325 °C, conversions are too low and only ca. 10% of olefins and methanol are obtained (Figures 5.7a and 5.7b). The fast deactivation zone takes a couple of hours until almost constant concentrations are attained ($y_{\text{DME}} \approx 0.9$). When temperature is increased up to 375 °C, a faster deactivation is observed (Figures 5.7c and 5.7d). In these cases, the fast deactivation zone takes ca. 6 h and the catalyst undergoes an almost total deactivation in this time. The concentration of olefins, the main products, quickly decreases during the first 6 h, as well as those of the rest of products. After 15 h on stream, DME is the only component of the reaction medium.

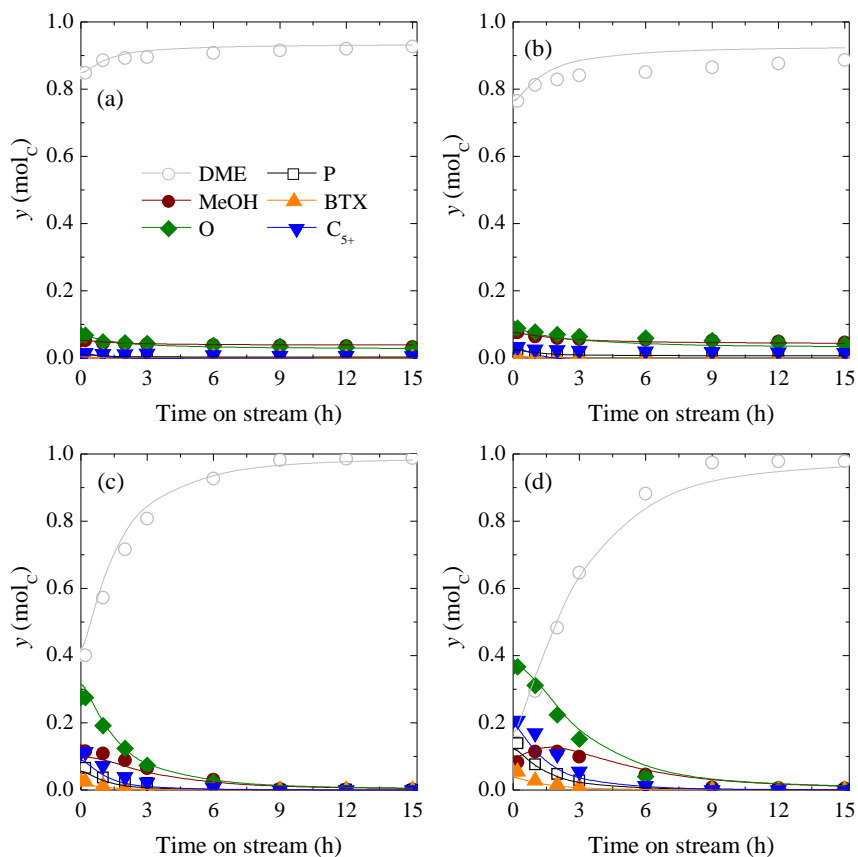


Fig. 5.7. Comparison of the experimental data (symbols) to those predicted by the model (lines) for the evolution with time of the molar fractions using the CZ15 catalyst. (a) 325 °C, $\tau = 1.0 \text{ g h mol}_C^{-1}$; (b) 325 °C, $\tau = 2.0 \text{ g h mol}_C^{-1}$; (c) 375 °C, $\tau = 0.5 \text{ g h mol}_C^{-1}$; (d) 375 °C, $\tau = 1.0 \text{ g h mol}_C^{-1}$.

5.3 Relevant magnitudes of the model

From the model, the evolution with time and the longitudinal position of the composition of the reaction medium can be studied. However, the calculation of two magnitudes is specially relevant in the simulations, the water concentration in the reaction medium and the activity. The computation of these magnitudes plays a key role in the simulation results and will be important in the reactor design models dealt with in Chapter 6.

5.3.1 Water concentration

Water concentration in the product stream can be analyzed following different strategies:

- (i) The Stabilwax column of the microGC provided with a TCD detector is able to detect water. Water signal is not easy to follow and the peak tends to oscillate in position and intensity, giving a noisy signal. Hence, the precision of the detection of water is lower than that of the rest of the compounds.
- (ii) An oxygen balance provides an estimation of the amount of water for each experimental point. Assume that the precision of DME and methanol detection is much higher regarding the stability of the signal. Also assume that other oxygenates are not formed as they are not identified from chromatographic analyses. Then, water content can be easily calculated from the amount of fed oxygen (DME or mixtures DME/water) and the one analyzed at the outlet of the reactor.
- (iii) The model includes carbon and oxygen balance coefficients in the used **A** matrix (similar to equation (4.26)). Moreover, it takes the water formation and consumption into account following the reaction network in Scheme 5.2. Then, a computation of the water concentration at the outlet of the reactor can be made by the model.

In the ideal situation in which the experimental data fitting were perfect, the two last methods should give the same values. Because of the noise of the experimental data for water, these points are not used for the calculation of the errors in Figure 5.3. From now, the values of the model calculations will be assumed good enough for designing the DTO process, so trying to be as much consistent as possible, the model predictions for water concentration are used for the discussion. As expected, the differences observed with the values estimated by an oxygen balance are proportional to the errors observed for DME and methanol in the fitting of the experimental data analyzed in Section 5.1 (note the negligible CO_x concentration).

Figure 5.8 shows the evolution with τ (proportional to the longitudinal position of the reactor) of the water concentration at different temperatures for the CZ140 (Figure 5.8a) and CZ15 catalysts (Figure 5.8b). The dashed line indicates the maximum concentration of water in mol mol_C^{-1} that can be achieved from the oxygen in the feed. An asymptotic tendency is observed for all temperatures and both catalysts, playing the conversion of DME a key role in the shape of the curve. A faster increase in the water concentration is observed when the temperature is increased. CZ140 catalyst shows a sharp rupture curve at 400 °C in the τ range of 1.0–2.0 g h mol_C^{-1} . However, a value lower than $0.2 \text{ mol mol}_C^{-1}$ is observed at 325 °C and $\tau = 6.5 \text{ g h mol}_C^{-1}$.

The same trend is followed when CZ15 catalyst is analyzed (Figure 5.8b), but considering the highest activity of this more acid catalysts. Note the different values of the X axis. Although similar values can be observed at 325 °C and $\tau = 2.0 \text{ g h mol}_C^{-1}$, higher concentrations of water with this catalyst are computed increasing temperature. Especially, a value of $0.25 \text{ mol mol}_C^{-1}$ is predicted at 375 °C and $\tau = 2.0 \text{ g h mol}_C^{-1}$ for the CZ140 catalyst, whereas an increase up to $0.42 \text{ mol mol}_C^{-1}$ is obtained for the CZ15 catalyst.

Taking into account the relation between τ and the longitudinal position of the reactor defined in equation (4.37), and the previously introduced reactants-driven deactivation or burning cigar mechanism [94], the water concentration can

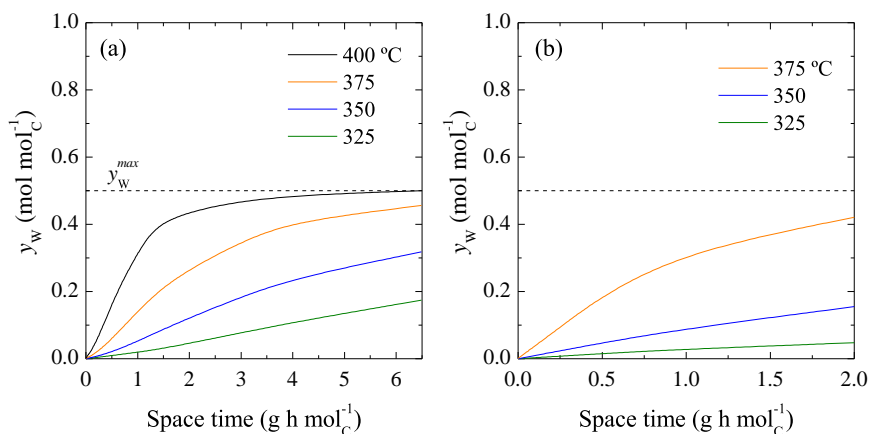


Fig. 5.8. Effect of temperature on the evolution with space time of the water concentration in the reaction medium using the (a) CZ140 and (b) CZ15 catalysts. $t = 0 \text{ h}$.

be directly associated with the catalyst deactivation. This validates again the deactivation equation discrimination and form in Table 5.1. The highest deactivation degree and amount of coke observed in the first part of the reactor coincide with the situation in which no water is present in the reaction medium. The profiles depicted in Figure 5.8 corresponds to values of $t = 0$. Therefore, the reaction front will be displaced to higher values of τ when the first part of the reactor is fully deactivated at values of $t > 0$. Bleken et al. [103] highlighted a wider reaction zone with a non-clearly observed coke profile when the activity of the catalyst is decreased. This happens at lower reaction temperatures. A softer profile of water is also obtained, which is in accordance with the more homogeneous coke deposition along the catalytic bed experimentally observed after DTO runs.

The evolution with time of the water concentration for different τ values with the CZ140 catalyst is shown in Figure 5.9. The previously discussed two zone deactivation can also be observed in the water concentration. At 325 and 350 °C (Figures 5.9a and 5.9b), the CZ140 is faster deactivated at the first hours on stream when τ is increased. This leads to a faster drop in the water concentration. Nevertheless, water concentration decreases slower and with a softer profile when τ is increased at 375 and 400 °C (Figures 5.9c and 5.9d). An almost constant tendency is indeed observed at 400 °C with the highest τ , reaching the maximum value of water concentration allowed. Regarding the results at these conditions (Figure 5.5d), almost full conversion of DME and methanol was predicted, which explains this result.

5.3.2 Activity

The evolution with time of the activity longitudinal profile must be calculated for the computation of the evolution with time and reactor position of the reaction medium. As a computational variable included in the \mathbf{u} vector of equation (4.12), a can be monitored and its evolution with time at the outlet of the reactor for different τ and temperature values is depicted in Figure 5.10 for the CZ140 catalyst. A significant influence of temperature on the τ -dependency of the activity can be observed. At 325 °C (Figure 5.10a), the evolution with time of a is barely affected by the space time (or the longitudinal position as previously stated). Values between 0.42 and 0.49 are calculated after 15 h on stream in the τ range of 1.0–6.5 g h mol_C⁻¹. A remarkable effect of τ is otherwise shown by the catalyst at 400 °C (Figure 5.10d). The illustrated results are selected in a narrower τ range (0.25–3.25 g h mol_C⁻¹), observing a values from 0.4 to 0.9 after 15 h on stream when τ is increased. This is in agreement with the wider reaction zone and the more homogeneous deactivation when the catalyst is less active [103].

At lower temperatures, the catalytic bed is more homogeneously deactivated

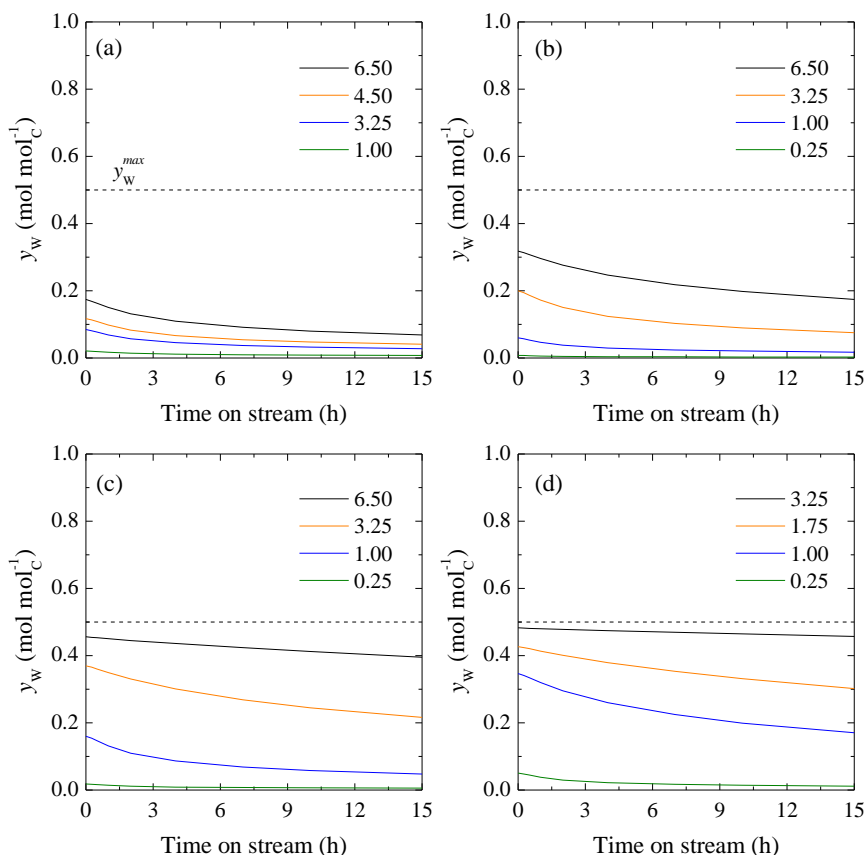


Fig. 5.9. Effect of space time (in g h mol_C^{-1}) on the evolution with time of the water concentration in the reaction medium using the CZ140 catalyst at (a) 325 °C, (b) 350 °C, (c) 375 °C and (d) 400 °C.

and then, a decreases more or less uniformly for all τ values. Increasing temperature, the reaction zone is narrower and located at the initial positions of the catalytic bed. Hence, a decays faster at low values of τ . A better understanding of this reasoning can be achieved with the simulated contour maps with τ of the activity at 0.5, 5, 10 and 15 h on stream depicted in Figures 5.11a (325 °C), 5.11b (350 °C), 5.11c (375 °C) and 5.11d (400 °C).

The reaction zone (and then the deactivation zone) goes clearly narrower as temperature is increased. From 0.5 h on stream, the deactivation zone is almost

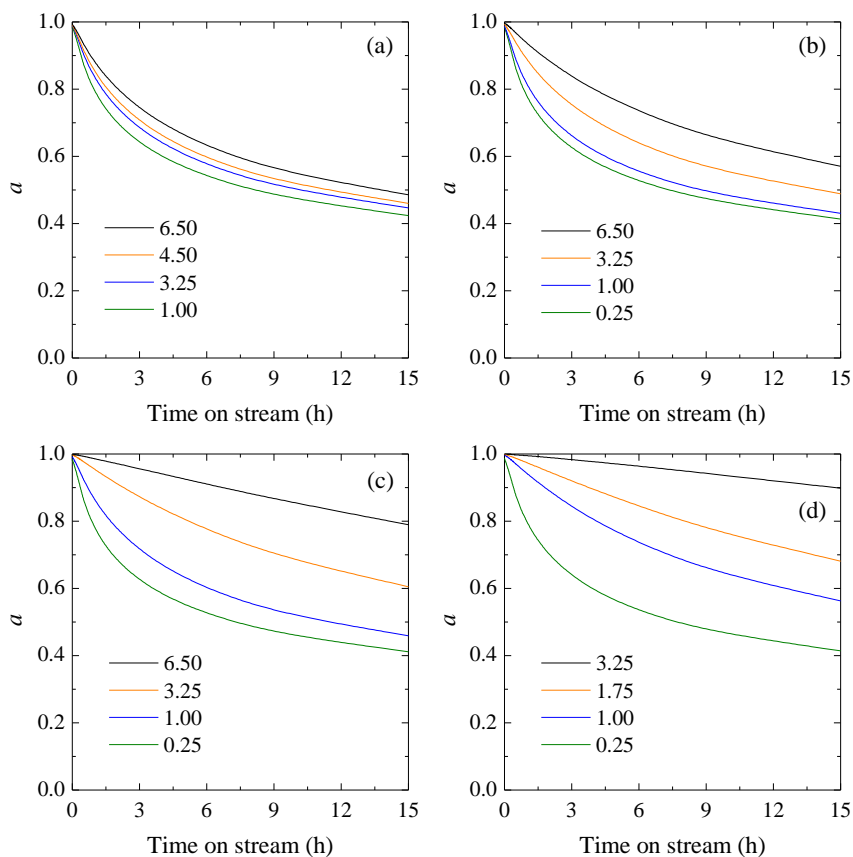


Fig. 5.10. Effect of space time (in g h mol_C^{-1}) on the evolution with time of the activity of the CZ140 catalyst at the outlet of the reactor at (a) 325 °C, (b) 350 °C, (c) 375 °C and (d) 400 °C.

extended to the whole reactor at 325 °C (Figure 5.11a) and the differences are more and more severe as time increases. The deactivation zone is concentrated at the beginning of the reactor (low values of τ) at 400 °C (Figure 5.11d). In terms of space time values, after 15 h on stream,

$$\begin{aligned}
 a < 0.5 & \text{ with } \tau < 6.50 \text{ g h mol}_C^{-1} \text{ at } 325 \text{ °C}; \\
 a < 0.5 & \text{ with } \tau < 3.75 \text{ g h mol}_C^{-1} \text{ at } 350 \text{ °C}; \\
 a < 0.5 & \text{ with } \tau < 1.75 \text{ g h mol}_C^{-1} \text{ at } 375 \text{ °C}; \\
 a < 0.5 & \text{ with } \tau < 0.75 \text{ g h mol}_C^{-1} \text{ at } 400 \text{ °C}.
 \end{aligned}$$

Another interesting observation from the results in Figure 5.10 is the tendency of a to reach a constant value after certain time. Previously, we discussed the high value of d obtained for the CZ140 catalyst. The high value was attributed to a mathematical tool that allows an activity in the steady state to be reached without considering any other parameter. Figure 5.10 clearly shows this performance and an asymptotic value of activity at ca. 0.3 can be deduced from the curves.

A d value of ca. 1.6 is calculated for the CZ15 catalyst (Table 5.3), which suggests that this behavior is not achieved. The results in Figure 5.12 confirms

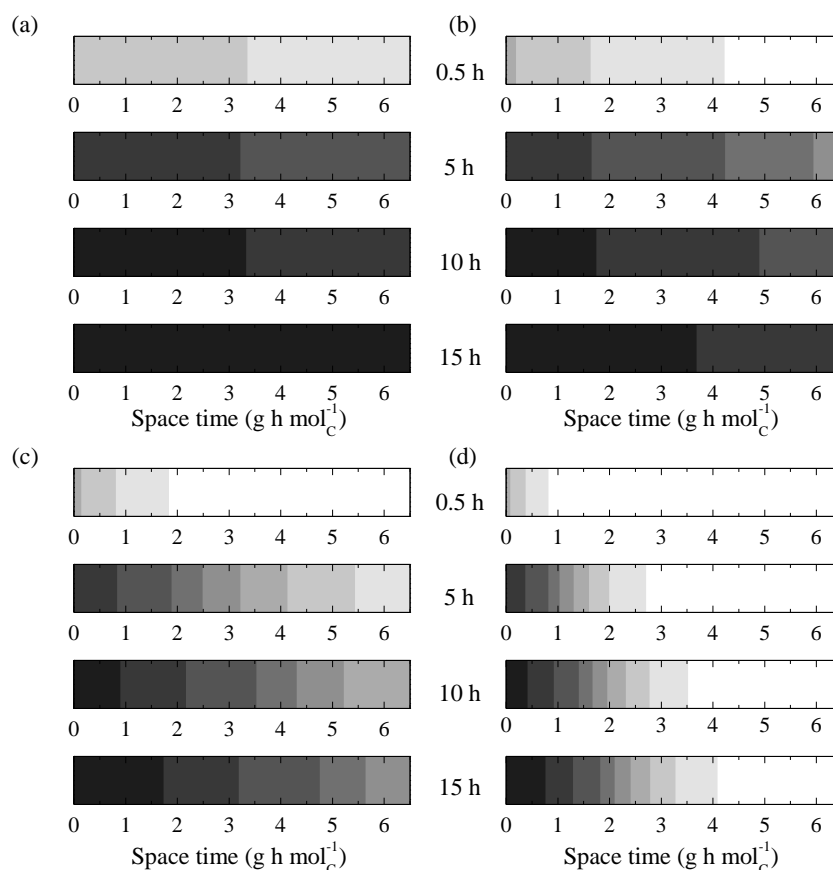


Fig. 5.11. Evolution with time of the simulated contour maps with space time of the activity of the CZ140 catalyst at (a) 325 °C, (b) 350 °C, (c) 375 °C and (d) 400 °C. Color map from $a = 0.3$ (black) to $a = 1$ (white).

our hypothesis. As observed, a tends to reach a value of 0 after the catalyst is submitted to the reaction medium certain time. Activity drop is also predicted much faster with this catalyst, which is in accordance with the results observed in this Chapter and with the coke analyses studied in Section 3.3. Both total content of coke and the content of coke fraction C_3 were found higher in the more acid CZ15 catalyst. This fraction was attributed to the one deposited within the zeolite crystals and with this result, we can prove that it causes a fast and severe activity loss. Comparing the results for the same τ value, higher a is always observed at higher temperature, which also confirms the evolution with time of the reaction zone and the catalyst deactivation explained for the less acid CZ140 catalyst. Also note that the activity parameter is a function of the initial reaction rate, which varies depending on the temperature.

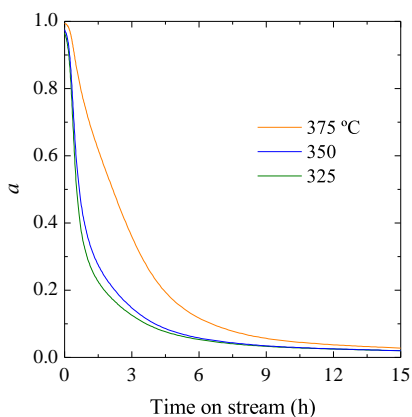


Fig. 5.12. Effect of temperature on the evolution with time of the activity of the CZ15 catalyst at the outlet of the reactor. $\tau = 2.0 \text{ g h mol}^{-1}$.

Chapter 6

Simulation of reactors with catalyst circulation for DTO process

This Chapter deals with the design of reactors with catalyst circulation and the reactor-regenerator system for the DTO process. The computation methodology and kinetic expressions are detailed in the previous Chapters. Here, the adaptation of the convection-dispersion-reaction equation for modeling different reactor configurations (moving and fluidized bed reactors) is explained. A model of parallel compartments developed in-house is introduced for the consideration of the residence time distribution of the catalyst particles in a given fluidized bed reactor. A fluidized bed regenerator is also designed considering a reactivation kinetic model. The dual reactor-regenerator system consists of two coupled fluidized bed units. In this case, the population balance theory is used for taking the activity distribution function of the catalyst into account. Part of the results in this Chapter have been published in *Chem. Eng. J.* **2020**, *379*, 122260.

6.1 Model of reactors with catalyst circulation

The simulation of the reactor for catalytic processes with complex reaction networks and deactivation requires a matrix methodology for solving the general convection-dispersion-reaction equation. This is in-depth explained in Section 4.3 for the *n*-pentane catalytic cracking in a packed bed reactor. However, different reactor configurations, including those with particle circulation, can be simulated with an adaptation of the general equation. The methodology developed in this Chapter is mainly focused on the rigorous consideration of deactivation in the simulation of the reactors. For this reason, isobaric and isothermal conditions are considered, and simple gas and solid flow models are used. The main requirement for this approach is the suitable definition of the catalyst activity, computed by taking the *past history* of the catalyst into account as detailed in Section 4.2 [130, 268].

The tools introduced herein are the conservation equation for the available active sites, an original parallel compartment (PC) model and the population balance (PB) theory. The PC model allows the consideration of the residence time distribution of the catalyst particles (RTD) in a fluidized bed reactor. The activity distribution function of a catalyst stream (f_a) circulating in a dual reactor-regenerator system can be simulated by applying the combined PB-PC model, hence considering the RTD and f_a . The methodology is used with the kinetic models for the DTO process computed in Chapter 5. Because of the lower deactivation of the HZSM-5 zeolite than that of SAPO-34, a moving bed reactor is also studied as an alternative to the fluidized bed reactor for the DTO process.

6.1.1 Conservation equation for the activity

Activity is a dimensionless property of the catalyst, and is assumed to be associated with the fraction of available active sites in this approach. A balance of activity/active sites in a moving catalytic bed has the following expression that relates the deactivation rate (r_d) and the convection-dispersion terms, characteristic of the catalyst movement,

$$\frac{da}{dt} = -\frac{d}{dz} \left[v_{cat}a - D_{cat} \frac{da}{dz} \right] - r_d, \quad (6.1)$$

defined for a time value $t > 0$ and a longitudinal position $0 < z < L$, where v_{cat} is the linear velocity of the catalyst particles and D_{cat} is the dispersion coefficient associated with the particle movement.

This is just an adaptation of the equation (4.12) in which

$$\Phi_0 = 1, \quad \Phi_I = 1, \quad \Phi_{II} = -1 \quad (6.2)$$

and both the linear velocity and dispersion coefficient are associated with the particles.

This mathematical tool allows a computationally fast and understandable approach to describe the solid regime in different reactor configurations without assuming excessively high errors. Hence, the ratio between the convection and dispersion contribution gives the reactor configuration to be simulated. The Bodenstein number (Bo) is the counterpart of Pe number for the solid phase, and is defined as

$$Bo = \frac{v_{cat}L}{D_{cat}}. \quad (6.3)$$

This parameter quantifies the contribution of the convective and dispersive transport of a particle in a catalytic bed of length L [225]. Thus, ideal regimes of plug flow and complete mixing are respectively reached when $Bo \rightarrow \infty$ and $Bo \rightarrow 0$. High values of Bo ($> 10^3$) mean negligible dispersion of the activity and thus correspond to regimes with package catalyst particles. Otherwise, low values of Bo ($< 10^{-5}$) indicate an almost uniform activity along the catalytic bed, characteristic of fluidized bed regimes. Therefore, this is the crucial parameter for defining the solid regime. Table 6.1 summarizes the values of v_{cat} and D_{cat} , which define the convection and dispersion terms of equation (6.1). The studied reactor

Table 6.1. Definition of the convection and dispersion terms in equation (6.1) for the different reactor configurations.

Convection term	Dispersion term
<i>Packed bed reactor (PBR)</i>	
$v_{cat} = 0$	$D_{cat} = 0$
<i>Moving bed reactor (MBR)</i>	
$v_{cat} = \pm \frac{L}{\tau_m}$	$D_{cat} = 0$
<i>Non-circulating fluidized bed reactor (NCFBR)</i>	
$v_{cat} \rightarrow 0$	$D_{cat} \rightarrow \infty$
<i>Circulating fluidized bed reactor (CFBR)</i>	
$v_{cat} = \frac{q_{cat}}{S}$	$D_{cat} \rightarrow \infty$

configurations are schematized in Figure 6.1. These considerations for the simulation of reactors with deactivation can also be applied to the design of a regenerator, using the reactivation kinetics in such cases.

Packed bed reactor

The packed bed reactor (PBR) is the most elementary and easy to handle configuration of Figure 6.1. For this reason, it is the main configuration operated at laboratory scale in order to collect experimental data and compute kinetic models, as the ones presented herein. The catalyst particles are packaged (Figure 6.1a) and then, v_{cat} and D_{cat} are null (Table 6.1). The convection-dispersion-reaction equation for the activity is reduced to the source term, obtaining the simplification in equation (4.10).

Moving reactor

Moving bed reactors (MBR, Figure 6.1b) are suitable in cases in which the production is required constant but the catalyst deactivation is relatively fast. The MTO/DTO process using HZSM-5 zeolites could be considered as example, because deactivation is slower than that registered with SAPO-34 catalysts [269]. An ideal non-dispersive movement of catalyst particles is assumed in order to describe the moving bed regime (plug flow model). For a given reactor section (S) and assuming constant the bed density (ρ), the linear velocity of the catalyst (v_{cat}) can be defined as a function of the mean residence time (τ_m) of a particle in the

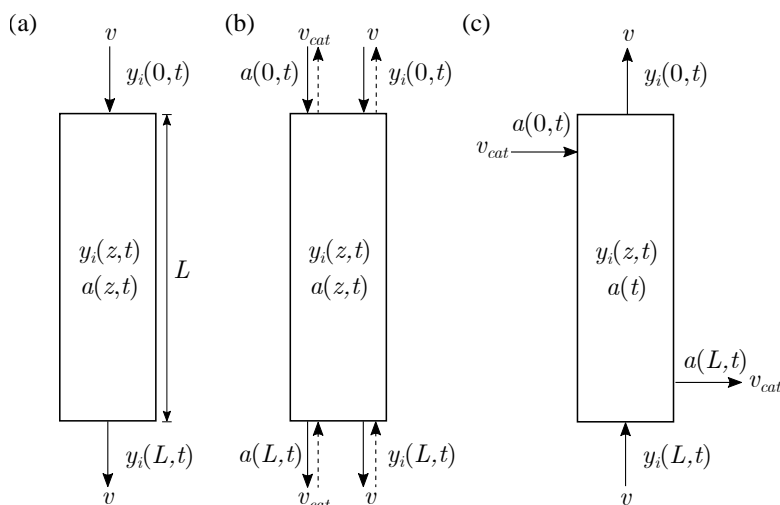


Fig. 6.1. Simplified diagram of the (a) packed bed, (b) moving bed and (c) fluidized bed reactor configurations.

catalytic bed (Table 6.1). In this case, two different contact regimes must also be differentiated depending on the direction of the gas and solid flows: co-current and counter-current. This determines the positive or negative value of v_{cat} indicated in Table 6.1. As examples of this reactor configuration, the riser of a FCC unit corresponds to the particular case of co-current MBR in which gas and solid flows have equal and very low residence time (< 5 s), whereas downer reactors present a descending solid flow and allow operating with co-current (descending) or counter-current (ascending) gas flow [270, 271]. The simulation of the MBR can be more complex in the specific case of fed catalyst regenerated in a fluidized bed combustor. In this case, an activity distribution function at the entrance of the reactor must be considered.

Fluidized bed reactor

The main advantage of fluidized bed reactors (Figure 6.1c) is the easier way to obtain isothermal conditions than that of other configurations. Moreover, the particle movement enables the catalyst particles to circulate continuously (if desired) in order to ensure steady yields if the catalyst is regenerated. A uniform activity in the whole bed should be taken into account for the reactor design according to the ideal random movement of particles [184]. This means a Bo value so low as the dispersion of the catalyst activity would tend to very high values (Table 6.1). Two kinds of fluidized bed reactors must be differentiated depending on the catalyst particles circulation: non-circulating and circulating fluidized bed reactors (NCFBR and CFBR, respectively). Based on that, v_{cat} is negligible in the case of NCFBR.

In contrast to the behavior of a MBR, in which all particles in the bed are moved according to a plug flow model, the design of a CFBR is conditioned by the existence of a residence time distribution (RTD) of catalyst particles associated with the complete mixing of solids in a bubbling fluidized bed [224, 227]. Hence, catalyst deactivation would lead to an activity distribution that must be taken into account. This RTD profile is given by the \mathbf{E} curve and can be expressed as a function of the evolution with time of the activity [231, 232]

$$f_a = \frac{\mathbf{E}}{\frac{da}{dt}}, \quad (6.4)$$

being f_a defined as the activity distribution function.

The rigorous consideration of the RTD and f_a in the design of CFBRs is relatively easy when simple kinetic networks and deactivation equations are considered. The best examples can be found in the fundamental literature of chemical reactor

design reported by Levenspiel [185] or Fogler [186]. However, two major considerations mainly related to computational limitations must be dealt with, when the integration of simple derivatives is not allowed: (i) the complexity of the reaction network with multiple steps, whose kinetics are described by concentration-dependent equations, and; (ii) feeding the reactor with catalyst particles that have an activity distribution function derived from its regeneration in a fluidized bed regenerator. These considerations lead to the following calculation hindrances:

- The presence of an activity distribution function means the existence of different groups of particles with different activity for each value of time t and longitudinal position z . Considering the method used up to now, the implementation allows the consideration of a vector of activity \mathbf{a}_j previously defined, whose precision can be increased ($j >$ number of steps of the reaction network) to more accurately reproduce the f_a curve [269]. Then, a discretization of an activity vector is required.
- Each of this group of particles with activity a at time t in a position z can spend a determined time in the catalytic bed according to the RTD. This means that equation (6.4) must be taken into account for each of the group of particles already discretized. The easiest solution should be a new discretization of the RTD, that is, the \mathbf{E} curve.

Let n_1 and n_2 be the number of discretizations of an activity vector and the \mathbf{E} curve, respectively. Then, equation (4.12) must be solved $n_1 \times n_2$ times for a number of variables $n_l + n_1$, being n_l the number of lumps. For an easy reaction scheme of the MTO process, the number of discretizations required for obtaining reliable simulations turned out to be 100 for the activity and 50 for the \mathbf{E} curve [269]. In this case, $5 \cdot 10^3$ evaluations of a system of $100 + n_l$ equations would be necessary in each iteration. However, this method can only support uniform values of activity ($a = 1$) at the entrance of the reactor, avoiding the case study of a reactor-regenerator system (assuming a fluidized bed regenerator). A more accurate approach is required for this complex mathematical system. Our proposal is the integration of a model of parallel compartments developed in-house and the population balance theory into the already developed system of equations.

6.1.2 Parallel compartment (PC) model

The circulation of catalyst particles in a fluidized bed reactor makes the problem more difficult mathematically and more computationally expensive. The presented model proposes an original approach to consider the residence time distribution (RTD) of particles based on a system of parallel compartments with catalyst circulation (Figure 6.2), all of them in a fluidized regime. For accomplishing that,

a discretization of the \mathbf{E} curve is carried out by dividing the catalyst particles in groups with the same residence time.

Thereby, let n_r be the number of particle groups and let τ_r be the residence time of each r group. Then, the \mathbf{E} curve for a complete mixed solid can be discretized considering the cumulative \mathbf{F} curve as illustrated in the Figure 6.3. The CFBR is described by the n_r parallel compartments depicted in Figure 6.2. Note that the section of each compartment (S_r) is different, as well as the relative velocity between gas and solid, being constant the gas linear velocity (v) and the catalyst flow rate in each r compartment ($q_{cat,r}$), defined as

$$q_{cat,r} = \frac{q_{cat}}{n_r} = v_{cat,r} S_r, \tag{6.5}$$

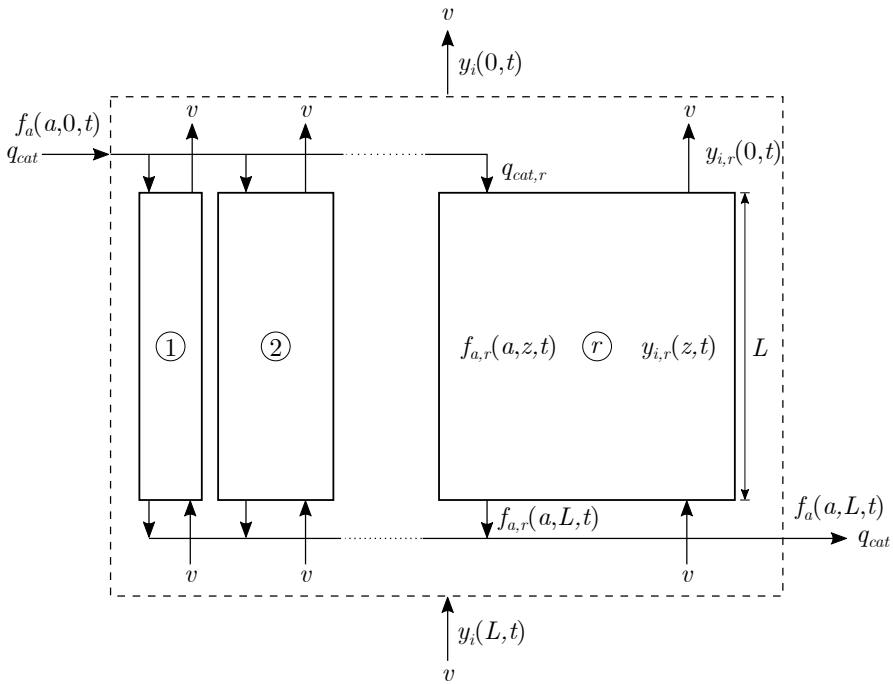


Fig. 6.2. Parallel compartment model for describing a circulating fluidized bed reactor.

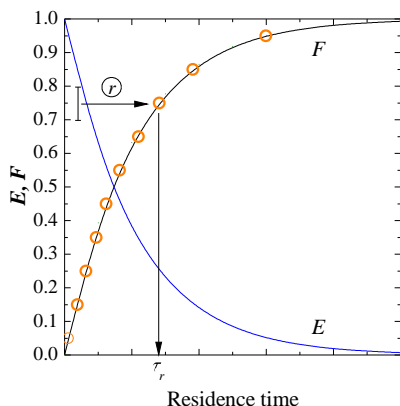


Fig. 6.3. Distribution of the catalyst particles in each compartment based on the E and cumulative F curves for a complete mixed solid in a CFBR.

where q_{cat} is the total catalyst flow rate, $v_{cat,r}$ is the linear velocity of each r group of catalyst particles and S_r fulfills

$$S = \sum_{r=1}^{n_r} S_r. \quad (6.6)$$

The conservation equation of each i lump in each r compartment is defined by the equation (4.3) previously introduced in Section 4.2, and can be rewritten as a function of n_r

$$\varepsilon \frac{\partial \mathbf{y}_{i,r}}{\partial t} = -\frac{\partial}{\partial z} \left[v \mathbf{y}_{i,r} - D \frac{\partial \mathbf{y}_{i,r}}{\partial z} \right] + \frac{RT}{PN_C} \rho \mathbf{r}_{i,r}, \quad (6.7)$$

defined for $i = 1, \dots, n_l$ and $r = 1, \dots, n_r$, where $\mathbf{y}_{i,r}$ and $\mathbf{r}_{i,r}$ are respectively the vectors of molar fractions and formation rates of each i lump in each r compartment. The latter is calculated according to equation (4.7) considering the partial pressure profiles of the reactant and products in each r compartment. For calculating the molar fraction $\mathbf{y}_i(0, t)$ at the outlet of the reactor (see Figure 6.2), the number and size of compartments must be taken into account. Then, the molar fractions are recalculated following the mass balance in all the compartments, with

$$F_r = \frac{vP}{RT} S_r \quad (6.8)$$

and

$$F = \frac{vP}{RT}S = \frac{vP}{RT} \sum_{r=1}^{n_r} S_r, \quad (6.9)$$

where F and F_r are the total molar flow rate and the molar flow rate in each r compartment, respectively.

6.1.3 Integration of the population balance (PB) theory

The design of each unit of a dual reactor-regenerator system, using the PC model for fluidized bed reactors, requires considering the evolution of each population of particles with a given activity. In these cases, the fed catalyst in each unit presents an activity distribution function, derived from the RTD in the other one. Although several works were reported on this modeling problem [230–232], the consideration of the RTD and f_a is not trivial. The population balance theory offers an accurate and rigorous tool for calculating the evolution with time of the activity distribution function in each unit [231].

Let $f_{a,r}(a, z, t)$ be the mass density of the catalyst particles of each population with a activity (also known as the activity distribution function) in each r compartment of the diagram in Figure 6.2. Then, the general convection-dispersion-reaction equation for a compartment can be rewritten as

$$\frac{\partial f_{a,r}}{\partial t} = -\frac{\partial}{\partial z} \left[v_{cat,r} f_{a,r} - D_{cat} \frac{\partial f_{a,r}}{\partial z} \right] + \frac{\partial (f_{a,r} r_{a,r})}{\partial a}, \quad (6.10)$$

defined for $t > 0$, $0 < z < L$, $0 < a < 1$ and $r = 1, \dots, n_r$, where $r_{a,r}$ is the rate of activity change with time in each r compartment.

The form of the equation (6.10) is similar to the above presented equation (6.1). The main modification is the inclusion of the activity (a) as a third independent variable due to the dependency of f_a on a . This solves one of the hindrances defined as a discretization of a vector a is no longer required. The complexity of adding a third independent variable cannot be by far compared with the computational requirement attained to the sequenced resolution of equation (6.1) for each discretization of the vector \mathbf{a}_j .

The population balance-based equation considers a standard rate of activity change $r_{a,r}$ related to each of the activity populations. The calculation of this $r_{a,r}$ varies depending on the simulated unit, reactor or regenerator. Likewise, the computation of the equation slightly changes.

Reactor unit

In a reactor unit, $r_{a,r}$ takes the value of the deactivation rate,

$$r_{a,r} = \frac{da}{dt} = -r_d \quad (6.11)$$

Solving the equation (6.10) requires initial and boundary conditions, in this case respect to z and a . Assuming that the activity distribution function at $t = 0$ (f_{a0}) is known, and considering Robin and Neumann boundary conditions for z

$$f_{a,r}(a, z, 0) = f_{a0} \quad (6.12)$$

$$-v_{cat,r}[f_{a,r}(a, 0, t) - f_{a0}] + \frac{\partial}{\partial z} f_{a,r}(a, 0, t) = 0 \quad (6.13)$$

$$\frac{\partial}{\partial z} f_{a,r}(a, L, t) = 0. \quad (6.14)$$

The boundary conditions with respect to a in the reactor unit are

$$r_d(0, z, t) = 0 \quad (6.15)$$

$$f_{a,r}(1, z, t) = 0. \quad (6.16)$$

The calculation of the formation rates of each i lump ($\mathbf{r}_{i,r}$) requires obtaining an activity value for the computation of $\mathbf{r}_{j,r}$ using equations (4.7) and (4.9). However, the consideration of the population balance, which converts a into an additional independent variable, makes necessary the use of an auxiliary activity for the calculations in each t time, computed as the average activity at a given t time

$$\bar{a}_r = \int_0^1 a f_{a,r} da. \quad (6.17)$$

Solving the population balance theory-based equations in each r compartment also requires accounting for the consistency of the total number of particles, represented by each population. This is included in the mathematical method with the following restriction

$$\int_0^1 f_{a,r} da = 1. \quad (6.18)$$

Once solved the system of partial differential equations in each compartment, the activity distribution function at the outlet of the reactor ($f_a(a, L, t)$) in Figure

6.2) is calculated considering the particle balance in equation (6.5)

$$f_a(a, L, t) = \frac{\sum_{r=1}^{n_r} q_{cat,r} f_{a,r}(a, L, t)}{q_{cat}}. \quad (6.19)$$

Equations (6.7) and (6.10) can be solved simultaneously in order to calculate f_a in each time step. Note that the computed f_a value is the same at any given longitudinal position z of the reactor in our approach because of the consideration of the complete mixing regime, thus fulfilling

$$f_a(a, z, t) = f_a(a, L, t). \quad (6.20)$$

Regenerator unit

In the regenerator unit, $r_{a,r}$ is the reactivation rate (r_r) during the coke combustion. A potential expression similar to those previously reported [230, 231] is used

$$r_{a,r} = \frac{da}{dt} = r_r = k_r(1-a)^m, \quad (6.21)$$

where k_r is the reactivation kinetic constant and m is the reactivation order. These two parameters are fitted to the experimental results of activity recovery at several combustion time values.

The same initial and boundary conditions with respect to z are used (equations (6.12), (6.13) and (6.14)), whereas the boundary conditions with respect to a are redefined, considering the reactivation

$$f_{a,r}(0, z, t) = 0 \quad (6.22)$$

$$r_r(1, z, t) = 0. \quad (6.23)$$

The boundary conditions of the deactivation and reactivation rates (equations (6.15) and (6.23), respectively) are given by each corresponding expressions of equations (6.11) and (6.21). And regarding the set of four boundary conditions with respect to a , particles with $a = 0$ and $a = 1$ cannot be respectively deactivated or reactivated. These conditions not only allow the resolution of the equation (6.10), but also stabilize the resolution method.

Dual reactor-regenerator system

Once described a CFBR by the PB-PC model, modeling the reactor-regenerator system consists of considering a continuous catalyst flow rate circulating between both units. With this aim, the two independent models of CFBR depicted in Figure 6.4 are simultaneously solved.

Assume that the reactor is described by a catalytic bed length L , a section S

and r parallel compartments. Also assume that the regenerator is described by a catalytic bed length L' , a section S' and r' parallel compartments. Then, the catalyst flow rate (q_{cat}) is the same in both units and the catalyst exiting the reactor with an activity distribution function f_a is fed into the regenerator with an activity distribution function f'_a and vice versa, fulfilling

$$f_a(a, 0, t) = f'_a(a, L', t) \tag{6.24}$$

and

$$f'_a(a, 0, t) = f_a(a, L, t). \tag{6.25}$$

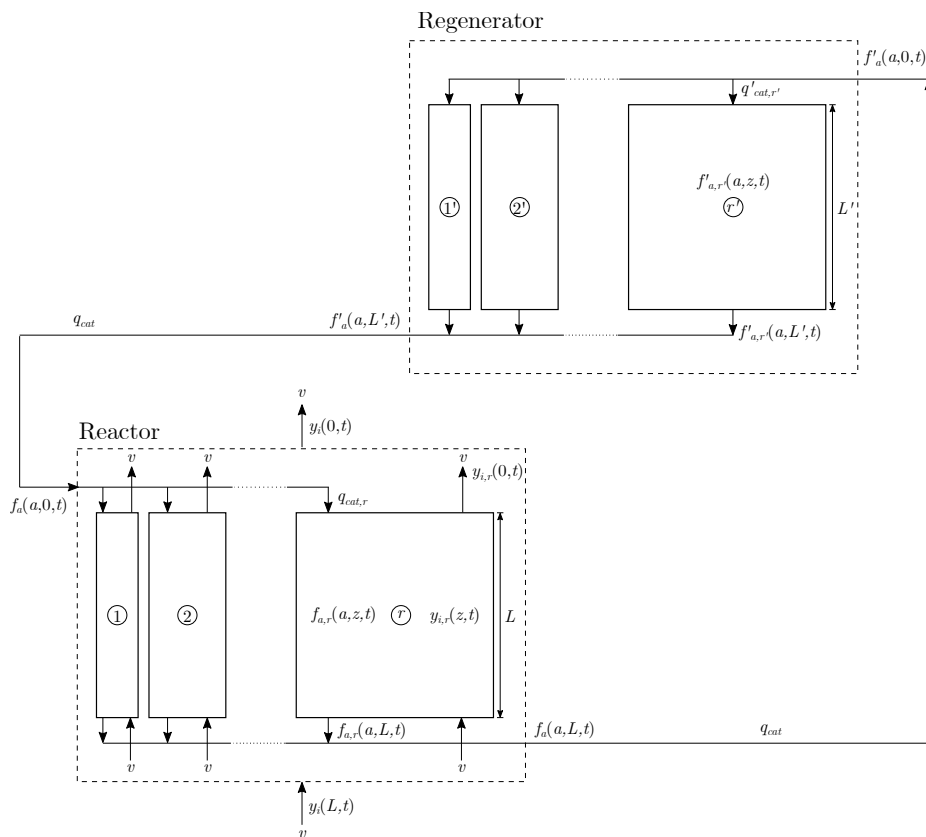


Fig. 6.4. Diagram of a circulating fluidized bed reactor-regenerator system based on the PB-PC model.

6.2 Moving bed reactor

As above introduced, the packed bed reactor (PBR) configuration is the one used for most of experimental setups at laboratory scale. This is our case and therefore, the simulation of the PBR coincides with the lines depicted in the figures of the previous Chapter 5. The product distribution obtained for the CZ140 catalyst and the initial activity profiles with the space time calculated for different temperatures are respectively shown in Figures 5.4 and 5.11. Moreover, the evolution with time of the reaction medium composition and of the activity at the outlet of the reactor are shown in Figures 5.5 and 5.10, respectively.

Similar to the results of PBR, the design equations for a moving bed reactor (MBR) provide longitudinal profiles of activity and conversion and their evolution with time. The simulations were carried out assuming the same reactor size that the PBR used for collecting the experimental data. Then, an effective catalytic bed length of 10 cm and diameter of 1 cm was considered. This allows us to simulate the simple addition of a solid valve to the used reactor, providing a continuous catalyst flow. The main goal is to compare the simulation results in a setup as similar as possible to that available.

Due to the catalyst circulation, the model predicts an initial unsteady state in which the reaction evolves until reaching an operational steady state. After this point, a constant activity longitudinal profile over time can be observed in the reactor. This profile, the conversion and product distribution depend on the reaction conditions. The MBR also allows two different contact regimes to be simulated: co-current and counter-current flows, as displayed in Figure 6.1b. Each configuration is referred to the relative gas/solid flows direction. The two different feeding possibilities would also have a significant impact on the activity profiles and simulation results. A crucial parameter for designing the MBR is the residence time of the catalyst (τ_m), defined as the time that a particle spends inside the catalytic bed and controlled by the catalyst mass flow rate.

6.2.1 Unsteady state

The simulations consider that a gas with the feed composition is initially in contact with a catalytic bed of $a = 1$. From this time, the reaction starts and both gas and catalyst begin moving with each corresponding flow rate. The evolution with time of the activity of the CZ140 catalyst and of the molar fractions of products is shown in Figure 6.5 for four different reaction conditions.

Considering negligible the dispersive transport of the catalyst in any case ($Bo \rightarrow \infty$), two different τ_m values (1 and 10 h) and different reaction conditions were simulated in a co-current MBR. The steady state is reached at different values

of time mostly depending on τ_m , and afterwards the results are constant. Thus, it takes ca. 2 and 15 h for values of τ_m of 1 (Figures 6.5a and 6.5c) and 10 h, respectively (Figures 6.5b and 6.5d). This corresponds to more or less 2 times the value of τ_m .

An increase in τ_m also leads to more severe drops of the activity at the outlet of the reactor. Values above 0.8 are observed for $\tau_m = 1$ h (Figures 6.5a and 6.5c),

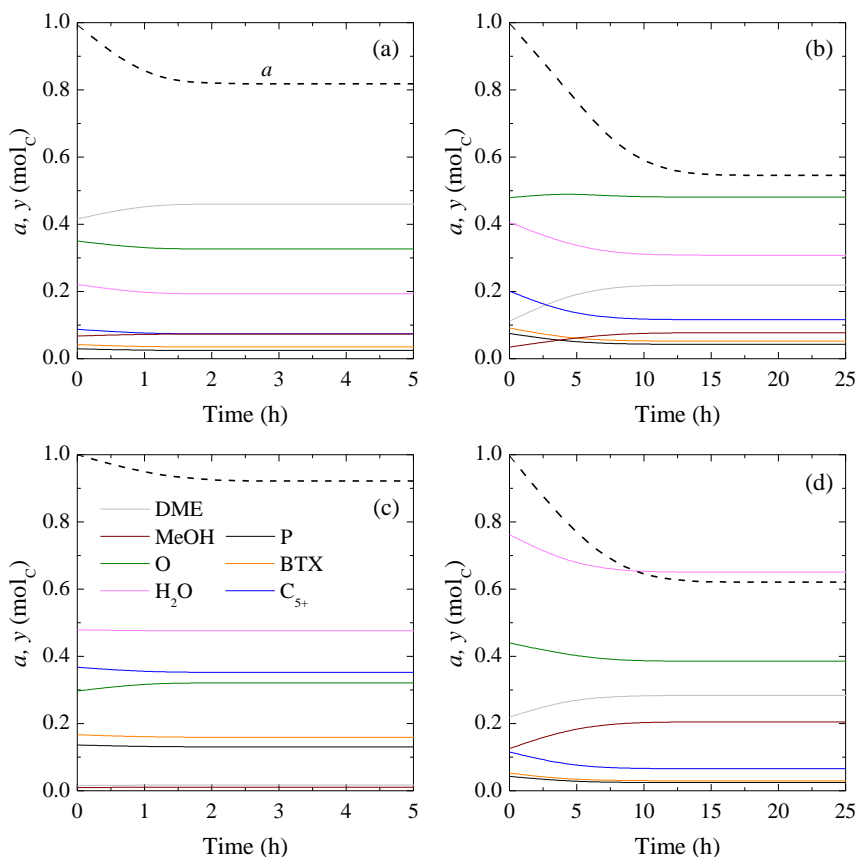


Fig. 6.5. Evolution with time of the activity of the CZ140 catalyst (dashed line) and the molar fractions (solid lines) in a co-current MBR using: (a) 375 °C, $\tau = 1.5$ g h mol_C⁻¹, DME:W = 1:0 and $\tau_m = 1$ h; (b) 400 °C, $\tau = 1.5$ g h mol_C⁻¹, DME:W = 1:0 and $\tau_m = 10$ h; (c) 400 °C, $\tau = 3.0$ g h mol_C⁻¹, DME:W = 1:0 and $\tau_m = 1$ h; (d) 400 °C, $\tau = 3.0$ g h mol_C⁻¹, DME:W = 1:1 and $\tau_m = 10$ h.

whereas values below 0.65 are shown with $\tau_m = 10$ h (Figures 6.5b and 6.5d). In terms of product distribution, clearly differentiated results are obtained depending on the reaction conditions. Low conversions with maximum selectivity to olefins can be achieved at the outlet of the reactor using low values of temperature, τ and τ_m (Figure 6.5a). Increasing τ_m and temperature, the conversion into olefins can be boosted (Figure 6.5b), which also leads to an increase in the amount of water and C₅₊ hydrocarbons as main byproducts. Otherwise, increasing space time with $\tau_m = 1$ h allows full conversion to be reached (Figure 6.5c). This situation promotes a higher extent of the reaction network, with C₅₊ hydrocarbons being the main obtained product. And this can be totally inhibited by co-feeding water with DME (Figure 6.5d). The presence of higher amount of water (ca. 0.8 mol mol_C⁻¹ at $t = 0$) increases the concentration of methanol, as DME hydration is favored, as well as the selective production of olefins.

6.2.2 Effect of process variables

According to the simulations, the reactor should perform stable after the required time for achieving the steady state. Then, the effect of the process variables on the activity longitudinal profiles and yields of products can be evaluated. Figures 6.6a and 6.6b display the steady-state activity profile and yields of products at the outlet of the reactor, respectively. Maximum activity values are observed at $z = 0$ as the catalyst is fed at the entrance of the reactor.

Similar to the performance of the PBR (Figure 5.11), an increase in the temperature leads to slightly higher values of the activity at high values of z (Figure 6.6a). This was attributed to the narrower reaction zone increasing temperature [103], but also to the higher presence of water that attenuates catalyst deactivation according to equation (5.5). Indeed, co-feeding water with a DME:W of 1:1 leads to a softer activity profile with higher a values. This result suggests that the reaction zone is widened with the presence of water in the reaction medium, which is in accordance with the as well attenuated reaction rates (equation (5.3)). Moreover, the model for the MBR predicts that catalyst deactivation is more remarkable upon increasing τ_m . Nevertheless, the effect of temperature and co-feeding water are quite similar for both τ_m values.

In general terms, higher conversions at the outlet of the reactor ($z = L$) are predicted for $\tau_m = 1$ h than those for $\tau_m = 10$ h (Figure 6.6b). Note that the conversion (X) can be defined as the sum of the yields of products (Y), being negligible the yields of CH₄ and CO_x. A significant increase in the conversion is observed upon increasing temperature. And the decay of the conversion when water is co-fed is even more pronounced. In all cases, olefins are the main products

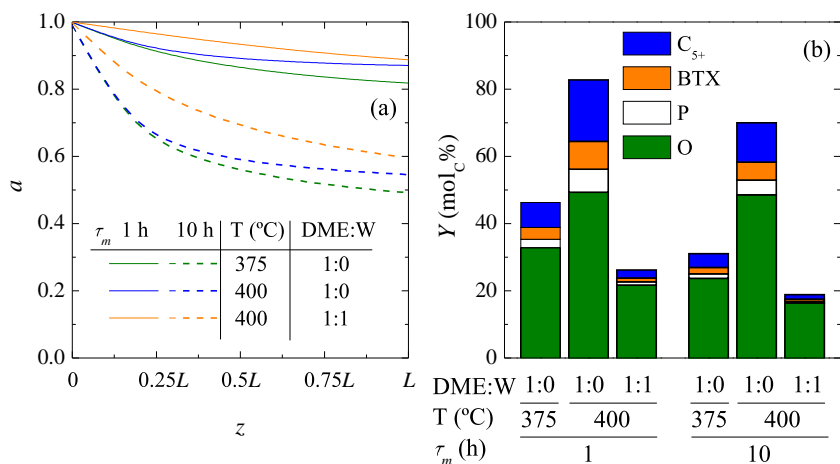


Fig. 6.6. Effect of temperature, DME:W ratio and τ_m on (a) the steady-state activity profile of the CZ140 catalyst and (b) the yields of products at the outlet of the reactor. $\tau = 1.5 \text{ g h mol}_C^{-1}$.

and, as we discussed in details in Section 3.2, the formation of byproducts is promoted at higher values of conversion (400 °C and DME:W = 1:0). A yield of C_{5+} hydrocarbons of ca. 20% is obtained at these conditions using $\tau_m = 1 \text{ h}$.

6.2.3 Effect of contact regime

MBR offers the possibility of changing the direction of gas and solid flows (Figure 6.1b). This causes interesting modifications of the reactor performance. Once reached the steady state, the activity profiles (Figures 6.7a and 6.7b) and the yields of products (Figures 6.7c and 6.7d) at $\tau_m = 1$ and 10 h of both configurations are compared. Note that the fresh catalyst is fed at $z = L$ in a counter-current MBR, which explains the opposite evolution with z of the activity.

In the case of a concentration-independent deactivation equation, where a is not a function of the partial pressure of any component of the reaction medium, these profiles should be symmetric and the intersection point should coincide with $z = 0.5L$. The gray lines in Figures 6.7a and 6.7b indicate this point of the reactor. This is not our case and a strong influence of the direction of gas and solid flows is observed. Regarding the simulations without co-feeding water (DME:W = 1:0), a more pronounced deactivation is observed in the co-current MBR near $z = 0$,

which is attenuated along z . This leads to slightly higher values of yields of products at $z = L$ (Figures 6.7c and 6.7d) for the counter-current MBR. Nevertheless, the obtained yields are very similar, which is accentuated in the case of $\tau_m = 1$ h, with $a > 0.8$ at any condition and reactor longitudinal position (Figure 6.7a).

The effect of deactivation is more severe at $\tau_m = 10$ h, so this performance of the catalytic bed is easily noted (Figure 6.7b). These simulations are in accordance

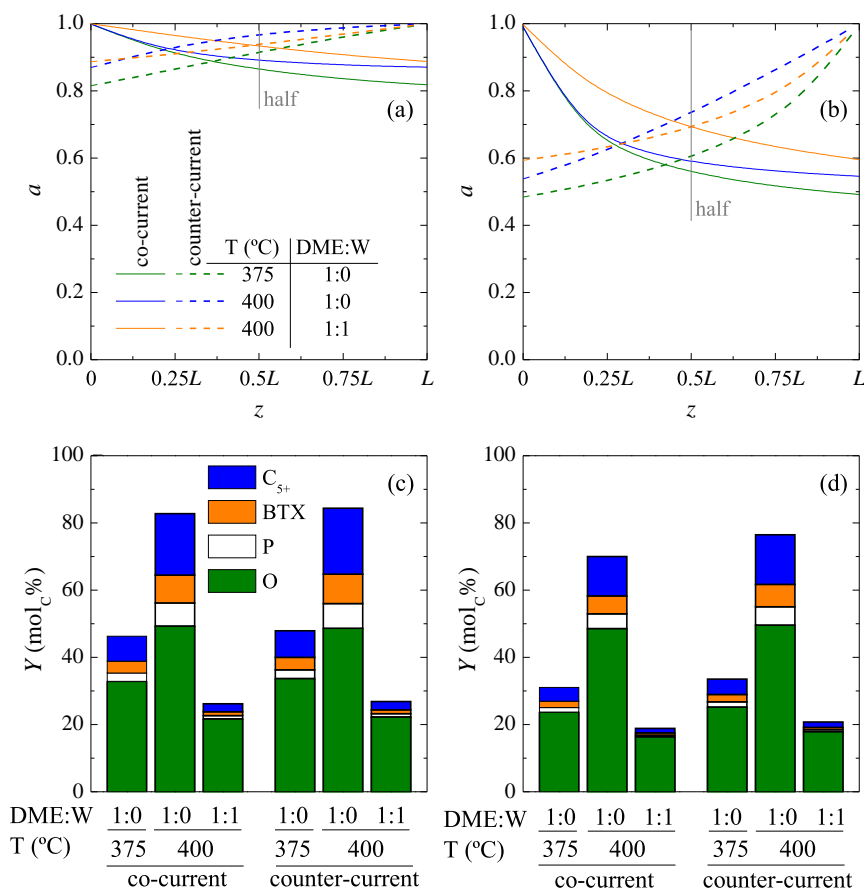


Fig. 6.7. Effect of MBR contact regime, co-current (solid lines) and counter-current (dashed lines), on the steady-state (a, b) activity profile of the CZ140 catalyst with the space time and (c, d) yields of products using (a, c) $\tau_m = 1$ h and (b, d) $\tau_m = 10$ h. $\tau = 1.5$ g h mol_C⁻¹.

with the extent of the reaction zones discussed in Section 5.3. Feeding DME and fresh catalyst at $z = 0$ generates a narrower reaction zone that results in a faster deactivation at $z < 0.5L$. In contrast, the counter-current configuration allows the catalyst to be fed in the reactor zone with lower concentration of DME and methanol. Hence, a slower deactivation must be observed at $z > 0.5L$ according to the definition of the equation (5.9).

Again, water plays an important role in the process and the inhibition of both, reaction and deactivation rates, tends to equalize the activity profiles in both cases. Independently on the τ_m value, the steady-state activity profiles are almost symmetric when a DME:W ratio of 1:1 is fed into the reactor (see the orange lines in Figures 6.7a and 6.7b). High water concentration gives relevance to the denominator of equations (5.4) and (5.6), which approaches reaction and deactivation rates to concentration-independent equations. As a consequence, almost the same conversion and yields of products are predicted using both contact regimes in the steady state.

6.3 Fluidized bed reactor

Simulations of the circulating fluidized bed reactor (CFBR) for the DTO process were carried out in order to illustrate the PB-PC model methodology explained before, with the deactivation and reactivation equations presented in Section 6.1. The results for each unit working independently are explained in this Section (reactor) and the following Section (regenerator). Afterwards, using as a reference the results of each unit, a study of the dual reactor-regenerator system is detailed in Section 6.5. In all cases, the evolution with time of the variables during the calculation is shown.

From the simulations of the reactor, different results are studied. First, the predicted evolution with time of the activity distribution function, conversion and yields of products during the unsteady state is evaluated. In this study, different mean residence times of the catalyst (τ_m) and activity distribution functions at the entrance of the reactor ($f_a(a, 0, t)$) are tested. From these results, the required time for reaching the steady state is extracted. The effect of the operation conditions on the steady-state activity distribution function, conversion and yields of products is then analyzed. Different conditions are evaluated in all cases, such as the space time, temperature, DME-to-water (DME:W) ratio and τ_m . The performance of the CZ140 and CZ15 catalysts are also compared.

6.3.1 Unsteady state

The simulation of the unsteady state is required for predicting the reactor operation at the steady state (activity distribution function, conversion and yields of products). The results herein correspond to simulations in which the initial activity distribution function of the catalytic bed and concentration in the gas are assumed equal to those fed (same initial and left boundary condition)

$$f_a(a, z, 0) = f_{a0} = f_a(a, 0, t) \quad (6.26)$$

and

$$\mathbf{y}(z, 0) = \mathbf{y}_0 = \mathbf{y}(L, t). \quad (6.27)$$

Note that the reactants are fed at the longitudinal position $z = L$ in the diagram of Figure 6.2. The size of the modeled reactor corresponds to a fluidized bed reactor at laboratory scale previously reported for the MTO reaction [188], with a bed height of 25 cm and internal diameter of 2.54 cm. The gas velocity is increased with respect to that used in the PBR in order to operate in a complete fluidized regime (ca. 3 cm s⁻¹). This also implies an adjustment of the catalyst weight for maintaining a constant space time value.

Our consideration of the activity (a) as an independent variable instead of a dependent one avoids the pronounced effect of the discretization reported elsewhere for the CFBR design [269]. This is a significant improvement not only due to the reduction of the mathematical uncertainty, but also because a lower number of parallel compartment (n_r) can be used for describing the system (Figure 6.4). A value of $n_r = 10$ is systematically used, achieving reliable results and decreasing notably the computation time. Figures 6.8a and 6.8b show the evolution with time of the activity distribution function (f_a) for certain τ values using the CZ140 and CZ15 catalysts, respectively. The corresponding evolution with time of the conversion (X) and yields of products (Y_i) are depicted in Figures 6.8c and 6.8d. These results are predicted at 375 °C with DME:W = 1:0 and using $\tau_m = 5$ h. The catalyst flow rate indicated in Figure 6.2 is derived from the τ_m value and catalyst loading previously set with the space time. A normalized probability density function (PDF) is used for the activity distribution function at the entrance of the reactor ($f_a(a, 0, t)$). These functions reproduce the probability of a variable falling within a particular range, defined with mean and variance values. In this case, $f_a(a, 0, t)$ is centered at $a = 0.9$, reproducing the performance of a partially deactivated catalyst.

f_a evolves towards lower a values with time and its evolution depends on the catalyst. The CZ15 catalyst (Figure 6.8b) shows a faster and more severe deactivation than that of CZ140 catalyst. At any given time, f_a is displaced towards lower values of activity with the more acid CZ15 catalyst, which is consistent with the higher deactivation of this catalyst observed in Sections 3.3 and 5.2. The reactor unit reaches the steady state in all cases after ca. 25 h of operation with $\tau_m = 5$ h. Then, the displayed value of f_a after 25 h (brown line in Figures 6.8a and 6.8b) corresponds to the constant shape of f_a shown by the catalysts from this time on. At this point, the a range of the CZ140 and CZ15 catalysts are respectively $0.3 < a < 1$ (Figure 6.8a) and $0 < a < 1$ (Figure 6.8b). This behavior was expected regarding the evolution of the activity at the outlet of the PBR shown in Figures 5.10 and 5.12 for the CZ140 and CZ15 catalysts, respectively.

Similar conclusions can be deduced from the results of evolution with time of the conversion depicted in Figures 6.8c and 6.8d (dashed lines). The maximum is observed at the beginning of the reaction, when the activity of the catalyst is the highest. Subsequently, it decreases and tends to a constant value in the steady state. The conversion is influenced by τ , which is quite lower for the CZ15 catalyst (1.0 g h mol^{-1}). However, its tendency is a function of the evolution of f_a previously observed. CZ140 catalyst reaches a steady-state conversion near to the maximum. CZ15 catalyst undergoes a significant drop of the conversion from the maximum at ca. 71% to a steady-state value of ca. 29%. For both catalysts, the

steady-state values of conversion are achieved at shorter times than those observed for f_a . This suggests that the changes in f_a from these values of time can be neglected in terms of the gas phase performance. At the simulated conditions, olefins are the main products followed by C_{5+} hydrocarbons. Note that these reaction conditions were selected aiming for the highest production of olefins (see the PBR performance in Figures 5.4 and 5.6).

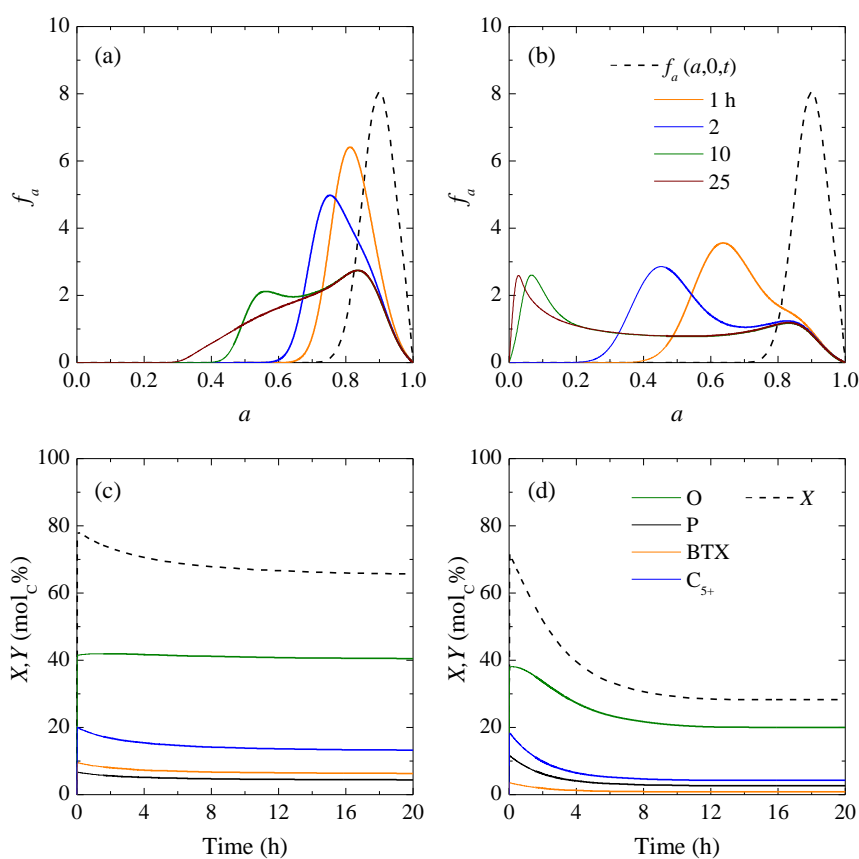


Fig. 6.8. Evolution with time of (a, b) the activity distribution function, (c, d) the conversion and yields of products for (a, c) the CZ140 catalyst using $\tau = 3.5 \text{ g h mol}_C^{-1}$, and (b, d) the CZ15 catalyst using $\tau = 1.0 \text{ g h mol}_C^{-1}$. $375 \text{ }^\circ\text{C}$, $\tau_m = 5 \text{ h}$, DME:W = 1:0.

Effect of the mean residence time of the catalyst

A key role in the evolution of the CFBR is played by τ_m . The time that the catalyst spends inside the reactor will determine the one required for reaching the steady state and hence, the steady-state values of f_a , conversion and yields of products. Figures 6.9a-c show the evolution with time of f_a at different conditions and Figure 6.9d displays the corresponding evolution with time of the conversion. The results in Figure 6.9a illustrates the situation in which τ_m is duplicated in comparison to

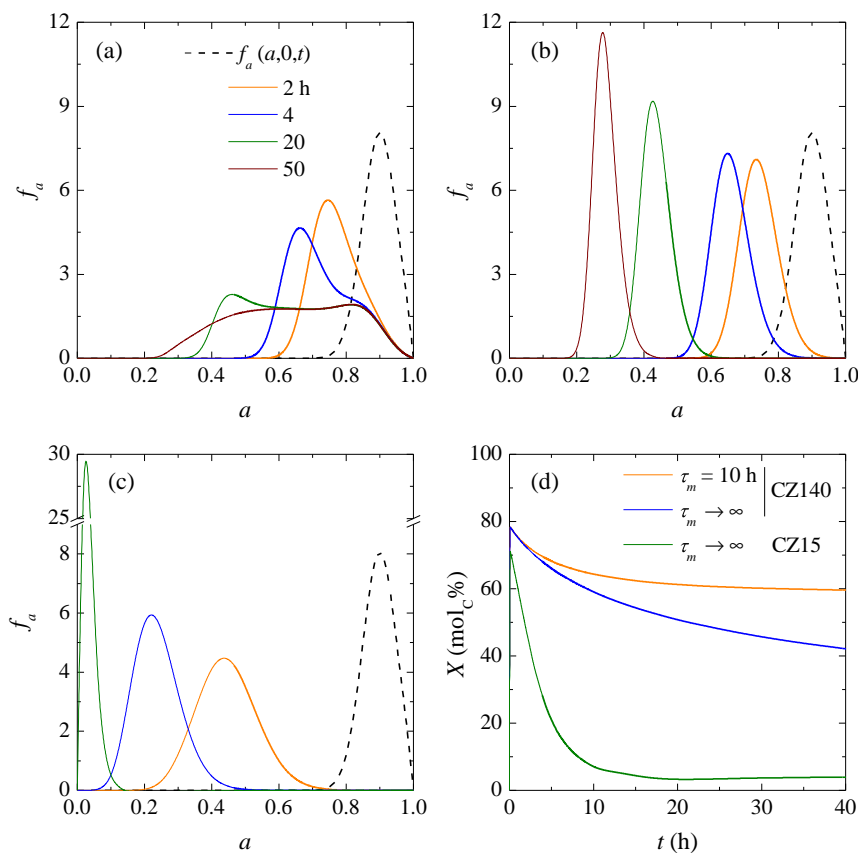


Fig. 6.9. Evolution with time of (a, b, c) the activity distribution function and (d) the conversion for the CZ140 catalyst using $\tau = 3.5 \text{ g h mol}^{-1}$ with (a) $\tau_m = 10 \text{ h}$ and (b) $\tau_m \rightarrow \infty$, and (c) the CZ15 catalyst using $\tau = 1.0 \text{ g h mol}^{-1}$ with $\tau_m \rightarrow \infty$. $375 \text{ }^\circ\text{C}$, DME:W = 1:0.

those in Figure 6.8a. Increasing τ_m from 5 to 10 h leads to a shift of f_a towards lower values of a , being the deactivation faster at higher values of τ_m . The steady-state f_a (after 50 h in the case of $\tau_m = 10$ h, Figure 6.9a) is displaced to a minimum value of $a = 0.25$. The distribution is wider in the a range than that of Figure 6.8a ($\tau_m = 5$ h), where a main maximum is observed near to that of $f_a(a, 0, t)$. This is explained by the contribution of the convection term in equation (6.10). With low τ_m values, v_{cat} is high enough compared to the source term, represented by the deactivation rate. In terms of reactor operation, this means that the catalyst particles do not spend enough time in the reactor in order to be significantly deactivated.

The deactivation kinetics of each catalyst has also an important influence on the reactor performance. Figures 6.9b and 6.9c show the results for the extreme case of $\tau_m \rightarrow \infty$ for the CZ140 and CZ15 catalysts, respectively. These simulations correspond to a non-circulating fluidized bed reactor (NCFBR with $v_{cat} \rightarrow 0$, see Table 6.1). In this configuration, f_a shifts towards lower a values and its shape becomes narrower upon increasing time. The role of deactivation kinetics is crucial here. CZ140 catalyst shows an asymptotic tendency to $a \rightarrow 0.3$ when $t \rightarrow \infty$ (Figure 6.9b). This result is in accordance with the activity evolution at the outlet of the PBR observed in Figure 5.10. Otherwise, CZ15 catalyst exhibits a trend towards $a \rightarrow 0$ when $t \rightarrow \infty$ (Figure 6.9c), consistent with that observed at the outlet of the PBR (Figure 5.12). These behaviors lead to pronounced differences in the evolution with time of the conversion (Figure 6.9d), observing a faster drop of the conversion to values near 0 after 15 h for the CZ15 catalyst. In contrast, the conversion undergoes a slow decay over time with the CZ140 catalyst, decreasing from 78 to 42% after 40 h.

Effect of the f_a at the entrance of the unit

The evolution with time of f_a is affected by the the location of the activity distribution function at the entrance of the reactor ($f_a(a, 0, t)$). This effect is studied in Figure 6.10 for analogous conditions to those depicted in Figure 6.9a: 375 °C, $\tau = 3.5 \text{ g h mol}_C^{-1}$ and $\tau_m = 10$ h. Figure 6.10a shows the results for $f_a(a, 0, t)$ centered at $a = 0.7$, which can be compared to those results in Figure 6.9a for $f_a(a, 0, t)$ centered at $a = 0.9$. Figure 6.10b depicts the simulation results obtained for a narrow $f_a(a, 0, t)$ centered at $a = 0.99$. This case can be attributed to the performance of the reactor when fresh or totally regenerated catalyst is fed into the reactor ($a \rightarrow 1$).

f_a evolves towards lower a values with time, depending the width and location of the peaks on $f_a(a, 0, t)$. The bimodal distribution previously observed in Figure 6.9a after 20 h is barely obtained with $f_a(a, 0, t)$ centered at $a = 0.7$ (Figure 6.10a). Only a second hump is observed (green line). The steady-state f_a is a distribution

with a maximum located at $a = 0.6$ and lower variance than that observed in Figure 6.9a, which is in accordance with the slower deactivation rate of particles with lower initial activity (see equation (5.5)). This can be better observed in the evolution with time of the activity at the outlet of the PBR. The calculated slope of the curves in Figure 5.10 is markedly decreased at lower a values, which explains the slower deactivation of the fed CZ140 catalyst with $f_a(a, 0, t)$ centered at $a = 0.7$.

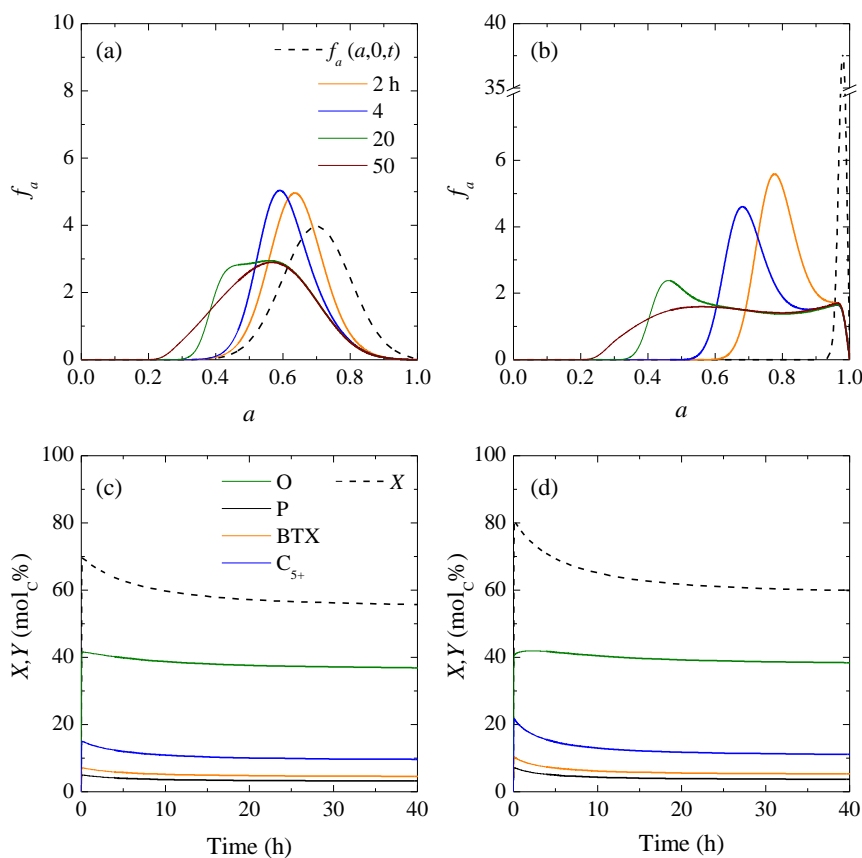


Fig. 6.10. Evolution with time of (a, b) the activity distribution function of the CZ140 catalyst, (c, d) the conversion and yields of products for $f_a(a, 0, t)$ centered at (a, c) $a = 0.7$ and (b, d) $a = 0.99$. 375 °C, $\tau = 3.5 \text{ g h mol}^{-1}$, $\tau_m = 10 \text{ h}$, DME:W = 1:0.

In contrast, f_a has two marked maxima after 20 h when the fed catalyst is assumed to have an activity near to 1 (Figure 6.10b). The evolution with time of the population with lower a values is faster in this case, which is consistent with the previous discussion. A flatter steady-state f_a in the range $0.2 < a < 1$ is predicted.

An increase in the steady-state conversion can be observed upon increasing the central point of $f_a(a, 0, t)$ from 0.7 (Figure 6.10c) to 0.99 (Figure 6.10d). The maximum is higher in the case of more active fed catalyst (ca. 81% in Figure 6.10d), and its drop is faster, with steady-state conversions around 60% in both cases. A similar behavior is observed for the yields of products. But interestingly, the yield of olefins barely decreases over time, whereas those of paraffins, BTX and C₅₊ suffer more pronounced decays (especially in Figure 6.10d). Therefore, the catalyst deactivation mainly affects the secondary reactions of olefins towards byproducts.

6.3.2 Effect of process variables

The most valuable results for the CFBR design are those at the steady state, where the catalytic bed exhibits a constant f_a and the reactor operates at constant conversion and product distribution. According to the results in the unsteady state, at least $(5 \times \tau_m)$ h is required for reaching the steady state. After this time, the errors in the simulations are lower than those observed in the experimental data fitting in Chapter 5. Therefore, the results in this section corresponds to the simulations at $(5 \times \tau_m)$ h in all cases, aiming for the optimization of the calculation time for each run. The effect of the main reaction conditions is studied here, considering the space time (τ), temperature, DME:water (DME:W) ratio in the feed and catalyst acidity. In all cases, a $f_a(a, 0, t)$ centered at 0.9 is used and, once reached the steady state, the shape of f_a and the yields of products are evaluated. Note that the direct comparison of f_a is not straightforward because its evolution depends on the initial reaction rate according to the activity definition. And this rate changes at different reaction conditions. Also note that the sum of the yields corresponds to the total conversion, previously defined in equation (3.1).

The effect of τ on the steady-state f_a and the yields of products is shown in Figure 6.11a and 6.11b, respectively. The increase in τ shifts the f_a towards higher values of activity, suggesting that lower space time values favor the catalyst deactivation. Moreover, the conversion is boosted from ca. 40% up to ca. 85%. This performance was expected as the deactivation equation (5.5) is a function of the concentration of oxygenates (DME and methanol). The higher concentration of water in the reaction medium upon increasing the conversion can be deduced from the reaction network in Scheme 5.2. Thus, high conversions limit the concentration of oxygenates and increase the one of water, which is an attenuating factor for catalyst deactivation. The higher concentration of water could explain this result.

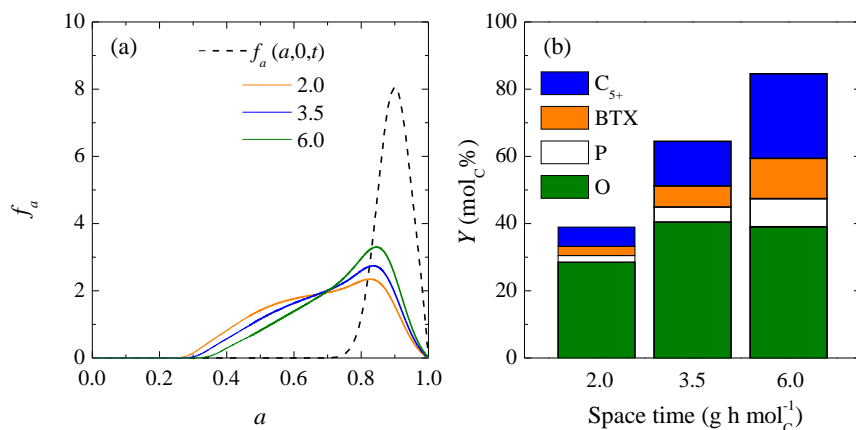


Fig. 6.11. Effect of space time on the steady-state (a) activity distribution function and (b) yields of products for the CZ140 catalyst. 375 °C, $\tau_m = 5$ h, DME:W = 1:0.

Nevertheless, the increase in the conversion of the DTO process leads to the formation of secondary products. As observed in Figure 6.11b, the maximum of olefins is obtained using $\tau = 3.5 \text{ g h mol}_C^{-1}$, but the highest selectivity to olefins is obtained using the lowest $\tau = 2.0 \text{ g h mol}_C^{-1}$. With $\tau = 6.0 \text{ g h mol}_C^{-1}$, the yield of byproducts (paraffins, BTX and C₅₊) is higher than that of olefins (> 40%). Especially, the yield of C₅₊ hydrocarbons is above 25%.

The temperature directly affects the reaction and deactivation kinetic constants (equations (5.2) and (5.5), respectively). Its effect on the steady-state f_a and yields of products is depicted in Figure 6.12a and 6.12b, respectively. Clear evidences of the influence of temperature on the steady-state f_a are not observed in Figure 6.12a. However, the increase in the temperature from 350 °C up to 400 °C displaces the distribution towards values of $a = 0.9$. This can be explained in a similar way to the τ influence in regards of the steady-state yields of products in Figure 6.12b. The conversion markedly increases from ca. 18% to ca. 80% upon increasing temperature from 350 to 400 °C, with the consequent decrease in the oxygenate concentration and increase in that of water. Other explanation can be given by the reaction zones described for the PBR in Figure 5.11. A narrower reaction zone was observed upon increasing temperature, leading to more severe deactivation longitudinal profiles. The continuous movement of particles in the fluidized bed reactor avoids the formation of these profiles and the severe activity profile is diluted in the whole catalytic bed. In terms of f_a , this means a higher overall activity of the

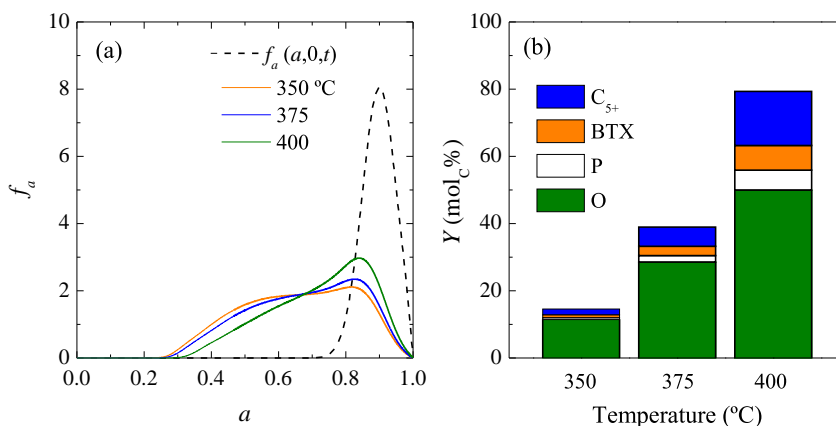


Fig. 6.12. Effect of temperature on the steady-state (a) activity distribution function and (b) yields of products for the CZ140 catalyst. $\tau = 2.0 \text{ g h mol}_C^{-1}$, $\tau_m = 5 \text{ h}$, DME:W = 1:0.

catalytic bed upon increasing temperature, that is, a shift of f_a towards higher values of a .

Part of the discussion of these results are attributed to the water concentration in the reaction medium. The effect of water can be studied by using same values of τ and temperature and varying the DME:W ratio in the feed. Figures 6.13a and 6.13b show the effect of co-feeding water with different DME:W ratios on the steady-state f_a at 375 °C and 400 °C, respectively. The corresponding yields of products are depicted in Figures 6.13c and 6.13d. As explained, the attenuating role of water in both reaction (equation (5.2)) and deactivation rates (equation (5.5)) is evidenced. The increase in the amount of co-fed water from a DME:W ratio of 1:0 to 1:2 significantly shifts the steady state f_a towards higher a values at both temperatures. However, this goes hand in hand with pronounced decreases in the conversion and yields of olefins. In these simulation results, the concentration of methanol in the product stream is illustrated (Figures 6.13c and 6.13d). A marked increase in the selectivity to methanol is predicted when water is co-fed, which is caused by the promotion of DME hydration (step 1 in Scheme 5.2). Indeed, the promotion of this reaction, the estimated lower reactivity of methanol than that of DME (see Table 5.2) and the inhibition of the reaction rates by the presence of water almost suppress the formation of products when DME:W = 1:2 in the feed is used.

Conditions of higher catalyst activity and faster deactivation are also tested by

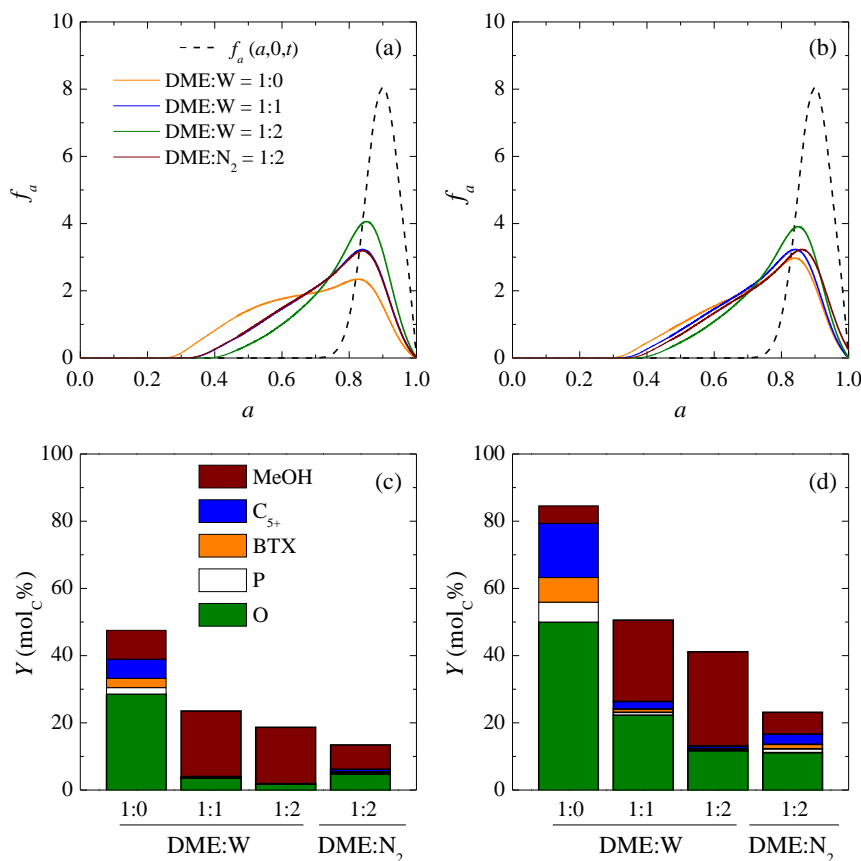


Fig. 6.13. Effect of the DME dilution in water (W) and N₂ on the steady-state (a, b) activity distribution function and (c, d) yields of products for the CZ140 catalyst at (a, c) 375 °C and (b, d) 400 °C. $\tau = 2.0 \text{ g h mol}_C^{-1}$, $\tau_m = 5 \text{ h}$.

increasing the temperature. A steady-state yield of olefins of 50% is attained at 400 °C without co-feeding water (Figure 6.13d). Significant decreases to ca. 23% and ca. 14% are shown using DME:W ratios of 1:1 and 1:2, respectively. Nevertheless, increases in the selectivity to olefins from ca. 63% to 82% and 87% are respectively estimated due to the active contribution of water in the reaction network.

This can be confirmed with simulations using the same dilution of DME in inert N₂. In this case, the reduction of the partial pressure of the oxygenates is the only factor affecting the reaction and deactivation rates. At both temperatures, the

steady-state f_a is near to that observed using half of water in the feed (DME:W = 1:1, Figures 6.13a and 6.13b). In terms of yields, an overall decrease is predicted, even obtaining lower yields of products (including methanol) than those with the same amount of co-fed water at 375 °C (Figure 6.13c). Nevertheless, the effect of water is more remarkable at 400 °C, where the same yield of olefins is obtained with both diluents using the same ratio, but higher selectivity (without considering methanol) is observed using water (Figure 6.13d). At both temperatures, an inverse correlation is predicted between the yields of C₅₊ byproducts and methanol. Relatively high yields of C₅₊ hydrocarbons are observed without co-feeding water, conditions at which the catalyst deactivation is also promoted. In contrast, a significant increase in the yield of methanol is estimated when water is co-fed, which practically suppresses the secondary reactions that form the C₅₊ byproducts.

Although these conditions are suitable for illustrating the strong influence of water in the reaction, their selection should be subjected to productivity criteria. In this regard, the amount of co-fed water, space time, temperature and mean residence time should be chosen avoiding the remarkable decrease in the yield of olefins observed in Figures 6.13c and 6.13d, but aiming for the attenuation of catalyst deactivation and maximizing the selectivity to olefins. This situation can be reached at higher values of mean residence time, when the deactivation degree increases.

6.3.3 Comparison of the catalysts

From the simulation results in the unsteady state, the different performance of the CZ140 and CZ15 catalysts were evidenced. For a clearer comparison, the steady-state f_a and yields of products are shown in Figures 6.14a and 6.14b, respectively. The results do not correspond to the optimal operation conditions showed before, but to the same conditions in both cases: 375 °C, $\tau = 2.0 \text{ g h mol}_C^{-1}$, $\tau_m = 5$ and DME:W = 1:0. Thereby, the role of acidity in the process can be evaluated. The difference in the steady-state f_a is remarkable. The CZ15 catalyst exhibits a wider distribution in the whole activity range ($0 < a < 1$), with an important contribution of the population located at $a < 0.2$ (Figure 6.14a). As discussed in this Section, these are values that cannot be reached with the CZ140 catalyst because of the different deactivation kinetics of each catalyst. An important contribution of the population at $a > 0.7$ is also predicted by the model for both catalysts. This is attributable to those catalyst particles that spend the less time in the reactor and exit without suffering a significant deactivation.

The comparison of the yields of products at the same conditions suggests the higher activity of the CZ15 catalyst (Figure 6.14b). The higher extent of the reaction mechanism with this catalyst can be deduced. The selective production of olefins with the CZ140 catalyst is reduced in favor of the formation of byproducts.

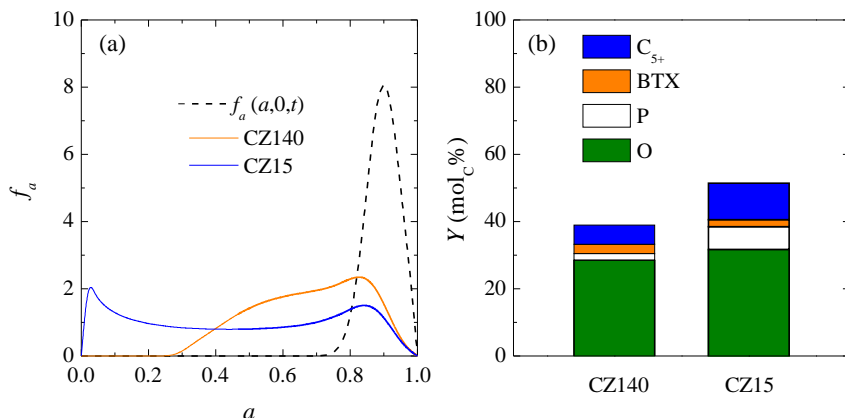


Fig. 6.14. Steady-state (a) activity distribution function and (b) yields of products for the CZ140 and CZ15 catalysts. 375 °C, $\tau = 2.0 \text{ g h mol}_C^{-1}$, $\tau_m = 5 \text{ h}$, DME:W = 1:0.

In fact, similar yields of olefins (ca. 30%) are predicted for both catalysts with conversions of ca. 40% (CZ140 catalyst) and ca. 52% (CZ15 catalyst). According to the justification above, higher conversion levels were related with lower concentrations of oxygenates and higher concentrations of water, which attenuates the deactivation rate. This direct association can only be made for the same catalyst and kinetic model. The comparison of the deactivation kinetics in Tables 5.2 and 5.3 indicates a threefold faster deactivation for the CZ15 catalyst (with higher k_d), less attenuated by the concentration of water (with lower K_d) and without reaching a steady value of activity ($d \approx 1$).

All in all, a strict analysis for a direct comparison of the catalysts is not easy. Each one presents optimal operation conditions, at which the concentration of olefins can be maximized. These conditions are far different from catalyst to catalyst. The more acid CZ15 catalyst would require much lower space time values in order to overcome the higher strength and density of acid sites. In reactors with catalyst circulation, this could also be solved by using much lower residence time values of the catalyst. It is also worth mentioning that the production of some byproducts as BTX can also be attractive, as detailed in Chapter 4. Nonetheless, this option would require the design of experiments and simulation of the reactor with this specific goal.

6.4 Fluidized bed regenerator

The regenerator in the DTO process consists of a second CFBR, where the coke is burnt off and the activity of the catalyst is partially recovered [67, 230]. The PB-PC model can be applied in order to simulate the performance of the regenerator. The model for the combustor is simpler than that for the reactor. The main goal of a regenerator is to burn off as much coke as possible, thus trying to recover the total activity of the fresh catalyst ($a \rightarrow 1$). With this aim, air in excess is used and the expression of the reactivation kinetics corresponds to an equation independent on the concentration of O_2 in the gas phase. This is a significant simplification of the CFBR model as: (i) the time that the catalyst spends in the combustor determines the reactivation degree, and; (ii) the mathematical method does not require the evaluation of a complex kinetic model for the combustion with excess of air.

As a consequence of this simplification a gas flow model is not required. And therefore, this unit is simplified in Figure 6.4, avoiding the flows of gas in the representation of the parallel compartment diagram. The simulation of the combustor is then reduced to the solution of the conservation equations for the catalyst in the PB-PC model. According to the general equation (6.10), the only difference in terms of computation between the fluidized bed reactor studied in the previous section and the regenerator is the rate of activity change ($r_{a,r}$), in this case the reactivation rate (r_r).

6.4.1 Reactivation kinetics

As defined in Section 6.1, a potential expression is considered for r_r (equation (6.21)), similar to those used by Weng and Chen [231] and Li et al. [230]. In a previous work, combustion experiments at 550 °C with excess of air in a fluidized bed reactor were performed. The activity loss of the catalyst was monitored during the reaction and used catalysts with different deactivation degree were fed into the combustor. The activity recovery during the combustion were studied and fitted to a reactivation model. Gayubo et al. [232] proposed a complex reactivation model for the activity recovery by the combustion of coke in an agglomerated catalyst based on the same HZSM-5 zeolite. Their expression contains a time-dependent exponential factor as

$$a = 1 - (1 - a_0) \exp [-(b_1 t + b_2 t^2)], \quad (6.28)$$

where a_0 is the activity at the entrance of the regenerator and the parameters b_1 and b_2 depend on the value of a_0 .

Our simplification only uses potential expressions, resulting the integration of the equation (6.21) in

$$a = 1 - [(1 - a_0)^{1-m} - (1 - m)k_r t]^{1-m}. \quad (6.29)$$

Values of $k_r = 1.8 \text{ h}^{-1}$ and $m = 0.59$ provide the best fitting of the data, and the comparison of this model (continuous line) to that previously proposed by Gayubo et al. [232] (dashed line) is depicted in Figure 6.15. A small deviation of the data predicted by our model (solid lines) is observed. The time-dependency of the equation proposed by Gayubo et al. [232] can also destabilize the method because of the small oscillations in the reactivation rate observed at $a_0 < 0.3$ (Figure 6.15b). This is not a problem for the CZ140 catalyst because a steady value of a of ca. 0.4 was observed in all cases (Section 5.3). However, the CZ15 catalyst presents values of $a \rightarrow 0$ for $t > 9 \text{ h}$ at any given condition at the outlet of the PBR, as observed in Figure 5.12. Therefore, the simulation of the regeneration of this catalyst will require a kinetic equation with a stable reactivation rate in the whole a range. The optimization of the computation methodology due to the use of a time-independent reactivation rate equation (equation (6.21)) is also significant. For these reasons, the recalculation of the reactivation kinetics was required for simulating the combustor in the dual system.

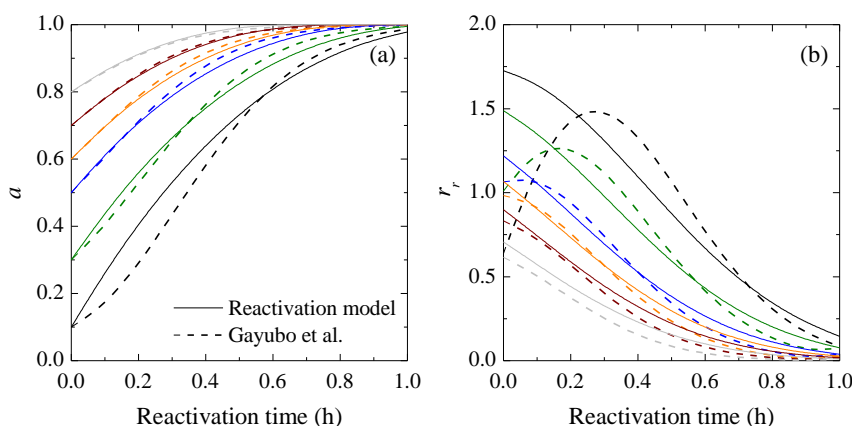


Fig. 6.15. Comparison of (a) the simulated activity recovery and (b) the reactivation rate with the proposed model and that reported by Gayubo et al. [232].

6.4.2 Effect of f_a' at the entrance of the unit

According to the results in the Figure 6.15, the catalyst recovers the activity as a function of time, being the required time for a total reactivation dependent on the activity at the entrance of the regenerator. The evolution with time of f_a' is studied, assuming an initial catalytic bed partially deactivated and a combustion in excess of air at 550 °C. Again, the initial activity distribution function (f_{a0}') is assumed equal to that at the entrance of the regenerator ($f_{a0}' = f_a'(a, 0, t)$). In a circulating fluidized bed regenerator, the activity distribution function of the catalyst entering the regenerator $f_a'(a, 0, t)$ is located at lower a values than the activity distribution function at the outlet. The catalyst is reactivated following the expression of equation (6.29).

The effect of this $f_a'(a, 0, t)$ is studied in a similar way as for the reactor in the previous Section. First, the evolution with time of f_a' during the unsteady state is analyzed. Afterwards, the required time for reaching the steady state is set and a comparison of the steady-state f_a' for different mean residence time values is carried out.

Different $f_a'(a, 0, t)$ centered at 0.01 (practically uniform activity of $a \rightarrow 0$), 0.1, 0.25 and 0.5 are tested, and the evolution with time of f_a' during the unsteady state is depicted in Figures 6.16 for a given $\tau_m = 1$ h. Upon increasing time, the main activity population is progressively shifted towards higher a values. After 3 h, the regenerator practically reaches the steady state and f_a' shows a maximum near to $a = 1$ for all tested $f_a'(a, 0, t)$ and $\tau_m = 1$ h. The tale of the distribution is a function of the $f_a'(a, 0, t)$, including the whole range $0 < a < 1$ in the case of Figure 6.16a and a shorter one ($0.2 < a < 1$) in the case of Figure 6.16d. A second maximum is observed at a values near to the central point of $f_a'(a, 0, t)$, corresponding to the amount of particles fed with this a value.

The effect of $f_a'(a, 0, t)$ on the reactivation rate can be observed by comparing the results estimated after 0.5 h of regeneration. A second population is observed at higher a values than those of $f_a'(a, 0, t)$. The maximum of this population is located at ca. 0.6 when $f_a'(a, 0, t)$ is centered at $a = 0.01$ (Figure 6.16a) and $a = 0.1$ (Figure 6.16b). The location of this population is estimated at $a = 0.8$ in Figure 6.16d. Only a shift of 0.3 is observed from the initial location of the maximum in comparison to the displacement of 0.6 shown in Figure 6.16a. This is a consequence of the direct dependency of r_r on $(1-a)$ shown in equation (6.21). Therefore, faster reactivation rates are predicted for catalyst particles with higher deactivation degree.

The τ_m in the regenerator, and so the size of the unit, should be selected as a function of the catalyst deactivation as later discussed. Therefore, the study of

the effect of τ_m in the regenerator is useful for the future selection of the operation conditions in the dual reactor-regenerator system. The catalyst exhibits a constant f'_a after 3 h, which corresponds to three times the value of τ_m . Similar to the behavior in the reactor, a given particle fed into the regenerator at $t = 0$ (with $\tau_m = 1$ h) will presumably have enough time to exit the reactor after 3 h. A steady performance of the combustor is achieved after this time. Figure 6.17 shows the effect of τ_m on the steady-state f'_a for the different $f'_a(a, 0, t)$. Four different τ_m are tested from the smallest value of 0.1 h to the extreme case of $\tau_m \rightarrow \infty$, which

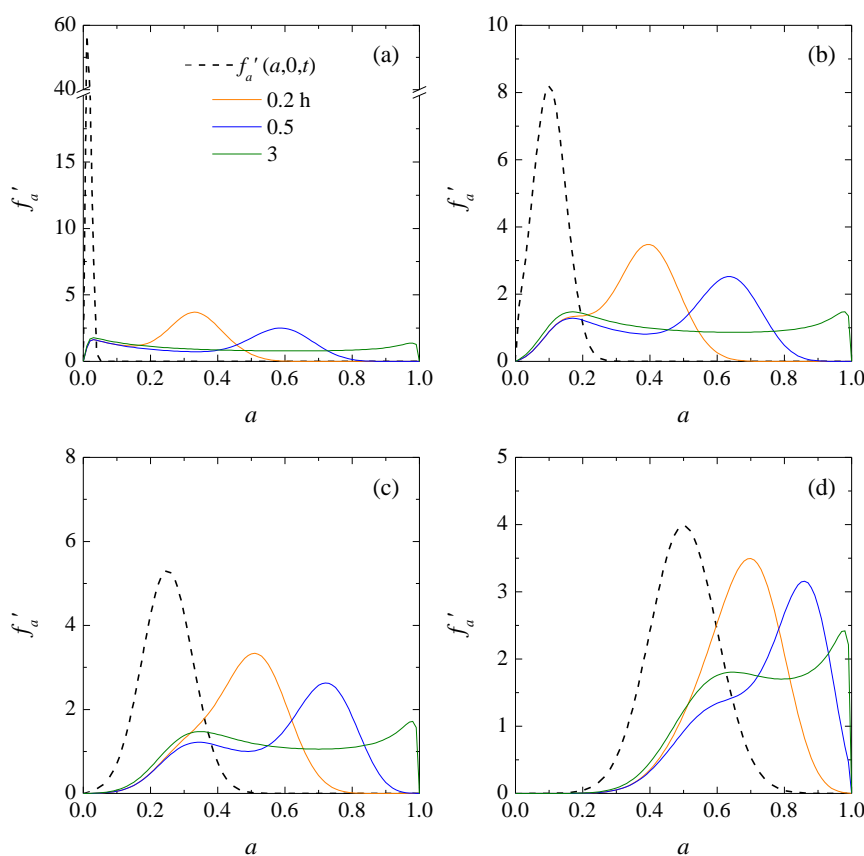


Fig. 6.16. Evolution with time (in h) of the activity distribution function in the regenerator for $f'_a(a, 0, t)$ centered at (a) $a = 0.01$, (b) $a = 0.1$, (c) $a = 0.25$ and (d) $a = 0.5$. 550 °C, $\tau_m = 1$ h.

corresponds to a NCFBR.

The evolution of f'_a when $\tau_m \rightarrow \infty$ should be consistent with the results of activity recovery shown in Figure 6.15a for different values of a_0 . The value of f'_a in the regenerator is quite similar after 1 h for all the used $f_a(a, 0, t)$ when $\tau_m \rightarrow \infty$, indicating that the catalyst activity is indeed almost totally recovered. This is in accordance with the complete reactivation displayed in Figure 6.15a after 1 h. However, in all cases a distribution in $0.9 < a < 1$ is calculated. The incomplete reactivation is attributed to the combined consideration of the RTD and f'_a in a

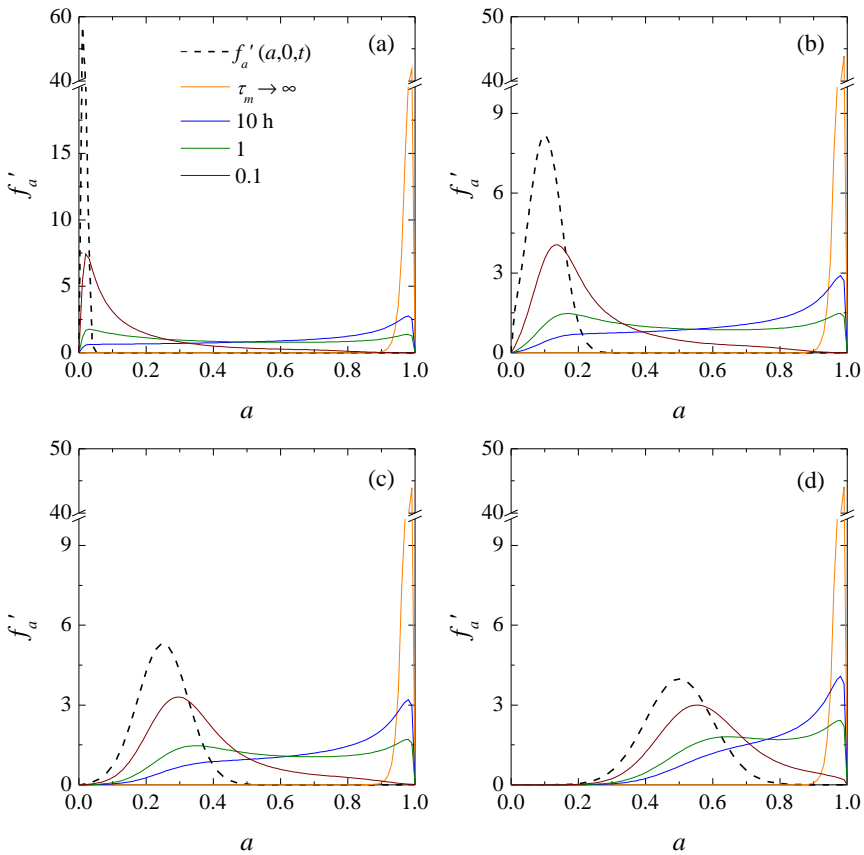


Fig. 6.17. Effect of the mean residence time of the catalyst on the steady-state activity distribution function in the regenerator for $f'_a(a, 0, t)$ centered at (a) $a = 0.01$, (b) $a = 0.1$, (c) $a = 0.25$ and (d) $a = 0.5$. 550 °C.

CFBR by the PB-PC model (see Section 6.3) and the use of a saturating reactivation kinetics. The smallest compartment in Figure 6.2 simulates the performance of catalyst particles that find a preferential path and barely spend time in the regenerator, explaining the deviation of the distribution with values of $a < 1$.

Significant variations are observed in all cases of Figure 6.17 when τ_m is decreased. A f'_a mainly displaced towards $a = 1$ is attained with $\tau_m = 10$ h, whereas a very low reactivation degree is achieved using $\tau_m = 0.1$ h. The short time spent by the catalyst inside the regenerator explains this result, which leads to values of f'_a similar to those of $f'_a(a, 0, t)$. At the extreme limit of $\tau_m = 0$ h (not depicted), the condition $f'_a = f'_a(a, 0, t)$ is fulfilled.

6.5 Reactor-regenerator system

After studying each unit individually, the dual reactor-regenerator system is simulated in this Section. Modeling the reactor-regenerator system consists of considering a continuous catalyst circulation between both units. A simplified diagram of the system is shown in Figure 6.18, where the gas and solid flows are depicted with single and double lines, respectively. The nomenclature for denoting the activity distribution functions in the reactor and regenerator for any given time and longitudinal position are respectively f_a and f'_a . In the simulations, the same initial activity distribution function (at $t = 0$) is used in both units

$$f_{a0} = f'_{a0}. \quad (6.30)$$

Note that the simulation of the dual reactor-regenerator system requires setting the activity distribution function at the entrance of each unit equal to the one at the outlet of the other at any given time. Therefore,

$$f_{a0} \neq f_a(a, 0, t) = f'_a, \quad (6.31)$$

$$f'_{a0} \neq f'_a(a, 0, t) = f_a. \quad (6.32)$$

As assumed in the reactor simulation (Section 6.3), the initial and left boundary conditions for the gas conservation equation are equal (equation (6.27)).

For the simulations, the catalyst flow rate between the units, and the reactor volume (data in Section 6.3) were selected. The mean residence time of the catalyst in the reactor ($\tau_{m,R}$) is varied, whereas the one in the regenerator was fixed

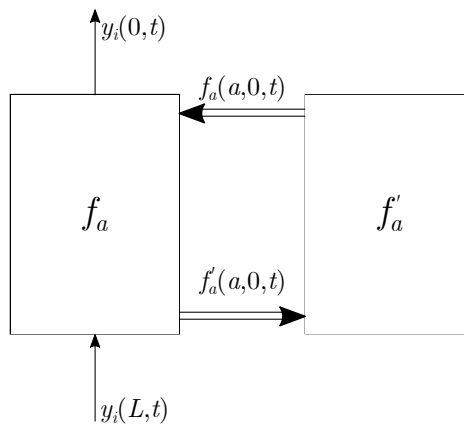


Fig. 6.18. Simplified diagram of the dual reactor-regenerator system.

($\tau_{m,Reg} = 1$ h), aiming for a high reactivation degree according to the results in the previous Section. Hence, the volume of the regenerator was adjusted for closing the catalyst circulation balance.

The simulations of the dual system requires the selection of a time step (δt) in which the system of PDEs defined in equations (6.7) and (6.10) for each unit is solved before feeding the particles coming from the other one. This leads to certain mathematical uncertainty, which was evaluated prior to the simulations. Setting a value of $\delta t = 10^{-1}$ h, the simulations of the dual system were performed until the steady state was reached. This consideration was established with a minimum simulation time of $3 \times (\tau_{m,R} + \tau_{m,Reg})$ and an error $< 10^{-2}$ between the activity distribution function in each unit in t and $t + \delta t$.

The evolution of the system is followed during the unsteady state, where the catalyst is deactivated in the reactor and reactivated in the regenerator. After the required time, the operation reaches the steady state and the influence of the process variables can be evaluated.

6.5.1 Unsteady state

The evolution with time of the activity distribution functions in the reactor and the regenerator is respectively shown in Figures 6.19a and 6.19b for initial f_{a0} and f'_{a0} centered at $a = 0.9$. The reaction conditions are selected as the most suitable for the production of olefins with the CZ140 catalyst according to the results in previous Sections: 375 °C, $\tau = 3.5$ g h mol⁻¹ and DME:W = 1:0. As expected the catalyst is deactivated over time in the reactor and f_a shifts towards lower a values. Due to the kinetics of the DTO process using the CZ140 catalyst, the steady-state f_a is obtained with a values higher than 0.3, which is in accordance with the results observed in Figure 6.8a only with the reactor. Nevertheless, the evolution with time in the dual reactor-regenerator system is different as the operation also depends on the regeneration. The catalyst in the reactor and fed into the regenerator presents a bigger population of particles with $a < 0.7$ over the operation time. This leads to a wider f_a distribution, and a consequent increase in the population of particles with lower activity in the regenerator. The result is a steady-state f_a more displaced towards low a values than that observed when catalyst with $f_a(a, 0, t)$ centered at $a = 0.9$ is continuously fed into the reactor (Figure 6.8a).

The initial f_{a0}/f'_{a0} has important influence on the evolution with time of both the reactor and regenerator units. Figures 6.19c and 6.19d depict the evolution with time of f_a and f'_a under the same operation conditions but using a wider initial f_{a0}/f'_{a0} centered at $a = 0.7$. This result corresponds to a more deactivated catalyst than that simulated in Figures 6.19a and 6.19b. The performance of a

catalyst with an activity distribution function in the $0.4 < a < 1$ range from the beginning of the simulation is then evaluated. A slower deactivation rate can be observed in the reactor, consistent with the direct dependency of the deactivation rate on the activity parameter (equation (5.5)). As the modification of the f_a of the catalyst fed into the regenerator is significantly lower in this case, the results in the regenerator are quite reproducible over time (Figure 6.19d).

The effectiveness of the computation methodology can be evaluated with the

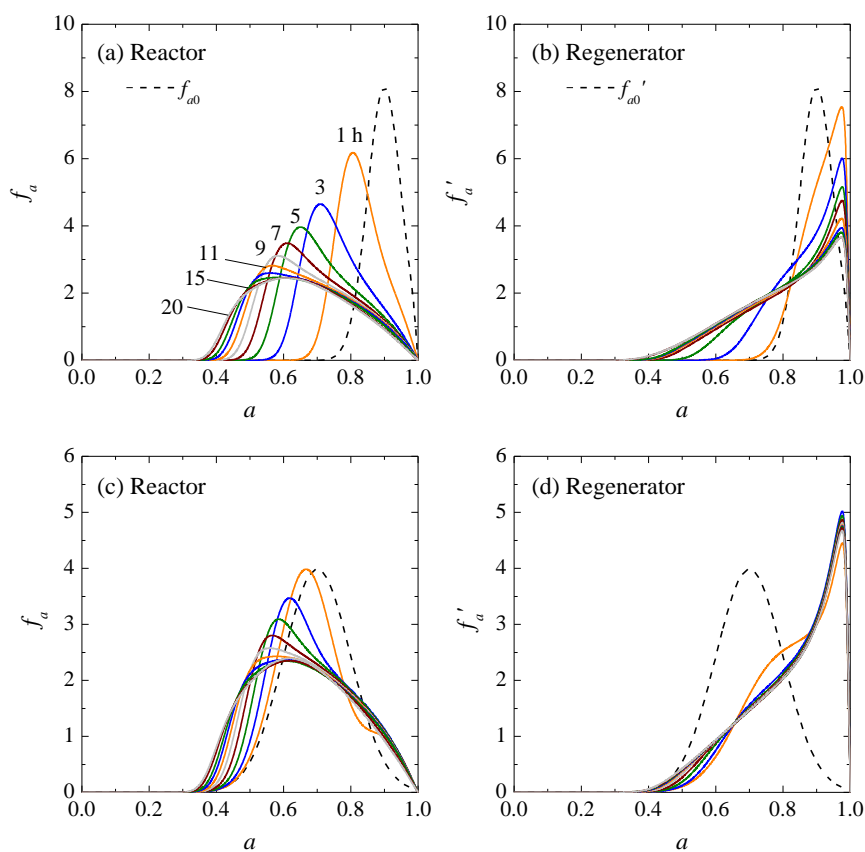


Fig. 6.19. Simultaneous evolution with time of the activity distribution functions in the (a, c) reactor and (b, d) regenerator for f_{a0}/f'_{a0} centered at (a, b) $a = 0.9$ and (c, d) $a = 0.7$ using the CZ140 catalyst. $375\text{ }^\circ\text{C}$, $\tau = 3.5\text{ g h mol}^{-1}$, $\tau_{m,R} = 5\text{ h}$, $\text{DME:W} = 1:0$, $\tau_{m,Reg} = 1\text{ h}$.

extreme case in which the initial catalytic bed is assumed to have high deactivation degree. The activity of the catalyst should increase gradually in the regenerator, and from this point, decrease in the reactor to a similar steady-state f_a value to those observed in Figure 6.19. The simultaneous evolution with time of f_a and f'_a is depicted in Figures 6.20a and 6.20b, respectively. After 0.5 h, the catalyst is partially reactivated in the regenerator and a large population at $a = 0.8$ is observed in Figure 6.20b (orange line). The corresponding f_a in the reactor still contains an important contribution of particles with $a < 0.4$. The evolution with time of the curves evidences that the catalytic bed is reactivated during the operation (Figure 6.20b) and the presence of catalyst with $a < 0.4$ in the reactor disappears gradually. Because of the deactivation kinetics of CZ140 catalyst, the activity tends to reach values of 0.4, thus observing a local minimum in f_a around this value.

A small population of particles at $a = 0.2$ is still observed in the reactor after 20 h (Figure 6.20a). This occurs due to the strict consideration of the E curve by the PB-PC model. According to the schematic representation in Figure 6.2, there is always a big enough compartment that simulates the presence of catalyst particles in the reactor with very high residence time values. In addition, a small enough compartment for the simulation of particles that find preferential paths and bypass the regenerator is also taken into account. Therefore, the population at $a = 0.2$ will be completely removed at values of $t \rightarrow \infty$. As this is not representative of a

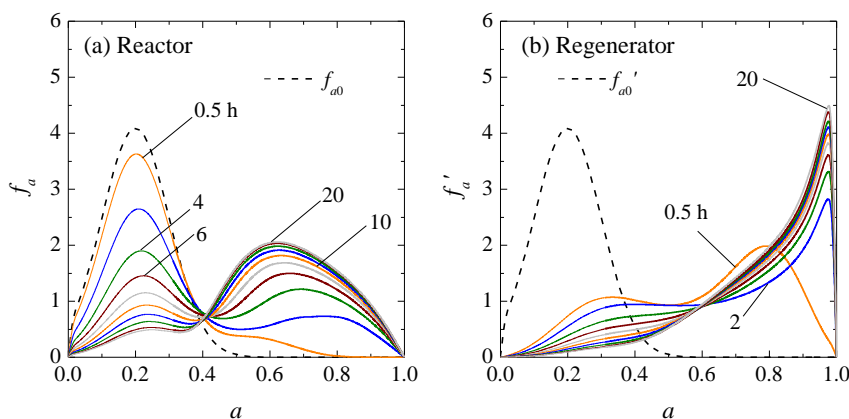


Fig. 6.20. Simultaneous evolution with time of the activity distribution function in the (a) reactor and (b) regenerator for f_{a0}/f'_{a0} centered at $a = 0.2$ using the CZ140 catalyst. 375 °C, $\tau = 3.5 \text{ g h mol}_C^{-1}$, $\tau_{m,R} = 5 \text{ h}$, DME:W = 1:0, $\tau_{m,Reg} = 1 \text{ h}$.

realistic operation, the calculation error after 20 h can be assumed, thus considering that the (pseudo)steady state is reached.

A more understandable overview of the reactor operation during this unsteady state can be provided by the performance of the gas phase reaction and the definition of average activity values in the reactor and regenerator (\bar{a}). This is an illustrative magnitude of the results obtained in Figures 6.19 and 6.20, calculated as

$$\bar{a} = \begin{cases} \int_0^1 a f_a da & \text{Reactor} \\ \int_0^1 a f'_a da & \text{Regenerator} \end{cases} . \quad (6.33)$$

Figures 6.21a and 6.21b show the evolution with time of the conversion and the average activity values in the reactor and regenerator. The results correspond to the simulations of the dual reactor-regenerator system with initial f_{a0}/f'_{a0} centered at 0.9, 0.7 (Figure 6.19) and 0.2 (Figure 6.20). A clear modification of the evolution with time of the conversion is observed. The activity of the catalyst with f_{a0}/f'_{a0} centered at 0.9 leads to a faster increase in the conversion up to a maximum of ca 78%. This value slightly decreases to values of ca. 65% in the steady state. Interestingly, the same steady-state conversion is reached by the catalyst using an

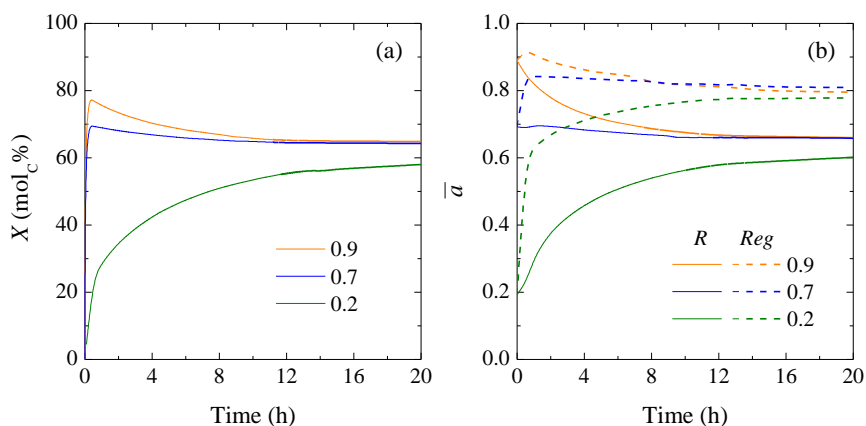


Fig. 6.21. Evolution with time of (a) the conversion and (b) the average activity in the reactor (solid lines) and regenerator (dashed lines) for f_{a0}/f'_{a0} centered at $a = 0.9$, $a = 0.7$ and $a = 0.2$ using the CZ140 catalyst. 375 °C, $\tau = 3.5 \text{ g h mol}^{-1}$, $\tau_{m,R} = 5 \text{ h}$, $\text{DME:W} = 1:0$, $\tau_{m,Reg} = 1 \text{ h}$.

initial f_{a0}/f'_{a0} centered at 0.7, despite the slower initial increase. At the same conditions in the reactor and regenerator, f_a , conversions and yields should be the same in the steady state independently on the used f_{a0}/f'_{a0} . The evolution of the conversion is significantly slower when the initial f_{a0}/f'_{a0} is centered at 0.2, and the same value is not achieved after 20 h of operation. This is consistent with the initial low activity, which needs to be reactivated during the first hours of operation, as observed in Figure 6.20.

This is also noted in the evolution with time of the average activity of the catalyst (Figure 6.21b). The initial value of $\bar{a} = 0.9$ decreases with time in both units, explaining the decrease in the conversion. An almost constant value of $\bar{a} = 0.7$ is observed in the case of an initial f_{a0}/f'_{a0} centered at this value. In the regenerator, \bar{a} reaches a value of ca. 0.83, which is also maintained almost constant with time. The increasing tendencies of \bar{a} in the reactor and regenerator are parallel to that observed for conversion in the case of f_{a0}/f'_{a0} centered at 0.2. This explains the required activity recovery during the first hours of operation in order to reach the predicted conversion of 59% after 20 h. In all cases, slow changes of conversion and \bar{a} are observed after 15 h, indicating that the observed modifications in f_a/f'_a from this time have not much influence in terms of conversions.

6.5.2 Effect of process variables

The effect of process variables can be evaluated with the comparison of the results in the steady state. The steady-state activity distribution function in the reactor and regenerator and the yields of products obtained at different conditions are depicted in Figure 6.22. Note that different values of mean residence time of the catalyst in the reactor ($\tau_{m,R}$) are tested, whereas a fixed value of $\tau_{m,Reg} = 1$ h is used in all cases. Hence, the simulation time differs as a function of the required time to reach the operation steady state. These conditions are again selected aiming for a maximum production of olefins. Figures 6.22a and 6.22b show the steady-state value of f_a (solid lines) and f'_a (dashed lines) at 375 °C, $\tau = 3.5$ g h mol $^{-1}$ and 400 °C, $\tau = 1.5$ g h mol $^{-1}$, respectively. At any given condition, f_a is in the $0.3 < a < 1$ range as it is previously discussed. With a $\tau_{m,R} = 2$ h, the population of catalyst particles with $a < 0.5$ is negligible at both conditions because of the short time that the particles spend in the catalytic bed. However, the increase in $\tau_{m,R}$ up to 10 h leads to a maximum in f_a at a values of ca. 0.4.

In spite of the similar tendency and shape of f_a obtained for both temperatures at the simulated conditions, the yields of products are slightly different. Higher conversions, yields and selectivities of olefins are predicted at 400 °C (Figure 6.22d), as previously discussed in Chapter 5. This result can be explained by the definition of the activity as the ratio between the reaction rate at t time and that at zero

time but at the same reaction condition. Then, the faster initial reaction rate at 400 °C can explain the slightly higher conversions at this temperature despite the similar f_a shape.

The same comparison can be made for the more acid CZ15 catalyst, and the effect of the mean residence time of the catalyst in the reactor ($\tau_{m,R}$) on the steady-state f_a , f'_a and yields of products is depicted in Figures 6.23a and 6.23b, respectively. In the previous Section 6.3, a more significant deactivation of the

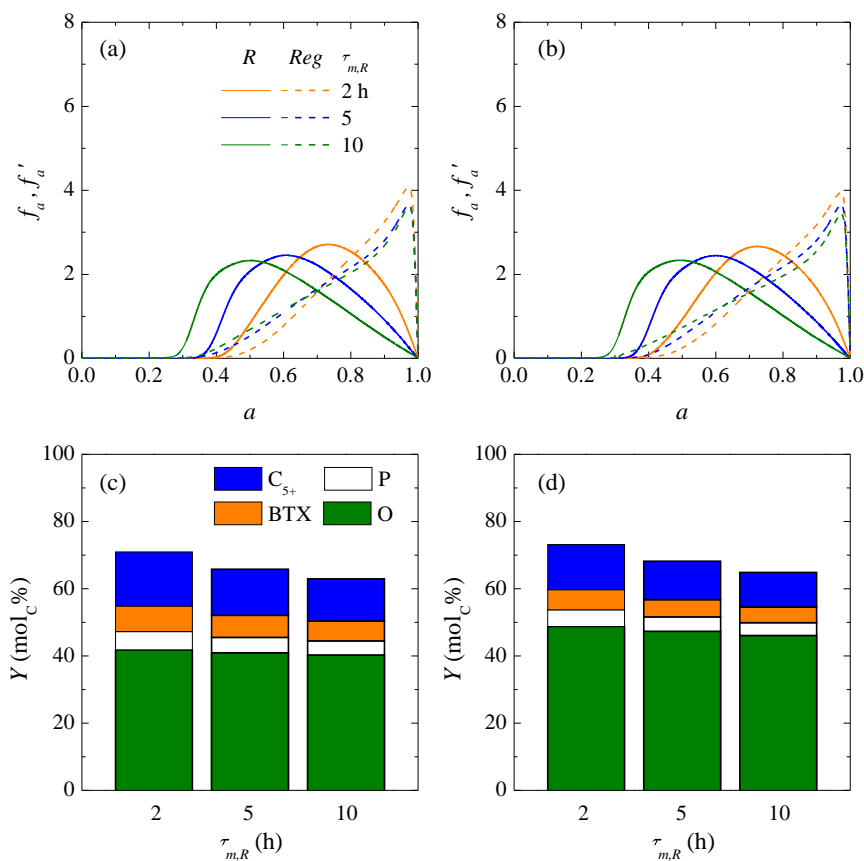


Fig. 6.22. Effect of the mean residence time in the reactor on the steady-state (a, b) activity distribution function in the reactor and regenerator and (c, d) yields of products for the CZ140 catalyst at (a, c) 375 °C, $\tau = 3.5 \text{ g h mol}_C^{-1}$ and (b, d) 400 °C, $\tau = 1.5 \text{ g h mol}_C^{-1}$. DME:W = 1:0, $\tau_{m,Reg} = 1 \text{ h}$.

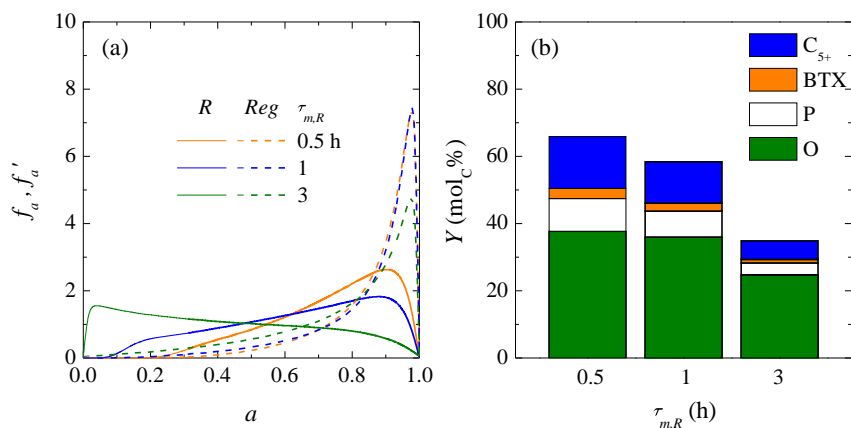


Fig. 6.23. Effect of the mean residence time in the reactor on the steady-state (a) activity distribution function in the reactor and regenerator and (b) yields of products for the CZ15 catalyst. 375 °C, $\tau = 1.0 \text{ g h mol}_C^{-1}$. DME:W = 1:0, $\tau_{m,Reg} = 1 \text{ h}$.

CZ15 catalyst than that of the CZ140 catalyst was observed using $\tau_{m,R} = 5 \text{ h}$. Therefore, values of $\tau_{m,R}$ from 0.5 to 3 h are evaluated for this catalyst.

As the kinetic model for this catalyst predicts a more severe deactivation, the simulated trends for the operation in the dual reactor-regenerator system are more evident. The increase in $\tau_{m,R}$ clearly displaces f_a to lower a values. As a consequence, f'_a also presents a contribution of particles with low a values and lower contribution of those with values of $a \rightarrow 1$.

A more remarkable influence of $\tau_{m,R}$ on the steady-state yields of products is also observed (Figure 6.23b). The significant deactivation degree of the CZ15 catalyst in the steady state using a value of $\tau_{m,R} = 3 \text{ h}$ leads to lower values of conversion, also attenuating the formation of byproducts (yields of ca. 30% for $\tau_{m,R} = 0.5 \text{ h}$ and ca. 12% for $\tau_{m,R} = 3 \text{ h}$). For these two $\tau_{m,R}$ values, the conversion decreases from ca. 68% to ca. 35%. Nevertheless, the highest selectivity to olefins is obtained at these conditions of higher deactivation degree because of the lower extent of the MTO/DTO mechanism.

At the studied conditions, olefins are the main products but significant yields of C_{5+} hydrocarbons are also observed. For this reason, the valorization of this fraction has been the second case study in this thesis (Chapter 4). Several simulations of the dual reactor-regenerator system were performed in a wider range of operating conditions in order to provide an operation map in which the maximum yields

of these two products can be obtained using the CZ140 catalyst. Three different temperatures are tested (350, 375 and 400 °C) and the effect of space time and the mean residence time of the catalyst in the reactor is evaluated. Figure 6.24 shows the simulated contour maps of the yields of olefins and C₅₊ hydrocarbons at these three temperatures: 350 °C (Figures 6.24a and 6.24b), 375 °C (Figures 6.24c and 6.24d) and 400 °C (Figures 6.24e and 6.24f).

The higher extent of the mechanism when the temperature is increased can

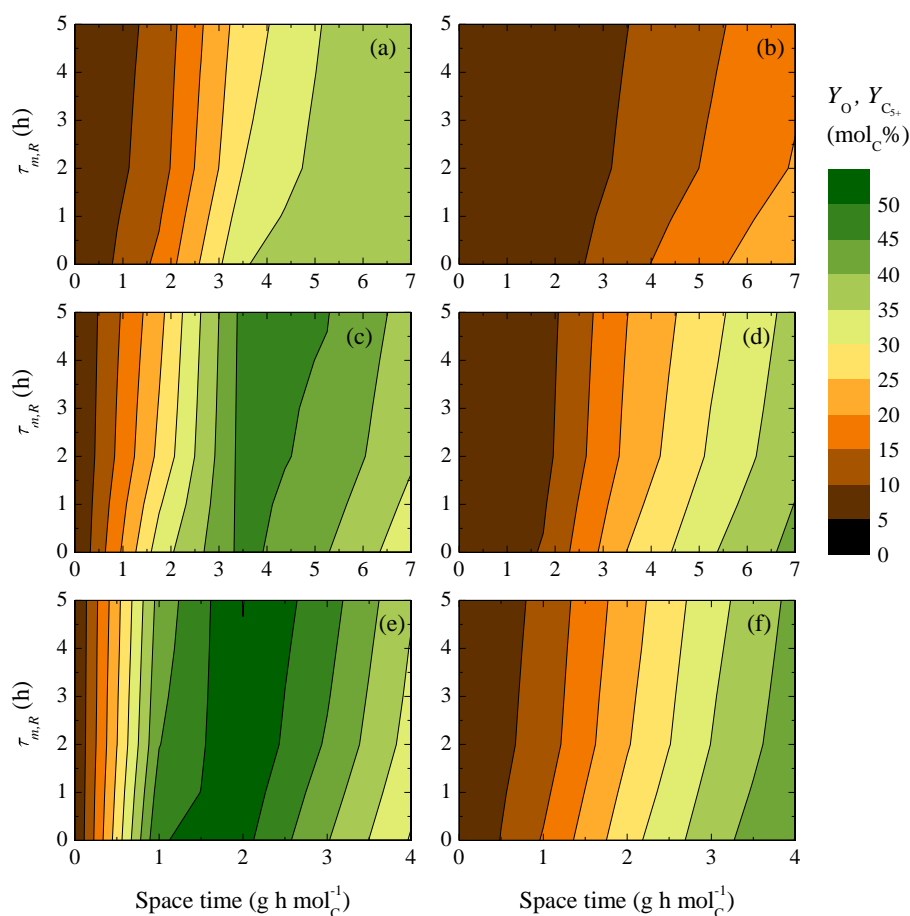


Fig. 6.24. Simulated contour maps with space time and mean residence time in the reactor of the yield of (a, c, e) olefins and (b, d, f) C₅₊ hydrocarbons for the CZ140 catalyst at (a, b) 350 °C, (c, d) 375 °C and (e, f) 400 °C. DME:W = 1:0, $\tau_{m,Reg} = 1$ h.

be well noted. At 350 °C, a maximum yield of olefins of 40% is observed at the highest space time value ($\tau = 7 \text{ g h mol}_C^{-1}$, Figure 6.24a), with the lowest yields of C_{5+} hydrocarbons ($< 25\%$, Figure 6.24b). Upon increasing temperature, maximum yields of olefins of ca. 50% are obtained at lower values of τ . Please note the different scale of the X axis in Figures 6.24e and 6.24f (400 °C). The decrease in the yields of olefins leads to maximum productions of C_{5+} hydrocarbons, whose yields are maximized at 400 °C with a value of 45% at $\tau = 4 \text{ g h mol}_C^{-1}$.

In all cases, the same trend with the mean residence time of the catalyst is observed. Higher τ values are required for maintaining the production when $\tau_{m,R}$ is increased. In other words, higher amounts of catalyst are needed when the mean time in the reactor increases. Increasing the mean residence time of the catalyst in the reactor or decreasing the space time leads to more severe deactivation of the catalyst in the steady state. Hence, a compromise should be reached between these two process variables in order to regulate the degree of catalyst deactivation and attain the desired production. A similar analysis could also be done for selectivity values, completing the full operational map of DTO process.

6.6 Final remarks on the design of DTO process

The simulation of the DTO process has required a first experiment design in a PBR that allowed enough and good-quality data to be collected in order to develop a proper kinetic model of the reaction. These stages towards the simulation of a catalytic process has been followed in the story-line of the thesis, being the simulation of the reactor-regenerator system the final goal of the work. The spotlight has been on a crucial factor as the catalyst deactivation and therefore, several aspects have been neglected but must be considered for the design of a catalytic process.

Regarding the simulation of the CFBR, the first approach for the comparison of deactivation kinetics and reduction of the variables of the system has been the consideration of ideal plug flow and complete mixing flow models for gas and solid, respectively. In the ideal situation, this could provide good enough results in order to approximate accurately the performance of this reactor configuration and evaluate the influence of the catalyst deactivation. But the operation of a fluidized bed reactor is highly dependent on the hydrodynamics of the process at certain operation regimes. The design of a CFBR aiming for a scale-up and obtaining reproducible results at larger scale would require not only the incorporation of hydrodynamics models for the catalyst movement but also for the gas phase. The formation of bubbles in the catalytic bed and the gas-solid contact would be a crucial parameter in the process implementation and further validation of the model estimations at larger scale would be necessary.

Even though the importance of the mechanical resistance of the catalyst has been mentioned in this thesis and an agglomerated catalyst was selected due to this factor, more accurate predictions could be obtained from the simulations by considering an attrition model that takes it into account. In a simple way, a mean lifetime due to the attrition could be attributed to the catalyst particles and a purge stream could be added between the reactor and regenerator units. This strategy is indicated in the Figure 6.25, where an overall diagram is illustrated including most of the topics mentioned in the thesis. Green arrows indicate the processes that have been studied herein, whereas the orange ones refer to those that require further work. The dual reactor-regenerator system with continuous circulation of the catalyst between the units has been designed. However, feeding fresh catalyst and purging spent one would be a requisite for a steady production at larger scales in a fluidized bed reactor (orange double line of solid circulation).

A strategy of the regenerator as a complementary process has also been assumed for the simulation of the system. Then, its size has been adjusted according to the parameters set for the reactor by closing the catalyst flow balance. The residence time of the catalyst in the regenerator has also been set for a suitable regeneration. Nevertheless, the process implementation would require a deeper study of

the regenerator, establishing a fixed size of both units and controlling the catalyst circulation with intermediate stages for catalyst storage.

One of the motivation that has driven the study of the catalytic cracking of paraffins is the abundant production of C_{5+} hydrocarbons in the product stream of DTO process using HZSM-5 zeolites. As observed in previous Chapters, this could be avoided by working at specific reaction conditions. However, if the valorization of these products is aimed, several separation operations will be mandatory in order to purify the streams. Although reactants, water and most of the products could be separated in a relatively easy way by rectification because of its different boiling point, some advanced separation process could be necessary for the separation of products as olefins and paraffins with similar carbon chain length.

Other aspects that could be neglected due to their apparent simplicity would also need further investigation. Recirculating a product stream of a mixture

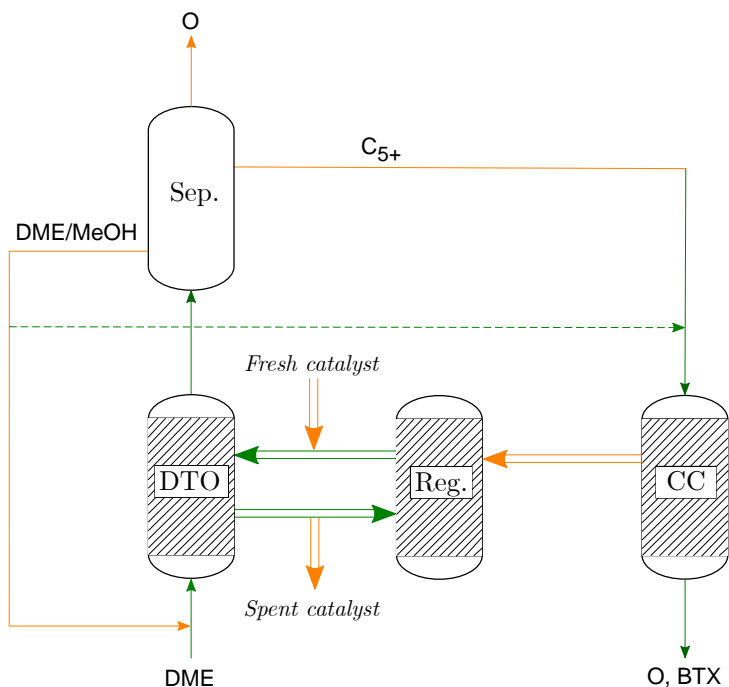


Fig. 6.25. Diagram of the proposed DTO process integrating the catalyst regeneration (Reg.), the product stream separation (Sep.), the catalytic cracking (CC) of paraffins and the combined reaction of oxygenates and paraffins (dashed lines). Green lines: studied in this thesis, orange lines: further work required.

DME/methanol (with or without water) is a direct assumption when the ability of separating the products is available. However, the kinetic model developed herein does not consider the methanol co-fed with DME. As repeatedly explained in this thesis, the kinetic model predicts different reactivity for DME and methanol. Therefore, specific experimental data with this feed will be recommended, thus refining the kinetic parameters for reliable predictions of the product distribution using DME/methanol mixtures.

The necessity of regenerating the catalyst after the cracking of paraffins sounds likewise obvious. Hence, the possibilities of using a reactor configuration with catalyst circulation or a set of parallel packed bed reactors should be studied for this reaction. Furthermore, the same regenerator unit could be used for both processes aiming for the integration and energy intensification of the process. Also following the integration strategy, the combined reaction of oxygenates and paraffins studied in Chapter 3 can be contemplated (dashed line in Figure 6.25). Evidently, all these proposals would require the reconsideration of the first stages of the work in order to direct the experimental planning and data analyses to energy and process integration considerations. Not to mention the ultimate factor that decides the viability of a process implementation: the economic optimization.

Chapter 7

Conclusions

On the fundamentals of DTO process, catalytic cracking of paraffins and their combined conversion

The good performance of HZSM-5 zeolite-based catalysts in the DTO process is due to its selectivity to light olefins, stability and regenerability through the combustion of coke. These catalysts are also able to intensify the production of light olefins or BTX through the cracking of C_{5+} paraffins, one of the main byproducts of the DTO process. The stability of the catalyst is a consequence of the zeolite porous structure, and can be enhanced by its agglomeration in a mesoporous matrix of $\gamma\text{-Al}_2\text{O}_3$, which provides the catalyst with the required mechanical resistance.

The experimental results on the conversion, yields and product distribution during the DTO reaction in a wide range of operation conditions (temperature, space time and DME concentration in the feed) allow a lump-based reaction network to be established. The steps of the kinetic scheme are coherent with the dual cycle mechanism proposed for the MTO process. In the conversion of DME, the formation of coke is directly related to a favored condensation of the intermediates of the arene cycle. A relevant role in this pathway is played by the catalyst acidity, whereas the presence of water decreases the initial reaction rate of DME conversion, the formation of coke and its evolution towards more condensed carbon structures.

A reaction network of lumps is also proposed from the results of *n*-pentane catalytic cracking, supported by the reported carbocations-based mechanisms. *n*-Pentane is one of the less reactive compounds of the C_{5+} hydrocarbon lump defined for the conversion of DME. Some interesting results are also observed from their combined reaction, which is explained by a synergistic effect of the intermediates of both mechanisms. At certain conditions, the conversion of the paraffin is activated by the presence of DME. Furthermore, the deactivation of the catalyst during the DTO reaction can be mitigated by co-feeding *n*-pentane.

On the kinetic modeling of reactions

The developed methodology for the calculation of kinetic models is based on solving the convection-dispersion-reaction equation in an integral packed reactor. It is a useful tool in order to predict the evolution with time of catalytic processes with complex reaction networks and deactivation kinetics dependent on the composition of the reaction medium. The application of this methodology and the ability to take the *past history* of the catalyst into account are evaluated in the conversion of DME and the cracking of *n*-pentane. The consideration of the activity is a key factor for modeling both reactions, and the concentration of water plays a key role in the kinetic model of DTO reaction. The robustness of the models is described by the fitting of the experimental data, the definition of the reaction steps according

to the mechanisms and the coherency of the kinetic parameters with the extent of these steps as a function of the catalyst acidity.

On the simulation of reactors with deactivation

The proposal of a general methodology for the design of reactors with deactivation helps to advance in a forgotten topic within the literature. The methodology is also based on the convection-dispersion-reaction equation for the gas reactant and products and the catalyst. The definition of the convection and dispersion terms determines the reactor configuration to be simulated: packed bed, moving bed and non-circulating/circulating fluidized bed reactors.

The simulation of this latter presents an added difficulty. The residence time distribution of the solid must be taken into account, for which a parallel compartment (PC) model is proposed. The activity distribution function derived from the residence time distribution of the solid is also considered by combining this model with the population balance theory (PB-PC model). The possibility for its application to numerous catalytic processes with fast catalyst deactivation increases the value of this versatile methodology.

On the design of a dual reactor-regenerator system for the DTO process

The dual reactor-regenerator system for the DTO process is modeled considering fluidized regime with catalyst circulation between both units. The established relation activity-time allows the activity distribution to be determined in each unit and their dependency to be studied. The reactor design using this activity-time consideration for deactivation is a complementary and probably more reliable alternative to the experimentally limited relations activity-content of coke.

The effect of reaction conditions and mean residence time of the catalyst on the product distribution during the unsteady and steady states is well-predicted by the PB-PC model. The possibilities offered by this model and the quality of the kinetic models derived from the experimental data are tested at several reaction conditions for the studied catalysts with different acidity. In both cases, the optimal operation conditions for maximum productions of light olefins is established. The influence of these conditions on the obtained byproducts is also remarkable.

The easy application of this model not only to the DTO process but also to other catalytic processes with fast deactivation makes the methodology encouraging within the general literature of Chemical Reaction Engineering.

On the relevance of the result for the DTO process implementation

The relevance of this thesis is worth mentioning in terms of the methodology developed for the kinetic modeling and reactor design of catalytic processes with

deactivation. A very useful first approach to a reactor performance in any other process can be provided with the suitable experimental data and this computation methodology. The PB-PC model could also be coupled with different flow models for the gas and solid phases, as the ones derived from the two-phase models, thus providing further reliability. Aiming for a hypothetical scale-up of the process, the model can also be combined with attrition models and validated with experiments carried out at larger scales for a refinement of the kinetic parameters. Other studied aspects, as the intensification of light olefins production through the valorization of the paraffin byproducts of the DTO process, could also be interesting from the industrial point of view.

List of Figures

1.1	Production of DME in (a) two stages with metallic (white) and acid catalysts (gray) and in one stage with (b) a bifunctional catalyst and (c) a structured core-shell catalyst.	5
1.2	Schematic packed bed membrane reactor for the direct synthesis of DME over a bifunctional catalyst.	5
1.3	(a) Effect of temperature on the methanol and DME conversions and (b) product distribution in the presence of ethylene (50%) at 350 °C (adapted from [45]).	7
1.4	Comparison of the product distribution for the conversion of (a) methanol (adapted from [45]) and (b) DME (adapted from [44] and [55]). 350 °C.	9
1.5	Schematic three-zone packed bed reactor profile for the MTO/DTO reaction (adapted from [94]).	17
1.6	Relation between the scale of modeling strategy and the prediction of the process performance.	27
1.7	Stages of the design and optimization of catalytic processes (adapted from [197]).	35
1.8	Relationship between the time scale of deactivation, reactor configuration and operation strategy (adapted from [199]).	36
2.1	Stages of the preparation procedure for the zeolite-based catalysts.	44
2.2	Diagram of the reaction system.	48
3.1	Comparison of the XRD patterns of the Z15 zeolite and the CZ15 catalyst.	57
3.2	(a) N ₂ adsorption-desorption isotherms and (b) <i>t</i> BA TPD of the Z140 zeolite, the matrix and the CZ140 catalyst.	58
3.3	Product distribution for DTO process using the matrix. 400 °C, $\tau = 2 \text{ g h mol}^{-1}$, $t = 0 \text{ h}$	59

3.4	Evolution with oxygenate conversion of the selectivity to (a) the primary olefins, (b) C ₂₋₄ paraffins, (c) <i>i</i> -butene and <i>i</i> -C ₄₋₅ paraffins and (d) C ₅₊ hydrocarbons, BTX and CO _x + CH ₄ using CZ140 catalyst.	61
3.5	Evolution with oxygenate conversion of the selectivity to (a) the primary olefins, (b) C ₂₋₄ paraffins, (c) <i>i</i> -butene and <i>i</i> -C ₄₋₅ paraffins and (d) C ₅₊ hydrocarbons, BTX and CO _x + CH ₄ using CZ15 catalyst.	63
3.6	Effect of the matrix on (a) the evolution with time of the conversion and (b) the content of each coke fraction deposited on the used CZ15 catalyst and Z15 zeolite. 350 °C, $\tau = 1.0 \text{ g z h mol}_C^{-1}$	65
3.7	TPO profiles of (a) the used Z15 zeolite at 350 °C, the used CZ15 catalyst at (b) 350 °C and (c) 400 °C and (d) the used CZ140 catalyst at 400 °C. $\tau = 1.0 \text{ g z h mol}_C^{-1}$	67
3.8	Effect of catalyst acidity on (a) the evolution with time of the conversion and (b) the content of each coke fraction deposited on these used catalysts at 350 and 400 °C. $\tau = 1.0 \text{ g h mol}_C^{-1}$	69
3.9	Effect of temperature on the evolution with time of the conversion for (a) the CZ15 and (b) the CZ140 catalysts and on the content of each coke fraction deposited on the used (c) CZ15 and (d) CZ140 catalysts. $\tau = 1.0 \text{ g h mol}_C^{-1}$	71
3.10	Effect of the dilution in N ₂ and water (W) on the evolution with time of the conversion at (a) 350 °C and (b) 400 °C and on the content of each coke fraction deposited on the used CZ15 catalysts at (c) 350 °C and (d) 400 °C. $\tau = 1.0 \text{ g h mol}_C^{-1}$	74
3.11	Evolution with time of the conversion and yields of olefins and the rest of hydrocarbons in reaction-regeneration cycles using the CZ15 catalyst. (a) 350 °C, $\tau = 1.0 \text{ g h mol}_C^{-1}$; (b) 350 °C, $\tau = 0.5 \text{ g h mol}_C^{-1}$. Regeneration conditions indicated in the figure after a temperature ramp from 350 to 550 °C.	77
3.12	Evolution with time of the conversion and yields of olefins and the rest of hydrocarbons in reaction-regeneration cycles at 400 °C and $\tau = 0.5 \text{ g h mol}_C^{-1}$ using the (a) CZ15 and (b) CZ140 catalysts. Regeneration conditions indicated in the figure after a temperature ramp from 400 to 550 °C in air.	78
3.13	Effect of co-feeding different DME/nC ₅ ratios on (a) the initial nC ₅ conversion and evolution with time of nC ₅ and DME conversions in individual (hollow symbols) and combined reactions (filled symbols) with DME:nC ₅ ratios in the feed of (b) 1:1, (c) 4:1 and (d) 9:1, using the CZ15 catalyst. 400 °C, $\tau = 0.5 \text{ g h mol}_C^{-1}$	81

3.14	Effect of OX:nC ₅ ratio in the feed on the initial nC ₅ conversion using the CZ140 catalyst. 500 °C, $\tau = 1.0 \text{ g h mol}_C^{-1}$	83
3.15	Effect of OX:nC ₅ ratio in the feed on the evolution with time of nC ₅ and DME conversions in individual (hollow symbols) and combined reactions (filled symbols) with co-fed DME:nC ₅ ratios of (a) 1:9, (b) 1:4 and (c) 1:1 using the CZ140 catalyst and (d) effect of co-feeding N ₂ and nC ₅ on the evolution with time of DME conversion. 500 °C, $\tau = 1.0 \text{ g h mol}_C^{-1}$	84
4.1	Effect of temperature on the evolution with (a) space time ($t = 0$) and (b) time ($\tau = 0.6 \text{ g h mol}_C^{-1}$) of the nC ₅ conversion with the CZ15 catalyst.	89
4.2	Evolution with time of the yields of products at (a) 550 °C with $\tau = 0.3 \text{ g h mol}_C^{-1}$ and (b) 400 °C with $\tau = 1.1 \text{ g h mol}_C^{-1}$ using the CZ15 catalyst.	90
4.3	CFM images of (a) the fresh (reflection) and (b) a used CZ15 catalyst (excitation wavelength, 488 and 561 nm).	91
4.4	TPO profiles of the used CZ15 catalyst at (a) different temperatures ($\tau = 0.6 \text{ g h mol}_C^{-1}$) and (b) space time values (in g h mol_C^{-1}). $t = 15 \text{ h}$	92
4.5	(a) Evolution with space time of the content of coke at different temperatures and (b) its effect on the BET specific surface area and acidity of the CZ15 catalyst with $\tau = 1.0 \text{ g h mol}_C^{-1}$. $t = 15 \text{ h}$	93
4.6	Selectivity to products with CZ15 and CZ140 catalysts at (a) 500 °C and (b) 550 °C and evolution with time of each conversion at (c) 500 °C and (d) 550 °C using different space time values (in g h mol_C^{-1}).	94
4.7	Evolution with time of the yields of products using the CZ15 catalyst with (a) $\tau = 0.15 \text{ g h mol}_C^{-1}$ and (b) $\tau = 1.00 \text{ g h mol}_C^{-1}$ and the CZ140 catalyst with (c) $\tau = 0.30 \text{ g h mol}_C^{-1}$ and (d) $\tau = 4.00 \text{ g h mol}_C^{-1}$. 550 °C.	96
4.8	Block diagram for the computation of the kinetic parameters.	102
4.9	Effect of hydrocarbon chain length on the conversion of paraffins and the selectivity to products to CZ15 catalyst. 500 °C, $\tau = 0.3 \text{ g h mol}_C^{-1}$, $t = 0 \text{ h}$	104
4.10	Yields of products in the thermal cracking of nC ₅ . 550 °C; $\tau = 0 \text{ g h mol}_C^{-1}$; $t = 0 \text{ h}$	108

4.11	Comparison of the experimental data (symbols) to those predicted by the model (lines) for the evolution with (a, b) space time and (c, d) time of the molar fractions using the CZ15 catalyst. (a) 400 °C, $t = 0$ h; (b) 550 °C, $t = 0$ h; (c) 500 °C, $\tau = 0.15$ g h mol $^{-1}$; (d) 550 °C, $\tau = 0.6$ g h mol $^{-1}$	114
4.12	Comparison of the experimental data (symbols) to those predicted by the model (lines) for the evolution with (a, b) space time and (c, d) time of the molar fractions using the CZ140 catalyst. (a) 500 °C, $t = 0$ h; (b) 550 °C, $t = 0$ h; (c) 500 °C, $\tau = 4.5$ g h mol $^{-1}$; (d) 550 °C, $\tau = 4.0$ g h mol $^{-1}$	116
4.13	Simulated maximum yields of (a) olefins and (b) BTX obtained at different temperatures with the CZ15 and CZ140 catalysts, respectively.	118
4.14	Simulated contour maps with space time and time of the activity for the (a) CZ15 and (b) CZ140 catalysts at 550 °C.	119
4.15	Simulated contour maps with space time and time of the yield of (a) BTX and (b) olefins and the selectivity to (c) BTX and (d) olefins for the (a, c) CZ15 and (b, d) CZ140 catalysts at 550 °C.	120
5.1	Parity plot for the calculated and experimental data of molar fractions in the DTO process using the CZ140 catalyst at (a) 325 °C, (b) 350 °C, (c) 375 °C, (d) 400 °C.	131
5.2	Comparison of the average (a) kinetic constants and (b) apparent activation energy values for the groups of steps of the reaction network of DTO process using the CZ140 catalyst.	132
5.3	Comparison of the errors and significance test result for the deactivation equation tested for DTO process using the CZ140 catalyst.	133
5.4	Comparison of the experimental data (symbols) to those predicted by the model (lines) for the evolution with space time of the molar fractions using the CZ140 catalyst at (a) 325 °C, (b) 350 °C, (c) 375 °C and (d) 400 °C. $t = 0$	134
5.5	Comparison of the experimental data (symbols) to those predicted by the model (lines) for the evolution with time of the molar fractions using the CZ140 catalyst. (a) 325 °C, $\tau = 4.5$ g h mol $^{-1}$; (b) 350 °C, $\tau = 3.25$ g h mol $^{-1}$; (c) 375 °C, $\tau = 1.7$ g h mol $^{-1}$; (d) 400 °C, $\tau = 3.25$ g h mol $^{-1}$	136
5.6	Comparison of the experimental data (symbols) to those predicted by the model (lines) for the evolution with space time of the molar fractions using the CZ15 catalyst at (a) 350 °C and (b) 375 °C. $t = 0$	138

5.7	Comparison of the experimental data (symbols) to those predicted by the model (lines) for the evolution with time of the molar fractions using the CZ15 catalyst. (a) 325 °C, $\tau = 1.0 \text{ g h mol}_C^{-1}$; (b) 325 °C, $\tau = 2.0 \text{ g h mol}_C^{-1}$; (c) 375 °C, $\tau = 0.5 \text{ g h mol}_C^{-1}$; (d) 375 °C, $\tau = 1.0 \text{ g h mol}_C^{-1}$	139
5.8	Effect of temperature on the evolution with space time of the water concentration in the reaction medium using the (a) CZ140 and (b) CZ15 catalysts. $t = 0 \text{ h}$	141
5.9	Effect of space time (in g h mol_C^{-1}) on the evolution with time of the water concentration in the reaction medium using the CZ140 catalyst at (a) 325 °C, (b) 350 °C, (c) 375 °C and (d) 400 °C.	143
5.10	Effect of space time (in g h mol_C^{-1}) on the evolution with time of the activity of the CZ140 catalyst at the outlet of the reactor at (a) 325 °C, (b) 350 °C, (c) 375 °C and (d) 400 °C.	144
5.11	Evolution with time of the simulated contour maps with space time of the activity of the CZ140 catalyst at (a) 325 °C, (b) 350 °C, (c) 375 °C and (d) 400 °C. Color map from $a = 0.3$ (black) to $a = 1$ (white).	145
5.12	Effect of temperature on the evolution with time of the activity of the CZ15 catalyst at the outlet of the reactor. $\tau = 2.0 \text{ g h mol}_C^{-1}$	146
6.1	Simplified diagram of the (a) packed bed, (b) moving bed and (c) fluidized bed reactor configurations.	150
6.2	Parallel compartment model for describing a circulating fluidized bed reactor.	153
6.3	Distribution of the catalyst particles in each compartment based on the \mathbf{E} and cumulative \mathbf{F} curves for a complete mixed solid in a CFBR.	154
6.4	Diagram of a circulating fluidized bed reactor-regenerator system based on the PB-PC model.	158
6.5	Evolution with time of the activity of the CZ140 catalyst (dashed line) and the molar fractions (solid lines) in a co-current MBR using: (a) 375 °C, $\tau = 1.5 \text{ g h mol}_C^{-1}$, DME:W = 1:0 and $\tau_m = 1 \text{ h}$; (b) 400 °C, $\tau = 1.5 \text{ g h mol}_C^{-1}$, DME:W = 1:0 and $\tau_m = 10 \text{ h}$; (c) 400 °C, $\tau = 3.0 \text{ g h mol}_C^{-1}$, DME:W = 1:0 and $\tau_m = 1 \text{ h}$; (d) 400 °C, $\tau = 3.0 \text{ g h mol}_C^{-1}$, DME:W = 1:1 and $\tau_m = 10 \text{ h}$	160
6.6	Effect of temperature, DME:W ratio and τ_m on (a) the steady-state activity profile of the CZ140 catalyst and (b) the yields of products at the outlet of the reactor. $\tau = 1.5 \text{ g h mol}_C^{-1}$	162

6.7	Effect of MBR contact regime, co-current (solid lines) and counter-current (dashed lines), on the steady-state (a, b) activity profile of the CZ140 catalyst with the space time and (c, d) yields of products using (a, c) $\tau_m = 1$ h and (b, d) $\tau_m = 10$ h. $\tau = 1.5$ g h mol _C ⁻¹	163
6.8	Evolution with time of (a, b) the activity distribution function, (c, d) the conversion and yields of products for (a, c) the CZ140 catalyst using $\tau = 3.5$ g h mol _C ⁻¹ , and (b, d) the CZ15 catalyst using $\tau = 1.0$ g h mol _C ⁻¹ . 375 °C, $\tau_m = 5$ h, DME:W = 1:0.	167
6.9	Evolution with time of (a, b, c) the activity distribution function and (d) the conversion for the CZ140 catalyst using $\tau = 3.5$ g h mol _C ⁻¹ with (a) $\tau_m = 10$ h and (b) $\tau_m \rightarrow \infty$, and (c) the CZ15 catalyst using $\tau = 1.0$ g h mol _C ⁻¹ with $\tau_m \rightarrow \infty$. 375 °C, DME:W = 1:0.	168
6.10	Evolution with time of (a, b) the activity distribution function of the CZ140 catalyst, (c, d) the conversion and yields of products for $f_a(a, 0, t)$ centered at (a, c) $a = 0.7$ and (b, d) $a = 0.99$. 375 °C, $\tau = 3.5$ g h mol _C ⁻¹ , $\tau_m = 10$ h, DME:W = 1:0.	170
6.11	Effect of space time on the steady-state (a) activity distribution function and (b) yields of products for the CZ140 catalyst. 375 °C, $\tau_m = 5$ h, DME:W = 1:0.	172
6.12	Effect of temperature on the steady-state (a) activity distribution function and (b) yields of products for the CZ140 catalyst. $\tau = 2.0$ g h mol _C ⁻¹ , $\tau_m = 5$ h, DME:W = 1:0.	173
6.13	Effect of the DME dilution in water (W) and N ₂ on the steady-state (a, b) activity distribution function and (c, d) yields of products for the CZ140 catalyst at (a, c) 375 °C and (b, d) 400 °C. $\tau = 2.0$ g h mol _C ⁻¹ , $\tau_m = 5$ h.	174
6.14	Steady-state (a) activity distribution function and (b) yields of products for the CZ140 and CZ15 catalysts. 375 °C, $\tau = 2.0$ g h mol _C ⁻¹ , $\tau_m = 5$ h, DME:W = 1:0.	176
6.15	Comparison of (a) the simulated activity recovery and (b) the reactivation rate with the proposed model and that reported by Gayubo et al. [232].	178
6.16	Evolution with time (in h) of the activity distribution function in the regenerator for $f'_a(a, 0, t)$ centered at (a) $a = 0.01$, (b) $a = 0.1$, (c) $a = 0.25$ and (d) $a = 0.5$. 550 °C, $\tau_m = 1$ h.	180
6.17	Effect of the mean residence time of the catalyst on the steady-state activity distribution function in the regenerator for $f'_a(a, 0, t)$ centered at (a) $a = 0.01$, (b) $a = 0.1$, (c) $a = 0.25$ and (d) $a = 0.5$. 550 °C.	181

- 6.18 Simplified diagram of the dual reactor-regenerator system. 183
- 6.19 Simultaneous evolution with time of the activity distribution functions in the (a, c) reactor and (b, d) regenerator for f_{a0}/f'_{a0} centered at (a, b) $a = 0.9$ and (c, d) $a = 0.7$ using the CZ140 catalyst. 375 °C, $\tau = 3.5 \text{ g h mol}_C^{-1}$, $\tau_{m,R} = 5 \text{ h}$, DME:W = 1:0, $\tau_{m,Reg} = 1 \text{ h}$. . . 185
- 6.20 Simultaneous evolution with time of the activity distribution function in the (a) reactor and (b) regenerator for f_{a0}/f'_{a0} centered at $a = 0.2$ using the CZ140 catalyst. 375 °C, $\tau = 3.5 \text{ g h mol}_C^{-1}$, $\tau_{m,R} = 5 \text{ h}$, DME:W = 1:0, $\tau_{m,Reg} = 1 \text{ h}$ 186
- 6.21 Evolution with time of (a) the conversion and (b) the average activity in the reactor (solid lines) and regenerator (dashed lines) for f_{a0}/f'_{a0} centered at $a = 0.9$, $a = 0.7$ and $a = 0.2$ using the CZ140 catalyst. 375 °C, $\tau = 3.5 \text{ g h mol}_C^{-1}$, $\tau_{m,R} = 5 \text{ h}$, DME:W = 1:0, $\tau_{m,Reg} = 1 \text{ h}$. 187
- 6.22 Effect of the mean residence time in the reactor on the steady-state (a, b) activity distribution function in the reactor and regenerator and (c, d) yields of products for the CZ140 catalyst at (a, c) 375 °C, $\tau = 3.5 \text{ g h mol}_C^{-1}$ and (b, d) 400 °C, $\tau = 1.5 \text{ g h mol}_C^{-1}$. DME:W = 1:0, $\tau_{m,Reg} = 1 \text{ h}$ 189
- 6.23 Effect of the mean residence time in the reactor on the steady-state (a) activity distribution function in the reactor and regenerator and (b) yields of products for the CZ15 catalyst. 375 °C, $\tau = 1.0 \text{ g h mol}_C^{-1}$. DME:W = 1:0, $\tau_{m,Reg} = 1 \text{ h}$ 190
- 6.24 Simulated contour maps with space time and mean residence time in the reactor of the yield of (a, c, e) olefins and (b, d, f) C_{5+} hydrocarbons for the CZ140 catalyst at (a, b) 350 °C, (c, d) 375 °C and (e, f) 400 °C. DME:W = 1:0, $\tau_{m,Reg} = 1 \text{ h}$ 191
- 6.25 Diagram of the proposed DTO process integrating the catalyst regeneration (Reg.), the product stream separation (Sep.), the catalytic cracking (CC) of paraffins and the combined reaction of oxygenates and paraffins (dashed lines). Green lines: studied in this thesis, orange lines: further work required. 194

List of Tables

2.1	Analysis conditions for the chromatographic columns.	52
3.1	Porous and acid properties of the zeolites, the matrix and the catalysts from N_2 and tBA adsorption-desorption.	58
3.2	Kinetic parameters of the combustion of each coke fraction deposited on the surface of CZ15 and CZ140 catalysts.	66
3.3	Porous and acid properties of the used CZ15 and CZ140 catalysts at different reaction conditions from N_2 and tBA adsorption-desorption.	70
4.1	Total content of coke, specific surface area and acidity of the fresh and used catalysts at 500 and 550 °C. $\tau = 1.0 \text{ g h mol}_C^{-1}$	97
4.2	Proposed deactivation equations for the catalytic cracking of nC_5	109
4.3	Statistic comparison of the kinetic models formed by the reaction networks RN_1 , RN_2 or RN_3 and the deactivation equation DE_3	110
4.4	Statistic comparison of the kinetic models formed by the reaction network RN_3 and the deactivation equations DE_1 - DE_5	111
4.5	Kinetic constants at 500 °C and apparent activation energy values for the catalytic cracking of nC_5 over CZ15 catalyst.	113
4.6	Kinetic constants at 500 °C and apparent activation energy values for the catalytic cracking of nC_5 over CZ140 catalyst.	115
4.7	Average kinetic constants at 500 °C, apparent activation energy values and kinetic parameter ratios for CZ15 and CZ140 catalysts.	117
5.1	Proposed deactivation equations (DE) for the DTO process.	128
5.2	Kinetic and adsorption constants at 350 °C, apparent activation energy and adsorption heat values for the DTO process over CZ140 catalyst.	130
5.3	Kinetic and adsorption constants at 350 °C, apparent activation energy and adsorption heat values for the DTO process over CZ15 catalyst.	137

- 6.1 Definition of the convection and dispersion terms in equation (6.1)
for the different reactor configurations. 149

List of Schemes

1.1	Reaction network for the direct synthesis of DME.	3
1.2	Origin of (a) Brønsted and (b) Lewis acid sites in zeolites.	10
1.3	Proposed route for the formation of the methoxy species from (a) DME and (b) methanol (adapted from [75]).	11
1.4	Proposed routes for the formation of the first C–C bond from methoxy species through (a) methoxymethyl cation mechanism, (b) methane-formaldehyde mechanism (both adapted from [79]), (c) carbene insertion mechanism and (d) carbonylation mechanism (both adapted from [73]).	12
1.5	Proposed scheme for the dual cycle mechanism (adapted from [87]).	14
1.6	Proposed route for the bimolecular cracking mechanism of paraffins (adapted from [135]).	20
1.7	Proposed route for the monomolecular cracking mechanism of paraffins (adapted from [135]).	21
1.8	Proposed route for oligomerization-cracking mechanism of paraffins (adapted from [135]).	22
1.9	Proposed route for cyclization-aromatization mechanism of paraffins (adapted from [143]).	23
1.10	Plausible routes for the enhanced catalytic cracking of paraffins by the intermediates of methanol conversion (a) <i>via</i> hydride transfer by a SMS or (b) <i>via</i> carbenium ion from the first olefin.	24
1.11	Proposed MTO reaction network for a microkinetic model (adapted from [164]). MeOH ₂ ⁺ , DMO ⁺ = adsorbed species; R ⁺ = alkoxy species; H ⁺ , bs = acid and basic sites; OM = oxonium methylene. . .	29
1.12	Proposed lump-based reaction network for the MTH reaction (adapted from [166]). O = C ₂ ⁼ + C ₃ ⁼ + C ₄ ⁼	30
3.1	Lump-based adaptation of the dual cycle mechanism for DTO process.	64
3.2	Lump-based adaptation of the dual cycle mechanism for co-fed DME and nC ₅ conversion.	79

- 4.1 Proposed reaction network RN_1 for the catalytic cracking of nC_5 . . . 105
- 4.2 Proposed reaction network RN_2 for the catalytic cracking of nC_5 . . . 106
- 4.3 Proposed reaction network RN_3 for the catalytic cracking of nC_5 . . . 107

- 5.1 Lump-based simplification of the dual cycle mechanism for DTO
process. 124
- 5.2 Proposed reaction network for DTO process. 125

Nomenclature

ΔH	Heat associated with the adsorption, kJ mol^{-1}
a	Activity
a_0	Activity at the entrance of the regenerator
a_j	Activity for each j step of the reaction network
\bar{a}	Average activity of the catalyst at the outlet of the reactor/regenerator
\bar{a}_r	Average activity of the catalytic bed of each r compartment
Bo	Bodenstein number
C_C	Total content of coke, g g^{-1}
C_{C_k}	Content of each k coke fraction, g g^{-1}
D	Effective dispersion constant of the gas, $\text{m}^2 \text{h}^{-1}$
D_{cat}	Dispersion coefficient associated to the particle movement, $\text{m}^2 \text{h}^{-1}$
d	Deactivation order
E	E curve
E_d	Apparent activation energy of deactivation kinetics, kJ mol^{-1}
E_j	Apparent activation energy of each j step of the reaction network, kJ mol^{-1}
E_k	Apparent activation energy for the combustion of each k coke fraction, kJ mol^{-1}
F	Total molar flow rate, $\text{mol}_C \text{h}^{-1}$
F	F curve

F_i	Molar flow rate of each i lump, $\text{mol}_C \text{ h}^{-1}$
F_r	Molar flow rate in each r compartment, $\text{mol}_C \text{ h}^{-1}$
F_{DME}^0	Molar flow rate of DME at the entrance of the reactor in terms of C units
$F_{\text{nC}_5}^0$	Molar flow rate of nC_5 at the entrance of the reactor in terms of C units
f_a	Activity distribution function
f_{a0}	Initial activity distribution function
$f_{a,r}$	Activity distribution function in each r compartment
K	Adsorption constant for methanol and water, bar^{-1}
K_d	Adsorption constant for water related to the attenuation of catalyst deactivation, bar^{-1}
K^*	Adsorption constant for methanol and water at the reference temperature, bar^{-1}
K_d^*	Adsorption constant for water related to the attenuation of catalyst deactivation at the reference temperature, bar^{-1}
k_d	Deactivation kinetic constant, $\text{bar}^{-1} \text{ h}^{-1}$
k_j	Kinetic constant of each j step of the reaction network
k_r	Reactivation kinetic constant, h^{-1}
k_j^*	Kinetic constant of each j step of the reaction network at the reference temperature
k_k^*	Apparent kinetic constant for the combustion of each k coke fraction at the reference temperature, $\text{h}^{-1} \text{ bar}^{-1}$
L	Catalytic bed length
m	Reactivation order
N_C	(Carbon molar flow rate)/(total molar flow rate) ratio, $\text{mol}_C \text{ mol}^{-1} \text{ h}^{-1}$
n	Number of experimental data
n_e	Total number of experiments
$n_{e,0}$	Total number of initial experimental data

$n_{e,d}$	Total number of experimental data at $t > 0$
n_l	Number of lumps
n_p	Number of parameters of the model
n_r	Number of the parallel compartments
P	Pressure, bar
P_R	partial pressure of the reactant R
P_{O_2}	Partial pressure of O_2 , bar
Pe	Peclet number
q_{cat}	Total catalyst flow rate, $m^3 h^{-1}$
$q_{cat,r}$	Catalyst flow rate in each r compartment, $m^3 h^{-1}$
R	Universal gas constant
$R_{15/140}$	Ratio between the kinetic parameters computed for the CZ15 and CZ140 catalysts
$r_{a,r}$	Rate of activity change with time in each r compartment, h^{-1}
r_d	Deactivation rate, h^{-1}
r_i	Formation rates of each i lump
r_j	Reaction rate of each j step of the reaction network, $mol_C g^{-1} h^{-1}$
r_r	Reactivation rate, h^{-1}
S	Reactor section, m^2
S_r	Section of each r parallel compartment, m^2
SSE	Sum of squares errors between experimental and calculated data
SSE_C	Sum of squares errors between experimental and calculated data for the combustion of coke
T	Temperature, K
T^*	Reference temperature, K
t	time, h

V	Reactor volume, m^3
v	Linear velocity of the gas, m h^{-1}
v_{cat}	Linear velocity of the catalyst particles, m h^{-1}
$v_{cat,r}$	Linear velocity of each r group of catalyst particles, m h^{-1}
x_k	Mass fraction of each k coke fraction, g g^{-1}
y_i	Molar fraction of each i lump in terms of contained C units
y_i^e	Experimental molar fraction of each i lump in terms of contained C units
$y_{i,0}$	Initial molar fraction of each i lump in terms of contained C units
$y_{i,0}^e$	Initial experimental molar fraction of each i lump in terms of contained C units
z	Longitudinal position of the reactor, m

Abbreviations

$t\text{BA}$	<i>tert</i> -Butylamine
CFBR	Circulating bed reactor
CFD	Computational fluid dynamics
CZ140	Catalyst of zeolite with $\text{Si/Al} = 140$
CZ15	Catalyst of zeolite with $\text{Si/Al} = 15$
DE	Deactivation equation
DFT	Density functional theory
DTO	Dimethyl ether-to-olefins process
LM	Levenberg-Marquardt
MBR	Moving bed reactor
MMC	Methoxymethyl cation
MTG	Methanol-to-gasoline process
MTH	Methanol-to-hydrocarbons reaction

MTO	Methanol-to-olefins process
NCFBR	Non-circulating bed reactor
PB	Population balance
PBR	Packed bed reactor
PC	Parallel compartments
RN	Reaction network
S_{BET}	Specific surface area, $\text{m}^2 \text{g}^{-1}$
S_{ext}	External surface area, $\text{m}^2 \text{g}^{-1}$
SMS	Surface methoxy species
V_{mes}	Mesopore volume, $\text{cm}^3 \text{g}^{-1}$
V_{micr}	Micropore volume, $\text{cm}^3 \text{g}^{-1}$
Z140	Zeolite with Si/Al = 140
Z15	Zeolite with Si/Al = 15

Greek Symbols

F	Fisher distribution
α	Confidence level
ε	Effective bed-particle porosity
θ	Term of reaction rate attenuation by the adsorption of methanol and water
θ_d	Term of deactivation rate attenuation by the adsorption of water
ν	Degree of freedom
ξ	Number of experimental runs repeated at the same conditions
ρ	Catalytic bed density, kg m^3
σ^2	Variance
τ	Space time, g h mol_C^{-1}
τ_m	Mean residence time of the catalyst particles, h

τ_r	Residence time of each r particle group
Φ	Coefficients of the vector conservation equation
ϕ	Deactivation function in coke-dependent deactivation models
ω_i	Weight factor for each i lump

Lumps

BTX	Benzene, Toluene and Xylene aromatics
C ₅₊	Long-chained hydrocarbons
DME	Dimethyl ether
HC	Rest of HC without olefins
MeOH	Methanol
O	Light olefins
OX	Oxygenated compounds, dimethyl ether and methanol
P	Light paraffins
W	Water

Subscripts

0	At $t = 0$
cp	Coke precursor cp
i	Lump i
j	Step j of the reaction network
k	Coke fraction k
R	Reactant R
r	Parallel compartment r

Superscripts

*	At the reference temperature
e	Experimental value

Vectors and Matrices

0	Matrix of zeros
A	Matrix of carbon balance coefficients
a_j	Vector of the activity for each <i>j</i> step of the reaction network
E	Vector of the apparent activation energies of each <i>j</i> step of the reaction network and for deactivation kinetics, kJ mol ⁻¹
E_d	Vector of the apparent activation energies of deactivation kinetics, kJ mol ⁻¹
E_j	Vector of the apparent activation energies of each <i>j</i> step of the reaction network, kJ mol ⁻¹
I	Identity matrix
J	Jacobian matrix
J_d	Jacobian matrix for the deactivation kinetics
J_j	Jacobian matrix for the reaction kinetics
k	Vector of the kinetic constant for each <i>j</i> step of the reaction network and the deactivation kinetic constants
k_d	Vector of the deactivation kinetic constants, bar ⁻¹ h ⁻¹
k_j	Vector of the kinetic constants for each <i>j</i> step of the reaction network
k*	Vector of the kinetic constant for each <i>j</i> step of the reaction network and the deactivation kinetic constants at the reference temperature
k_d*	Vector of the deactivation kinetic constants at the reference temperature, bar ⁻¹ h ⁻¹
k_j*	Vector of kinetic constant for each <i>j</i> step of the reaction network at the reference temperature
OF	Objective function vector
p_i	Vector of the partial pressures of each <i>i</i> lump
r	Vector of the reaction rates of each <i>j</i> step of the reaction network and the deactivation rates
r_d	Vector of deactivation rates, h ⁻¹

\mathbf{r}_i	Vector of the formation rates of each i lump
$\mathbf{r}_{i,r}$	Vector of the formation rates of each i lump in each r compartment
\mathbf{r}_j	Vector of the reaction rates of each j step of the reaction network, $\text{mol}_C \text{g}^{-1} \text{h}^{-1}$
$\mathbf{r}_{j,0}$	Vector of the initial reaction rates of each j step of the reaction network, $\text{mol}_C \text{g}^{-1} \text{h}^{-1}$
$\mathbf{r}_{j,r}$	Vector of the reaction rates of each j step of the reaction network in each r compartment, $\text{mol}_C \text{g}^{-1} \text{h}^{-1}$
\mathbf{r}_1	Vector of the formation rates of each i lump and the deactivation rates
\mathbf{y}_0	Vector of the initial molar fractions of each i lump
\mathbf{y}_i	Vector of the molar fractions of each i lump in terms of contained C units
$\mathbf{y}_{i,r}$	Vector of the molar fractions of each i lump in each r compartment in terms of contained C units

References

- [1] Y. K. Park, C. W. Lee, N. Y. Kang, W. C. Choi, S. Choi, S. H. Oh, D. S. Park, *Catal. Surv. Asia* **2010**, *14*, 75–84.
- [2] S. Park, S. Inagaki, Y. Kubota, *Catal. Today* **2016**, *265*, 218–224.
- [3] C. Arcoumanis, C. Bae, R. Crookes, E. Kinoshita, *Fuel* **2008**, *87*, 1014–1030.
- [4] GESTIS Substance database.
- [5] S. Ahlgren, A. Baky, S. Bernesson, Å Nordberg, O. Norén, P. A. Hansson, *Biosyst. Eng.* **2008**, *99*, 145–155.
- [6] J. J. Sciarra, C. J. Sciarra in *Kirk-Othmer Encycl. Chem. Technol.* (Ed.: I. John Wiley & Sons), **2012**.
- [7] G. Restrepo, M. Weckert, R. Brüggemann, S. Gerstmann, H. Frank, *Environ. Sci. Technol.* **2008**, *42*, 2925–2930.
- [8] M. C. Bauer, A. Kruse, *Fuel* **2019**, *254*, 115703.
- [9] H. Javanmard, M. Seyyedi, S. A. Jones, S. M. Nielsen, *Energy Fuels* **2019**, *33*, 10718–10727.
- [10] T. H. Fleisch, A. Basu, R. A. Sills, *J. Nat. Gas Sci. Eng.* **2012**, *9*, 94–107.
- [11] M. Y. Kim, S. H. Yoon, B. W. Ryu, C. S. Lee, *Fuel* **2008**, *87*, 2779–2786.
- [12] L. Jie, L. Shenghua, L. Yi, W. Yanju, L. Guangle, Z. Zan, *Energy Fuels* **2010**, *24*, 2465–2469.
- [13] X. Su, K. Zhang, Y. Snatenkova, Z. Matieva, X. Bai, N. Kolesnichenko, W. Wu, *Fuel Process. Technol.* **2020**, *198*, 106242.
- [14] L. Oar-Arteta, A. Remiro, A. T. Aguayo, J. Bilbao, A. G. Gayubo, *Ind. Eng. Chem. Res.* **2015**, *54*, 9722–9732.
- [15] J. Ereña, R. Garoña, J. M. Arandes, A. T. Aguayo, J. Bilbao, *Catal. Today* **2005**, *107-108*, 467–473.
- [16] A. García-Trenco, A. Martínez, *Appl. Catal. A Gen.* **2012**, *411-412*, 170–179.

- [17] Z. Azizi, M. Rezaeimanesh, T. Tohidian, M. R. Rahimpour, *Chem. Eng. Process.* **2014**, *82*, 150–172.
- [18] D. A. Bulushev, J. R. Ross, *Catal. Today* **2011**, *171*, 1–13.
- [19] A. T. Aguayo, J. Ereña, D. Mier, J. M. Arandes, M. Olazar, J. Bilbao, *Ind. Eng. Chem. Res.* **2007**, *46*, 5522–5530.
- [20] G. A. Olah, A. Goepfert, G. K. S. Prakash, *J. Org. Chem.* **2009**, *74*, 487–498.
- [21] U. Mondal, G. D. Yadav, *J. CO₂ Util.* **2019**, *32*, 299–320.
- [22] U. Mondal, G. D. Yadav, *J. CO₂ Util.* **2019**, *32*, 321–338.
- [23] G. Bonura, M. Cordaro, C. Cannilla, F. Arena, F. Frusteri, *Appl. Catal. B Environ.* **2014**, *152-153*, 152–161.
- [24] M. Cai, V. Subramanian, V. V. Sushkevich, V. V. Ordonsky, A. Y. Khodakov, *Appl. Catal. A Gen.* **2015**, *502*, 370–379.
- [25] S. Asthana, C. Samanta, A. Bhaumik, B. Banerjee, R. K. Voolapalli, B. Saha, *J. Catal.* **2016**, *334*, 89–101.
- [26] F. Frusteri, G. Bonura, C. Cannilla, G. Drago Ferrante, A. Aloise, E. Catizzone, M. Migliori, G. Giordano, *Appl. Catal. B Environ.* **2015**, *176-177*, 522–531.
- [27] A. Ateka, I. Sierra, J. Ereña, J. Bilbao, A. T. Aguayo, *Fuel Process. Technol.* **2016**, *152*, 34–45.
- [28] M. Cai, A. Palčić, V. Subramanian, S. Moldovan, O. Ersen, V. Valtchev, V. V. Ordonsky, A. Y. Khodakov, *J. Catal.* **2016**, *338*, 227–238.
- [29] M. Sánchez-Contador, A. Ateka, A. T. Aguayo, J. Bilbao, *Fuel Process. Technol.* **2018**, *179*, 258–268.
- [30] M. Sánchez-Contador, A. Ateka, M. Ibáñez, J. Bilbao, A. T. Aguayo, *Renew. Energy* **2019**, *138*, 585–597.
- [31] T. A. Semelsberger, K. C. Ott, R. L. Borup, H. L. Greene, *Appl. Catal. B Environ.* **2005**, *61*, 281–287.
- [32] N. Diban, A. M. Urtiaga, I. Ortiz, J. Ereña, J. Bilbao, A. T. Aguayo, *Chem. Eng. J.* **2013**, *234*, 140–148.
- [33] N. Diban, A. M. Urtiaga, I. Ortiz, J. Ereña, J. Bilbao, A. T. Aguayo, *Ind. Eng. Chem. Res.* **2014**, *53*, 19479–19487.
- [34] P. Rodríguez-Vega, PhD thesis, University of the Basque Country (UPV/EHU), **2019**.

- [35] C. D. Chang, A. J. Silvestri, *J. Catal.* **1977**, *47*, 249–259.
- [36] H. Koempel, W. Liebner, *Stud. Surf. Sci. Catal.* **2007**, *167*, 261–267.
- [37] P. Pérez-Urriarte, A. Ateka, A. T. Aguayo, A. G. Gayubo, J. Bilbao, *Chem. Eng. J.* **2016**, *302*, 801–810.
- [38] P. Pérez-Urriarte, A. Ateka, A. G. Gayubo, T. Cordero-Lanzac, A. T. Aguayo, J. Bilbao, *Chem. Eng. J.* **2017**, *311*, 367–377.
- [39] T. Forester, R. Howe, *J. Am. Chem. Soc.* **1986**, *109*, 5076–5082.
- [40] J. Valecillos, H. Manzano, A. T. Aguayo, J. Bilbao, P. Castaño, *Chem-CatChem* **2019**, *11*, 5444–5456.
- [41] H. Yamazaki, H. Shima, H. Imai, T. Yokoi, T. Tatsumi, J. N. Kondo, *J. Phys. Chem. C* **2012**, *116*, 24091–24097.
- [42] P. Pérez-Urriarte, A. Ateka, M. Gamero, A. T. Aguayo, J. Bilbao, *Ind. Eng. Chem. Res.* **2016**, *55*, 6569–6578.
- [43] Y. Li, M. Zhang, D. Wang, F. Wei, Y. Wang, *J. Catal.* **2014**, *311*, 281–287.
- [44] P. Pérez-Urriarte, A. Ateka, A. T. Aguayo, J. Bilbao, *Catal. Lett.* **2016**, *146*, 1892–1902.
- [45] N. Nesterenko, J. Aguilhon, P. Bodart, D. Minoux, J. P. Dath in *Zeolites Zeolite-like Mater.* **2016**, pp. 189–263.
- [46] J. Chen, J. Li, Y. Wei, C. Yuan, B. Li, S. Xu, Y. Zhou, J. Wang, M. Zhang, Z. Liu, *Catal. Commun.* **2014**, *46*, 36–40.
- [47] S. Askari, R. Halladj, M. Sohrabi, *Microporous Mesoporous Mater.* **2012**, *163*, 334–342.
- [48] W. Dai, X. Wang, G. Wu, N. Guan, M. Hunger, L. Li, *ACS Catal.* **2011**, *1*, 292–299.
- [49] W. Dai, G. Wu, L. Li, N. Guan, M. Hunger, *ACS Catal.* **2013**, *3*, 588–596.
- [50] S. Ahmed, *J. Porous Mater.* **2012**, *19*, 111–117.
- [51] L. R. Aramburo, S. Teketel, S. Svelle, S. R. Bare, B. Arstad, H. W. Zandbergen, U. Olsbye, F. M. De Groot, B. M. Weckhuysen, *J. Catal.* **2013**, *307*, 185–193.
- [52] M. Ibañez, P. Pérez-Urriarte, M. Sánchez-Contador, T. Cordero-Lanzac, A. T. Aguayo, J. Bilbao, P. Castaño, *Catalysts* **2017**, *7*, 254–266.
- [53] U. Olsbye, S. Svelle, M. Bjrgen, P. Beato, T. V. Janssens, F. Joensen, S. Bordiga, K. P. Lillerud, *Angew. Chem. Int. Ed.* **2012**, *51*, 5810–5831.

- [54] B. P. C. Hereijgers, F. Bleken, M. H. Nilsen, S. Svelle, K. P. Lillerud, M. Bjørgen, B. M. Weckhuysen, U. Olsbye, *J. Catal.* **2009**, *264*, 77–87.
- [55] S. G. Lee, H. S. Kim, Y. H. Kim, E. J. Kang, D. H. Lee, C. S. Park, *J. Ind. Eng. Chem.* **2014**, *20*, 61–67.
- [56] Q. Sun, Z. Xie, J. Yu, *Nat. Sci. Rev.* **2018**, *5*, 542–558.
- [57] I. Yarulina, A. D. Chowdhury, F. Meirer, B. M. Weckhuysen, J. Gascon, *Nat. Catal.* **2018**, *1*, 398–411.
- [58] E. T. Vogt, B. M. Weckhuysen, *Chem. Soc. Rev.* **2015**, *44*, 7342–7370.
- [59] T. Cordero-Lanzac, A. Ateka, P. Pérez-Urriarte, P. Castaño, A. T. Aguayo, J. Bilbao, *Ind. Eng. Chem. Res.* **2018**, *57*, 13689–13702.
- [60] S. M. Almutairi, B. Mezari, E. A. Pidko, P. C. Magusin, E. J. Hensen, *J. Catal.* **2013**, *307*, 194–203.
- [61] K. Y. Lee, S. W. Lee, S. K. Ihm, *Ind. Eng. Chem. Res.* **2014**, *53*, 10072–10079.
- [62] I. Yarulina, K. De Wispelaere, S. Bailleul, J. Goetze, M. Radersma, E. Abou-Hamad, I. Vollmer, M. Goesten, B. Mezari, E. J. M. Hensen, J. S. Martínez-Espín, M. Morten, S. Mitchell, J. Perez-Ramirez, U. Olsbye, B. M. Weckhuysen, V. Van Speybroeck, F. Kapteijn, J. Gascon, *Nat. Chem.* **2018**, *10*, 804–812.
- [63] S. Bailleul, I. Yarulina, A. E. Hoffman, A. Dokania, E. Abou-Hamad, A. D. Chowdhury, G. Pieters, J. Hajek, K. De Wispelaere, M. Waroquier, J. Gascon, V. Van Speybroeck, *J. Am. Chem. Soc.* **2019**, *141*, 14823–14842.
- [64] R. Khare, Z. Liu, Y. Han, A. Bhan, *J. Catal.* **2017**, *348*, 300–305.
- [65] T. Álvaro-Muñoz, C. Márquez-Álvarez, E. Sastre, *Catal. Today* **2012**, *179*, 27–34.
- [66] S. Mitchell, N. L. Michels, J. Pérez-Ramírez, *Chem. Soc. Rev.* **2013**, *42*, 6094–6112.
- [67] P. Tian, Y. Wei, M. Ye, Z. Liu, *ACS Catal.* **2015**, *5*, 1922–1938.
- [68] N. L. Michels, S. Mitchell, J. Pérez-Ramírez, *ACS Catal.* **2014**, *4*, 2409–2417.
- [69] P. Pérez-Urriarte, M. Gamero, A. Ateka, M. Díaz, A. T. Aguayo, J. Bilbao, *Ind. Eng. Chem. Res.* **2016**, *55*, 1513–1521.
- [70] T. Shoinkhorova, A. Dikhtiarenko, A. Ramirez, A. Dutta Chowdhury, M. Caglayan, J. Vittenet, A. Bendjeriou-Sedjerari, O. S. Ali, I. Morales-Osorio, W. Xu, J. Gascon, *ACS Appl. Mater. Interfaces* **2019**, *11*, 44133–44143.

- [71] D. Lesthaeghe, V. Van Speybroeck, G. B. Marin, M. Waroquier, *Angew. Chem. Int. Ed.* **2006**, *45*, 1714–1719.
- [72] Y. Liu, S. Müller, D. Berger, J. Jelic, K. Reuter, M. Tonigold, M. Sanchez-Sanchez, J. A. Lercher, *Angew. Chem. Int. Ed.* **2016**, *55*, 5723–5726.
- [73] A. D. Chowdhury, K. Houben, G. T. Whiting, M. Mokhtar, A. M. Asiri, S. A. Al-Thabaiti, M. Baldus, B. M. Weckhuysen, *Angew. Chem. Int. Ed.* **2016**, *55*, 1–7.
- [74] N. Y. Chen, W. J. Reagan, *J. Catal.* **1979**, *59*, 123–129.
- [75] Y. Jiang, M. Hunger, W. Wang, *J. Am. Chem. Soc.* **2006**, *128*, 11679–11692.
- [76] A. T. Aguayo, A. G. Gayubo, R. Vivanco, A. Alonso, J. Bilbao, *Ind. Eng. Chem. Res.* **2005**, *44*, 7279–7286.
- [77] T. Omojola, D. B. Lukyanov, N. Cherkasov, V. L. Zholobenko, A. C. Van Veen, *Ind. Eng. Chem. Res.* **2019**, *58*, 16479–16488.
- [78] J. Li, Z. Wei, Y. Chen, B. Jing, Y. He, M. Dong, H. Jiao, X. Li, Z. Qin, J. Wang, W. Fan, *J. Catal.* **2014**, *317*, 277–283.
- [79] Z. Wei, Y. Y. Chen, J. Li, P. Wang, B. Jing, Y. He, M. Dong, H. Jiao, Z. Qin, J. Wang, W. Fan, *Catal. Sci. Technol.* **2016**, *6*, 5526–5533.
- [80] T. Omojola, D. B. Lukyanov, A. C. van Veen, *Int. J. Chem. Kinet.* **2019**, *51*, 528–537.
- [81] Z. Wei, Y. Y. Chen, J. Li, W. Guo, S. Wang, M. Dong, Z. Qin, J. Wang, H. Jiao, W. Fan, *J. Phys. Chem. C* **2016**, *120*, 6075–6087.
- [82] P. N. Plessow, F. Studt, *ACS Catal.* **2017**, *7*, 7987–7994.
- [83] I. M. Dahl, S. Kolboe, *J. Catal.* **1994**, *149*, 458–464.
- [84] S. Xu, A. Zheng, Y. Wei, J. Chen, J. Li, Y. Chu, M. Zhang, Q. Wang, Y. Zhou, J. Wang, F. Deng, Z. Liu, *Angew. Chem. Int. Ed.* **2013**, *52*, 11564–11568.
- [85] W. Dai, C. Wang, M. Dyballa, G. Wu, N. Guan, L. Li, Z. Xie, M. Hunger, *ACS Catal.* **2015**, *5*, 317–326.
- [86] S. Ilias, A. Bhan, *ACS Catal.* **2013**, *3*, 18–31.
- [87] J. S. Martinez-Espin, M. Mortén, T. V. Janssens, S. Svelle, P. Beato, U. Olsbye, *Catal. Sci. Technol.* **2017**, *7*, 2700–2716.
- [88] M. Bjørgen, S. Svelle, F. Joensen, J. Nerlov, S. Kolboe, F. Bonino, L. Palumbo, S. Bordiga, U. Olsbye, *J. Catal.* **2007**, *249*, 195–207.
- [89] J. Chen, J. Li, C. Yuan, S. Xu, Y. Wei, Q. Wang, Y. Zhou, J. Wang, M. Zhang, Y. He, S. Xu, Z. Liu, *Catal. Sci. Technol.* **2014**, *4*, 3268–3277.

- [90] J. S. Martinez-Espin, K. De Wispelaere, M. Westgård Erichsen, S. Svelle, T. V. Janssens, V. Van Speybroeck, P. Beato, U. Olsbye, *J. Catal.* **2017**, *349*, 136–148.
- [91] S. Svelle, M. Visur, U. Olsbye, Saepurahman, M. Bjørgen, *Top. Catal.* **2011**, *54*, 897–906.
- [92] C. M. Wang, Y. D. Wang, Z. K. Xie, *J. Catal.* **2013**, *301*, 8–19.
- [93] A. Hwang, D. Prieto-Centurion, A. Bhan, *J. Catal.* **2016**, *337*, 52–56.
- [94] U. Olsbye, S. Svelle, K. P. Lillerud, Z. H. Wei, Y. Y. Chen, J. F. Li, J. G. Wang, W. B. Fan, *Chem. Soc. Rev.* **2015**, *44*, 7155–7176.
- [95] D. Chen, K. Moljord, A. Holmen, *Microporous Mesoporous Mater.* **2012**, *164*, 239–250.
- [96] F. L. Bleken, T. V. Janssens, S. Svelle, U. Olsbye, *Microporous Mesoporous Mater.* **2012**, *164*, 190–198.
- [97] G. Seo, J. H. Kim, H. G. Jang, *Catal. Surv. Asia* **2013**, *17*, 103–118.
- [98] M. Guisnet, P. Magnoux, *Appl. Catal. A Gen.* **2001**, *212*, 83–96.
- [99] M. Guisnet, L. Costa, F. R. Ribeiro, *J. Mol. Catal. A Chem.* **2009**, *305*, 69–83.
- [100] M. Vandichel, D. Lesthaeghe, J. V. der Mynsbrugge, M. Waroquier, V. Van Speybroeck, *J. Catal.* **2010**, *271*, 67–78.
- [101] E. Borodina, H. Sharbini Harun Kamaluddin, F. Meirer, M. Mokhtar, A. M. Asiri, S. A. Al-Thabaiti, S. N. Basahel, J. Ruiz-Martinez, B. M. Weckhuysen, *ACS Catal.* **2017**, *7*, 5268–5281.
- [102] H. Schulz, *Catal. Today* **2010**, *154*, 183–194.
- [103] F. L. Bleken, K. Barbera, F. Bonino, U. Olsbye, K. P. Lillerud, S. Bordiga, P. Beato, T. V. Janssens, S. Svelle, *J. Catal.* **2013**, *307*, 62–73.
- [104] D. Rojo-Gama, M. Signorile, F. Bonino, S. Bordiga, U. Olsbye, K. P. Lillerud, P. Beato, S. Svelle, *J. Catal.* **2017**, *351*, 33–48.
- [105] J. Goetze, B. M. Weckhuysen, *Catal. Sci. Technol.* **2018**, *8*, 1632–1644.
- [106] Z. Wan, G. K. Li, C. Wang, H. Yang, D. Zhang, *Appl. Catal. A Gen.* **2018**, *549*, 141–151.
- [107] D. S. Wragg, A. Grønvold, A. Voronov, P. Norby, H. Fjellvåg, *Microporous Mesoporous Mater.* **2013**, *173*, 166–174.
- [108] D. Mores, J. Kornatowski, U. Olsbye, B. M. Weckhuysen, *Chem. Eur. J.* **2011**, *17*, 2874–2884.

- [109] I. Pinilla-Herrero, U. Olsbye, C. Márquez-Álvarez, E. Sastre, *J. Catal.* **2017**, *352*, 191–207.
- [110] E. Epelde, M. Ibañez, A. T. Aguayo, A. G. Gayubo, J. Bilbao, P. Castaño, *Microporous Mesoporous Mater.* **2014**, *195*, 284–293.
- [111] L. Qi, J. Li, L. Wang, C. Wang, L. Xu, Z. Liu, *Catal. Sci. Technol.* **2017**, *7*, 2022–2031.
- [112] L. Qi, J. Li, L. Wang, L. Xu, Z. Liu, *Catal. Sci. Technol.* **2017**, *7*, 894–901.
- [113] J. Liu, S. Zhao, X. Chen, B. Shen, *Fuel* **2016**, *166*, 467–472.
- [114] X. Huang, H. Li, W. D. Xiao, D. Chen, *Chem. Eng. J.* **2016**, *299*, 263–275.
- [115] S. M. Sadrameli, *Fuel* **2015**, *140*, 102–115.
- [116] S. M. Sadrameli, *Fuel* **2016**, *173*, 285–297.
- [117] N. Rahimi, R. Karimzadeh, *Appl. Catal. A Gen.* **2011**, *398*, 1–17.
- [118] K. Yang, Y. Yin, S. Lai, L. Zhu, J. Zhang, W. Lai, Y. Lian, W. Fang, *Catal. Lett.* **2018**, *148*, 3570–3582.
- [119] J. Liu, N. He, Y. Zhao, L. Lin, W. Zhou, G. Xiong, H. Xie, H. Guo, *Catal. Lett.* **2018**, *148*, 2069–2081.
- [120] A. Corma, E. Corresa, Y. Matthieu, L. Sauvanaud, S. Al-Bogami, M. Ghrami, A. Bourane, *Catal. Sci. Technol.* **2017**, *7*, 12–46.
- [121] X. Hou, Y. Qiu, Y. Tian, Z. Diao, X. Zhang, G. Liu, *Chem. Eng. J.* **2018**, *349*, 297–308.
- [122] X. Hou, Y. Qiu, E. Yuan, F. Li, Z. Li, S. Ji, Z. Yang, G. Liu, X. Zhang, *Appl. Catal. A Gen.* **2017**, *543*, 51–60.
- [123] X. Hou, Y. Qiu, X. Zhang, G. Liu, *Chem. Eng. J.* **2017**, *307*, 372–381.
- [124] B. Valle, A. G. Gayubo, A. T. Aguayo, M. Olazar, J. Bilbao, *Energy Fuels* **2010**, *24*, 2060–2070.
- [125] P. He, A. Wang, S. Meng, G. M. Bernard, L. Liu, V. K. Michaelis, H. Song, *Catal. Today* **2018**, *323*, 94–104.
- [126] Q. Li, F. Zhang, J. Jarvis, P. He, M. M. Yung, A. Wang, K. Zhao, H. Song, *Fuel* **2018**, *219*, 331–339.
- [127] K. Kubo, T. Takahashi, H. Iida, S. Namba, A. Igarashi, *Appl. Catal. A Gen.* **2014**, *482*, 370–376.
- [128] K. Urata, S. Furukawa, T. Komatsu, *Appl. Catal. A Gen.* **2014**, *475*, 335–340.

- [129] T. Cordero-Lanzac, A. T. Aguayo, P. Castaño, J. Bilbao, *React. Chem. Eng.* **2019**, *4*, 1922–1934.
- [130] T. Cordero-Lanzac, A. T. Aguayo, A. G. Gayubo, P. Castaño, J. Bilbao, *Chem. Eng. J.* **2018**, *331*, 818–830.
- [131] S. Schallmoser, T. Ikuno, M. F. Wagenhofer, R. Kolvenbach, G. L. Haller, M. Sanchez-Sanchez, J. A. Lercher, *J. Catal.* **2014**, *316*, 93–102.
- [132] S. M. Opalka, T. Zhu, *Microporous Mesoporous Mater.* **2016**, *222*, 256–270.
- [133] C. Song, Y. Chu, M. Wang, H. Shi, L. Zhao, X. Guo, W. Yang, J. Shen, N. Xue, L. Peng, W. Ding, *J. Catal.* **2017**, *349*, 163–174.
- [134] H. Konno, T. Okamura, T. Kawahara, Y. Nakasaka, T. Tago, T. Masuda, *Chem. Eng. J.* **2012**, *207-208*, 490–496.
- [135] S. Kotrel, H. Knözinger, B. C. Gates, *Microporous Mesoporous Mater.* **2000**, *35-36*, 11–20.
- [136] M. Boronat, P. M. Viruela, A. Corma, *J. Am. Chem. Soc.* **2004**, *126*, 3300–3309.
- [137] X. Dupain, M. Makkee, J. A. Moulijn, *Appl. Catal. A Gen.* **2006**, *297*, 198–219.
- [138] A. Corma, J. Planelles, J. Sánchez-Marín, F. Tomás, *J. Catal.* **1985**, *93*, 30–37.
- [139] T. F. Narbeshuber, H. Vinek, J. A. Lercher, *J. Catal.* **1995**, *157*, 388–395.
- [140] J. S. Buchanan, J. G. Santiesteban, W. O. Haag, *J. Catal.* **1996**, *158*, 279–287.
- [141] S. Babitz, B. Williams, J. Miller, R. Snurr, W. Haag, H. H. Kung, *Appl. Catal. A Gen.* **1999**, *179*, 71–86.
- [142] X. Hou, Y. Qiu, E. Yuan, X. Zhang, G. Liu, *Appl. Catal. A Gen.* **2017**, *537*, 12–23.
- [143] Y. Ono, H. Kitagawa, Y. Sendoda, *J. Japan Pet. Inst.* **1987**, *30*, 77–88.
- [144] J. C. Vedrine, P. Dejaifve, E. D. Garbowski, E. G. Derouane, *Stud. Surf. Sci. Catal.* **1980**, *5*, 29–37.
- [145] J. R. Anderson, Y. F. Chang, R. J. Western, *J. Catal.* **1989**, *118*, 466–482.
- [146] R. Javaid, K. Urata, S. Furukawa, T. Komatsu, *Appl. Catal. A Gen.* **2015**, *491*, 100–105.
- [147] A. Martin, S. Nowak, B. Lücke, H. Günschel, *Appl. Catal.* **1989**, *50*, 149–155.

- [148] B. Lücke, A. Martin, H. Günschel, S. Nowak, *Microporous Mesoporous Mater.* **1999**, *29*, 145–157.
- [149] D. Mier, A. T. Aguayo, A. G. Gayubo, M. Olazar, J. Bilbao, *Chem. Eng. J.* **2010**, *160*, 760–769.
- [150] S. M. Yu, J. F. Wu, C. Liu, W. Liu, S. Bai, J. Huang, W. Wang, *Angew. Chem. Int. Ed.* **2015**, *54*, 7363–7366.
- [151] G. Roohollahi, M. Kazemeini, A. Mohammadrezaee, R. Golhosseini, *AIChE J.* **2012**, *58*, 2456–2465.
- [152] A. Kazemi, M. Beheshti, R. Khalili, *Chem. Eng. Sci.* **2017**, *172*, 385–394.
- [153] F. Chang, Y. Wei, X. Liu, Y. Qi, D. Zhang, Y. He, Z. Liu, *Catal. Lett.* **2006**, *106*, 171–176.
- [154] S. Standl, O. Hinrichsen, *Catalysts* **2018**, *8*, 626–715.
- [155] S. N. Khadzhiev, M. V. Magomedova, E. G. Peresyphkina, *Pet. Chem.* **2015**, *55*, 503–521.
- [156] L. T. Zhu, W. Y. Ma, Z. H. Luo, *Chem. Eng. Res. Des.* **2018**, *137*, 141–153.
- [157] M. Gao, H. Li, M. Yang, J. Zhou, X. Yuan, P. Tian, M. Ye, Z. Liu, *Chem. Eng. J.* **2019**, *377*, 119668.
- [158] S. Soltanali, R. Halladj, A. Rashidi, M. Bazmi, F. Bahadoran, *Chem. Eng. Res. Des.* **2016**, *106*, 33–42.
- [159] V. Van Speybroeck, K. De Wispelaere, J. Van Der Mynsbrugge, M. Vandichel, K. Hemelsoet, M. Waroquier, *Chem. Soc. Rev.* **2014**, *43*, 7326–7357.
- [160] K. Hemelsoet, J. V. D. Mynsbrugge, K. D. Wispelaere, M. Waroquier, V. V. Speybroeck, *ChemPhysChem* **2013**, *14*, 1526–1545.
- [161] G. F. Froment, *Catal. Rev.* **2005**, *47*, 83–124.
- [162] T. Y. Park, G. F. Froment, *Ind. Eng. Chem. Res.* **2001**, *40*, 4172–4186.
- [163] T. Y. Park, G. F. Froment, *Ind. Eng. Chem. Res.* **2001**, *40*, 4187–4196.
- [164] M. Sedighi, H. Bahrami, J. Towfighi, *J. Ind. Eng. Chem.* **2014**, *20*, 3108–3114.
- [165] P. J. Becker, N. Serrand, B. Celse, D. Guillaume, H. Dulot, *Fuel* **2016**, *165*, 306–315.
- [166] A. T. Aguayo, D. Mier, A. G. Gayubo, M. Gamero, J. Bilbao, *Ind. Eng. Chem. Res.* **2010**, *49*, 12371–12378.
- [167] L. Ying, X. Yuan, M. Ye, Y. Cheng, X. Li, Z. Liu, *Chem. Eng. Res. Des.* **2015**, *100*, 179–191.

- [168] C. Ortega, V. Hessel, G. Kolb, *Chem. Eng. J.* **2018**, *354*, 21–34.
- [169] J. Hao, Y. Zhao, M. Ye, Z. Liu, *Adv. Powder Technol.* **2015**, *26*, 734–741.
- [170] B. Lu, J. Zhang, H. Luo, W. Wang, H. Li, M. Ye, Z. Liu, J. Li, *Chem. Eng. Sci.* **2017**, *171*, 244–255.
- [171] R. Y. Brogaard, B. M. Weckhuysen, J. K. Nørskov, *J. Catal.* **2013**, *300*, 235–241.
- [172] A. Izadbakhsh, A. Khatami, *React. Kinet. Mech. Cat.* **2014**, *112*, 77–100.
- [173] G. F. Froment, *Appl. Catal. A Gen.* **2001**, *212*, 117–128.
- [174] D. Chen, H. P. Rebo, A. Grønvd, K. Moljord, A. Holmen, *Microporous Mesoporous Mater.* **2000**, *35-36*, 121–135.
- [175] D. Chen, A. Grønvd, K. Moljord, A. Holmen, *Ind. Eng. Chem. Res.* **2007**, *46*, 4116–4123.
- [176] R. B. Rostami, M. Ghavipour, Z. Di, Y. Wang, R. M. Behbahani, *RSC Adv.* **2015**, *5*, 81965–81980.
- [177] X. Yuan, H. Li, M. Ye, Z. Liu, *AIChE J.* **2019**, *65*, 662–674.
- [178] Y. Zhang, M. Li, E. Xing, Y. Luo, X. Shu, *Catal. Commun.* **2019**, *119*, 67–70.
- [179] S. Gao, S. Xu, Y. Wei, Q. Qiao, Z. Xu, X. Wu, M. Zhang, Y. He, S. Xu, Z. Liu, *J. Catal.* **2018**, *367*, 306–314.
- [180] S. Müller, Y. Liu, M. Vishnuvarthan, X. Sun, A. C. Van Veen, G. L. Haller, M. Sanchez-Sanchez, J. A. Lercher, *J. Catal.* **2015**, *325*, 48–59.
- [181] C. H. Collett, J. McGregor, *Catal. Sci. Technol.* **2016**, *6*, 363–378.
- [182] J. Zhou, J. Zhang, Y. Zhi, J. Zhao, T. Zhang, M. Ye, Z. Liu, *Ind. Eng. Chem. Res.* **2018**, *57*, 17338–17347.
- [183] P. Magnoux, H. S. Cerqueira, M. Guisnet, *Appl. Catal. A Gen.* **2002**, *235*, 93–99.
- [184] X. Yuan, H. Li, M. Ye, Z. Liu, *Chem. Eng. J.* **2017**, *329*, 35–44.
- [185] O. Levenspiel, *Chemical Reaction Engineering*, 3rd, John Wiley & Sons, New York, **1999**.
- [186] H. S. Fogler, *Elements of Chemical Reaction Engineering*, 3rd, Prentice-Hall, London, **1999**.
- [187] D. Kunii, O. Levenspiel, *Fluidization Engineering*, 2nd, Butterworth-Heinemann, Boston, **1991**.

- [188] A. T. Aguayo, A. G. Gayubo, J. M. Ortega, M. Olazar, J. Bilbao, *Catal. Today* **1997**, *37*, 239–248.
- [189] A. G. Gayubo, A. T. Aguayo, A. E. Sánchez Del Campo, P. L. Benito, J. Bilbao, *Stud. Surf. Sci. Catal.* **1999**, *126*, 129–136.
- [190] M. Luo, Y. Fu, B. Hu, D. Wang, B. Wang, G. Mao, *Appl. Catal. A Gen.* **2019**, *570*, 209–217.
- [191] T. I. Batova, E. K. Khivrich, G. N. Shirobokova, N. V. Kolesnichenko, Y. V. Pavlyuk, G. N. Bondarenko, *Pet. Chem.* **2013**, *53*, 383–387.
- [192] K. De Wispelaere, C. S. Wondergem, B. Ensing, K. Hemelsoet, E. J. Meijer, B. M. Weckhuysen, V. Van Speybroeck, J. Ruiz-Martínez, *ACS Catal.* **2016**, *6*, 1991–2002.
- [193] T. V. Janssens, S. Svelle, U. Olsbye, *J. Catal.* **2013**, *308*, 122–130.
- [194] A. G. Gayubo, A. T. Aguayo, A. L. Morán, M. Olazar, J. Bilbao, *AIChE J.* **2002**, *48*, 1561–1571.
- [195] S. L. Scott, *ACS Catal.* **2018**, *8*, 8597–8599.
- [196] M. Argyle, C. Bartholomew, *Catalysts* **2015**, *5*, 145–269.
- [197] J. A. Moulijn, J. Pérez-Ramírez, R. J. Berger, G. Hamminga, G. Mul, F. Kapteijn, *Catal. Today* **2003**, *81*, 457–471.
- [198] T. Bligaard, R. M. Bullock, C. T. Campbell, J. G. Chen, B. C. Gates, R. J. Gorte, C. W. Jones, W. D. Jones, J. R. Kitchin, S. L. Scott, *ACS Catal.* **2016**, *6*, 2590–2602.
- [199] J. A. Moulijn, A. E. van Diepen, F. Kapteijn, *Appl. Catal. A Gen.* **2001**, *212*, 3–16.
- [200] O. Levenspiel, A. Sadana, *Chem. Eng. Sci.* **1978**, *33*, 1393–1394.
- [201] S. Krishnaswamy, J. R. Kittrell, *Ind. Eng. Chem. Process Des. Dev.* **1979**, *18*, 399–403.
- [202] J. Corella, J. M. Asua, J. Bilbao, *Chem. Eng. Sci.* **1980**, *35*, 1447–1449.
- [203] A. G. Gayubo, J. M. Arandes, A. T. Aguayo, M. Olazar, J. Bilbao, *Chem. Eng. Sci.* **1993**, *48*, 2741–2752.
- [204] V. W. Weekman, *Ind. Eng. Chem. Process Des. Dev.* **1968**, *7*, 252–256.
- [205] G. N. Miertschin, R. Jackson, *Can. J. Chem. Eng.* **1971**, *49*, 514–521.
- [206] P. Le Goff, *Int. Chem. Eng.* **1983**, *23*, 225–237.
- [207] J. M. Arandes, J. Bilbao, *Chem. Eng. Res. Des.* **1986**, *64*, 461–466.

- [208] D. O. Borio, M. Menéndez, J. Santamaria, *Ind. Eng. Chem. Res.* **1992**, *31*, 2699–2707.
- [209] S. Yurchak, *Stud. Surf. Sci. Catal.* **1988**, *36*, 251–272.
- [210] A. G. Gayubo, J. M. Arandes, A. T. Aguayo, M. Olazar, J. Bilbao, *Chem. Eng. J.* **1993**, *51*, 167–176.
- [211] M. Shirzad, M. Karimi, J. A. Silva, A. E. Rodrigues, *Ind. Eng. Chem. Res.* **2019**, *58*, 9179–9198.
- [212] M. S. Gyngazova, A. V. Kravtsov, E. D. Ivanchina, M. V. Korolenko, N. V. Chekantsev, *Chem. Eng. J.* **2011**, *176-177*, 134–143.
- [213] A. N. Zagoruiko, A. S. Belyi, M. D. Smolikov, A. S. Noskov, *Catal. Today* **2014**, *220-222*, 168–177.
- [214] S. Sahebdehfar, P. M. Bijani, M. Saeedizad, F. T. Zangeneh, K. Ganji, *Appl. Catal. A Gen.* **2011**, *395*, 107–113.
- [215] S. Rostom, H. de Lasa, *Chem. Eng. Process.* **2019**, *137*, 87–99.
- [216] K. S. Kang, C. H. Kim, K. K. Bae, W. C. Cho, S. U. Jeong, S. H. Kim, C. S. Park, *Int. J. Hydrogen Energy* **2012**, *37*, 3251–3260.
- [217] B. Jiang, X. Feng, L. Yan, Y. Jiang, Z. Liao, J. Wang, Y. Yang, *Ind. Eng. Chem. Res.* **2014**, *53*, 4623–4632.
- [218] B. Jiang, B. Zhou, Y. Jiang, X. Feng, Z. Liao, Z. Huang, J. Wang, Y. Yang, *Chem. Eng. Res. Des.* **2017**, *122*, 52–62.
- [219] H. V. Ly, D. H. Lim, J. W. Sim, S. S. Kim, J. Kim, *Energy* **2018**, *162*, 564–575.
- [220] M. Kashyap, M. R. Tadiboyina, C. Okolo, S. Al-Mutairi, *Particuology* **2020**, *50*, 127–134.
- [221] M. R. Abbasi, A. Shamiri, M. A. Hussain, S. H. Aghay Kaboli, *J. Chem. Technol. Biotechnol.* **2019**, *94*, 2433–2451.
- [222] A. T. Jarullah, N. A. Awad, I. M. Mujtaba, *Fuel* **2017**, *206*, 657–674.
- [223] M. P. Babu, Y. P. Setty, **2003**, *81*, 118–123.
- [224] G. Hofer, T. Märzinger, C. Eder, F. Pröll, T. Pröll, *Chem. Eng. Sci.* **2019**, *195*, 585–597.
- [225] P. Bachmann, A. Bück, E. Tsotsas, *Powder Technol.* **2016**, *301*, 1067–1076.
- [226] S. Geng, Y. Qian, J. Zhan, H. Zhang, G. Xu, X. Liu, *Powder Technol.* **2017**, *320*, 555–564.
- [227] J. Zhang, G. Xu, *Particuology* **2015**, *19*, 155–163.

- [228] X. Yuan, H. Li, M. Ye, Z. Liu, *Can. J. Chem. Eng.* **2019**, *97*, 500–510.
- [229] J. Zhang, B. Lu, F. Chen, H. Li, M. Ye, W. Wang, *Chem. Eng. Sci.* **2018**, *189*, 212–220.
- [230] H. Li, X. Yuan, M. Gao, M. Ye, Z. Liu, *AIChE J.* **2019**, *65*, 1149–1161.
- [231] H. S. Weng, T. L. Chen, *Chem. Eng. Sci.* **1980**, *35*, 915–924.
- [232] A. G. Gayubo, J. M. Ortega, A. T. Aguayo, J. M. Arandes, J. Bilbao, *Chem. Eng. Sci.* **2000**, *55*, 3223–3235.
- [233] P. Pérez-Urriarte, PhD thesis, University of the Basque Country (UPV/EHU), **2015**.
- [234] J. M. Kanervo, A. O. I. Krause, J. R. Aittamaa, P. H. Hagelberg, K. J. T. Lipiäinen, I. H. Eilos, J. S. Hiltunen, V. M. Niemi, *Chem. Eng. Sci.* **2001**, *56*, 1221–1227.
- [235] T. J. Keskitalo, K. J. Lipiäinen, A. O. Krause, *Chem. Eng. J.* **2006**, *120*, 63–71.
- [236] A. Ochoa, Á. Ibarra, J. Bilbao, J. M. Arandes, P. Castaño, *Chem. Eng. Sci.* **2017**, *171*, 459–470.
- [237] C. Querini, S. Fung, *Appl. Catal. A Gen.* **1994**, *117*, 53–74.
- [238] W. Dai, M. Scheibe, L. Li, N. Guan, M. Hunger, *J. Phys. Chem. C* **2012**, *116*, 2469–2476.
- [239] A. G. Gayubo, A. Alonso, B. Valle, A. T. Aguayo, J. Bilbao, *Appl. Catal. B Environ.* **2010**, *97*, 299–306.
- [240] S. N. Khadzhiev, M. V. Magomedova, E. G. Peresyphkina, *Pet. Chem.* **2014**, *54*, 245–269.
- [241] K. Leistner, A. Nicolle, D. Berthout, P. da Costa, *Combust. Flame* **2012**, *159*, 64–76.
- [242] A. S. Al-Dughaiter, H. de Lasa, *Ind. Eng. Chem. Res.* **2014**, *53*, 15303–15316.
- [243] W. Dai, G. Cao, L. Yang, G. Wu, M. Dyballa, M. Hunger, N. Guan, L. Li, *Catal. Sci. Technol.* **2017**, *7*, 607–618.
- [244] D. Mier, A. G. Gayubo, A. T. Aguayo, M. Olazar, J. Bilbao, *AIChE J.* **2011**, *57*, 2841–2853.
- [245] A. G. Gayubo, A. T. Aguayo, M. Olazar, R. Vivanco, J. Bilbao, *Chem. Eng. Sci.* **2003**, *58*, 5239–5249.
- [246] A. T. Aguayo, A. G. Gayubo, J. Ereña, A. Atutxa, J. Bilbao, *Ind. Eng. Chem. Res.* **2003**, *42*, 3914–3921.

- [247] P. M. Allotta, P. C. Stair, *ACS Catal.* **2012**, *2*, 2424–2432.
- [248] P. Castaño, J. Ruiz-Martínez, E. Epelde, A. G. Gayubo, B. M. Weckhuysen, *ChemCatChem* **2013**, *5*, 2827–2831.
- [249] G. T. Whiting, F. Meirer, M. M. Mertens, A.-J. Bons, B. M. Weiss, P. A. Stevens, E. de Smit, B. M. Weckhuysen, *ChemCatChem* **2015**, *7*, 1312–1321.
- [250] D. Mier, A. T. Aguayo, M. Gamero, A. G. Gayubo, J. Bilbao, *Ind. Eng. Chem. Res.* **2010**, *49*, 8415–8423.
- [251] B. Valle, P. Castaño, M. Olazar, J. Bilbao, A. G. Gayubo, *J. Catal.* **2012**, *285*, 304–314.
- [252] G. Caeiro, R. H. Carvalho, X. Wang, M. A. Lemos, F. Lemos, M. Guisnet, F. Ramôa Ribeiro, *J. Mol. Catal. A Chem.* **2006**, *255*, 131–158.
- [253] T. Ando, *Linear Algebra Appl.* **1995**, *223-224*, 57–64.
- [254] R. D. Skeel, M. Berzins, *SIAM J. Sci. Stat. Comput.* **1990**, *11*, 1–32.
- [255] K. Levenberg, *Quart. Appl. Math.* **1944**, *2*, 164–168.
- [256] D. W. Marquardt, *J. Soc. Ind. Appl. Math.* **1963**, *11*, 431–441.
- [257] A. Janda, B. Vlaisavljevich, L. C. Lin, S. Mallikarjun Sharada, B. Smit, M. Head-Gordon, A. T. Bell, *J. Phys. Chem. C* **2015**, *119*, 10427–10438.
- [258] H. Li, S. A. Kadam, A. Vimont, R. F. Wormsbecher, A. Travert, *ACS Catal.* **2016**, *6*, 4536–4548.
- [259] A. Miyaji, Y. Iwase, T. Nishitoba, N. Q. Long, K. Motokura, T. Baba, *Phys. Chem. Chem. Phys.* **2015**, *17*, 5014–5032.
- [260] R. R. Pinto, P. Borges, M. A. N. D. A. Lemos, F. Lemos, F. R. Ribeiro, *Appl. Catal. A Gen.* **2004**, *272*, 23–28.
- [261] A. Bhan, S. H. Hsu, G. Blau, J. M. Caruthers, V. Venkatasubramanian, W. N. Delgass, *J. Catal.* **2005**, *235*, 35–51.
- [262] X. Hou, Y. Qiu, X. Zhang, G. Liu, *RSC Adv.* **2016**, *6*, 54580–54588.
- [263] A. G. Gayubo, A. Alonso, B. Valle, A. T. Aguayo, M. Olazar, J. Bilbao, *Fuel* **2010**, *89*, 3365–3372.
- [264] J. Palomo, M. A. Rodríguez-Cano, J. Rodríguez-Mirasol, T. Cordero, *Chem. Eng. J.* **2019**, *378*, 122198.
- [265] P. Kumar, J. W. Thybaut, S. Svelle, U. Olsbye, G. B. Marin, *Ind. Eng. Chem. Res.* **2013**, *52*, 1491–1507.
- [266] J. F. Haw, D. M. Marcus, *Top. Catal.* **2005**, *34*, 41–48.
- [267] A. Monzón, E. Romeo, A. Borgna, *Chem. Eng. J.* **2003**, *94*, 19–28.

-
- [268] A. G. Gayubo, A. T. Aguayo, A. Alonso, J. Bilbao, *Ind. Eng. Chem. Res.* **2007**, *46*, 1981–1989.
- [269] T. Cordero-Lanzac, A. T. Aguayo, A. G. Gayubo, P. Castaño, J. Bilbao, *Chem. Eng. J.* **2020**, *379*, 122260.
- [270] Y. Cheng, C. Wu, J. Zhu, F. Wei, Y. Jin, *Powder Technol.* **2008**, *183*, 364–384.
- [271] G. Peng, P. Dong, Z. Li, J. Wang, W. Lin, *Chem. Eng. J.* **2013**, *230*, 406–414.

